

UC Berkeley

UC Berkeley Electronic Theses and Dissertations

Title

An Integrated Approach to Three-Dimensional Bioprinting at Subfreezing Temperatures

Permalink

<https://escholarship.org/uc/item/4qr525cb>

Author

Ukpai, Gideon

Publication Date

2020

Supplemental Material

<https://escholarship.org/uc/item/4qr525cb#supplemental>

Peer reviewed|Thesis/dissertation

An Integrated Approach to Three-Dimensional Bioprinting
at Subfreezing Temperatures

By

Gideon C Ukpai

A dissertation submitted in partial satisfaction of the

requirements for the degree of

Doctor of Philosophy

in

Engineering - Mechanical Engineering

in the

Graduate Division

of the

University of California, Berkeley

Committee in charge:

Professor Boris Rubinsky, Chair

Professor Chris Dames

Professor Kevin Healy

Summer 2020

An Integrated Approach to Three-Dimensional Bioprinting
at Subfreezing Temperatures

Copyright 2020
By
Gideon Ukpai

Abstract

An Integrated Approach to Three-Dimensional Bioprinting at Subfreezing Temperatures

by

Gideon Ukpai

Doctor of Philosophy in Mechanical Engineering

University of California, Berkeley

Professor Boris Rubinsky, Chair

There are over 100,000 patients on the US transplant list alone, and millions more needing transplants globally. Many of these transplant patients have little hope of getting a replacement organ in time to ensure survival. On-demand fabrication of organs and tissues using tissue engineering could provide a solution and save the lives of millions of transplant patients and patients with end-stage organ failure. A major component of fabricating these artificial tissues and organs is the construction of a scaffold, often with the cells incorporated, that simulates the appropriate tissue environment and guides the formation of complex tissue structures. Three-dimensional (3D) bioprinting has emerged as the most promising approach for developing these scaffold constructs, but despite significant advances, the technique faces various challenges. Some factors that have thus far limited the production of clinically relevant constructs include, insufficient mechanical properties for fabrication of full-scale organs, unsustainably long print times, and poor survival of the biological matter during and after printing due to lack of vascularization. Current techniques and emerging methods still fall short of addressing some of these limitations, so in order for continued advancement in this field, alternative approaches are needed.

This work explores in detail a novel technique of doing 3D bioprinting at subfreezing temperatures, called 3D cryoprinting. 3D cryoprinting incorporates the benefits of ice formation at subfreezing temperatures and the flexibility afforded by super soft biomaterials to improve the fabrication of soft tissue scaffolds. This method utilizes controlled freezing to improve mechanical properties of the printed matrix while simultaneously cryopreserving the biological matter. In order to establish 3D cryoprinting as a viable alternative for 3D bioprinting, the challenges and unknown parameters associated with 3D cryoprinting such as the solidification in large objects, cell viability, structural stability during melting, and mass manufacturability are tackled. Several methods and models to control and understand freezing during cryoprinting are developed, including a thermal phase change model for controlling the freezing rate of biological matter during cryoprinting, which substantially improves the process outcome. A method that enables the preservation of the geometric shape after thawing, a crucial element to the viability of 3D cryoprinting, is also developed. And to speed up manufacture and enable mass manufacturing a modified process of cryoprinting is developed, called parallel multilayer cryolithography. The culmination of this work

demonstrates that 3D cryoprinting could be a viable alternative for the fabrication of complex 3D tissue and organ scaffolds, especially in cases of super soft tissue scaffolds where other bioprinting methods have proven inadequate.

Professor Boris Rubinsky
Dissertation Committee Chair

To my family

Table of Contents

Table of Contents	ii
1. Introduction	1
1.1. Motivation and background	1
1.2. Current approaches to three-dimensional (3D) bioprinting	1
1.3. Materials used for 3D bioprinting	5
1.4. Challenges in 3D bioprinting and tissue engineering.....	8
1.5. Three-dimensional (3D) bioprinting at subfreezing temperatures	9
1.6. Thesis overview.....	10
2. Control and optimization of 3D cryoprinting	13
2.1. Introduction	13
2.2. Mathematical model for 3D cryoprinting	14
2.2.1. Thermal model of the phase-change problem.....	15
2.2.2. Extrusion model for the printing process	20
2.2.3. Algorithm for 3D cryoprinting simulation.....	21
2.2.4. Thermophysical parameters for simulation.....	22
2.3. Results.....	23
2.3.1. Variation with printing speed	23
2.3.2. Variation with surface temperature.....	24
2.3.3. Experimental Validation of Mathematical Model.....	25
2.3.4. Addition of cryogenic cooling fluid for control	29
2.3.5. Prediction of cell survivability.....	32
2.4. Discussion and conclusion.....	33
3. Freezing modulated cross-linking for stability of fabricated frozen scaffolds.....	36
3.1. Introduction	36
3.2. 1-D mathematical analysis of freezing modulated cross-linking.....	38
3.2.1. Case 1: Melting of the slab is much faster than diffusion of salt	42
3.2.2. Case 2: Melting rate is comparable to the rate of the diffusion of the salt.....	44
3.3. Results and discussion.....	45
3.4. Conclusion.....	52
4. Microstructure and mechanical properties of cryoprinted constructs	54
4.1. Introduction	54
4.2. Analysis of directional solidification of aqueous solutions	55
4.2.1. Mathematical model of directional device.....	55
4.2.2. Results and validation of device design.....	62

4.3.	Design of directional solidification device	69
4.4.	Experimental studies of ice formation and microstructure using directional solidification..	70
4.4.1.	Effect of cross-linking on ice morphology.....	70
4.4.2.	Effect of cross-linking application sequence on resulting alginate microstructure.....	73
4.4.3.	Effect of cross-linking density on alginate microstructure	75
	Effect of directional microstructure on mechanical properties of alginate.....	77
4.5.	Discussion and conclusion	79
5.	<i>Parallel multilayer cryolithography for mass manufacturing</i>	82
5.1.	Introduction	82
5.2.	Principles of parallel additive manufacturing	83
5.3.	Device description and implementation	86
5.3.1.	Parallel MLCL device.....	86
5.3.2.	Implementation	87
5.4.	Discussion and conclusion	91
6.	<i>Conclusion</i>	93
6.1.	Major findings	93
6.2.	Future perspective	95
6.3.	Closing statement	96
7.	<i>Bibliography</i>	97
8.	<i>Appendix.....</i>	107
8.1.	Code for Extrusion 3D printing thermal phase change model	107
8.2.	Algorithm for thermal image analysis for 3D cryoprinting experiments.....	170
8.3.	Finite difference scheme for directional solidification model	172
8.4.	Algorithm for directional solidification model.....	174

List of Figures

2.1	Schematic of 3D cryoprinting	14
2.2	Diagram showing heat flow through (a) an internal finite difference node (b) a boundary finite difference node (c) an edge finite difference node (d) a corner finite difference node	16
2.3	An example showing the (a) temperature distribution, (b) phase distribution, and (c) cooling rate distribution at a specific time instant ($t = 1.7s$) for printing of CAL at a rate of 50mm/s onto a surface at $-5^{\circ}C$. (d) Temperature distribution, (e) phase distribution, and (f) cooling rate at the same instant ($t = 1.7s$) for printing of CAL at a rate of 25mm/s (0.5x speed) onto a surface at $-5^{\circ}C$. (g) Solidification cooling rate at different heights at a specific location during the printing of CAL onto a surface at $-5^{\circ}C$ for a range of print speeds (h) Solidification cooling rate at different heights at a specific location during the printing of CAL at 50mm/s for a range of surface temperatures	24
2.4	(a) Picture of experimental showing the 3D printer and position of thermal imaging camera (b) Side view image from Ultimaker Cura showing the slicing of the wall to be printed into 15 layers (c) Top view from Ultimaker Cura of the printed object showing the path of the print head for each layer	26
2.5	Experimental validation of model. (a) Thermal Camera Infrared image capture during printing while printing the second layer (2 mins after the start of the print, print speed 1mm/s and surface temperature $-10^{\circ}C$) (b) Plot of the temperature distribution predicted from the model while printing the second layer (2 mins after the start of the print, print speed 1mm/s and surface temperature $-10^{\circ}C$) (c) Comparison of the temperature evolution at point AA from the experiment and similar points B1, B2, and B3 from the simulated model (d) Thermal Camera Infrared image capture of the temperature distribution during printing of the third layer for Case 2 (print speed 1mm/s and surface temperature $-20^{\circ}C$) (e) Thermal Camera Infrared image capture of the temperature distribution during printing of the third layer for Case 3 (print speed 0.5mm/s and surface temperature $-20^{\circ}C$) (f) Thermal Camera Infrared image capture of the temperature distribution during printing showing the melted and overflow of unfrozen material. (g) A picture of the printed wall during experiments showing melting and overflow of unfrozen material (10mm scale bar)	28
2.6	(a) Illustration of the process of cryoprinting in air (b) Temperature distribution (c) Phase distribution, and (d) cooling rate distribution for a hollow rectangular column being printed in air onto a cold surface at $-5^{\circ}C$. (e) An Illustration of the process of cryoprinting using a cryofluid at a controlled level (f) Temperature distribution (g) Phase distribution, and (h) cooling rate distribution for a hollow rectangular column being printed using a cryofluid at $-5^{\circ}C$. (i) Comparison of the temperature and phase fraction over time for a specific location in each layer of the printed column for printing in air and printing using a cryofluid (j) Comparison of the cooling rate and phase fraction over time for a specific location in each layer of the printed column for printing in air and printing using a cryofluid (k) Experimental example showing the melting of a hollow cylindrical column while printing in air [1]. Reproduced with permission from Adamkiewicz	31

	et al. (l) Experimental example showing the successful print (no melting) of the same hollow cylindrical column while using liquid nitrogen as a cryofluid [1]. Reproduced with permission from Adamkiewicz et al. (m) Comparison of the solidification cooling rate in different layers for cryoprinting in air and cryoprinting with a liquid cryofluid	
2.7	(a) Predicted survival probability for the cryoprinting of a bio-ink containing stem cells onto a surface at -5°C in an air surrounding and in a cryofluid (b) Predicted survival probability for the printing of different types of cells, showing the variability in the survival from layer to layer for different cells printed at -10°C	33
3.1	Schematic of the geometry for the melting-diffusion-reaction problem in a semi-infinite medium	38
3.2	Comparison of the concentration profiles from the full solution (Eqs. (3.24)-(3.26)) and first approximate, $A + G \equiv 1$ (Eqs. (3.36)-(3.38)) for all three species. ($2\tau Le Ste = 0.5$, $K = 10$, $Ste = 0.01$)	47
3.3	Variation of the concentration of the three species with dimensionless variables (a) τ (constant $K = 10$ and $Ste = 0.01$) (b) K (constant $2\tau Le Ste = 0.5$ and $Ste = 0.01$), and dimensionless parameter (c) Stefan number (constant $2\tau Le Ste = 0.5$ and $K = 10$)	48
3.4	Variation of the concentration of the three species with dimensionless variables (a) τ (constant $K = 10$) (b) K (constant $\tau = 0.1$), for the regime where melting proceeds much faster than the diffusion of the salt (Case 1)	49
3.5	Comparison of the solution of Case 1 - melting proceeding much faster than the diffusion of the salt to its approximate upper and lower bound solutions for (a) $\tau = 0.01$ $K = 10$ (b) $\tau = 1$ $K = 10$ (c) $K = 0.1$ $\tau = 0.1$ (d) $K = 1000$ $\tau = 0$	50
3.6	Variation of the concentration of the three species with dimensionless variable K , for the regime where rate of melting equals the rate of diffusion of the salt (Case 2)	51
3.7	Comparison of the solution of Case 2 - rate of melting equals the rate of diffusion of the salt to its approximate upper and lower bound solutions for (a) $K = 0.1$ (b) $K = 1000$	52
4.1	Schematic of the directional solidification process	56
4.2	The stationary reference frame for the mathematical model comprising a portion of the specimen and substrate over the high temperature surface, the entire gap, l , and a portion of the specimen and substrate over the low temperature surface ..	59
4.3	Numerical iteration algorithm for determining the interface location and temperature distribution for a given set of device and freezing layer parameters ..	61
4.4	(a) Interface shape through the thickness of the specimen for different values of velocity. (b) Normalized freezing rate, $F(y)l/((T_c - T_h)v)$, through the thickness of the specimen for different values of velocity. (c) Temperature at the bottom ($y = d_{SS}$) and top of the specimen ($y = d + d_{SS}$) as it moves across the gap (d) Interface shift over entire specimen thickness, s_{shift} , as a function of velocity (e) Interface shift over entire specimen thickness, s_{shift} , as a function of	65

	specimen thickness (f) Interface shift over entire specimen thickness, s_{shift} , as a function of temperature gradient across gap	
4.5	Comparison of the normalized mean freezing rate, $F_{mean}l/(T_c - T_h)v$ obtained from the model with that obtained from using the approximate empirical equation (Eqn. (4.21)) for different variations in the freezing device and specimen parameters. This figure shows that there is an agreement between the model and the empirical equation (Eqn. (4.21))	67
4.6	(a) Experimental setup showing the directional solidification of 4% alginate solution in a 1.5mm thick specimen holder. (b) Location of the thermocouples to record temperature history during freezing. The two thermocouples were placed at the same x – location within the sample and different y – locations. One was placed at the bottom to measure the temperature closer to the substrate while the other was placed at the top surface of the specimen to measure the temperature within the specimen farthest away from the substrate (c) Measured temperature profiles at the top and bottom of the specimen frozen on a horizontal directional device across a fixed temperature gradient	68
4.7	Detailed diagram of the directional device designed	70
4.8	Picture of the experimental setup for monitoring the directional solidification on an aqueous solution	72
4.9	Images obtained from the video of the directional freezing process of an alginate sample that is part crosslinked and part non-crosslinked (a) The ice dendrites forming within the non-crosslinked portion of the alginate sample as its frozen on the directional stage (b) Ice crystal dendrites as the freezing interface approaches the interface between the crosslinked and the non-crosslinked region. (c) Random ice nucleation in the crosslinked portion leads to the amorphous ice crystal structure as ice pockets form in the crosslinked region of the alginate. The ice is opaque	73
4.10	Micrographs showing the difference in microstructure for directionally frozen structures crosslinked before freezing (a&b) from those crosslinked after directional freezing (c&d) at 100x (a&c) and 200x (b&d) magnifications. (200um scale bars)	75
4.11	Micrographs showing the difference in microstructure as a function of cross-linking (a) Transverse cross section of 0.03125x crosslinked alginate (b) Transverse cross section of 0.0625x crosslinked alginate (c) Transverse cross section of 0.125x crosslinked alginate (d) Lateral cross section of 0.03125x crosslinked alginate (e) Lateral cross section of 0.0625x crosslinked alginate (f) Lateral cross section of 0.125x crosslinked alginate (g) Top section of 0.03125x crosslinked alginate (h) Top cross section of 0.0625x crosslinked alginate (i) Top cross section of 0.125x crosslinked alginate (500um scale bars)	77
4.12	(a) Comparison of elastic moduli for different compositions of alginate frozen directionally and crosslinked either before or after freezing. (b) Comparison of failure stress for different compositions of alginate frozen directionally and crosslinked either before or after freezing. Data were analyzed using t tests ($p < 0.05$)	79

5.1	Process outline of the steps involved for the assembly of a biological product using parallel multilayer cryolithography	84
5.2	Modified outline of the MLCL process using a controlled temperature surface ...	86
5.3	Device for the implementation of parallel additive manufacturing. (a) overall setup for experiment showing the 2-D printer for layer printing, robot arm for movement of layers, build platform, and cryogenic bath (b) CAD model of redesigned extrusion mechanism for the extrusion of high viscosity biomaterials (c) modified printing platform showing interchangeable lithography plate	87
5.4	Step by step illustration of the parallel multilayer cryolithography process (a) printing of single layer (b) a single printed 2-D layer (c) several printed layers of the cylinder ready for assembly (d) single layer on robot platform about to be picked up for assembly (e) movement and assembly of layer on assembly platform by robot (f) first layer on assembly platform (g) after assembly of four layers on assembly platform (h) finished assembly of cylinder (1cm scale bar unless otherwise stated)	89
5.5	Example of a finished cylinder and its cross section showing continuity. (a) top view of fully assembled cylinder (b) side view of fully assembled cylinder consisting of 10 layers (c) cross section of cylinder showing continuity between the layers (1cm scale bar unless otherwise stated)	90
5.6	An example of more complex ring and grid structures showing the thin layers and the assembly process (a) single layer of the ring structure, about 500um thick (b) side view of fully assembled ring structure after the 10th layer (c) full assembly of ring structure that could represent a blood vessel (30mm OD and 20mm ID) (d)(e) single layer of grid structure (1cm scale bar unless otherwise stated)	91
A8.1	Finite difference formulation showing the different types of elements and nodes and various form of energy in and out of each element	172

List of Tables

2.1	Thermophysical Properties of water	22
2.2	Summary of the print settings used for the experimental validation	26
4.1	Physical and thermophysical properties of water	63
4.2	Properties of the stainless-steel substrate	63

Acknowledgements

I would like to express my deepest thanks to my advisor Professor Boris Rubinsky for his support and advice during my Ph.D. He has been an excellent mentor to me in my four years here at Berkeley, offering encouraging words when I needed them and inspiring me to pursue certain areas of research. Under his supervision, I was introduced to the field of 3D bioprinting, tissue engineering, and cryopreservation and was able to combine those with my interest and background in thermal sciences in an impactful way. His encouragement to explore new ideas and publish my work have made me the researcher and engineer that I am today. His ideas provided the inspiration for this work and his advice as chair of the dissertation committee has led to its successful completion. I am forever grateful for his support.

I am also very grateful to Professors Chris Dames, Kevin Healy, Van Carey, and Stephen Morris for being on my oral qualifying examination and for helping me further my understanding of heat transfer, biomaterials, thermodynamics, and fluids. I learned a lot from each of their classes and their advice before and after the qualifying exam were invaluable to the completion of this work. Special thanks also to Prof. Dames and Prof. Healy who also agreed to review this dissertation.

The members of the biothermal lab have also been a significant help to me over the past few years. I would particularly like to thank my lab colleagues Matthew Powell-Palm and Dr. Chenang Lyu who I had the privilege to work alongside for several years. Matthew and I worked side by side a few feet away from each other for about three years and he was always available to discuss research ideas and offer suggestions whenever I needed them. Him and Chenang were always there to motivate me to do better and to recognize the strengths in my work when I had doubts. They made the last four years an enjoyable and fruitful experience. I would also like to extend thanks to all the other lab members and visitors at the lab over the past four years that have enriched my experience both in and out of the lab. Special mentions to Dr. Gabriel Nastase, Xing Li, Yanpeng Lv, and Justin Aruda. I would also like to extend my gratitude to some of my collaborators at the USDA Western Regional Research Center who I also had the pleasure of working with, Cristina Bilbao and Amanda Sinrod. I would also like to thank previous master's students in the lab, Joseph Sahyoun, Robert Stuart, Sky Wang, Zichen Xiao, who built some of the devices I used to perform some of this work. Special mentions to Bartek Zawada, Gabi Directo, and David Luzzio who have supported my work in some capacity during their time in the lab. And of course, to everyone else whom I have worked with in some capacity during my time here.

I would also like to acknowledge all the friends I have made throughout my time here in Berkeley. They have made the PhD experience one to remember and cherish. They added the much-needed balance outside of the lab and outside of the grad school experience. Notably, my friends and roommates at the Trash Palace and later at the Pristine Palace whose company and friendship kept me going.

Finally, I would like to thank my family for their support all through my educational journey and helping me to reach this point. Particularly, my parents Sunny and Ngozi Ukpai, who ensured I always had the opportunity and freedom to pursue my dreams. Without their support and continual encouragement, I would not have been able to start or finish this program. They sacrificed a lot to make my dreams a reality and for that I am most grateful.

Chapter 1

1. Introduction

1.1. Motivation and background

Organ transplantation is one of the most significant medical developments of the 20th century. It is the last lifeline for many patients facing end stage organ failure and a favorable alternative for patients with life threatening illnesses. But despite these possibilities, it is still generally inaccessible to many. In the United States (US) alone, there are over 100,000 patients on the transplant list and about 20 of them die every day waiting for a transplant [2]. One reason for the lengthy list in the US and worldwide, is the significant shortage of transplantable organs resulting from limited preservation times especially for delicate organs like the hearts and lungs which last a measly 4 - 6 hours outside of the donor body[2]. Despite recent improvements in organ preservation and organ transplantation techniques, currently, only 10% of the worldwide organ transplantation needs are being met [3], partially due to the limited number of organ donors. Since this demand for transplants cannot be fully satisfied by donor organs alone, there is a need for alternative solutions to supplement organ supply. Tissue engineering is a possible solution; it provides a way to develop replacement organs or repair damaged tissue [4–7]. If human organs can be generated artificially, on demand, we could potentially solve the organ supply crisis.

This idea kickstarted the field of tissue engineering, defined by the initiators Robert Langer and Joseph Vacanti, as a way to combine engineering and biology to create artificial tissue or repair damaged tissue [8]. They proposed the combination of cells and growth factors into biodegradable scaffolds which can then be cultivated in vitro to form living tissue and organs [8]. Since then, researchers have applied similar concepts to try to develop tissue constructs for applications in preclinical drug screening [9–11], disease modeling [10,12], tissue repair [13,14], and artificial organs for transplants [4–7], with varying levels of success. Various methods have been used to generate these biodegradable scaffolds¹ on which the tissues are built, like salt leaching, extruded fibers, emulsion freeze-drying, gas foaming, electrospinning, and most recently three-dimensional (3D) printing. Of all these methods 3D printing appears to be the most promising for the development of complex tissue and organs e.g. [15,16] and has become a large focus of the tissue engineering field².

1.2. Current approaches to three-dimensional (3D) bioprinting

Three-dimensional (3D) bioprinting for tissue engineering is an extensively studied area of bioengineering research [15–24]. It is an effective method of generating geometrically complex

¹ Generation of scaffolds are an essential part of tissue engineering. The scaffolds provide an initial template for the cells to form the appropriate anatomy and also perform critical extracellular matrix (ECM) functions.

² Although the generation of scaffolds are an important part of artificial organ development, it is not the singular element. Organ creation also entails development of vasculature, maturation of cells and artificial constructs, and cryopreservation. We will focus on just scaffold development.

3D tissue scaffolds, typically made of aqueous hydrogels or other biodegradable biological materials, that mimic the functions of the native extracellular matrix (ECM) in regulating cell behavior. These scaffolds act as temporary ECM until the cells are able to replace the artificial scaffold with native ECM [25–27]. 3D bioprinting allows for the precise placement of cells and additive factors in a 3D cell culture volume therefore enabling the creation of realistic tissue constructs with appropriate cell types, cell density, and mechanical properties [10,19,25,26] making it more advantageous than other tissue engineering techniques. In addition, 3D bioprinting potentially facilitates the automation, customization, and control of a wide range of parameters such as porosity, pore size, cell distribution, and vasculature [19]. There are several 3D biomaterial printing platforms [28]. Some aimed at producing acellular scaffolds [29,30] and some aimed at producing complete tissues with cells [17,31]. In the former, acellular scaffolds with the requisite matrix characteristics are constructed and later infused with cells [1,32–35]. While the latter attempts to generate complete tissues by simultaneously 3D printing cells and the scaffold [31,36,37]. Recent focus of the field has been on this latter approach of using bioactive formulations to develop scaffolds with increased biofunctionality and improved cell matrix interactions [25].

Some of the different techniques used by researchers to fabricate these engineered tissue structures are described below. The first 3D bioprinting technique utilized for tissue engineering with cell containing material was inkjet or droplet-on-demand bioprinting [38]. Because of its similarity to standard 2D inkjet printing it was easy to implement, relatively low cost and with the help of an array of nozzles in parallel, also high speed [27,38]. Ink cartridges of regular commercial inkjet printers could simply be refilled with cell containing hydrogel solutions called bio-inks. Inkjet bioprinting was first utilized in the patterning and precise deposition of cells and other biological matter [39] and has since progressed to use for the printing of complex three dimensional tissue constructs with multiple cell types [40]. In order to maintain printability of the fluid at the inkjet nozzle and still fabricate mechanically rigid constructs, complex 3D structures are formed by the cross-linking³ of the liquid droplets after they have been deposited from the nozzle in layers either through chemical cross-linking, thermal cross-linking, or photoinitiated cross-linking. The advantages of this technique are the high parallelization as a result of line by line printing enabled by multi-nozzle setups (as opposed to point by point printing) and reasonably high cell viability (70-90%) [27,41]. It is also possible to control the distribution of cells in a construct since the number of cells in a given droplet can be finely controlled [42]. Although an effective method, there are some issues and limitations associated with inkjet bioprinting such as the limited size of objects that can be printed. Due in part to the fact that early printers were modified versions of commercial printers with limited print area and in part to the limited capacity of the ink cartridges. In addition, inkjet bioprinting also suffers from settling effects in cell containing bio-inks and clogging in the nozzles, which have made this inadequate for producing large tissues [41].

Inkjet printing has still been used successfully for the fabrication of cell containing tissue scaffolds. Xu et al , for example, were able to utilize several inkjet nozzles and harness the fine control to fabricate tissue with multiple cell types using sodium alginate-collagen composite bio-

³ Cross-linking is a process of chemically bonding polymer chains to one another, usually forming a network structure of polymers bonded to each other at specific positions called cross-links. These cross-links can be formed by reactions that are initiated chemically, thermally, or via irradiation by light. The formation of these cross-links typically increases the rigidity of the polymer. In hydrogels cross-linking is employed to improve the mechanical properties, usually transforming them from viscous liquids to viscoelastic polymers.

ink ionically crosslinked after deposition [40]. Gao et al also used this technique successfully for the tissue engineering of bone and cartilage from human mesenchymal stem cells (hMSCs) [43]. Using the combination of poly ethylene glycol and gelatin methacrylate hydrogels (PEG-GelMA) that can be photopolymerized after deposition. They were able to selectively differentiate hMSCs in the hydrogel constructs to exhibit either osteogenic and chondrogenic characteristics. Compaan and colleagues also developed modified techniques that utilize sacrificial materials to provide reinforcement to slower gelling biomaterials like silk fibroin to generate structurally stable constructs while still benefitting from the fluid printability at the nozzle [44].

Another technique commonly used for bioprinting of cell-laden tissue constructs is extrusion bioprinting. Increased accessibility to commercial 3D fused deposition modeling (FDM) printers coincided with the use of FDM printers in the fabrication of scaffold structures using thermoplastic biodegradable polymers like polylactic acid (PLA)[45], polycaprolactone (PCL)[46] etc. But the requirement for high temperatures to melt⁴ these materials during extrusion made this process unsuitable for use with cells or other biological materials, which had to be later seeded on the fabricated scaffold. This led to the development of extrusion bioprinting, a process similar to FDM printing, that uses softer materials like hydrogels and could support the embedding of cells and other biological materials in the bio-ink. Extrusion bioprinting utilizes pneumatic, plunger/piston, or mechanical screw extruders to deliver a continuous stream of bio-ink. The force generated by these extruders are able to support the printing of more viscous bio-inks, encompassing a wider range of bio-ink materials and enabling higher cell densities than in inkjet bioprinting [27]. Extrusion bioprinting is the most popular technique for 3D bioprinting and is the basis for a lot of commercially available bioprinting platforms. A list of the most common commercial bioprinters is available in comprehensive reviews by Jiang et al. [25], and Ozbolat and Hospodiuk [47]. Some advantages of the extrusion technique include its relatively low cost, high customizability, and high cell density. As a result it has been widely used by researchers to print cell-laden tissue and organ platforms like degradable tissue constructs out of collagen/gelatin/alginate hydrogels [48], pancreatic tissue analogs from tissue strands made out of alginate [49], cartilage tissue, including ear and nose, using gellan gum and alginate hydrogels [50], and artificial liver tissue constructs using gelatin methacrylamide hydrogels [51], to name a few.

Despite its flexibility and scalability, extrusion bioprinting does however have some limitations like: low resolution when compared to other techniques; high shear stresses required for extrusion of viscous hydrogels which then affects cell viability; and the long times it takes to print large structures because of the point by point nature leading to dehydration and cell death [47,52]. So, to improve cell viability, less viscous hydrogels have to be used which in turn are often not sufficiently rigid, even with cross-linking, to fabricate large tissues. To address this, researchers have adopted hybrid techniques that incorporate synthetic polymers like PCL as temporary scaffolding with the soft cell-laden hydrogels to enable the printing of larger and more rigid tissues like bone and cartilage, with minimal damage to the cells [53–55]. In parallel, the Feinberg group at Carnegie Mellon University (CMU) have developed another method that utilizes temporary thermally reversible hydrogel support baths. The technique now known as freeform reversible embedding of suspended hydrogels (FRESH) engages buoyant forces in a surrounding shear thinning hydrogel suspension to counteract the gravitational load on the printed construct [56,57]. Here, the structure to be printed is fabricated within the hydrogel support bath which is

⁴ The material has to be raised to above its melting temperature or sometimes glass transition temperature to enable it to flow through the nozzle.

then liquefied and washed away after printing. In their most recent work with FRESH v2.0 they were able to achieve full scale fabrication of a 3D human heart scaffold using collagen, albeit without cells, and also fabricate heart ventricles, valves and vasculature with cells incorporated using dual-material printing, attaining spontaneous contraction in the ventricles seeded with cardiomyocytes [58]. The FRESH method has also been adopted by other researchers with some success. Noor et al have employed the process to develop hearts and vascularized cardiac patches [13]. In their experiments they were able to achieve good resolution for printing of scaled down hearts. Jeon et al. have also utilized the FRESH method to assemble cell laden microgels into 3D tissue structures [59].

Laser-assisted bioprinting is also another technique used for 3D bioprinting of cell-laden tissue [60]. This method uses lasers to excite an energy absorbing donor layer (ribbon) on the bottom of which a cell containing bio-ink is attached. The application of a laser pulse ejects a bio-ink droplet down to a receiving substrate where the droplet can then be crosslinked. The assembly of several droplets forms the 3D structure. This method has several advantages like high resolution compared to inkjet and extrusion, multiple materials and cells types, printing of highly viscous hydrogels, and much higher cell viability since there is no mechanical stress to cells [27]. Laser assisted printing at high resolutions and high speeds have been achieved by Guillotin et al [61]. They have been successfully used for the generation of skin from fibroblasts and keratinocytes [62] and for cell patterning. Despite its advantages and successful uses, laser-assisted bioprinting has seen much lower application than other methods and very few commercial systems are available. This is due to the high cost of the high-powered laser diodes required and the complexity of controlling laser systems. Also, the effect of the use of high-powered lasers on cell containing bio-inks is still not fully understood [27].

Stereolithography (SLA) has most recently been adapted for 3D bioprinting. This technique involves the use of light or lasers to selectively polymerize photosensitive polymers. Since SLA is light based it has much higher resolution, speed, and print quality [27,63,64]. It is also associated with high cell viability. Although one of the drawbacks of the ultraviolet light (UV) based SLA systems is the DNA of cells can be altered by the UV, researchers have transitioned to the use of visible light-based systems which do not have this issue. In fact Wang et al showed high cell viability using this system on blends of polyethylene glycol diacrylate (PEGDA) and gelatin methacrylate (GelMA) hydrogels [65]. And more recently Grigoryan and coworkers utilized projection stereolithography to construct complex vascular networks in biocompatible PEGDA hydrogels that can be used to simulate oxygen transfer in pulmonary and cardiovascular systems [24]. To improve the speed and scale of SLA techniques volumetric approaches to SLA printing have recently been developed. Instead of point by point curing of the polymer, computed axial lithography (CAL) is volume based to improve the speed of fabrication and enable the production of soft structures [66]. In that work, Kelly et al. were able to fabricate centimeter scale objects in 30 to 120 seconds that would normally take much longer and did so using super soft GelMA hydrogels with rigidity much lower than those previously achieved using other printing methods. Though this process has several advantages like speed of use and compatibility with even super soft hydrogel materials, the use of expensive photocurable polymers like GelMA adds significantly to the cost.

While there is a wide assortment of techniques and platforms being used for 3D bioprinting, many of which have been successful for the fabrication of complex engineered tissue scaffolds for regeneration of several organ systems [19], there are nonetheless many challenges to overcome before this technology is used for the fabrication of full anatomical scale replacement organs that

can be used for human organ transplants. Challenges such as the functionalization of multicellular organ scaffolds, the fabrication of large soft tissue and organs with low mechanical stiffness like the heart, lungs, and brain, vascularization of these tissue scaffolds during and after fabrication to enable maturation and functionalization, manufacturing at a scale sufficient to meet demand, and establishing regulatory processes for clinical translation. Therefore, new bioprinting techniques are still be required to solve some of these challenges. As a field, bioprinting is still rapidly evolving and as more advancement continues, more solutions will be developed that solve these as yet unresolved bioprinting and tissue engineering challenges.

1.3. Materials used for 3D bioprinting

Like the different techniques for bioprinting, there is also a wide range of materials being used for 3D bioprinting and tissue engineering [18]. Extensive reviews of these common biomaterials have been covered in [18] and [26]. In this section we summarize these materials.

The materials used for bioprinting are called bio-inks and usually consist of hydrogel polymers and cells. Hydrogels, which are also extensively used in tissue engineering and drug delivery, have become the material of choice for bioprinting because they possess viscoelastic mechanical properties similar to the extracellular matrix, have high water content, and allow for the mobility of embedded cells in 3D environment. These hydrogel materials are also usually biodegradable polymers with good biocompatibility that provide a favorable environment for growth and proliferation of cells in a scaffold. In applications, these bio-inks usually consist of the hydrogel pre-polymer solution mixed with the cells and are crosslinked during or after printing to form the solid structure. Cross-linking here is a process of linking the polymer chains together in ionic or covalent bonds to form a network structure that is generally stiffer. The cross-linking of hydrogels can be initiated by several means; with chemical additives, photoinitiation, and temperature change being the most common. For bioprinting applications rapid cross-linking of the bio-ink is desired in order to form sizable 3D solid structures.

The most commonly used hydrogel bio-inks could be grouped into naturally-derived polymers like collagen, alginate, agarose, chitosan, hyaluronic acid, cellulose, fibrin etc. and synthetic polymers like polyethylene glycol (PEG), polyacrylamide (PAAm), polylactic-co-glycolic acid (PLGA), polycaprolactone (PCL) etc. A brief survey of these bio-ink materials and their use in bioprinting literature follows.

Alginate is naturally derived polysaccharide comprising of mannuronic and guluronic acid units and obtained from seaweed. It is one of the most commonly used bioprinting materials because of its excellent biocompatibility, low cost, favorable viscosity, and ease of cross-linking. It can be rapidly ionically crosslinked using divalent cations making it quite favorably for different bioprinting techniques[36,48,60,64,67]. It is however bioinert and requires the addition of cell adhesion proteins like arginine-glycine-aspartic acid (RGD) or other hydrogels cell adhesion cites to support cellular functionality and proliferation.

Agarose is another naturally derived polysaccharide molecule found in the cell walls of red algae. It is a thermally responsive hydrogel which undergoes thermal gelation below its lower critical solution temperature gelation temperature (LCST) (around 30-40°C). It however has poor cell adhesion and spreading so is usually used as an additive in bio-inks requiring thermal gelation, rather than the main bio-ink material.

Collagen type I is a natural occurring triple helical biocompatible protein. Found in connective tissue and native ECM, it is one of the most abundant natural polymers in humans. As

a result, it is highly biocompatible and promotes cell adhesion, growth, and proliferation. It is also thermally responsive but slow gelling, forming fibrous structure with increase in temperature to around 37°C. But because gelation takes several minutes to an hour which is unfavorable in bioprinting, it has to be combined with other materials to maintain structure. Irrespective of this, it is still very frequently adopted in tissue engineering for its superior cell adhesion properties [58].

Gelatin is a similar fibrous water-soluble protein obtained from animals and also derivable from collagen. It also promotes cell attachment, differentiation, migration and proliferation. It is also thermosensitive and undergoes gelation below 35°C, but gels much faster at lower temperatures than collagen.

Hyaluronic acid is a linear non-sulfated polysaccharide naturally present in the connective tissue and human cartilage ECM. It is also widely used in tissue engineering because of its biocompatibility, controllable mechanics, degradability, and support for cell adhesion, proliferation and differentiation. Because of its weak mechanical properties, slow gelation rate, and rapid degradation it is also often combined with other materials when used as a bio-ink and has been modified by combination with methacrylate for enhanced mechanical properties and photopolymerization.

Chitosan is another polysaccharide derived from deacetylation of chitin. It is one of the most abundant polymers on earth and is found in nature in the exoskeleton of insects and crustaceans. It is insoluble in water above neutral pH and crosslinked by the neutralization of acetic acid in basic solution. Although it supports cell adhesion and proliferation, its unstable mechanical properties and harsh processing conditions makes it difficult to use for bioprinting with embedded cells.

Fibrin is a hydrogel formed naturally by the enzymatic reaction of thrombin and fibrinogen. It is a fibrous protein abundant in native ECM and possesses protease degradation domains and cell adhesion motifs to support cell growth and proliferation which make it an attractive candidate for bioprinting. It does however lack mechanical strength and therefore has to be combined with various other polymers to be useful as a bio-ink.

Cellulose is another naturally occurring polymer used for bioprinting. It is composed of glucose units attached together by glycosidic linkages. It is the most abundant naturally occurring polymer and present in plant cell walls. It has gained more interest for bioprinting applications because of its high-water holding capacity, mechanical properties, and biocompatibility. There are three main types namely: micro-fibrillated cellulose, nanocrystalline cellulose, and bacterial nanocellulose. To enable thermal gelation through hydrophobic interaction it can be modified to form Methylcellulose.

In attempts to replicate the natural ECM environment, the use of decellularized ECM (dECM) as a bio-ink has also been developed. The process usually requires chemical and physical removal of cells without damage to ECM. So far these dECM bio-inks have successfully been used for bioprinting of tissue [55] and are seen as a superior means of enhancing cell adhesion and functionality by simulating the appropriate mechanical properties and environment most favorable to cells [18].

Synthetic hydrogels have also been utilized for several bioprinting applications.

Pluronic® F-127 is a synthetic poloxamer-based polymeric compound. It is composed of polyethylene oxide and polypropylene oxide and available in various types which provide different functions and gelation characteristics. It is a thermally responsive hydrogel which undergoes reverse gelation with increase in temperature at around 10°C-40°C, depending on type.

Polyethylene glycol (PEG) is a hydrophilic polymer frequently used in bioprinting and other medical applications like for drug delivery. It is soluble in water, can be combined with biomolecules, enzymes and proteins, and has been shown to support cell survival even without cell adhesion components. It however does not form crosslinked networks and has poor mechanical strength but can be chemically modified to form PEG-based hydrogels. Acrylation with diacrylate (to form PEG-DA) and methacrylate (to form PEG-MA) can be used to improve its mechanical properties but requires photo-crosslinking with photo-initiators to obtain the desired mechanical properties. As such it is commonly used in SLA processes, like the use of PEG-DA to make complex alveolar models [24]. PEGDMA has also been used in inkjet printing by photopolymerization in combination with hMSCs to form bone or cartilage tissue [38].

GelMA (Gelatin methacrylate) is a hydrogel formed by the modification of gelatin with methacrylate so that it is enzymatically degradable yet mechanically stable when photo-crosslinked. It has a relatively high mechanical strength and low swelling ratio which has made it a good candidate for SLA processes as well using UV crosslinking with photo-initiators [65,66].

Polyacrylamide (PAAm) hydrogels are also another group of polymers used for bioprinting. They can be modified to be photocurable or into thermally responsive hydrogels [52]. However, being a synthetic polymer, it does not have great biocompatibility.

Other polymers like polylactic-co-glycolic acid (PLGA) have also been used extensively for tissue engineering and are now frequently used in bioprinting applications as well for more rigid tissue scaffolds like those for bones and cartilage. As previously mentioned, polycaprolactone (PCL) which has high mechanical strength, favorable biodegradability, and low melting point is being used in a lot of hybrid printing techniques and for several bioprinting applications like bone, ear cartilage, skeletal muscle [53] etc. Other synthetic materials which have been used are polylactic acid (PLA), poly vinyl alcohol (PVA), and polyurethane (PU), usually in combination with other hydrogels.

Requirements for bio-inks are such that, in most cases, a single polymer is not sufficient to achieve the desired configuration of biocompatibility, cell attachment, mechanical properties, and gelation characteristics so composite blends are commonly used. For example the collagen/alginate/gelatin blend used in [48], the gellan gum and alginate blend used in [50], or sodium alginate-collagen blend used in [40]. To augment cell attachment, differentiation, proliferation, cell activity, and biodegradation in some of the commonly used bio-inks, protein additives, growth factors and enzymes have also been added to bio-ink compositions.

Ultimately the choice of bio-inks to use depends a lot on application and desired tissue characteristics like printability, gelation kinetics, material strength, biocompatibility, control over biodegradation, biofunctionalization, and cell function [25]. As well as the printing mechanism since ideal fluid properties like viscosity and surface tension could vary from process to process. For some materials these characteristics can be obtained by varying concentration, temperature, or other processing conditions. For example, increased mechanical strength is usually associated with higher concentrations. But with continuous advancement and need for more and more specialized tissue characteristics the general trend in the bioprinting field is towards multi-material printing [52,58] and the development of novel bio-inks.

An emerging area of focus is in the fabrication of super soft tissues. In tissue engineering replication of the native ECM characteristics is very important since the ECM is responsible for various cell functions like cell motility and cell differentiation which are crucial to the functionalization of tissue constructs. One important characteristic of tissue ECMs is stiffness which widely varies based on tissue or organ type. Ranging from high stiffnesses on the order of

1GPa for bone tissue down to about 1kPa for soft tissue like the lungs and 0.1kPa for the brain tissue [68]. The fabrication of these soft tissue and organs therefore requires the use of super soft hydrogel materials of stiffness on the same order as these tissues of around 0.1kPa – 1kPa and lower. Bioprinting using these materials however presents several challenges like the fact that these super soft hydrogels are incapable of supporting the structure of a large organ like the lung or human heart, two soft tissue organs which are also severely lacking in the organ transplant supply chain. To overcome these challenges, new techniques of printing with these super soft hydrogels and/or novel bio-ink materials need to be developed.

1.4. Challenges in 3D bioprinting and tissue engineering

Numerous examples of 3D bioprinting successes are widely publicized, however, some challenges remain yet to be addressed. Some of those already mentioned include fabrication of anatomical scale multicellular organ scaffolds, fabrication of mechanically stable soft tissue and organs, vascularization to support functionalization and integration in-vivo, manufacturing at scale, and establishing regulatory processes for clinical translation. With the exception of the regulatory challenges, the common denominator among these challenges is scale both in terms of size of the object and scaling up to clinical use [18,23,26]. A cursory review of current bioprinting platforms (see 1.2) and numerous examples reveal a severe size limitation; most objects that have been made are on the few millimeters [13] to a couple of centimeters scale [56,57]. Focusing on just the bioprinting of tissue constructs, there are several issues limiting the size of fabricated scaffolds and tissue. One is the inability to create appropriate vascular networks to continue the delivery of nutrients and oxygen to cells and for waste removal [23]. For tissues larger than the diffusion limit of oxygen (100-200 μ m), the lack of appropriately distributed conduits will lead to nutrient deficiency and tissue necrosis [23]. Another issue is that the bio-inks used for fabrication of soft tissue are typically soft hydrogels or aqueous polymer mixtures with limited mechanical properties [18,26] incapable of supporting the construction of larger structures without significant external supports [14,56] or cross-linking [63,69]. Furthermore, the super soft hydrogel bio-inks used for soft tissues are not rigid enough to support convoluted shapes with lumens, typical of complex organs.

Currently, the leading approach to tackling these limitations is by modifications to bio-inks using processes like cross-linking or multi-material composites. However, with crosslinking, striking the right balance between printability, adequate rigidity, and biomimicking mechanical properties can be challenging [25,69], since composition and time after the onset of cross-linking influence the rheological behavior of many hydrogel bio-inks leading to unpredictable outcomes during printing [70,71]. Printing techniques like SLA where photocurable bio-inks are rapidly polymerized to form solids eliminates some of these issues [64]. However, the need for photosensitive hydrogels severely limits the material choices and increases cost. Additionally, in some cases, cells are exposed to potentially harmful UV radiation or other toxic additives. So, to eliminate those drawbacks other methods like step-wise cross-linking [69] utilize several levels of crosslinking to optimize for printability at the nozzle, rigidity of structure during printing, and appropriate stiffness after printing. Another promising method is freeform reversible embedding of suspended hydrogels (FRESH), which uses gel suspensions as support to counter the gravitational forces on the printed object and enable printing with much softer bio-inks [56].

Despite these developments, cross-linking alone has limitations for super soft tissue scaffolds like those made for brain, lung, and heart tissues, tissues with low yield strength and low

elastic modulus [68]. Because of the inherent need for the scaffolds to have similar mechanical properties to the real tissue, even after cross-linking, the material properties of these hydrogels are lacking. This presents issues since as the size of the printed object gets larger, the probability that the structure yields under its own weight increases, often leading to print failure and poor resolution. Though promising, approaches like the FRESH method have so far only been used for hydrogels with stiffnesses at least an order of magnitude higher than the stiffnesses for super soft tissue [32]. And the newly introduced computed axial lithography (CAL) method which has been used for fabrication of super soft structures is still being developed [66]. Therefore, there is a need for alternate approaches to developing large soft tissue at scale.

1.5. Three-dimensional (3D) bioprinting at subfreezing temperatures

The generation of artificial organs for transplant has been identified as a feasible pathway towards solving the organ supply crisis and saving the lives of millions globally. Organs most affected in the transplant cold chain happen to be the delicate soft tissue organs like the heart and lungs and generation of these organs artificially requires the creation of complex super soft 3D tissue structures which could be done using 3D bioprinting. Current 3D bioprinting techniques however remain inadequate for the creation of these super soft tissue scaffolds. Although vast amount of research efforts in tissue engineering are focused on solving these bioprinting issues, with research being done to optimize the fluids and structural properties of bio-inks, develop new 3D printing methods, develop functional bio-inks, isolate growth factors, improve cell survival etc., most of these efforts are not specifically aimed at fabrication of super soft hydrogels.

One minimally explored approach which could be beneficial in this regard is, the use of liquid to solid phase change (freezing) to temporarily stabilize these soft structures during the bioprinting process and thus enable the fabrication of stable super soft tissue scaffolds at the scale necessary for the building of organs. Recent work has shown that freezing can be used to improve mechanical structure and hence resolution during printing [72]. Freezing could also be used to address some of the other challenges facing current bioprinting processes. For example 3D printing can be slow which can cause biological matter to deteriorate during the long duration required for printing large structures with limited vasculature at adequate resolutions [10,23]. Lowering the temperature to slow down metabolism could reduce ischemic damage. In addition, for large scale distribution and storage of 3D tissue engineered constructs, preservation is needed – by refrigeration for short periods of time or by freezing for long periods of time. This necessitates the need for cryopreservation which poses certain challenges in large tissue and organs [73,74] but might be easier to achieve in smaller volume freezing during the bioprinting process.

Early work from our group demonstrated the feasibility of a 3D bioprinting process that incorporates freezing, called 3D cryoprinting [1]. In a similar work, Tan et al showed the advantages of this process for the fabrication of super soft hydrogels [32]. The work from Wang et al on cryogenic printing of hierarchically loaded structures showed that this process could work with cells containing bio-inks [35]. 3D cryoprinting incorporates control over temperature and phase therefore introducing additional bioprinting parameters that can now be manipulated to optimally balance printability, mechanical stiffness, and biomimicry.

Though the feasibility of the process has been demonstrated, in order for this technique to be adopted several outstanding questions still need to be answered. First, how to ensure solidification during the entire fabrication process? Although, the cryoprinting process is similar in concept to fused filament fabrication in 3D printing, there are some differences. In conventional

3D printing of molten plastics, the process is done at room temperature, and the phase transition temperature of the molten plastic is higher than room temperature so that upon deposition the material solidifies binding it to the adjacent elements and increasing its modulus therefore enabling the assembly of complex structures. In tissue engineering, freezing does the same for soft aqueous solutions. It facilitates the bonding between the elements and increased rigidity for the manufacturing of complex shaped objects – making them easier to handle and transport. While there have been previous examples of 3D bioprinting using freezing, individual control over the thermal history during freezing of each element was absent [32–35,75]. This is problematic because the thermal history could affect the quality and success of fabrication; for example, the rate of solidification would affect resolution and if limited can affect whether the object solidifies, resulting in structural failure. Secondly, how cell viability can be maximized during fabrication at subfreezing temperatures? Since cooling rate influences the viability of the cells during printing it would need to be optimized for best results after fabrication. In order to answer these and other questions, additional detailed work needs to be done to understand and further develop 3D cryoprinting. Such as the control of thermal history during 3D cryoprinting to optimize the fabrication of bioactive scaffolds at subfreezing temperatures, which can be done using mathematical models that incorporate thermal properties, process parameters, and knowledge of cell cryopreservation.

Fabricated scaffolds in their frozen form however, have minimal use. To be able to develop them into fully fledged tissue structures they need to be cultivated *in vivo* in a bioreactor, in a functionalization and maturation process that takes several weeks and is done at physiological temperature (37°C). A temperature that is above the freezing temperature of the aqueous bio-inks used for 3D cryoprinting which means that any structural rigidity gained from ice formation during freezing will be lost upon thawing. This leads to an additional question of how to maintain structure of the fabricated frozen scaffold after thawing? A question that needs to be answered before the 3D cryoprinting process can be reasonably considered a practical bioprinting technique.

Also, being a new technique, very little is understood on the effect of freezing during 3D cryoprinting on the mechanical integrity of the structures being fabricated and the biomaterial ink itself. Therefore, there is also a need for a fundamental exploration of the mechanical properties and microstructures generated from this new printing process.

1.6. Thesis overview

As previously discussed there are several advantages of 3D cryoprinting over conventional 3D bioprinting. One of which is its unique applicability to the fabrication of stable soft tissue scaffolds, a necessary component in the tissue engineering of soft tissue organs. This 3D cryoprinting process, however, introduces additional complexity such as: How to ensure solidification during printing? How to maximize cell viability while freezing during printing? How to thaw the construct after printing without losing stability? etc. In this work we will attempt to answer each of those questions. Our overarching goal in this thesis is to advance the field of 3D bioprinting by the development of a new technique of 3D bioprinting at subfreezing temperatures (3D cryoprinting), capable of enabling new possibilities with scaffold fabrication, like the fabrication of super soft tissue scaffolds. In trying to achieve that goal we develop a series of novel solutions geared at solving the different engineering challenges associated with 3D cryoprinting. Some independent solutions will be developed while other answers will be in support of or to improve the understanding of the field.

Firstly, because this technology entails fabrication at subfreezing temperatures it requires understanding of the temperature history during freezing as this controls solidification of the material, the object resolution, and the probability of cell survival in cell-laden tissue constructs. There is also a need to ensure that during the cryoprinting process the object being printed does not melt and collapse, since rigidity is provided by the ice. And a need to ensure that a significant percentage of cells survive the cryoprinting process when fabricating bioactive scaffolds. Therefore, in chapter 2, we will investigate a means to control the freezing process in order to maximize cell survival and improve the outcome of the printed biological scaffold. In order to achieve those outcomes, we develop a mathematical model to better understand and control the freezing happening during 3D extrusion bioprinting at subfreezing temperatures. In developing this mathematical model, we encounter the engineering challenge of dealing with a growing geometry in 3D space, which then requires the development of new modeling techniques that factor in continuous variation in an arbitrary growing geometry and the localized spatial and temporal thermal tracking of a solidifying material over the entire course of a simulated print. This extent of mathematical modeling for extrusion based additive manufacturing is the first of its kind. With these models we may be able to successfully control the fabrication of tissues scaffolds during 3D cryoprinting. The work included in chapter 2 was previously published in [76].

Successful control of the 3D cryoprinting process leads to the production of frozen scaffolds. The process of developing these scaffolds into fully mature tissue however requires that they are unfrozen. In the course of melting the structural rigidity gained as a result of ice formation during the cryoprinting process is lost, therefore eliminating any advantages provided by cryoprinting. Therefore, for 3D cryoprinting to remain practical, in chapter 3, we develop a new process called freezing modulated cross-linking to preserve the structure of the fabricated scaffold above its freezing temperature. This novel technique utilizes cross-linking to conserve the geometrical structure and mechanical properties of frozen scaffolds after thawing. The process uses freezing to modulate the cross-linking process to prevent premature structural failure during the melting. In chapter 3 we describe this method in detail and develop a mathematical model to better understand the parameters needed to ensure maximal structural stability during thawing. With this solution we would be able to successfully keep the geometric structure fabricated using 3D cryoprinting.

Another novel concern arising from the use of 3D cryoprinting is how it influences the resulting mechanical properties of the fabricated scaffold. Since mechanical properties are linked to microstructure, significant understanding can be gained by studying the microstructure that emerges during the formation of ice and the subsequent melting. To better understand the fundamental relationship between freezing parameters and microstructure, and the relationship between microstructure and mechanical properties, in chapter 4, we design an experimental platform developed with the help of thermal modeling and analysis. We use this experimental directional solidification apparatus to study how microstructure of a scaffold is affected by the various freezing and cross-linking processes, digging into the different ways of combining freezing and cross-linking to generate structure. Results of this mini study further our understanding of the phase change process occurring during 3D cryoprinting and its influence on a hydrogel bio-ink typically used in the tissue engineering field. Some of the work included in chapter 4 was previously published in [77].

The acknowledgement that 3D printing is a linear process, i.e. a 3D object is made of an assembly of single volume elements, in which one element is added to the other in one device, until the entire object is produced, shows that it does not lend itself to scale up for mass

manufacture in an economically feasible manner [78]. So, although this new 3D cryoprinting method promises to solve several challenges with 3D bioprinting, mass manufacturing is still required for it to be of practical use. Typically, successful high volume manufacturing technologies benefit from parallelization when moving from producing one part to much higher quantities [79]. Therefore, a new approach which leverages parallelization and integrates freezing to improve the manufacturability of biological scaffolds might be beneficial to 3D bioprinting. In chapter 5, we explore one such parallel technique called parallel multilayer cryolithography and outline working principles to guide future device development as well as show a proof of concept device to demonstrate advantages of this technique. The results of this work was previously published in [80].

Chapter 6 then concludes this thesis with a summary of the major findings from this work and future applications. This chapter synthesizes how this work accomplishes the initial aim of developing 3D cryoprinting techniques to advance the field of bioprinting and tissue engineering and gets us closer to the achievement of functional artificial organs to supplement the organ transplant supply. Some of the developed solutions could be applicable beyond 3D cryoprinting to other areas of tissue engineering, additive manufacturing, and cell biology. Some of the other findings from the fundamental studies also signal additional areas to be studied in future work.

Chapter 2

2. Control and optimization of 3D cryoprinting

2.1. Introduction

3D bioprinting has allowed for the fabrication of realistic tissue scaffolds geometries that aid in the development of human tissues and organs that could one day complement organ donations for transplants. The most common way of 3D bioprinting these solid scaffolds from liquid bio-inks is using cross-linking [63,81], typically initiated before or during printing [82]. Although cross-linking is suitable for the formation of geometrically and mechanically accurate scaffolds using biomimicking hydrogels, there are some limitations when using soft cell-laden hydrogels [32,81]. Mainly that the rigidity of these extremely soft bio-inks is not sufficient to support the geometric structure during printing and the shear stress on the cells could cause mechanical damage if the material is crosslinked before printing [25].

Recently, liquid to solid phase change (freezing) has been suggested as an alternative way to enable 3D bioprinting of larger scaffolds and scaffolds made using super soft hydrogels, with advantages like temporary and thermoreversible augmentation of mechanical properties during printing and improved resolution [1,32,33,35,83,84]. The use of freezing in bioprinting is similar in principle to extrusion-based (fused deposition modeling) 3D printing, where heated plastic is continuously deposited from an extruder in a constant stream onto the printing surface or previously printed layers at room temperature, causing it to solidify upon deposition. An analogous process can be used for bioprinting in which the bio-ink is printed onto a surface at subfreezing temperature [32]. Freezing temporarily increases the structural properties of soft bio-ink material during printing thus enabling the printing of larger objects. Although cross-linking is still required to maintain the structure after thawing, the viscosity and shear strength of the material can be lower, therefore improving printability [25]. The lower temperature also significantly slows down cellular metabolism, minimizing the risk of deterioration during bioprinting of larger structures which require long print times. These improvements in addition to preservation of the frozen object during and after printing, make this a plausible approach to 3D bioprinting. Furthermore, because each voxel is being frozen during the printing process rather than as a whole tissue, it is much easier to achieve the cooling rates required for optimal freezing of biological constructs which is advantageous for cryopreservation [85].

Typical methods of freezing during bioprinting, however, become restrictive when trying to print large structures. For example, in previous bioprinting methods where freezing has been used, the z-platform is maintained at the subfreezing temperature and drives the freezing [32]. Therefore, as the object being fabricated gets larger and the deposition plane rises farther away from the sub-freezing z-platform, the continuously varying freezing rate diminishes. Eventually freezing becomes conduction limited due to the buildup of material resistance from object being printed. To counter this limitation, a new method of printing at subfreezing temperatures described in [1], termed 3D cryoprinting, was developed. 3D cryoprinting utilizes control over the level of an auxiliary encompassing cryofluid bath to generate uniformly frozen and ice-controlled structure

in each printed element. This allows for the printing of larger structures and removes the size conduction limitation during printing. Figure 2.1 below illustrates this 3D cryoprinting method. The use of the liquid introduces two additional levers that can be controlled, fluid temperature and fluid level, and minimizes the area of the printed object exposed to room temperature air.

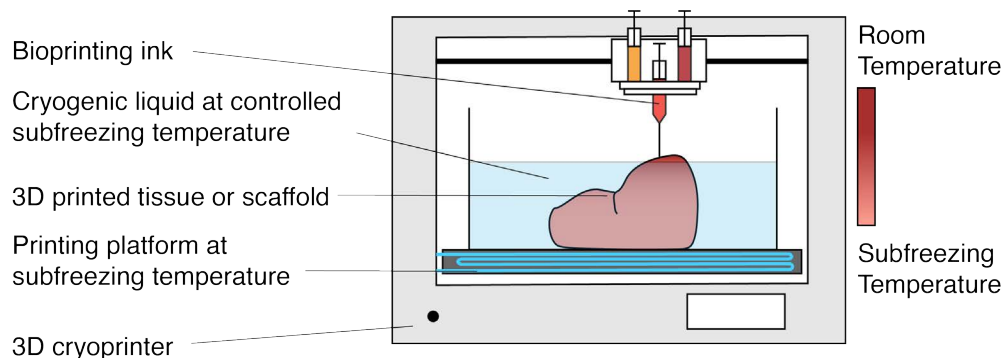


Figure 2.1: Schematic of 3D cryoprinting

Concern arises, however, when considering the fabrication of cell-laden soft tissue scaffolds, a crucial element for artificial organ development, using 3D cryoprinting. Freezing of biological material and bio-inks containing cells is not trivial. It is well established that cell survival and viability at subfreezing temperatures is dependent on freezing and warming rates [85–89]. Hence, for cryoprinting to be of practical use, the process has to be designed such that the cooling rate and composition maximize the chance of cell survival upon freezing. Control of the printing process can be achieved if there is a good understanding of the freezing process and how different printing parameters influence freezing rate and cell survival. This understanding can be obtained from repeated experimentation or with mathematical analysis of the 3D cryoprinting process.

Several researchers have highlighted the benefits of thermal analysis in the design of cryopreservation protocols [73,90]. In 3D printing of polymers and metals, thermal analysis has been used to predict bond formation [91], layer distortions [92,93], thermal stresses [94], and even the resulting material properties of the final product after manufacture [95–97]. In fact, the recent work by Neiva et al on a mathematical model for metal 3D printing with a continuously growing geometry shows how mathematical models of 3D printing processes can enhance understanding of additive manufacturing [98]. Adopting this idea, we develop a thermal phase change model for the bioprinting of an aqueous solution. The aim being to create a design tool for developing and evaluating 3D cryoprinting protocols. In this chapter we will describe the numerical finite difference model used and demonstrate the use of the model for predicting thermal history, cooling rate, cell survival, and freezing characteristics of each element for several example print scenarios. A model of this kind could prove beneficial to the advancement of 3D bioprinting of aqueous materials at low temperatures. To our knowledge, this model is a first of its kind, particularly in the context of bioprinting with phase change. The bulk of this chapter was previously published as [76].

2.2. Mathematical model for 3D cryoprinting

Mathematical models have previously been developed for 3D printing, with a majority focused on laser sintering/melting processes and none covering thermal history during extrusion-

based printing. A surprising finding given the ubiquity of extrusion-based 3D printers. In addition, thermal phase change models that exist for printing processes are quite limited and do not accurately account for growing geometries typical of an extrusion-based printing process. We therefore developed a model which couples the growing geometry and the thermal phase change. This mathematical model was developed in two parts: a standard thermal phase change model to handle thermal history and an extrusion model to handle the growing geometry.

2.2.1. Thermal model of the phase-change problem

Extrusion-based 3D cryoprinting is the continuous deposition of an aqueous bio-ink onto a surface at subfreezing temperature such that the liquid solidifies upon deposition forming a structurally rigid solid object. Phase change during this process is mostly dominated by conduction heat transfer. The temperature of each element during the phase change heat transfer process can be determined from the heat conduction equation. There are several approaches for solving liquid-solid phase change problems involving conduction. Most of these approaches rely on tracking or knowing the precise location of the freezing interface and the coupling of separate equations for the liquid and solid portions, which adds layers of complexity when dealing with 3D problems or using numerical techniques [99]. The enthalpy method is one that does not require knowledge of the location of the freezing interface nor the use of different equations for the liquid and solid. It therefore lends itself to problems of this kind where the domain is changing with time in 3D space [100]. Hence, for simplicity, the enthalpy form of the heat conduction equation outlined below was used

$$\nabla \cdot (k\nabla T) + q_{gen} = \rho \frac{\partial H(T)}{\partial t} \quad (2.1)$$

where $T(x, y, z, t)$ is the temperature at some position (x, y, z) at time, t . k is the thermal conductivity of the material, ρ is the density, and $H(T)$ is the enthalpy as a function of temperature. The use of the enthalpy formulation simplifies the phase change problem as the equation can be applied non-discriminately to the liquid and solid phases. This involves the conversion of the temperature terms to enthalpy using the expression below:

$$H(T) = \begin{cases} C_{p,s}(T - T_m), & T < T_m \\ fL, & T = T_m \\ C_{p,l}(T - T_m) + L, & T > T_m \end{cases} \quad (2.2)$$

Assuming constant specific heat, where $C_{p,s}$ is the specific heat capacity of the solid phase, $C_{p,l}$ the specific heat capacity of the liquid, f is the phase fraction, T_m is the melting temperature, and L is the latent heat of fusion.

To solve the problem, a 3D numerical finite difference model was developed as follows. First, a cubic domain was discretized into several cubic volumes with nodes, (i, j, k) , where i is the node index in the x-direction, j is the index in the y-direction, and k is the index in the z- direction as illustrated in Figure 2.2. Then, the energy equation was derived for an internal finite difference element i, j, k (Figure 2.2a) to yield equation (2.3) below

$$\rho_{i,j,k} \Delta x \Delta y \Delta z \frac{H_{i,j,k}^{n+1} - H_{i,j,k}^n}{\Delta t} = q_{x,cond}^- + q_{y,cond}^- + q_{z,cond}^- - q_{x,cond}^+ - q_{y,cond}^+ - q_{z,cond}^+ + q_{gen} \quad (2.3)$$

Where, i, j, k are the spatial discretization indices for the node and n is the time discretization.

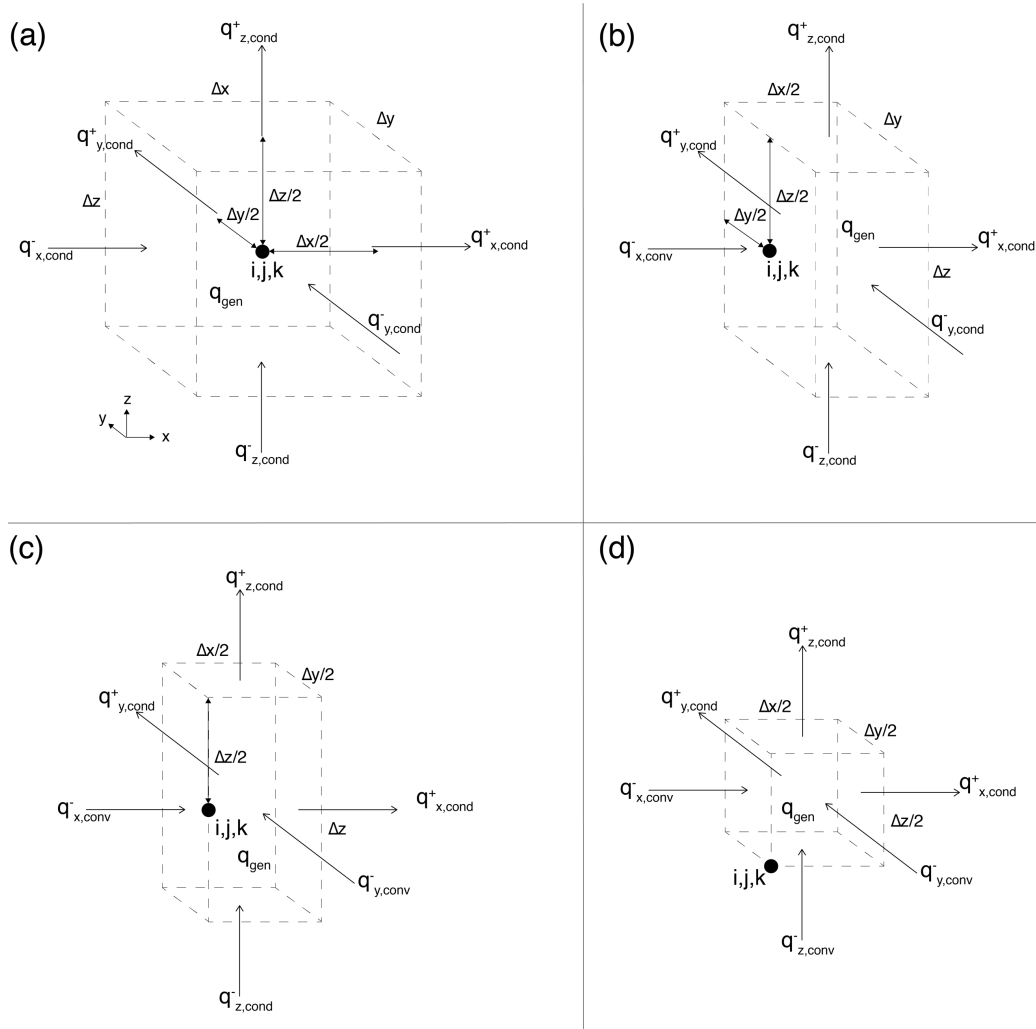


Figure 2.2: Diagram showing heat flow through (a) an internal finite difference node (b) a boundary finite difference node (c) an edge finite difference node (d) a corner finite difference node.

Substituting for the conductive heat flows from adjacent nodes yields

$$\begin{aligned}
\rho_{i,j,k} \Delta x \Delta y \Delta z \frac{H_{i,j,k}^{n+1} - H_{i,j,k}^n}{\Delta t} &= \frac{T_{i-1,j,k} - T_{i,j,k}}{\frac{\Delta x}{2k_{i-1,j,k}} + \frac{\Delta x}{2k_{i,j,k}}} \Delta y \Delta z + \frac{T_{i,j-1,k} - T_{i,j,k}}{\frac{\Delta y}{2k_{i,j-1,k}} + \frac{\Delta y}{2k_{i,j,k}}} \Delta x \Delta z + \frac{T_{i,j,k-1} - T_{i,j,k}}{\frac{\Delta z}{2k_{i,j,k-1}} + \frac{\Delta z}{2k_{i,j,k}}} \Delta x \Delta y \\
&- \frac{T_{i,j,k} - T_{i+1,j,k}}{\frac{\Delta x}{2k_{i,j,k}} + \frac{\Delta x}{2k_{i+1,j,k}}} \Delta y \Delta z - \frac{T_{i,j,k} - T_{i,j+1,k}}{\frac{\Delta y}{2k_{i,j,k}} + \frac{\Delta y}{2k_{i,j+1,k}}} \Delta x \Delta z - \frac{T_{i,j,k} - T_{i,j,k+1}}{\frac{\Delta z}{2k_{i,j,k}} + \frac{\Delta z}{2k_{i,j,k+1}}} \Delta x \Delta y \\
&+ q_{gen}
\end{aligned} \tag{2.4}$$

Defining thermal resistances (equation (2.5)),

$$R_x = \frac{\Delta x}{2k}, \quad R_y = \frac{\Delta y}{2k}, \quad R_z = \frac{\Delta z}{2k} \tag{2.5}$$

and substituting into equation (2.4), we get

$$\begin{aligned}
H_{i,j,k}^{n+1} - H_{i,j,k}^n &= \frac{\Delta t}{\rho_{i,j,k}} \left[\frac{T_{i-1,j,k} - T_{i,j,k}}{(R_{x,i-1,j,k} + R_{x,i,j,k}) \Delta x} + \frac{T_{i,j-1,k} - T_{i,j,k}}{(R_{y,i,j-1,k} + R_{y,i,j,k}) \Delta y} \right. \\
&+ \frac{T_{i,j,k-1} - T_{i,j,k}}{(R_{z,i,j,k-1} + R_{z,i,j,k}) \Delta z} - \frac{T_{i,j,k} - T_{i+1,j,k}}{(R_{x,i,j,k} + R_{x,i+1,j,k}) \Delta x} - \frac{T_{i,j,k} - T_{i,j+1,k}}{(R_{y,i,j,k} + R_{y,i,j+1,k}) \Delta y} \\
&\left. - \frac{T_{i,j,k} - T_{i,j,k+1}}{(R_{z,i,j,k} + R_{z,i,j,k+1}) \Delta z} + \frac{q_{gen}}{\Delta x \Delta y \Delta z} \right]
\end{aligned} \tag{2.6}$$

Defining,

$$A_x^- = \frac{1}{(R_{x,i-1,j,k} + R_{x,i,j,k}) \Delta x} \quad \text{and} \quad A_x^+ = \frac{1}{(R_{x,i,j,k} + R_{x,i+1,j,k}) \Delta x} \tag{2.7}$$

$$A_y^- = \frac{1}{(R_{y,i,j-1,k} + R_{y,i,j,k}) \Delta y} \quad \text{and} \quad A_y^+ = \frac{1}{(R_{y,i,j,k} + R_{y,i,j+1,k}) \Delta y} \tag{2.8}$$

$$A_z^- = \frac{1}{(R_{z,i,j,k-1} + R_{z,i,j,k}) \Delta z} \quad \text{and} \quad A_z^+ = \frac{1}{(R_{z,i,j,k} + R_{z,i,j,k+1}) \Delta z} \tag{2.9}$$

Substituting equations (2.7-2.9) into (2.6) and simplifying, the energy equation can be written as

$$\begin{aligned}
H_{i,j,k}^{n+1} - H_{i,j,k}^n &= \frac{\Delta t}{\rho_{i,j,k}} \left[A_x^- T_{i-1,j,k} + A_y^- T_{i,j-1,k} + A_z^- T_{i,j,k-1} + A_x^+ T_{i+1,j,k} + A_y^+ T_{i,j+1,k} \right. \\
&\left. + A_z^+ T_{i,j,k+1} - (A_x^- + A_y^- + A_z^- + A_x^+ + A_y^+ + A_z^+) T_{i,j,k} + \frac{q_{gen}}{\Delta x \Delta y \Delta z} \right]
\end{aligned} \tag{2.10}$$

To get the equation in terms of enthalpy, temperature can be replaced using the expression obtained from equation (2.2) to get the equation (2.11) below

$$T = T_m + \frac{H - fL}{C_p} \quad (2.11)$$

Where

$$f = \begin{cases} 0, & \text{if solid} \\ 1, & \text{if liquid} \end{cases} \quad (2.12)$$

Which results in the following space discretized explicit formulation for the enthalpy form of the energy equation to solve for new enthalpy at a node after some time Δt knowing the initial enthalpy of the node and surrounding nodes

$$\begin{aligned} H_{i,j,k}^{n+1} = & \left(1 - (A_x^- + A_y^- + A_z^- + A_x^+ + A_y^+ + A_z^+) \frac{\Delta t}{\rho_{i,j,k} C_{p,i,j,k}} \right) H_{i,j,k}^n \\ & + \frac{\Delta t}{\rho_{i,j,k}} \left[A_x^- \left(\frac{H - fL}{C_p} \right)_{i-1,j,k} + A_y^- \left(\frac{H - fL}{C_p} \right)_{i,j-1,k} + A_z^- \left(\frac{H - fL}{C_p} \right)_{i,j,k-1} \right. \\ & \left. + A_x^+ \left(\frac{H - fL}{C_p} \right)_{i+1,j,k} + A_y^+ \left(\frac{H - fL}{C_p} \right)_{i,j+1,k} + A_z^+ \left(\frac{H - fL}{C_p} \right)_{i,j,k+1} \right] \\ & + \frac{\Delta t}{\rho_{i,j,k}} \left[\frac{q_{gen}}{\Delta x \Delta y \Delta z} \right] \end{aligned} \quad (2.13)$$

Assuming no heat generation or externally applied heat flux (radiant or otherwise), the equation for enthalpy at an internal node can be reduced to

$$\begin{aligned} H_{i,j,k}^{n+1} = & \left(1 - (A_x^- + A_y^- + A_z^- + A_x^+ + A_y^+ + A_z^+) \frac{\Delta t}{\rho_{i,j,k} C_{p,i,j,k}} \right) H_{i,j,k}^n \\ & + \frac{\Delta t}{\rho_{i,j,k}} \left[A_x^- \left(\frac{H - fL}{C_p} \right)_{i-1,j,k} + A_y^- \left(\frac{H - fL}{C_p} \right)_{i,j-1,k} + A_z^- \left(\frac{H - fL}{C_p} \right)_{i,j,k-1} \right. \\ & \left. + A_x^+ \left(\frac{H - fL}{C_p} \right)_{i+1,j,k} + A_y^+ \left(\frac{H - fL}{C_p} \right)_{i,j+1,k} + A_z^+ \left(\frac{H - fL}{C_p} \right)_{i,j,k+1} \right] \end{aligned} \quad (2.14)$$

Temperature can then be calculated from the enthalpy by rearranging equation (2.2) to get

$$T = \begin{cases} T_m + \frac{H}{C_p}, & H < 0 \\ T_m, & 0 \leq H \leq L \\ T_m + \frac{H - L}{C_p}, & H > L \end{cases} \quad (2.15)$$

A similar derivation is repeated for a boundary node with convection heat transfer (Figure 2.2b) or insulated boundary to obtain

$$\begin{aligned}
H_{i,j,k}^{n+1} = & \left(1 - (A_{conv,x}^- + A_y^- + A_z^- + A_x^+ + A_y^+ + A_z^+) \frac{\Delta t}{\rho_{i,j,k} C_{p,i,j,k}} \right) H_{i,j,k}^n \\
& + \frac{\Delta t}{\rho_{i,j,k}} \left[A_{conv,x}^- T_\infty + A_y^- \left(\frac{H - fL}{C_p} \right)_{i,j-1,k} + A_z^- \left(\frac{H - fL}{C_p} \right)_{i,j,k-1} \right. \\
& \left. + A_x^+ \left(\frac{H - fL}{C_p} \right)_{i+1,j,k} + A_y^+ \left(\frac{H - fL}{C_p} \right)_{i,j+1,k} + A_z^+ \left(\frac{H - fL}{C_p} \right)_{i,j,k+1} \right]^n \quad (2.16)
\end{aligned}$$

Where

$$A_{conv,x} = \frac{h}{\Delta x} \quad (2.17)$$

h is the convection coefficient and T_∞ is the temperature of the surrounding. For an insulated boundary condition, $A_{conv} = 0$. For boundary nodes with a prescribed temperature, the enthalpy can be calculated directly using equation (2.2).

Likewise, equations were then derived for edge nodes (Figure 2.2c) and corner nodes (Figure 2.2d), yielding equations (2.18) and (2.19) respectively.

$$\begin{aligned}
H_{i,j,k}^{n+1} = & \left(1 - (A_{conv,x}^- + A_{conv,y}^- + A_z^- + A_x^+ + A_y^+ + A_z^+) \frac{\Delta t}{\rho_{i,j,k} C_{p,i,j,k}} \right) H_{i,j,k}^n \\
& + \frac{\Delta t}{\rho_{i,j,k}} \left[A_{conv,x}^- T_{\infty,1} + A_{conv,y}^- T_{\infty,2} + A_z^- \left(\frac{H - fL}{C_p} \right)_{i,j,k-1} + A_x^+ \left(\frac{H - fL}{C_p} \right)_{i+1,j,k} \right. \\
& \left. + A_y^+ \left(\frac{H - fL}{C_p} \right)_{i,j+1,k} + A_z^+ \left(\frac{H - fL}{C_p} \right)_{i,j,k+1} \right]^n \quad (2.18)
\end{aligned}$$

$$\begin{aligned}
H_{i,j,k}^{n+1} = & \left(1 - (A_{conv,x}^- + A_{conv,y}^- + A_{conv,z}^- + A_x^+ + A_y^+ + A_z^+) \frac{\Delta t}{\rho_{i,j,k} C_{p,i,j,k}} \right) H_{i,j,k}^n \\
& + \frac{\Delta t}{\rho_{i,j,k}} \left[A_{conv,x}^- T_{\infty,1} + A_{conv,y}^- T_{\infty,2} + A_{conv,z}^- T_{\infty,3} + A_x^+ \left(\frac{H - fL}{C_p} \right)_{i+1,j,k} \right. \\
& \left. + A_y^+ \left(\frac{H - fL}{C_p} \right)_{i,j+1,k} + A_z^+ \left(\frac{H - fL}{C_p} \right)_{i,j,k+1} \right]^n \quad (2.19)
\end{aligned}$$

The above finite difference equations are explicit in time and therefore the time steps are restricted by the following stability criteria

$$\frac{\Delta t}{\Delta x_i^2} < \frac{\rho C_p}{2k} \quad (2.20)$$

Where, $i = 1, 2, \text{ or } 3$ and $x_1 = x$, $x_2 = y$, and $x_3 = z$.

The initial and boundary conditions for the thermal problem were as follows. The printing material was assumed to be deposited at room temperature, T_∞

$$T(x, y, z, 0) = T_\infty \quad (2.21)$$

onto a printing surface at a subfreezing temperature, T_{surf}

$$T(x, y, 0, t) = T_{surf} \quad (2.22)$$

The top boundary surface was exposed to convective interaction with the surrounding air

$$k \frac{\partial T(x, y, z, t)}{\partial z} \Big|_{z=d} = h(T_\infty - T(x, y, d, t)) \quad (2.23)$$

Where h is the convection coefficient to air and T_∞ is the ambient temperature assumed as 20°C . All the other boundaries are exposed to air [32], a cooling fluid [1], or both as described below in equations (2.24)-(2.26).

$$k \frac{\partial T}{\partial x_i} \Big|_{x_i=0} = h(z)(T_\infty(z) - T(x_1, x_2, z, t)|_{x_i=0}) \quad (2.24)$$

Where,

$$h(z) = \begin{cases} h_{fluid}, & 0 < z < z_{fluid} \\ h_{air}, & z > z_{fluid} \end{cases} \quad (2.25)$$

and

$$T_\infty(z) = \begin{cases} T_{fluid}, & 0 < z < z_{fluid} \\ T_{air}, & z > z_{fluid} \end{cases} \quad (2.26)$$

The z -dependent boundary condition, permits the variation in level of the cooling fluid, z_{fluid} , to also simulate the modified cryoprinting process described in [1]. This method of cryoprinting involves the use of a cooling fluid at some subfreezing temperature. As the layers get printed, the fluid level is increased such that the level of the cooling fluid is a fixed distance away from the plane of deposition (current layer), therefore ensuring more uniform freezing conditions in the different layers.

2.2.2. Extrusion model for the printing process

The second component of this model is for the continuously growing geometry in the extrusion printing process. A typical challenge in mathematical models for 3D printing is the simulation of a continuously growing domain. We approach this uniquely using the extrusion model described below. In extrusion-based bioprinting, the biomaterial is extruded from a typically

circular nozzle in a continuous cylindrical rod, known as the filament. However, upon deposition, this filament geometry is commonly approximated as rectangular in most models [25]. Therefore, for our model, we start with a cubic domain with rectangular cross section. First, a 3D cubic voxel of a certain size, $\Delta x_{unit} \times \Delta y_{unit} \times \Delta z_{unit}$ with an initial temperature $T(x, y, z, 0) = T_{initial}$ and the boundary conditions previously described (equations (2.22)-(2.26)) is assumed to be deposited at some point on the x-y plane for $z = 0$. For the simulations performed, the starting voxel size for every new layer or new stream is assumed to be $1mm \times 1mm \times 1mm$ for a volume of $1\mu l$. To represent the continuous stream, the domain is increased at a fixed rate equal to the velocity of the printing. So, for a print in the positive x-direction the domain is extended by adding a cubic volume $\Delta x_{print} \times \Delta y_{unit} \times \Delta z_{unit}$ to an origin corresponding to the previous x-extent. Similar additions are made for building in the y and z directions, with the possibility of five possible directions (x+, x-, y+, y-, and z+). It is important to note that domain can only be added to, therefore the assumption that the z direction can only increase in the positive direction after a new layer has been started is valid. Also, increases in the z direction are assumed to be the start of a new layer, so the initial 3D cubic voxel is added instead. The addition of new volumes to extend the domain along the x or y directions is dependent on the print velocity, v by the following equation

$$\Delta t_{print} = \begin{cases} \frac{\Delta x_{print}}{v}, & \text{for addition in the } x - \text{direction} \\ \frac{\Delta y_{print}}{v}, & \text{for addition in the } y - \text{direction} \end{cases} \quad (2.27)$$

Where Δt_{print} is the time interval of deposition. So, the domain is extended by a cubic volume $\Delta x_{print} \times \Delta y_{unit} \times \Delta z_{unit}$ every Δt_{print} for a printing in either of the x directions. For example, in the subsequent simulations presented in this chapter, at a fixed print speed of 50mm/s (designated 1x speed unless otherwise stated) the Δx_{print} or Δy_{print} is fixed at 0.25mm so that the interval of deposition was 0.005s. This time interval was the maximum time interval used in the thermal model to ensure that the effect of continuous deposition was captured in the heat transfer calculations.

New print shapes are entered into the model as origins (x,y,z) and directions (0-5) where zero indicates a pause or delay in the print for some time interval and the numbers 1,2,3,4,5, correspond to +x, -x, +y, -y, and +z directions respectively. With this formulation a wide-ranging combination of geometric shapes could be made including words and complex scaffold geometries. A more elaborate 3D modelling system that permits the use of CAD files or STL objects could be developed based on this model.

2.2.3. Algorithm for 3D cryoprinting simulation

An algorithm which combines the thermal model and the printing model was developed in MATLAB® to calculate the temperature field $T(x, y, z, t)$ during 3D cryoprinting from the enthalpy equations (2.14-2.19) using the initial condition (equation (2.21)) and boundary conditions (equations (2.22-2.26)). The temperature results are used to calculate the phase fraction, f , from equation (2.12) and the cooling rate, F , from equation (2.28) below

$$F = -\frac{\partial T}{\partial t} = \frac{T(x, y, z, t) - T(x, y, z, t + \Delta t)}{\Delta t} \quad (2.28)$$

The algorithm consisted of two parts. The first part involved division of the shape into domains at discrete time steps to be calculated. A time interval for the heat transfer calculations, Δt , is chosen such that Δt_{print} is a multiple of Δt (i.e $\Delta t_{print} = B\Delta t$ where B is a positive integer). Then the domain is selected for each time step by checking whether the current time ($t^{n+1} = t^n + \Delta t$) is greater than or equal to the previous time of domain update plus the time interval of deposition ($t_{domain} + \Delta t_{print}$). Once the current domain has been determined based on the origin and direction, the temperature distribution and phase fraction from the previous time, and any new inputs if the domain size is increased, are used as the initial condition for the thermal phase change model. These initial temperature and phase fraction inputs are then used to calculate the initial enthalpy at the nodes. This enthalpy distribution is then used to calculate new temperature, phase fraction, and cooling rate distributions after time Δt using equations (2.14-2.25) in the thermal phase change model. This allows the domain to be updated at discrete time intervals Δt_{print} , while the temperature and phase distributions are calculated at intervals Δt such that the temperature history can be used for subsequent calculations even though the domain is changing. The use of a fixed grid finite difference scheme ensures consistency in the location of the temperature nodes after deposition even as the size and shape of the domain for calculation changes. The MATLAB® script written to execute the above algorithm is included in Appendix 8.1.

2.2.4. Thermophysical parameters for simulation

Several simulations were done for bioprinting of an aqueous hydrogel bio-ink containing mostly water. Here we assume a soft hydrogel bio-ink consisting of a low concentration sodium alginate solution containing cells at a density of about 1×10^6 cells per milliliter. Sodium alginate is a polysaccharide copolymer of β -D-mannuronic acid (M) and α -L-guluronic acid extracted from seaweed. It is commonly used for bioprinting due to its biocompatibility, high water content, and oxygen permeability. Low concentration sodium alginate hydrogels used for bioprinting usually consist of mostly water (>95% water) so for simplicity and due to the lack of documented thermophysical properties for these bio-inks, the following thermophysical properties for water were assumed (Table 2.1)

Table 2.1: Thermophysical Properties of water

Parameter	Values
Density of Water (liquid), ρ_l , (kg m^{-3})	1000
Thermal conductivity of Water (liquid), k_l , ($\text{W m}^{-1} \text{ }^\circ\text{C}^{-1}$)	0.6
Specific heat capacity of Water (liquid), $C_{p,l}$, ($\text{J kg}^{-1} \text{ }^\circ\text{C}^{-1}$)	4186
Density of Ice (solid), ρ_s , (kg m^{-3})[101]	$917 \times (1 - 1.17 \times 10^{-4}T)$
Thermal conductivity of Ice (solid), k_s , ($\text{W m}^{-1} \text{ }^\circ\text{C}^{-1}$)[101]	$1.16 \times (1.91 - 8.66 \times 10^{-2}T + 2.97 \times 10^{-5}T^2)$
Specific heat capacity of Ice (solid), $C_{p,s}$, ($\text{J kg}^{-1} \text{ }^\circ\text{C}^{-1}$)[101]	$185 + 6.89 \times (273 + T)$
Melting point of water, T_m , ($^\circ\text{C}$)	0
Latent heat of fusion, L (J kg^{-1})	333600

2.3. Results

With the above thermal phase change model for extrusion-based printing, we simulated cryoprinting of an aqueous solution under different conditions and evaluated the results against expectations and experimental observations. The model was also experimentally validated and shown to be representative. The model was also used to evaluate the effect of several printing conditions such as print speeds, surface temperatures, printing methods etc. on thermal history and cooling rates.

2.3.1. Variation with printing speed

As an example, we simulated the printing of the letters CAL onto a cold surface at -5°C at varying print speeds looking at temperature (Figure 2.3a), phase fraction (Figure 2.3b), and cooling rate (Figure 2.3c). As anticipated, the temperature distribution was generally colder for the slower printing speed (0.5x speed, 25mm/s) compared to the faster printing speed (1x speed, 50mm/s). To further illustrate this, snapshots at the same time instant ($t = 1.7\text{s}$), show the maximum temperature was higher in the faster print (Figure 2.3a) than in the slower print (Figure 2.3d). The snapshot at that time instant also shows that the model is capable of handling variability in print speed as one layer of the letters CAL had been printed in the 1x print speed (Figures 2.3a-c) while only the letter C and part of A had been printed for the slower 0.5x print speed (Figures 2.3d-f). The temperature difference is also clearly captured in the phase distribution plots which show a larger liquid region and solidifying region (mushy zone) in the faster print (Figure 2.3b) than in the slower print (Figure 2.3e). This is expected since, at slower print speed, each element is cooled for longer before a new room temperature element from the nozzle is added so the temperature is lower and more of the material solidifies at the slower speed. Higher cooling rates are observed in the faster print (Figure 2.3c) than the slower print (Figure 2.3f). These indicate that differences in print speed are considered in the model.

To further probe the variation with print speed, the temperature, phase distribution and cooling rate at a fixed location (see Figure 2.3a) were recorded over time. Values from four different z-heights (0.25mm, 0.5mm, 0.75mm, and 1mm) were stored for each probe location. Using the recorded cooling rate, the solidification cooling rate at each of those points was determined. The solidification cooling rate was defined as the cooling rate at the instant when the solution becomes solid (i.e. the rate of temperature change immediately after the phase fraction first equals 0). This solidification cooling rate was plotted as a function of the print speed as shown in Figure 2.3g. The results show that for a fixed surface temperature of -5°C , the cooling rate increases gradually as print speed decreases. A reasonable result since heat is being added at a slower rate from the addition of room temperature bio-ink in the slower prints. Also, as anticipated, the solidification cooling rate is much higher closer to the cooling surface. This solidification cooling rate behavior matches the cooling rate behavior observed in Figures 2.3c and f. It is important to note that the solidification cooling rate calculations have significant sensitivity to the time steps used for the calculations. If the time steps are too large such that the temperatures used to calculate the cooling rates are either side of the melting temperature, the calculated cooling rate tends to be lower than actual. An example of this behavior is observed for the 0.16x print speed at the 0.25mm and 0.5mm heights.

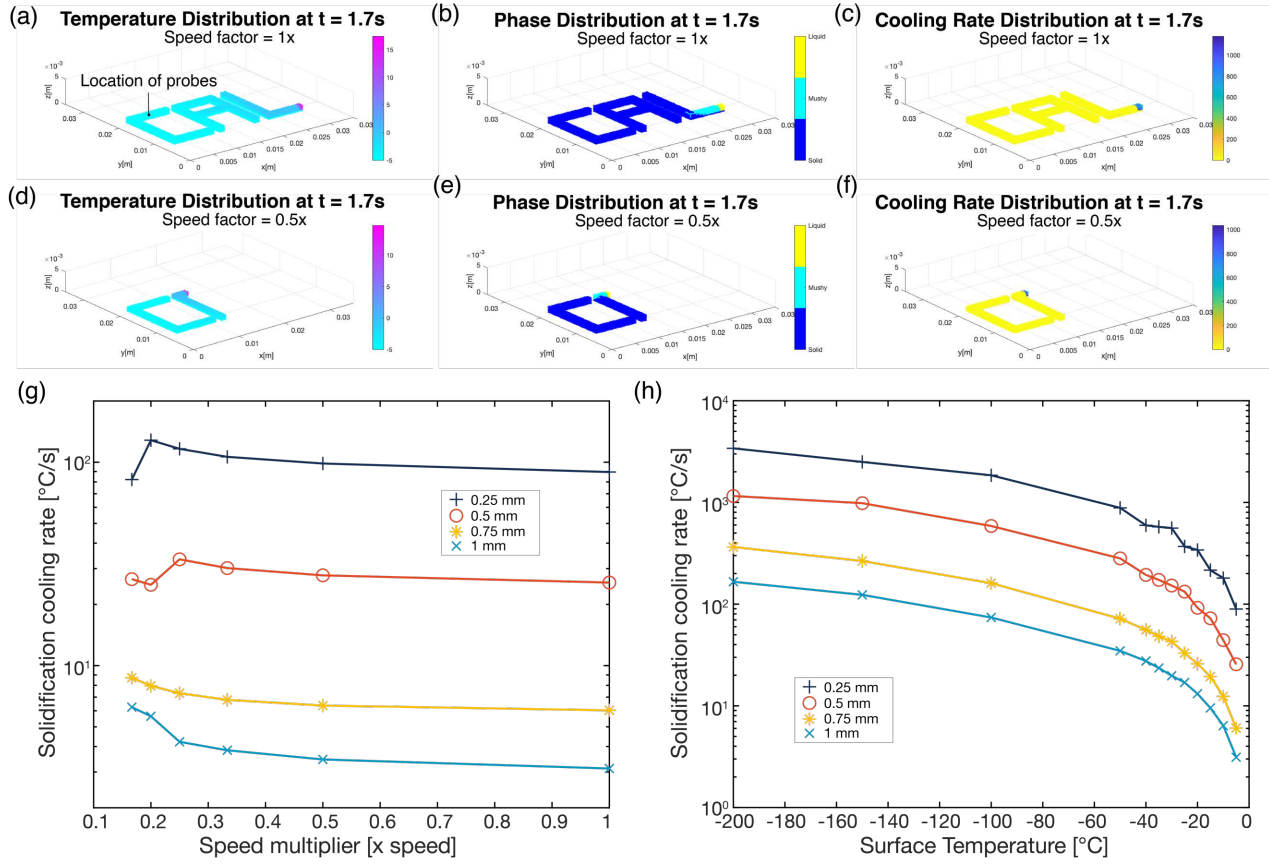


Figure 2.3: An example showing the (a) temperature distribution, (b) phase distribution, and (c) cooling rate distribution at a specific time instant ($t = 1.7\text{s}$) for printing of CAL at a rate of 50mm/s onto a surface at -5°C . (d) Temperature distribution, (e) phase distribution, and (f) cooling rate at the same instant ($t = 1.7\text{s}$) for printing of CAL at a rate of 25mm/s (0.5x speed) onto a surface at -5°C . (g) Solidification cooling rate at different heights at a specific location during the printing of CAL onto a surface at -5°C for a range of print speeds (h) Solidification cooling rate at different heights at a specific location during the printing of CAL at 50mm/s for a range of surface temperatures

2.3.2. Variation with surface temperature

With the probes in place, the dependence of solidification cooling rate on surface temperature was also queried. The cooling rate at different z -heights (0.25mm , 0.5mm , 0.75mm , and 1mm) during the printing of CAL, at a specific location during the print, were assessed for surface temperatures ranging from -5°C to -200°C . The solidification cooling rate was determined from the model as previously described. Clearly, as shown in Figure 2.3h, the cooling rate decreases for sensors farther away from the surface. Therefore, confirming that the dependence cooling rate with location is as expected. The model also shows an increase in cooling rate with decrease in surface temperature as is expected (Figure 2.3h). Solidification cooling rates range from 10^0 to over 10^3 simply by varying the surface temperature during printing. By controlling surface temperature and possibly printing speed a wide range of rates could be achieved. This control over cooling rate could be beneficial for cryopreservation, as critical cooling rates (CCR) for the preservation of a variety of cell types and biological matter could potentially be achieved. If a lower CCR is desired, the printing speed and/or the surface temperature could be increased.

Conversely, if a higher CCR is desired, the printing speed and/or the surface temperature could be decreased.

This allows the option of utilizing this model in an inverse manner to achieve a relatively constant CCR. By continuously varying the surface temperature and printing speed one can achieve a relatively constant CCR that is as close to the desired CCR for maximum viability in an entire 3D printed object. A recent thermal analysis of the freezing of human kidneys and rabbit kidney by Ehrlich et al showed the complexity of trying to scale whole organ vitrification protocols from animal models to human organs [73]. With control over the cooling rate of each element during a printing process, scaling issues associated with different sizes are less prominent. Each printed volume can simply be frozen at the ideal conditions required. In addition, the smaller freezing volumes would permit higher cooling rates thus minimizing the need for high concentrations of CPA for whole organ cryopreservation. Theoretically, a whole organ could be bioprinted and stored long term and then thawed and cultured when needed to obtain the fully functional organ.

2.3.3. Experimental Validation of Mathematical Model

Having established the usefulness of the model for understanding dependence of temperature distribution and cooling rates on several printing parameters, we validated that the model actually represents experimental observations. A description of the experiment setup, procedure, and results, are described below. The results from the experiments show the capability of the model to accurately predict temperature history at any point in the printed object during printing.

Materials:

A ZMorph VX Multi-Tool 3D Printer (ZMorph S.A., Poland) equipped with a paste extruder printing head and an 18-gauge needle as the nozzle was used for the printing. For the models, the inner diameter of the needle was assumed to be about 1mm in inner diameter (actual diameter is 0.84mm). Attached to the print bed was an ATS CP-1002 aluminum cold plate with a 4 in. x 4 in. Omega Kapton Polyimide insulated flexible heater KHA-404 (Omega Engineering, Norwalk, CT) and an Omega self-adhesive thermocouple type J (Omega Engineering, Norwalk, CT) sandwiched between the cooling plate and a thin copper sheet. The heater and thermocouple were attached to an Omega Platinum series CN32PT-220 temperature controller (Omega Engineering, Norwalk, CT) used to regulate the temperature of the printing surface. The cooling plate was cooled by circulating cooling fluid (60% Glycerol 40% water by volume) cooled by a Thermo Neslab RTE-140 cooling bath (Thermo Fisher Scientific, Waltham, MA) with an external flow circuit. The Neslab cooling bath was set to a few degrees lower than the set temperature and the temperature controller heats up the surface to keep it at the set temperature, $\pm 0.3^{\circ}\text{C}$. A FLIR B60 camera (FLIR systems, Wilsonville, OR) with a 240 x 240 resolution was mounted as shown in Figure 2.4a pointed at the front face of the sample and a sequence of pictures are captured at regular time intervals during the print. The printing ink was 2% w/v alginate (MW: 222g/mol) (Spectrum Chemical Mfg. Corp. Gardena, CA), made by dissolving the appropriate amount of sodium alginate in DI water.

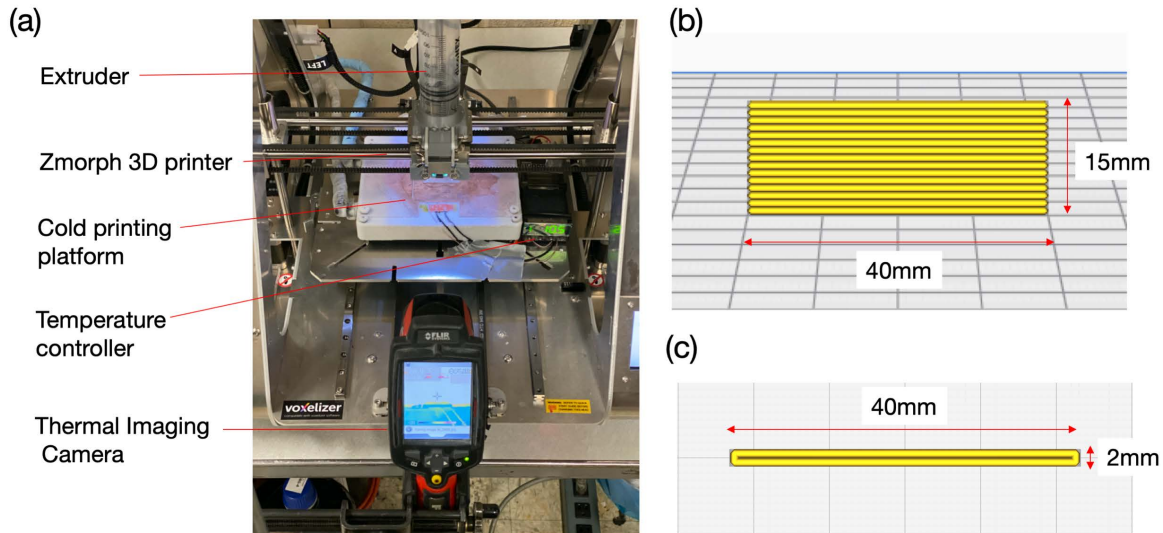


Figure 2.4: (a) Picture of experimental showing the 3D printer and position of thermal imaging camera (b) Side view image from Ultimaker Cura showing the slicing of the wall to be printed into 15 layers (c) Top view from Ultimaker Cura of the printed object showing the path of the print head for each layer.

Experimental procedure:

A 3D stereolithography (.STL) object is created using Onshape (Onshape, Cambridge, MA). The object was a 40mm x 2mm x 15mm wall as shown in Figures 2.4b & c. The .STL file is then sliced using a 3D print slicing application, Ultimaker Cura (Ultimaker B.V., Geldermalsen, the Netherlands), which converts 3D models into x, y, z movements, known as G-code. The object is sliced into 15 layers where each layer is 40mm x 2mm and 1mm thick (Figure 2.4b & c). Based on a 1mm nozzle size, the print path for each layer is 2 lines where one doubles back touching the other, as shown in Figure 2.4b. Print files are then generated for the two different print speeds outlined in Table 2.2 below. The G-code is then uploaded to the printer. The cooling system is turned on and the surface is set to the appropriate surface temperature corresponding to each case in Table 2.2. Three different print conditions were tested as outlined in Table 2.2. The parameters chosen were picked based on printability of the gel bio-ink used and the specifications of the thermal camera. Once the print starts, pictures are continuously captured until the material being deposited starts to overflow the print path before freezing. The print is aborted at this point as flow from the nozzle starts to separate from the object, forming larger droplets and leading to even more overflow. The thermal image capture is also halted since the overflow onto the surface of focus disrupts the measurements from the camera. The images obtained from the IR camera are then analyzed as described below.

Table 2.2: Summary of the print settings used for the experimental validation

Parameters	Print Speed	Printing Bed Surface Temperature
Case 1	1mm/s	-10°C
Case 2	1mm/s	-20°C
Case 3	0.5mm/s	-20°C

Boundary conditions used in the comparative simulations were as follows. Since the experiment was done for printing in room temperature air, the height of the cooling fluid, z_{fluid} ,

was set to zero and values for the boundary condition (equations (2.22-2.26)) were $h(z) = h_{air} = 50 \frac{W}{m^2}$ and $T_{\infty}(z) = T_{surr} = 20^{\circ}C$, to represent natural convection and the temperature of the surrounding.

Thermal Image Analysis:

The temperature at any given point on the captured IR image was determined using a custom MATLAB routine (Appendix 8.2). The algorithm determines the closest temperature and error in measurement based on a least squares method which minimizes the square root of the sum of squares of the difference between the Red (R), Green (G), and Blue (B) values of the selected pixel and the RGB values of corresponding pixels spanning the temperature colorbar located on the bottom of each image. Values for R, G, and B range from 0-255 so in cases without an exact match there could be several closest color matches. In these instances, the mean of temperatures of the closest matching colors is used and the standard deviation of those values is defined as the error in measurement.

Using this algorithm, the temperature at a given point during the print, a specific pixel of the 240 x 240 pixels closest to the location of interest, is selected and temperatures around the given pixel and 3 other surrounding pixels are measured and a graph of the temperature and error resulting from the image analysis is plotted. The selection of several pixels accounts for small vibrations and minimizes the error as a result of the low resolution of the thermal camera. By measuring the temperature of several images captured at regular time intervals, temperature evolution at specific points of interest were determined.

Results:

As shown in Figures 2.5a and 2.5b, at any particular time, the temperature distribution from the thermal images (Figure 2.5a) qualitatively looks similar to those from the model (Figure 2.5b). Likewise, the quantitative temperature values at a given point in the second layer of the printed object were recorded from experiment and generated for the model. These temperature evolutions over time were compared as shown in Figure 2.5c. From Figure 2.5c it is evident that the temperature of points B1, B2 and B3 (three points on the outward face of the 2nd layer, 10mm from the right boundary of the print) from the model fall within the error margins of the measured temperature at AA (a point in the second layer 10mm from the right boundary of the print) after 2.8 minutes. After 2.8mins, the predicted temperature midway within layer 2 (B2) is within 1% of the maximum uncertainty in the measured temperature (AA). Also, important to note from Figure 2.5c, is the rise in temperature at 2.2 mins (printing of second wall adjacent to and behind the wall face being monitored, see above methods for path of the print head), at 3.2 mins and at 3.6 mins (the printing of the third layer on top of the point of interest). These temperature increases occur in the experimental measurement at the same time and are of comparable magnitude to the increases in the model. Before about the 2.8 min mark, however, there is notable discrepancy in the temperatures from the instant that point is deposited (1.8 mins) to about 2.8 mins. This may be because of the rapid rate of temperature drop within this time frame. The temperature within that time changes at a much faster rate than can be captured by the thermal camera. This uncertainty in temperature measured is emphasized by the large error bars for the experimental values recorded between 1.8 mins and 2.8 mins. Other sources of uncertainty, could be the difference in emissivity of the liquid and solid phases and noise from proximity of the nozzle which could affect the measurements during solidification.

Temperature distributions for different print speeds and surface temperature conditions were also compared (see Table 2.2 for experimental parameters). As expected, and detailed in section 2.3.1, at comparative points during the print, the temperatures for the print speed of 1mm/s (Figure 2.5d) are higher (mean temperature is higher) than the temperatures for the print speed of 0.5mm/s (Figure 2.5e). The same can be seen when comparing printing at 1mm/s onto a surface at -20°C with printing onto a surface at -10°C (Figure 2.5e vs Figure 2.5a). These results agree with the trends in Figure 2.3 where slower print speeds and lower surface temperatures correspond to lower temperature distributions.

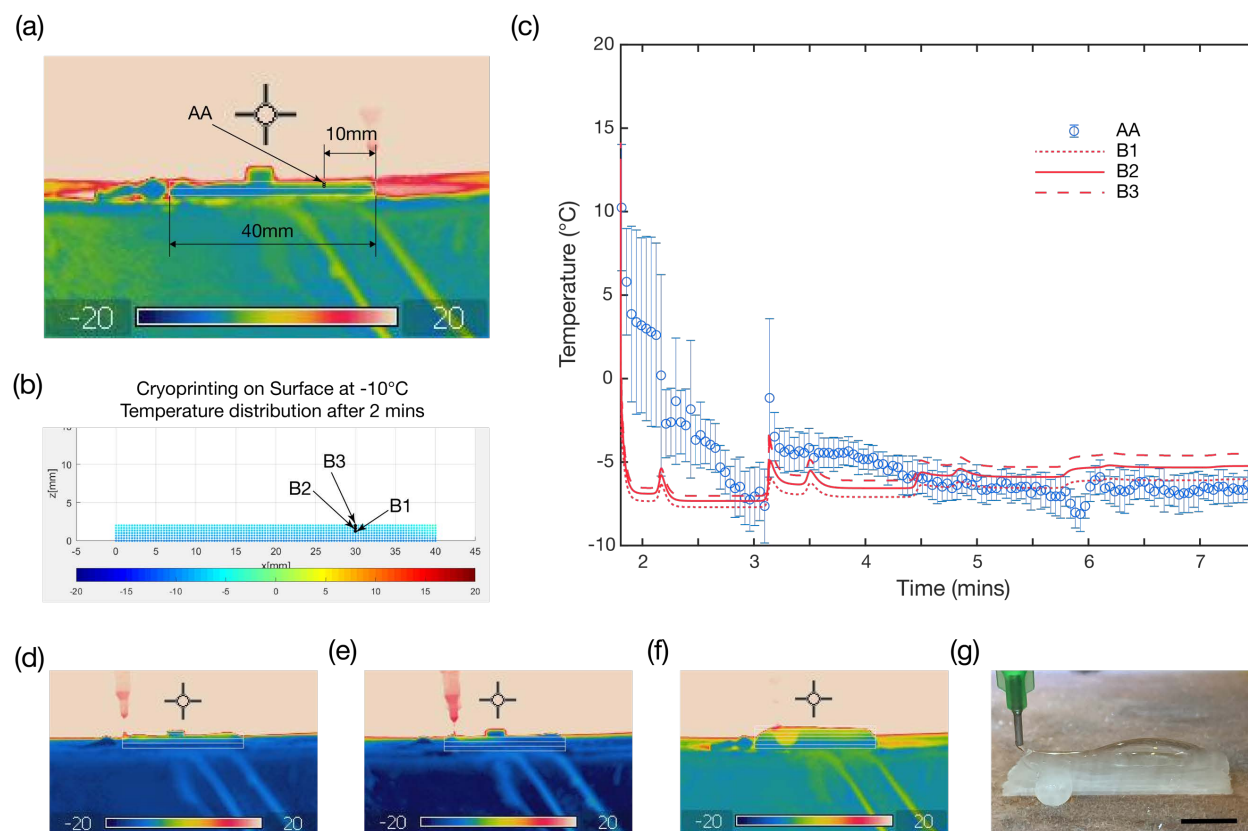


Figure 2.5: Experimental validation of model. **(a)** Thermal Camera Infrared image capture during printing while printing the second layer (2 mins after the start of the print, print speed 1mm/s and surface temperature -10°C) **(b)** Plot of the temperature distribution predicted from the model while printing the second layer (2 mins after the start of the print, print speed 1mm/s and surface temperature -10°C) **(c)** Comparison of the temperature evolution at point AA from the experiment and similar points B1, B2, and B3 from the simulated model **(d)** Thermal Camera Infrared image capture of the temperature distribution during printing of the third layer for Case 2 (print speed 1mm/s and surface temperature -20°C) **(e)** Thermal Camera Infrared image capture of the temperature distribution during printing of the third layer for Case 3 (print speed 0.5mm/s and surface temperature -20°C) **(f)** Thermal Camera Infrared image capture of the temperature distribution during printing showing the melted and overflow of unfrozen material. **(g)** A picture of the printed wall during experiments showing melting and overflow of unfrozen material (10mm scale bar).

Lastly, the model predicts when melting occurs during printing. This is of importance when determining print speed, nozzle size and surface temperature to use when 3D cryoprinting a scaffold. If melting starts to occur before the object is fully printed, the resolution suffers and the

structure falls apart. Figures 2.5f and 2.5g show melting occurring during experiment while the 6th layer is being printed. This agrees with the simulation from the model. It is also important to note that the melting begins at the left and right ends of the shape as seen in the temperature distribution and phase distribution predicted by the model. Once melting begins, the shape of the print changes; beginning at the left and right edges, the shape gets rounded. As seen from the experiment, the rounding begins at different layers depending on the surface temperature (beginning earlier at higher temperatures) and print speed (beginning earlier at higher print speeds). This also agrees with previous results discussed in 2.3.1 and 2.3.2.

The fact that the rounding begins earlier than the 6th layer in the experiment is partially due to fluid effects (surface tension and viscous forces) that govern the drop shape when the nozzle is momentarily stationary. These effects are not accounted for in the phase change model. They, however, may be responsible for melting beginning earlier in the experiments compared to the mathematical simulations.

Differences in the results between the experimental measurements and model, though minimal, could be due to one or more of the following factors: The difference in mean temperatures and the slower cooling rate of the experimental measurements could be attributed to the lower thermal conductivity of the alginate compared to that of the pure water (used in the model). We simulated runs for several different thermal conductivity values and found better matches when using lower thermal conductivity than water for the solid phase (data not shown). However, without reliable data on the thermal conductivity of the alginate solution and other sources of measurement error, we compared experimental results to the simulation with pure water. Lower cooling rates in the experiment could also be due to heat added from the nozzle which is not accounted for in the model. Temperature was also measured using an IR thermal camera which measures the surface temperature, and could be affected by differences in emissivity between the liquid and solid phases. The model also assumed rectangular cross-section for the extruded stream and does not consider surface tension and viscous effects that affect the shape of the stream being printed and frozen.

2.3.4. Addition of cryogenic cooling fluid for control

Unlike, in extrusion based plastic printing, the freezing process of aqueous bio-inks in room temperature air is limited by the rate of conduction from the cold surface. So, as the height of the build gets larger, freezing becomes more difficult as conduction through the large solidified object takes longer and the range of achievable cooling rates shrinks. An effect clearly demonstrated in the experimental validation results in section 2.3.3. For instance, if the bio-ink is deposited onto a surface at a fixed temperature of -5°C, by the time the print gets to a few centimeters in height, the printing rate either has to be slowed down significantly or even stopped to allow the previous layer to get to a low enough subfreezing temperature to not completely melt when the new layer at room temperature is deposited. This would hamper the speed of the printing process and negate one of the advantages of this method – the ability to make structurally stable large structures. Cryoprinting using a cryofluid bath solves this problem [1]. In this method, a cryofluid at subfreezing temperature is added to the printing area to convectively cool the layers that have been printed, at a faster rate. In [1], Adamkiewicz and Rubinsky hypothesize that by controlling the liquid level, for instance keeping it a layer below the current printing layer, the second layer and every subsequent layer experience the same cooling conditions so no matter how large the structure gets, the previous layer is always sufficiently cold to ensure freezing of the new material.

Using this model, we revisit this hypothesis. We analyzed the difference in temperatures and freezing conditions for cryoprinting of a hollow rectangular column in air as in [32] versus with the assistance of a cryofluid [1]. The boundary conditions were as follows. As illustrated in Figure 2.6a, for cryoprinting in air, the printed object is surrounded by room temperature air, so the height of the cooling fluid, z_{fluid} , was set to zero and values for the boundary condition (equations 2.23-2.25) were $h(z) = h_{air} = 50 \frac{W}{m^2}$ and $T_{\infty}(z) = T_{surr} = 20^{\circ}C$. For cryoprinting in a liquid cryofluid (Figure 2.6e), the printed object is surrounded by liquid up to some level, z_{fluid} , set to be one layer below the plane of printing for this analysis. A fluid convection coefficient, h_{fluid} , 100 times the value assumed for air, $5000 \frac{W}{m^2}$ was assumed and the fluid temperature, T_{fluid} , was set equal to the surface temperature. The assumed convection coefficient for the liquid was based on the thermal conductivity difference between air and most liquids and reported free convection coefficients for air and for water-based coolants.

Thermal history, phase distribution and cooling rates for both of these printing conditions were simulated for comparison. The results show that, at the same instant in time, the temperature distribution is colder while printing in the cryofluid (Figure 2.6f) compared to printing in air (Figure 2.6b). Similarly, from the phase distribution plots, there is a significantly larger region of liquid in the print in air (Figure 2.6c) compared to the liquid assisted case (Figure 2.6g). In fact, once the height of the print in air gets to the 12th layer it is unable to fully solidify new layers at that surface temperature. The print with the cryofluid, however, still forms solid layers. This result matches the experimental observation of Adamkiewicz and Rubinsky[1]. In the experiment performed in that study, they show the printed object melting as the print height gets to a certain point while printing in air (Figure 2.6k) whereas with the use of liquid nitrogen as a cryofluid, the printed cylinder remained intact and the print was completed (Figure 2.6l). An analysis of the cooling rates in both methods revealed the cooling enhancement provided by the cryofluid. The peak cooling rate while printing in air (Figure 2.6d) was markedly lower than the cooling rate while printing the same object using a cryofluid (Figure 2.6h). This result highlights the potential utility of a thermal printing model of this kind. A variety of other printing conditions could be analyzed, as well as the effect of different fluid heights, and fluid types with greater throughput and in less time than it would take to run experiments.

Temperature, phase fraction, and cooling rates were also recorded at specific locations in each layer to observe the thermal history and peak cooling rates from layer to layer. Figure 2.6i shows the temperature and phase fraction at similar locations in each layer. The temperature plot shows the recurrence of the exact same temperature profile from the second layer onwards for the printing in cryofluid, indicating a uniformity in cooling conditions from layer to layer (a result corroborated by Figure 2.6m). This differs from the increase in steady state temperature for each new layer for the case of printing in air. By the 13th layer the temperature no longer falls below the freezing point (comparatively the temperature for that layer in the cryofluid still decreases towards $-5^{\circ}C$). In the cooling rate plot in Figure 2.6j, the same pattern is observed. The cooling rate peaks decrease with increase in layer count while printing in air, whereas cooling rates stay consistent while printing in cryofluid.

From the cooling rate plots, solidification cooling rate was recorded as previously described. Figure 2.6m shows the solidification cooling rate in each layer for printing in air and for printing with a cryofluid. Immediately, a few things are apparent. First, the initial solidification cooling rate in the first layer is the same for both processes. This is indicative of the model being consistent since the first layer of both printing conditions does not involve the use of the cryofluid.

Secondly, there is no solidification cooling rate value for the 13th layer for the printing in air condition. This is consistent with all the other results for that condition showing that freezing does not occur at that print speed in this layer. Thirdly, the freezing rate after the second layer is constant for the printing in cryofluid while the freezing rate continues to decrease down to zero. This constant cooling rate when using the cryofluid enhances repeatability in the freezing rates from layer to layer. Lastly, by the 12th layer, the freezing rate for the printing with liquid is 10^4 times the cooling rate for the printing in air. This difference in freezing rates shows the advantage of using the cryofluid.

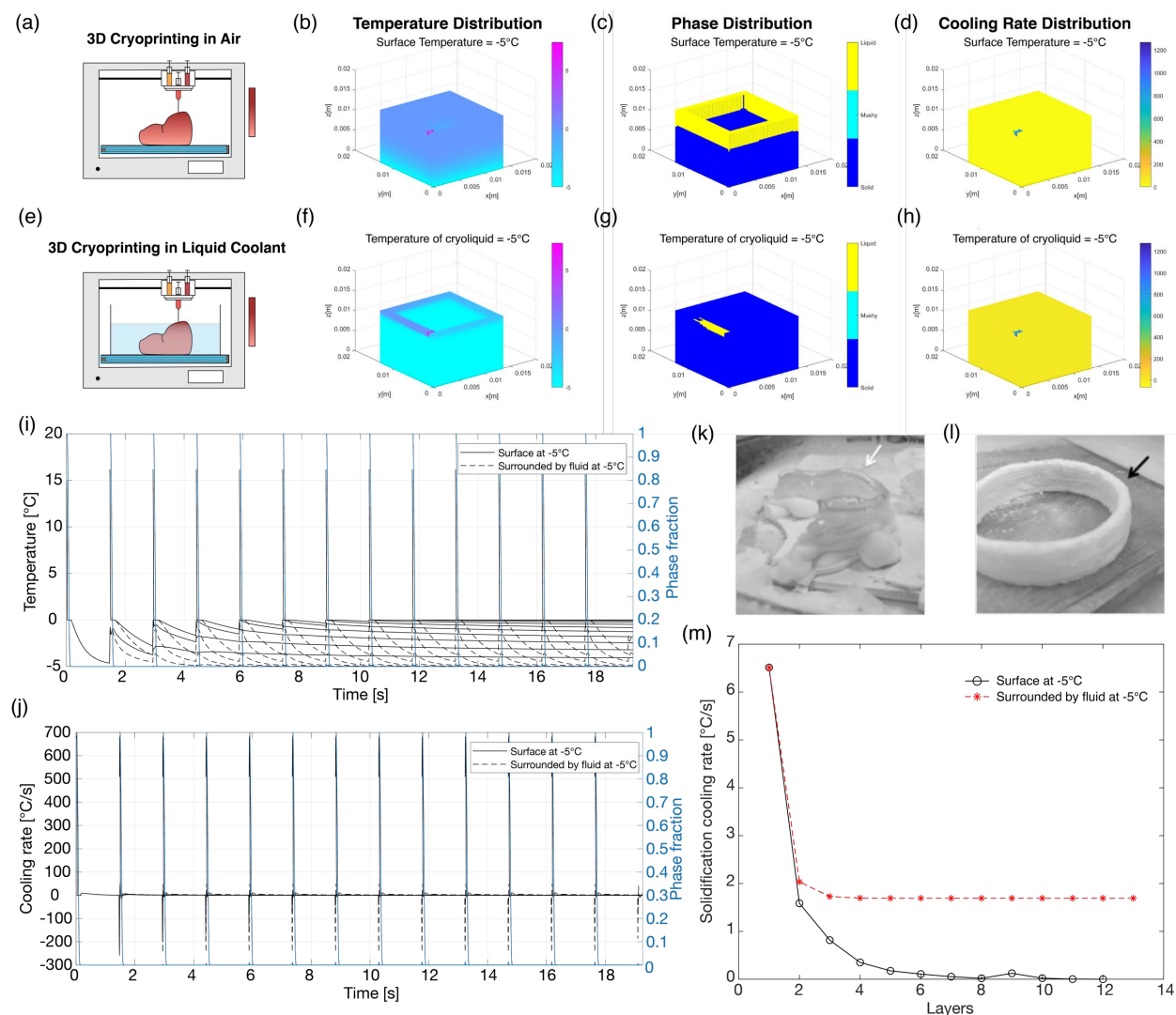


Figure 2.6: (a) Illustration of the process of cryoprinting in air (b) Temperature distribution (c) Phase distribution, and (d) cooling rate distribution for a hollow rectangular column being printed in air onto a cold surface at -5°C . (e) An Illustration of the process of cryoprinting using a cryofluid at a controlled level (f) Temperature distribution (g) Phase distribution, and (h) cooling rate distribution for a hollow rectangular column being printed using a cryofluid at -5°C . (i) Comparison of the temperature and phase fraction over time for a specific location in each layer of the printed column for printing in air and printing using a cryofluid (j) Comparison of the cooling rate and phase fraction over time for a specific location in each layer of the printed column for printing in air and printing using a cryofluid (k) Experimental example showing the melting of a hollow cylindrical column while printing in air [1]. Reproduced with permission from Adamkiewicz et al. (l)

Experimental example showing the successful print (no melting) of the same hollow cylindrical column while using liquid nitrogen as a cryofluid [1]. Reproduced with permission from Adamkiewicz et al. **(m)** Comparison of the solidification cooling rate in different layers for cryoprinting in air and cryoprinting with a liquid cryofluid

The method with the cryofluid also adds another layer of control to both the surface temperature and print speed, increasing the range of cooling rates that could be achieved. So, if the CCR needed is beyond the range achievable with varying print speeds or surface temperatures alone, the cryofluid could also be manipulated. The constant consistent cooling in multiple layers also means that in an inverse design tool where the printing conditions are to be determined so as to achieve a narrow band of CCR throughout an entire shape, it is much easier to arrive at a solution to a given 3D geometry.

2.3.5. Prediction of cell survivability

In the making of cell containing tissue scaffolds for tissue engineering, it is important that an ample proportion of cells being used survive the process. The survivability of these cells depends on various conditions including cell type, with embryonic stem cells and other stem cells finding it hard to survive tissue engineering processes [102]. So, it is essential to evaluate how these cells will handle the even harsher conditions experienced during 3D cryoprinting. Such as the formation of ice and change in osmotic balance during freezing which can cause significant damage to cells. Controlling the freezing process to balance these effects optimizes for cell survival and attainment of high cell yield. Furthermore, the encapsulation of cells in hydrogels has been shown to additionally improve cell survival rate, improving cell protection during freezing and thawing [102,103]. Therefore, in a controlled cryoprinting process using hydrogel bio-inks, the survival rate could be increased significantly by adequately regulating the freezing rate.

Using the cooling rates obtained from the model in combination with data for optimal cooling rates for stem cells and other cell types [104], cell survival can be predicted as a function of printing parameter. To demonstrate the enhanced control over cooling rate using the cooling liquid, we evaluate the survival probability of cells for a simulation of printing in air compared to printing in liquid. Figure 2.7a shows one such survival rate plot for bone marrow stem cells printed at -5°C . The results from this figure show that the survival probability can be maintained consistently at around 25% from the second layer onwards when printing with a cryofluid at -5°C . Whereas the survival probability fluctuates between 0% and the maximum of 65% when printing in air, onto a surface at -5°C . This result serves to highlight the importance of being able to control the freezing rate. After reaching the maximum at the 10th layer, the print in air diminishes back to zero for all the higher layers while, with the cryofluid, the viability is maintained regardless of layer height. Although, the cooling rate does not yield the maximum survival rate for all these layers, the parameters can be further tweaked so that the cell survival rate is maximum throughout when cryoprinting with a cryofluid.

Figure 2.7b shows how this ability to controllably vary freezing rate, can be used to manipulate cell survival in multicellular tissue. In Figure 2.7b, the cooling rates are allowed to vary from layer to layer such that the first to fourth layers support the survival of red blood cells (RBCs), the fourth to tenth layer support the survival of lymphocytes, and the eighth to twelfth layer most supports the survival of stem cells. This ability to vary survival probability spatially for different cell types could be beneficial in the generation of multicellular tissue. One can envision the varying of other parameters like print path, surface temperature, level of cryofluid, print speed,

nozzle speed etc., to spatially pattern a scaffold with voxel level precision for the formation of a complex tissue.

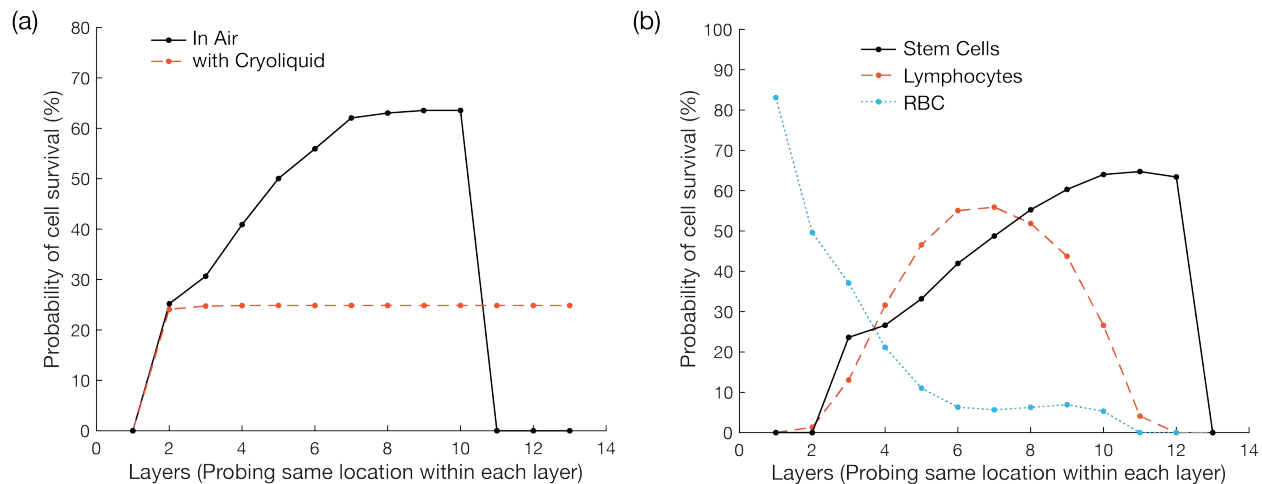


Figure 2.7: (a) Predicted survival probability for the cryoprinting of a bio-ink containing stem cells onto a surface at -5°C in an air surrounding and in a cryofluid (b) Predicted survival probability for the printing of different types of cells, showing the variability in the survival from layer to layer for different cells printed at -10°C .

It is important to emphasize that the cell viability predictions described above are for illustration purposes only. Since most bioprinting processes typically use stem cells that can be differentiated and functionalized more easily into tissue, the results showing the RBCs and Lymphocytes are not of much use in practice. In practice, the viability of the stem cells being used would need to be determined at various cooling rates to optimize the cryoprinting process for maximum cell survival. In addition, the data from [104] used in these predictions is for cryopreservation in cell culture media, whereas in actuality the cells are suspended in a hydrogel environment during cryoprinting which has been shown to significantly improve cell viability during cryopreservation [102]. Also, the addition of cryoprotectants like glycerol and DMSO can alter these survival probabilities as a function of cooling rate [88]. Although not strictly accurate predictors, these results show the potential use of this model for tissue patterning and optimizing of cell yield in cryoprinted tissue scaffolds. The current lack of accurate data on the impact of cooling rates on the viability of stem cells encapsulated in hydrogels and the impact of cryoprotectants on microencapsulated cells need to be rectified for better predictions. Therefore, a potential future area of research would be generating this survival rate data for the most common stem cells used for tissue engineering.

2.4. Discussion and conclusion

To conclude, we have developed a thermal phase change model for 3D cryoprinting as a tool to analyze or design 3D printing protocols for optimum cryopreservation of printed biological matter. We demonstrated the usefulness of the model by simulating a typical printing process under different printing conditions. We found a direct correlation between observed cooling rates and surface temperature as well as print speed. We also verified the advantages of a modified 3D

cryoprinting method which utilizes a cooling fluid to achieve higher and more uniform cooling rates throughout a 3D structure. This control over cooling rates can be employed to manipulate cell survival, predict, and maximize the survival probability of multiple cell types in complex tissue scaffolds. The model introduced in this study could potentially ease the testing and adoption of cryoprinting which would be beneficial for 3D bioprinting and tissue engineering in general. Some results from the thermal model suggests that cryoprinting could enable easier cryopreservation of large engineered tissue and organs, potentially circumventing some of the limitations associated with cryopreserving whole tissues or organs after bioprinting. If an organ is fabricated using cryoprinting instead, it is indeed easy to achieve the optimum cooling rates required for preservation.

To demonstrate the validity of this model, we performed a study measuring the temperature distribution using a thermal camera. The validation experiment was only done for the mode of printing in air since other surrounding liquids are not transparent to IR from the thermal camera. Nevertheless, the results sufficiently show the benefits of this model. There is agreement in temperatures within layers and in predictions of solidification. Better agreement between the model and experiments however, could be achieved by accounting for more experimental parameters in the model and better constraining the experimental setup.

In future work, the usefulness of this model can be further exemplified by also performing cell viability studies using cell laden bio-inks. We believe this process would be able to work with cells as Akiyama et al show that cell viability remains high after freezing during ink jet printing under specific conditions [85]. With the model, we can control the freezing conditions to ensure optimum cell viability. Additionally, there is also evidence that cell viability during freezing is improved when encapsulated in a hydrogel such as sodium alginate [105]. So future validation tests could be performed using low concentration (0-3%w/v) sodium alginate hydrogels with cell density of between 1×10^6 and 5×10^6 cells per milliliter.

As previously mentioned, freezing only temporarily improves the mechanical rigidity of the biomaterial being printed. Increasing the modulus of a hydrogel like sodium alginate from about 1kPa to about 1GPa for ice and the yield strength from O(2)Pa to over O(1)MPa. These differences are what makes this an advantageous process for the development of larger structures as the yield criterion for printing of a soft biomaterial, $\frac{\rho gh}{\sqrt{3}} \geq \tau_y$, shows [25]. Where ρ is the materials density, g is the acceleration due to gravity, h is the height of the object, and τ_y is maximum yield stress. The higher the yield strength, the larger the material that can be printed. However, since the printed object is used above the freezing point of ice, there has to be a means of making sure it remains solid upon thawing. For most hydrogels used in bioprinting, this is done by cross-linking. In order to maintain the structure of the object after printing cross-linking would still be required. Cryoprinting enables flexibility in how this cross-linking may be done. Because cross-linking is not required to maintain structure during printing, the material may now be crosslinked before printing, after printing, or partially before and completely after. This could improve printability as materials with lower viscosity can be extruded through smaller nozzles without applying excessive shear stress to the cells. In the ensuing chapters we will discuss the cross-linking method used to maintain structural rigidity after cryoprinting and investigate the effects of cross-linking sequence on the material properties.

Finally, with further development, this model could also be coopted as an inverse design tool to generate protocols that maintain constant cooling rates when working with delicate biological matter. Instead of evaluating cell survival for discrete printing parameters, a map of cells and their minimum target survival percentage can be used to generate printing protocols

where several parameters can vary in real time. Lastly, the generality of the developed thermal model means it is not constrained to a material type or phase change problems alone and could be extended to other areas of 3D printing where the understanding of thermal history is desired.

Chapter 3

3. Freezing modulated cross-linking for stability of fabricated frozen scaffolds

3.1. Introduction

In chapter 2, we introduced 3D cryoprinting which is a new method of 3D bioprinting at subfreezing temperatures that utilizes freezing instead of cross-linking to form solid structures from liquid bio-inks. This development enhances the possibility of generating large tissue scaffolds from soft biomaterials, which thus far, has been a significant challenge to the goal of anatomical-scale human organs. Similar to several bioprinting methods, the choice of bio-ink used is an essential element of 3D cryoprinting. Bio-ink materials play a crucial role in the cell interactions and ability to print [27,106]. One common material used for bioprinting is Alginate, because of its biocompatibility and tunable mechanical properties. Alginates are copolymers of β -D-mannuronic and α -L-guluronic acid that form viscous liquids when dissolved in water. Alginate is obtained from seaweed so it is naturally occurring and relatively abundant. In low concentrations, alginate is typically crosslinked to increase its mechanical strength and enable formation of complex structures hydrogel structures from alginate solutions [63,107]. Cross-linking is a process of linking polymer chains together into a network structure with limited chain movement and effectively higher molecular weight.

Similar to others, [108], we observed that the process of extrusion 3D printing is highly dependent on the rheology of the ink, which for alginate gels, depends on the degree of cross-linking and the composition of the gel. As a result, it can be difficult to print alginate hydrogels cross-linked prior to 3D printing, because the rheological properties vary with composition and time after the onset of cross-linking [70,71]. A possible solution is 3D cryoprinting using the alginate solution, prior to cross-linking, and achieving mechanical rigidity by freezing instead. Prior to forming the hydrogel, the rheological properties of the un-crosslinked alginate solution (lower shear stress) are preferable for extrusion through smaller nozzles [25]. Therefore, the use of alginate solution as the printing ink allows the use of smaller nozzles for bioprinting, thus permitting better resolution, structure, and shape during fabrication. This alginate printing ink, however, lacks mechanical rigidity before cross-linking which limits the size of printable objects.

3D cryoprinting uses freezing and can therefore provide this rigidity, enabling the use of un-crosslinked alginate solutions as bio-inks. Freezing has also been shown to generate porosity [109] and can be used to dictate microstructure in alginate. But freezing only works for small structures and current techniques cannot control the freezing induced microstructure in large 3D printed tissues. Following fabrication using cryoprinting, the printed scaffold has to be cultivated into living tissue, a process typically done in a bioreactor at physiological temperatures. Hence as the fabricated frozen tissue scaffold is brought to temperatures above the freezing point, the material returns to liquid and the enhanced mechanical properties provided by the ice formed during freezing are lost. So, there is a need to maintain the scaffold integrity during and after melting.

The use of alginate in the food industry and in the pharmaceutical industry for drug delivery suggests a possible solution. In the food industry, liquid food products mixed with alginate are cross-linked to form alginate gels by first generating the shape (prior to cross-linking) and then submerging the shape in a cross-linking solution for the diffusion of the crosslinker into the object. This commonly used technique in the food industry is known as spherification [110,111]. It is also used for the formation of gel beads in biotechnology [112]. A variant of this technique is known as reverse spherification which as the name suggests; reverses which media contains the crosslinker (crosslinker is mixed in food product and brought in contact with alginate). Other variants of these techniques which incorporate freezing are: cryogelation [109] and freezing reverse spherification [113]. These techniques are generally suitable for the formation of small spherical structures with thin cross-linked exteriors (gel exterior) and liquid interiors, but can be extended further to complete cross-linking.

Realizing this, we developed a technique in which the 3D printed object is cross-linked as it thaws in a solution containing the crosslinker. This technique called freezing modulated cross-linking provides a complete solution to the 3D printing of large objects using alginate. It is similar to the method used by Ho et al. for the preparation of porous scaffolds [114]. With freezing modulated cross-linking, the non-crosslinked alginate solution used as the 3D printing material would have preferred rheological properties during printing, the 3D cryoprinting fabrication process would generate a rigid 3D printed structure, and the diffusion of crosslinker into the melted part of the frozen scaffold melting as a result of submersion in a cross-linking solution will provide the final rigidity to the 3D printed object.

So, freezing modulated cross-linking is a compound and multifaceted process and one which to the best of our knowledge has not been studied for this application. Its complexity arises from the need to adjust the rate of melting relative to the diffusion of the crosslinker and the cross-linking reaction, because if the alginate object is melted too fast it could lose its mechanical structure prior to cross-linking, hence the terms freezing modulated. The frozen region that is impermeable to the crosslinker can be used to control the rate of cross-linking and extent of hydrogel formation. The goal of this study is to use a mathematical analysis to examine the feasibility and the governing parameters of this cross-linking during thawing. Here, the mathematical formulation is multipart and non-linear. It involves a process of heat transfer with phase transformation that describes the propagation of the melting front, the diffusion of the crosslinker⁵ in a domain with moving boundaries (change of phase interface), and the cross-linking reaction in the melted alginate to form the hydrogel.

To better understand this complex heat and mass transfer problem and to aid in designing protocols for more complex objects, we analyze this melting-diffusion-reaction process in a first order 1-D formulation of the problem. The primary goal being, to develop a fundamental understanding of what parameters affect the effectiveness of gel formation during melting. By using analytical approximations and dimensionless analysis, we can predict the effect of various design parameters on this process. The aim of the presented analysis is to characterize the problem and gain insight into the parameters governing this process, and not necessarily to solve the numerical problem for a complex structure.

⁵ In the case of alginate bio-inks the chemical crosslinker is usually a divalent cation salt, like salts containing Ba²⁺, Ca²⁺, Mg²⁺ etc.

3.2. 1-D mathematical analysis of freezing modulated cross-linking

A 1-D problem that describes cross-linking during melting of a frozen slab of alginate was formulated for analysis. In this formulation, the cross-linking reaction is driven by the diffusion of a Ca^{2+} based salt (such as CaCl_2 , CaCO_3 , CaSO_4 etc.) into the melted region of the alginate slab. Figure 3.1 shows the domain for the melting-diffusion-reaction problem to be analyzed.

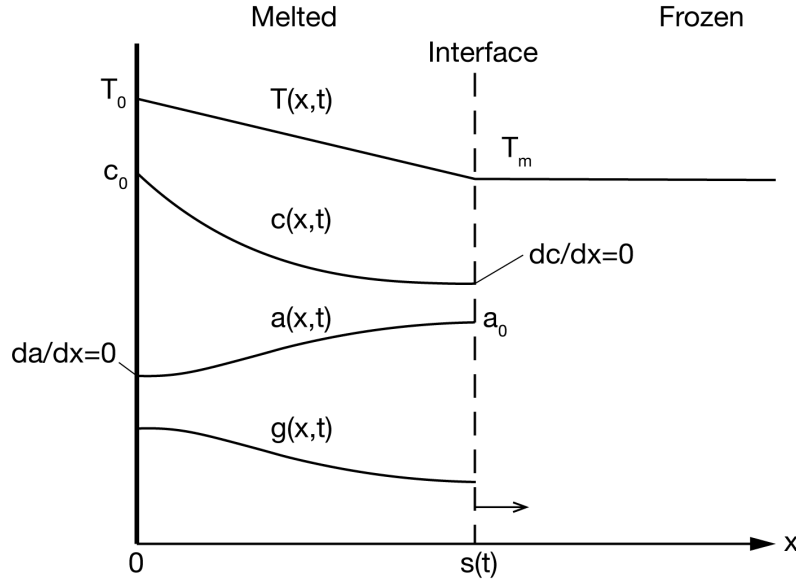


Figure 3.1: Schematic of the geometry for the melting-diffusion-reaction problem in a semi-infinite medium

Here, we will examine the problem in two different parts: (a) The melting problem and (b) the diffusion-reaction problem describing the diffusion of salt into the time varying melting domain and the cross-linking reaction to form gel.

First, the melting problem. This common phase change problem has been explored by many others [99] so only a brief description of the problem and its solution is outlined as follows. The temperature in the melted region can be determined by the heat equation

$$\frac{\partial T}{\partial t} = \alpha \frac{\partial^2 T}{\partial x^2}, \quad 0 < x < s(t), \quad t > 0 \quad (3.1)$$

Where α is the thermal diffusivity of the melted alginate. The initial condition is given by

$$T(x, t = 0) = T_m \quad (3.2)$$

Where T_m is the melting temperature of the alginate. There is a prescribed temperature on the outer boundary of the slab, $T_0 > T_m$

$$T(x = 0, t) = T_0 \quad (3.3)$$

At the melting interface the temperature is the melting temperature

$$T(x = s(t), t) = T_m \quad (3.4)$$

and an energy balance at the interface yields

$$-k \frac{\partial T}{\partial x} \Big|_{x=s(t)} = \rho L \frac{ds}{dt} \quad (3.5)$$

providing the last equation needed to determine the location of the moving melting interface, $s(t)$ at any time. Where k is the thermal conductivity, ρ is the density of the liquid, and L is the latent heat of melting.

Dimensionless variables, $\Theta = \frac{T-T_m}{T_0-T_m}$, $X = \frac{x}{s(t)}$, $\eta = \frac{t\alpha}{s(t)^2}$, and Stefan number, $Ste = \frac{k(T_0-T_m)}{\alpha\rho L}$ are substituted into Eqs. (3.1) – (3.5) to yield the following formulation for $\Theta(X, \eta)$

$$\left(1 - \frac{2\eta s}{\alpha} \frac{ds}{dt}\right) \frac{\partial \Theta}{\partial \eta} = \frac{\partial^2 \Theta}{\partial X^2}, \quad 0 < X < 1, \quad \eta > 0 \quad (3.6)$$

Which for quasi-steady conditions where the temperature becomes steady relative to the slow movement of the melting interface, reduces to

$$0 = \frac{\partial^2 \Theta}{\partial X^2}, \quad 0 < X < 1, \quad \eta > 0 \quad (3.7)$$

And η becomes a relatively constant parameter such that the velocity of the moving interface is

$$\frac{ds}{dt} = \frac{\alpha}{2\eta s} \quad (3.8)$$

This assumption of quasi-steady conditions is known to be valid for $Ste < 1$. Therefore, this is a reasonable assumption for dilute solutions of alginate, as the Ste for melting ice at room temperature is ~ 0.3 . Using the corresponding boundary and interface conditions Eq. (3.9) – (3.11)

$$\Theta(X = 0, \eta) = 1 \quad (3.9)$$

$$\Theta(X = 1, \eta) = 0 \quad (3.10)$$

$$\frac{\partial \Theta}{\partial X} \Big|_{X=1} = -\frac{1}{2\eta Ste} \quad (3.11)$$

The solution of the boundary value problem for dimensionless temperature and interface location are:

$$\Theta(X) = 1 - X \quad (3.12)$$

$$s = (2\alpha t Ste)^{\frac{1}{2}} \quad (3.13)$$

The location of the melting interface is the parameter that couples the melting problem to the diffusion-reaction problem since the position of the melting interface determines the domain over which to solve the diffusion-reaction problem. Granted, this is predicated on the assumption of negligible diffusion into the frozen alginate. An assumption that holds for ice which has a tight crystallographic structure limiting penetration into the frozen region by larger molecules.

Next, we examine the diffusion-reaction problem. This problem involves the diffusion and reaction kinetics of three different species: calcium salt concentration $c(x, t, s(t))$, free alginate concentration $a(x, t, s(t))$, and crosslinked alginate gel concentration $g(x, t, s(t))$. To determine these concentrations, we will use the diffusion-reaction model proposed by Mikkelsen and Elgsaeter [115], but assuming constant diffusion coefficient for the free alginate.

$$\frac{\partial c}{\partial t} = D_c \frac{\partial^2 c}{\partial x^2} - N_c \kappa c a (a + g), \quad 0 < x < s(t), \quad t > 0 \quad (3.14)$$

$$\frac{\partial a}{\partial t} = D_a \frac{\partial^2 a}{\partial x^2} - \kappa c a (a + g), \quad 0 < x < s(t), \quad t > 0 \quad (3.15)$$

$$\frac{\partial g}{\partial t} = \kappa c a (a + g), \quad 0 < x < s(t), \quad t > 0 \quad (3.16)$$

Where D_c is the diffusion coefficient of the calcium salt, D_a is the diffusion coefficient of the free alginate, κ is the reaction constant, and N_c is a stoichiometric coefficient representing the average number of calcium ions bound to each alginate dimer. The initial conditions are given by

$$c(x, t = 0) = 0 \quad (3.17)$$

$$a(x, t = 0) = a_0 \quad (3.18)$$

$$g(x, t = 0) = 0 \quad (3.19)$$

Where a_0 , is the initial concentration of frozen alginate. On the outer boundary, the salt concentration is fixed at c_0 and there is no diffusion of alginate out of the wall, so

$$c(x = 0, t) = c_0 \quad (3.20)$$

$$\left. \frac{\partial a}{\partial x} \right|_{x=0} = 0 \quad (3.21)$$

At the melting interface, there is no diffusion of salt into the frozen region and the concentration of free alginate is the same as in the frozen region

$$\left. \frac{\partial c}{\partial x} \right|_{x=s(t)} = 0 \quad (3.22)$$

$$a(s(t), t) = a_0 \quad (3.23)$$

Similar to the melting problem, dimensionless variables for position $X = \frac{x}{s(t)}$, time $\tau = \frac{tD_c}{s(t)^2}$, salt concentration $C = \frac{c}{a_0}$, free alginate concentration $A = \frac{a}{a_0}$, gel concentration $G = \frac{g}{a_0}$, reaction rate $K = \frac{\kappa s(t)^2 a_0^2}{D_c}$, and a dimensionless constant for the relative alginate diffusion coefficient $D = \frac{D_a}{D_c}$ can be introduced into Eqs. (3.14) – (3.23). This yields the dimensionless equations for $C(X, \tau, K)$, $A(X, \tau, K)$, $G(X, \tau, K)$:

$$(1 - 2\tau LeSte) \frac{\partial C}{\partial \tau} = \frac{\partial^2 C}{\partial X^2} - N_c KCA(A + G), \quad 0 < X < 1, \quad \tau > 0 \quad (3.24)$$

$$(1 - 2\tau LeSte) \frac{\partial A}{\partial \tau} = D \frac{\partial^2 A}{\partial X^2} - KCA(A + G), \quad 0 < X < 1, \quad \tau > 0 \quad (3.25)$$

$$(1 - 2\tau LeSte) \frac{\partial G}{\partial \tau} = KCA(A + G), \quad 0 < X < 1, \quad \tau > 0 \quad (3.26)$$

Where Le is the Lewis number, $Le = \frac{\alpha}{D_c}$, and the equation below, derived from combining Eqs. (3.8) and (3.13), has been used.

$$s \frac{ds}{dt} = \alpha Ste \quad (3.27)$$

The corresponding dimensionless initial and boundary conditions are

$$C(X, \tau = 0, K) = 0 \quad (3.28)$$

$$G(X, \tau = 0, K) = 0 \quad (3.29)$$

$$A(X, \tau = 0, K) = 1 \quad (3.30)$$

$$C(X = 0, \tau, K) = \frac{c_o}{a_0} = C_o \quad (3.31)$$

$$\left. \frac{\partial C}{\partial X} \right|_{X=1} = 0 \quad (3.32)$$

$$\left. \frac{\partial A}{\partial X} \right|_{X=0} = 0 \quad (3.33)$$

$$A(X = 1, \tau, K) = 1 \quad (3.34)$$

Note that K is now a variable, in addition to X and τ , because it varies with the location of the melting interface, $s(t)$, which is weakly time dependent.

The complete solution for the concentrations within the melted region can easily be obtained by solving the above coupled non-linear partial differential equations numerically using conventional methods.

While the numerical analysis for this set of coupled equations is straightforward, we are interested in also gaining insight into the effects of the different dimensionless parameters, to aid in designing freezing modulated cross-linking for more complex objects. In order to derive closed-form analytical solutions, and study the effect of the dimensionless parameters, we will apply some simplifications and analyze a few special cases. First, assume that there are no density changes during cross-linking such that the concentration of free alginate before cross-linking and the concentration of gel after cross-linking remains the same. This assumption draws from conservation of mass. This means that the concentration of gel and free alginate at any position should always sum to the initial concentration of free alginate at all times.

$$A + G \equiv 1 \quad (3.35)$$

This is a reasonable approximation if the alginate and salt solutions are dilute and there is negligible diffusion of the free alginate. Reported values for D_c and D_a would put the diffusivity ratio, D , in a range between 4×10^{-4} and 3×10^{-3} [116]. Therefore, for subsequent analysis we will take condition in Eq. (3.35) to be true and the diffusion-reaction equations reduce to

$$(1 - 2\tau LeSte) \frac{\partial C}{\partial \tau} = \frac{\partial^2 C}{\partial X^2} - N_c K C A, \quad 0 < X < 1, \quad \tau > 0 \quad (3.36)$$

$$(1 - 2\tau LeSte) \frac{\partial A}{\partial \tau} = D \frac{\partial^2 A}{\partial X^2} - K C A, \quad 0 < X < 1, \quad \tau > 0 \quad (3.37)$$

$$(1 - 2\tau LeSte) \frac{\partial G}{\partial \tau} = K C (1 - G), \quad 0 < X < 1, \quad \tau > 0 \quad (3.38)$$

This decouples one of Eq. (3.37) or (3.38) from (3.36), thus simplifying the problem. A solution of the above equations can also be obtained using conventional numerical methods. But instead, we will now analyze the following special cases and present closed-form approximate solutions, which when compared with the numerical solution can provide insight into the effect of the various dimensionless parameters.

3.2.1. Case 1: Melting of the slab is much faster than diffusion of salt

For $2\tau LeSte < 1$,

$$\frac{\partial C}{\partial \tau} = \frac{\partial^2 C}{\partial X^2} - N_c K C A, \quad 0 < X < 1, \quad \tau > 0 \quad (3.39)$$

$$\frac{\partial A}{\partial \tau} = D \frac{\partial^2 A}{\partial X^2} - KCA, \quad 0 < X < 1, \quad \tau > 0 \quad (3.40)$$

$$\frac{\partial G}{\partial \tau} = KC(1 - G), \quad 0 < X < 1, \quad \tau > 0 \quad (3.41)$$

This represents the regime where the interface moves substantially faster than the diffusion of the salt into the slab. The solution to this problem is determined by solving the above coupled equations. An approximate solution, can be determined however by treating each equation independently. First, solving for C from Eq. (3.39) assuming A is constant.

Case 1a - The upper bound: where $A = 0$. This considers an imagined situation in which all the alginate has fully been crosslinked and there is no free alginate left. Being a contrived scenario, it does not occur in real systems where there is continuously available alginate at the melting interface. Nonetheless, analyzing this condition sets an upper bound for the salt concentration. It provides a solution with the maximum salt concentration since it assumes no depletion of the salt for the cross-linking, as there is no free alginate available. Therefore, Eq. (3.39) reduces to

$$\frac{\partial C}{\partial \tau} = \frac{\partial^2 C}{\partial X^2}, \quad 0 < X < 1, \quad \tau > 0 \quad (3.42)$$

It is a case of pure diffusion and the solution for C is

$$C(X, \tau, K) = C_o \left(1 - \sum_{n=1}^{\infty} \frac{2}{\lambda_n} \sin(\lambda_n X) e^{-\lambda_n^2 \tau} \right) \quad (3.43)$$

Where,

$$\lambda_n = \frac{(2n-1)\pi}{2} \quad \text{for } n = 1, 2, 3, \dots$$

Case 1b - The lower bound: where $A = 1$. This provides a solution for an imaginary situation in which there is little to no gel formation, so the maximum amount of free alginate is available to react with the cross-linking salt. For this case, Eq. (3.39) reduces to

$$\frac{\partial C}{\partial \tau} = \frac{\partial^2 C}{\partial X^2} - N_c KC, \quad 0 < X < 1, \quad \tau > 0 \quad (3.44)$$

And similarly, the solution for C is

$$C(X, \tau, K) = C_o \left(\cosh(\sqrt{N_c K} X) - \tanh(\sqrt{N_c K}) \sinh(\sqrt{N_c K} X) - \sum_{n=1}^{\infty} \frac{2\sqrt{\lambda_n^2 - N_c K}}{\lambda_n^2} \sin(\sqrt{\lambda_n^2 - N_c K} X) e^{-\lambda_n^2 \tau} \right) \quad (3.45)$$

Where,

$$\lambda_n = \sqrt{\frac{\pi^2}{4}(2n-1)^2 + N_c K} \quad \text{for } n = 1, 2, 3, \dots$$

Next, assuming C is a constant, and solving for A from Eq. (3.40)

$$A(\tau, C(X, \tau), K) = e^{-Kc\tau} \quad (3.46)$$

Note that the assumption of $D \ll 1$ has been applied. Then, using Eq. (3.35), G is

$$G(\tau, C(X, \tau), K) = 1 - e^{-Kc\tau} \quad (3.47)$$

Note that Eq. (3.45) and (3.46) can also be obtained by first solving for G from Eq. (3.41). Lastly, by substituting C from *Case 1a* and *Case 1b*, we can determine estimates for free alginate and gel concentrations at the maximum possible and minimum possible salt concentrations, respectively. Additionally, for the parameters in which the maximum and minimum converge, an approximate closed-form solution can be determined.

3.2.2. Case 2: Melting rate is comparable to the rate of the diffusion of the salt

For $2\tau LeSte = O(1)$,

$$0 = \frac{\partial^2 C}{\partial X^2} - N_c K C A, \quad 0 < X < 1, \quad \tau > 0 \quad (3.48)$$

$$0 = D \frac{\partial^2 A}{\partial X^2} - K C A, \quad 0 < X < 1, \quad \tau > 0 \quad (3.49)$$

This represents the regime where the diffusion of the calcium salt is as fast as the melting, such that steady-state is achieved at each time instant (quasi-steady). Here the diffusion and the melting time scales match. This is the optimal scenario for freezing modulated cross-linking, because the 3D printed object will cross link upon melting and thereby yield an object with the maximal mechanical rigidity. Also, note that although the equations are independent of τ , the solution still varies with time since K will change with s , and s with time. Furthermore, s depends on the Stefan number – which in turn depends on the difference in temperature between the outer surface temperature and the melting temperature. The solution to this problem is determined by solving the above coupled equations. Similar to above, an approximate solution can be determined by treating each equation independently. First, solving for C from Eq. (3.48) assuming A is constant.

Case 2a - The upper bound: where $A = 0$, Eq. (3.48) reduces to

$$0 = \frac{\partial^2 C}{\partial X^2}, \quad 0 < X < 1, \quad \tau > 0 \quad (3.50)$$

and the solution for C is

$$C(X, K) = C_o \quad (3.51)$$

If there is no depletion then there is a uniform maximum concentration of calcium salt in the melted region at all times.

Case 2b - The lower bound: where $A = 1$, Eq. (3.48) reduces to

$$0 = \frac{\partial^2 C}{\partial X^2} - N_c K C, \quad 0 < X < 1, \quad \tau > 0 \quad (3.52)$$

and the solution for C is

$$C(X, K) = C_o (\cosh(\sqrt{N_c K} X) - \tanh(\sqrt{N_c K}) \sinh(\sqrt{N_c K} X)) \quad (3.53)$$

Next, assuming C is a constant, and solving for A from Eq. (3.49)

$$A(C(X, K), K) = \frac{\cosh\left(\sqrt{\frac{KC}{D}} X\right)}{\cosh\left(\sqrt{\frac{KC}{D}}\right)} \quad (3.54)$$

Then, using Eq. (3.35), G is

$$G(C(X, K), K) = 1 - \frac{\cosh\left(\sqrt{\frac{KC}{D}} X\right)}{\cosh\left(\sqrt{\frac{KC}{D}}\right)} \quad (3.55)$$

Lastly, by substituting C from *Case 2a* and *Case 2b*, we can estimate the free alginate and gel concentrations for the maximum possible (*Case 2a*) and minimum possible salt concentrations (*Case 2a*), respectively. Additionally, an approximate closed-form solution can be determined for the parameters where the maximum and minimum converge.

3.3. Results and discussion

Here we present select results for the concentrations of the three species in a melting slab from the analysis above. The numerical solutions for the systems of partial differential equations (PDEs) were obtained using the built in 1-D parabolic and elliptic PDEs solver in MATLAB® (pdepe). The number of equal size mesh elements along X was chosen to be 100, spanning from $X = 0$ to $X = 1$. The number of equal size mesh elements along τ was chosen to be 1000, spanning from $\tau = 0$ to $\tau = 1/2SteLe$. The numerical solutions for the systems of ordinary differential equation (ODEs) were obtained using the MATLAB® function for solving boundary value

problems (bvp4c). The algorithm is based on the fourth-order Lobatto IIIa method. The number of equal size mesh elements along X was chosen to be 100, spanning from $X = 0$ to $X = 1$. All the numerical results shown were generated using MATLAB on a MacBook Pro with a 2.7 GHz Dual-Core Intel Core i5 and 8 GB of RAM.

An important aspect of the analysis of the results is a comparison of the numerical analysis with the approximate closed-form solutions, to evaluate the effect of the different dimensionless parameters on the solution. Unless otherwise stated, below are the constants used to obtain the presented results:

- (i) Stefan number, Ste . An estimate of the Stefan number for melting of an ice slab with the outer wall at fixed room temperature of 25°C is approximately 0.3. The thermal properties of a dilute alginate solution can be closely approximated by that of water, but to ensure validity of the quasi-steady assumption $Ste = 0.01$ was used. This assumes the melting of the gel is at temperatures much less than room temperature.
- (ii) Lewis number, Le . Based on the thermal diffusivity of water at room temperature of $1.4 \times 10^{-7} \text{ m}^2/\text{s}$ and a mass diffusivity estimate of $1.2 \times 10^{-9} \text{ m}^2/\text{s}$ which in the middle of the range from [116] we chose $Le = 120$.
- (iii) Relative alginate diffusion coefficient, D . Previous reported values with CaCl_2 as the salt range from 4×10^{-4} at the lower end to 3×10^{-3} on the higher end [116]. Considering that the diffusion coefficients decreases with increased gel formation [115], we have opted for the more conservative, constant $D = 3 \times 10^{-3}$.
- (iv) Stoichiometric coefficient, N_c . As reported in [116], we will also use $N_c = 3.4$.
- (v) Initial salt concentration, C_o . The molecular weight of most common alginate powders is approximately 180-220 g/mol and the molecular mass of calcium salts most commonly used for cross-linking (CaCl_2 , CaCO_3 , CaSO_4 etc.) are in the range 90-150 g/mol. We have chosen $C_o = 1$, so for a given mole concentration, the mass concentrations of both solutions are at most different by a factor of two.

First, we evaluate the validity of the first approximation (Eq. (3.35)). Figure 3.2 compares the concentration profile from the full numerical solution (Eqs. (3.24)-(3.26)) to the concentration profile from the numerical solution for the approximation $A + G = 1$, (Eqs. (3.36)-(3.38)). The figure shows that, while the salt concentration from the approximate matches the real solution for the different values of D , the alginate concentrations and, more notably, the gel concentrations diverge for $D > 0.01$. This is because as the alginate diffusion coefficient gets higher, more of the free alginate molecules can diffuse into the region with low alginate concentration but high gel concentration. This leads to even more gel forming faster and the alginate concentration depleting quicker which causes higher gradients that then drive more alginate diffusion. This effect is prominent closer to the outer boundary of the slab where there is more calcium available to continue forming gel. Therefore, at high D values this mass migration of alginate molecules leads to non-uniform density and the assumption of Eq. (3.35) breaks down. From Figure 3.2 we can see that this divergence becomes noticeable at $D = 0.1$. As previously stated, the actual value of D is much less than 0.01 ($D = 3 \times 10^{-3}$) so we can say that for our analysis the approximation is adequate

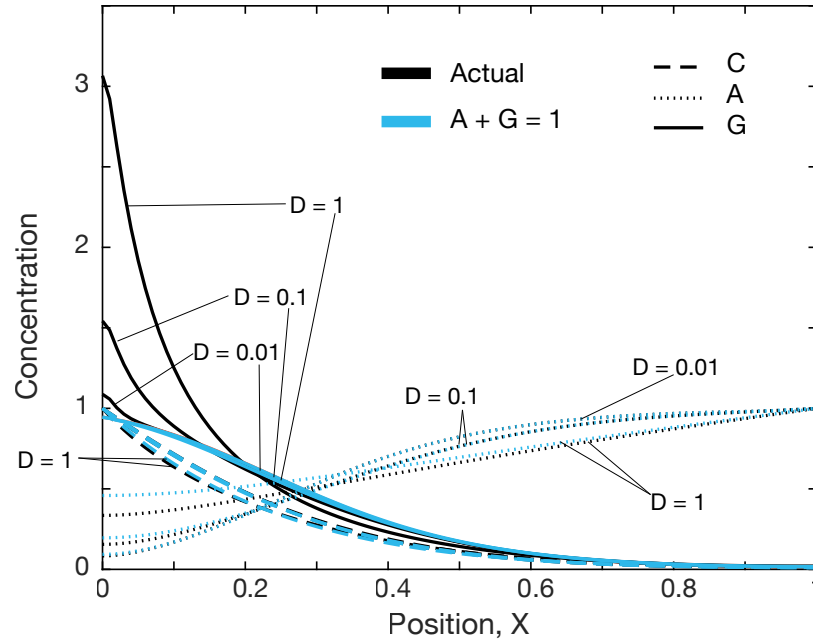


Figure 3.2: Comparison of the concentration profiles from the full solution (Eqs. (3.24)-(3.26)) and first approximate, $A + G \equiv 1$ (Eqs. (3.36)-(3.38)) for all three species. ($2\tau Le Ste = 0.5$, $K = 10$, $Ste = 0.01$)

Next, we looked at how the solution varied with time, by looking at the solution at different dimensionless times, τ (Figure 3.3a) and different reaction rates, K (Figure 3.3b). As stated previously, even though the dimensional reaction rate, κ , is a constant, in our formulation, K varies with interface position and therefore weakly with time. Figure 3.3a shows that as τ increases, salt concentration increases, alginate concentration decreases, and gel concentration increases. With time the amount of gel forming increases, as it should. Figure 3.3b shows that as K increases, salt concentration decreases, alginate concentration decreases, and gel concentration increases. This result for varying K can be interpreted in two different ways. First interpretation considers a fixed reaction rate where K only varies with $s(t)$. At small K , the slab is barely melted and the concentration of gel is still negligible as the reaction with the available calcium is yet to occur (diffusion is reaction limited). At large K , a large portion of the slab is melted but the penetration depth of the calcium is lagging behind so only part of melted portion has fully gelled (reaction is diffusion limited). The second interpretation considers reaction rates of differing magnitudes when the interface is at a fixed location. At small K , the cross-linking reaction proceeds relatively slowly such that although the calcium has diffused into the slab, there is negligible gel formation (diffusion is reaction limited). At large K , the cross-linking reaction proceeds very rapidly that it immediately consumes any available calcium, forming a region that is fully gelled and a sharp transition to a region with no gel formation as the calcium is consumed before it can diffuse into that region (reaction is diffusion limited).

We also looked at how the concentration profiles are affected by Stefan number. Stefan number is a parameter that can be varied by changing the temperature on the outer wall. By controlling this temperature, one can affect the general gelation profile in the melted portion. Figure 3.3c shows the concentration profiles for three different Stefan numbers (all much less than 1, so quasi-steady melting). As Stefan number decreases, calcium concentration increases, alginate concentration decreases, and gel concentration increases. This suggests that for best gelation

results when melting, the frozen object should be melted at low temperatures, as close to the melting point as possible.

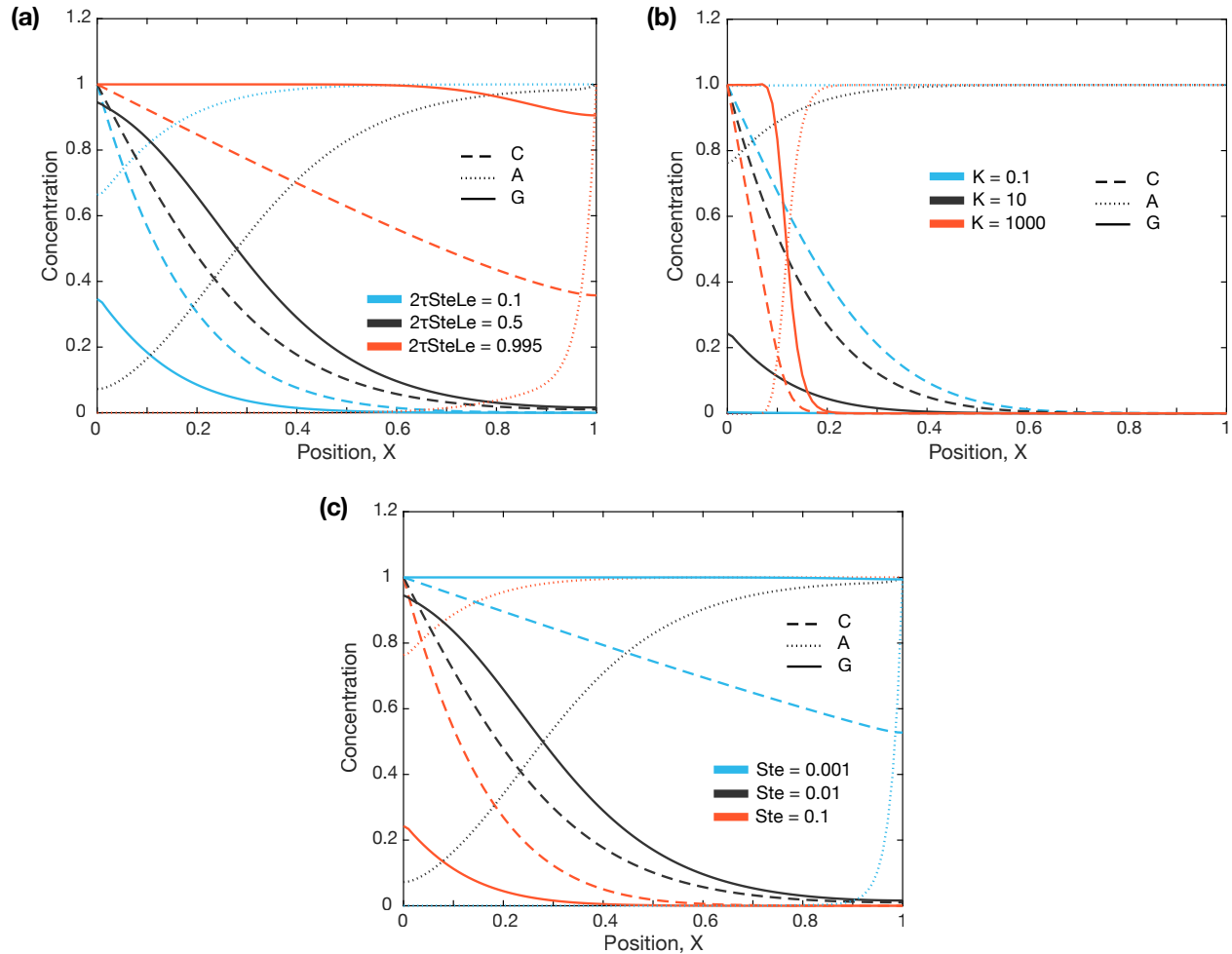


Figure 3.3: Variation of the concentration of the three species with dimensionless variables (a) τ (constant $K = 10$ and $Ste = 0.01$) (b) K (constant $2\tau LeSte = 0.5$ and $Ste = 0.01$), and dimensionless parameter (c) Stefan number (constant $2\tau LeSte = 0.5$ and $K = 10$)

The results of a few special cases were also evaluated. Starting with Case 1 – where the melting of the slab is much faster than the diffusion of the salt. We assessed the dependence of this solution for varying τ and K values (Figure 3.4). Similar to the full solution presented in Figure 3.3a, Figure 3.4a shows that as τ increases, salt concentration increases, alginate concentration decreases, and gel concentration increases. Also, Figure 3.4b shows that as K increases, salt concentration decreases, alginate concentration decreases, and gel concentration increases. Since Case 1 is a subset of the above solution for conditions in which $2\tau LeSte < 1$ the curves are similar in shape to the curves in Figure 3.3a for $2\tau LeSte = 0.1$. The gel concentration increases from the outer wall boundary, with a concave up profile and only starts to convex at the gel concentration approaches the peak of 1. Hence, the trends with τ and K are also similar to the solution above in Figure 3.3 where at small K the diffusion is reaction limited and at large K the reaction is diffusion limited.

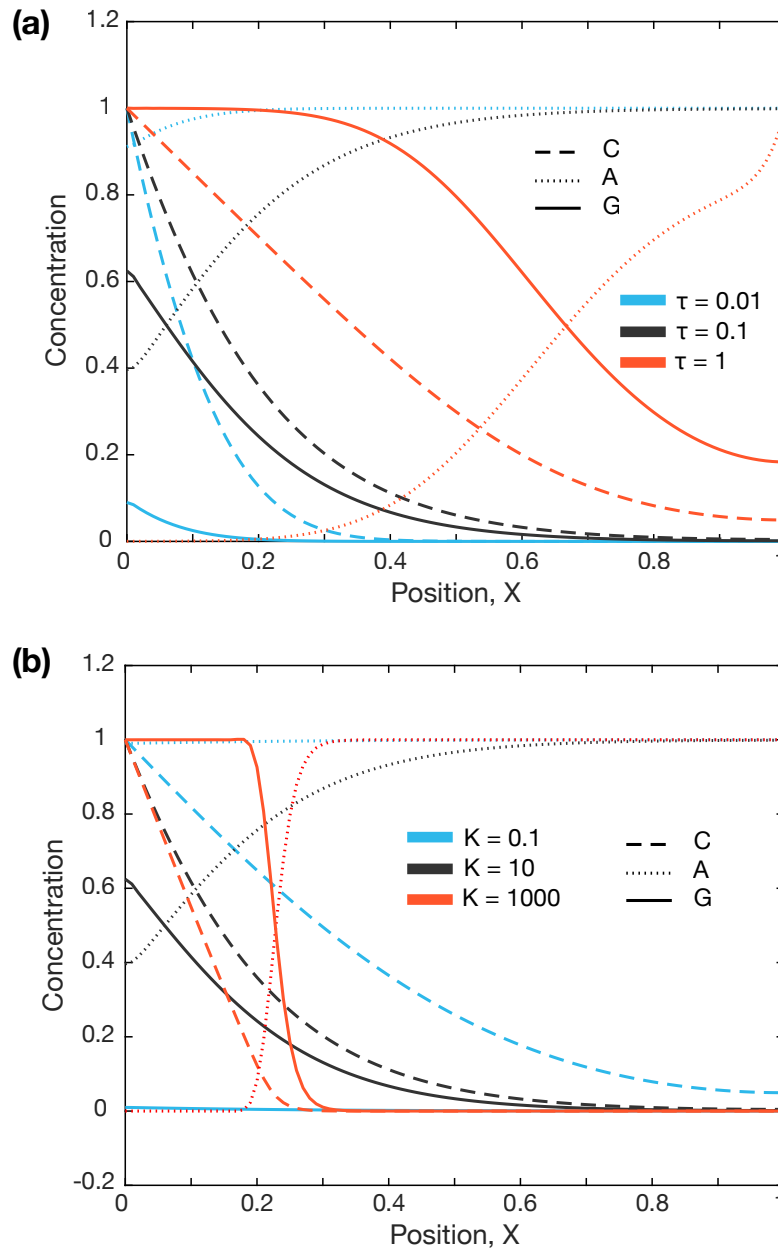


Figure 3.4: Variation of the concentration of the three species with dimensionless variables **(a)** τ (constant $K = 10$) **(b)** K (constant $\tau = 0.1$), for the regime where melting proceeds much faster than the diffusion of the salt (Case 1)

We compared the actual result (using Eqs. (3.39)-(3.41)) with the approximate upper bound solution (Case 1a) and lower bound solution (Case 1b). Figure 3.5 shows the real concentrations and the bounding concentrations for several combinations of τ and K . As seen from Figure 3.5a & c, Case 1a and 1b converge on real solution at small τ (Figure 3.5a) and small K (Figure 3.5c). They however prove poor approximations as τ and K get larger (Figure 3.5b & d respectively). This suggests that they are really only valid for small times. Nevertheless, despite the fact that Eq. (3.43) was derived for $A=0$, it provides a closed-form general solution for Case 1 when τ and K are small. Under conditions of small K , Eq. (3.45) converges to Eq. (3.43).

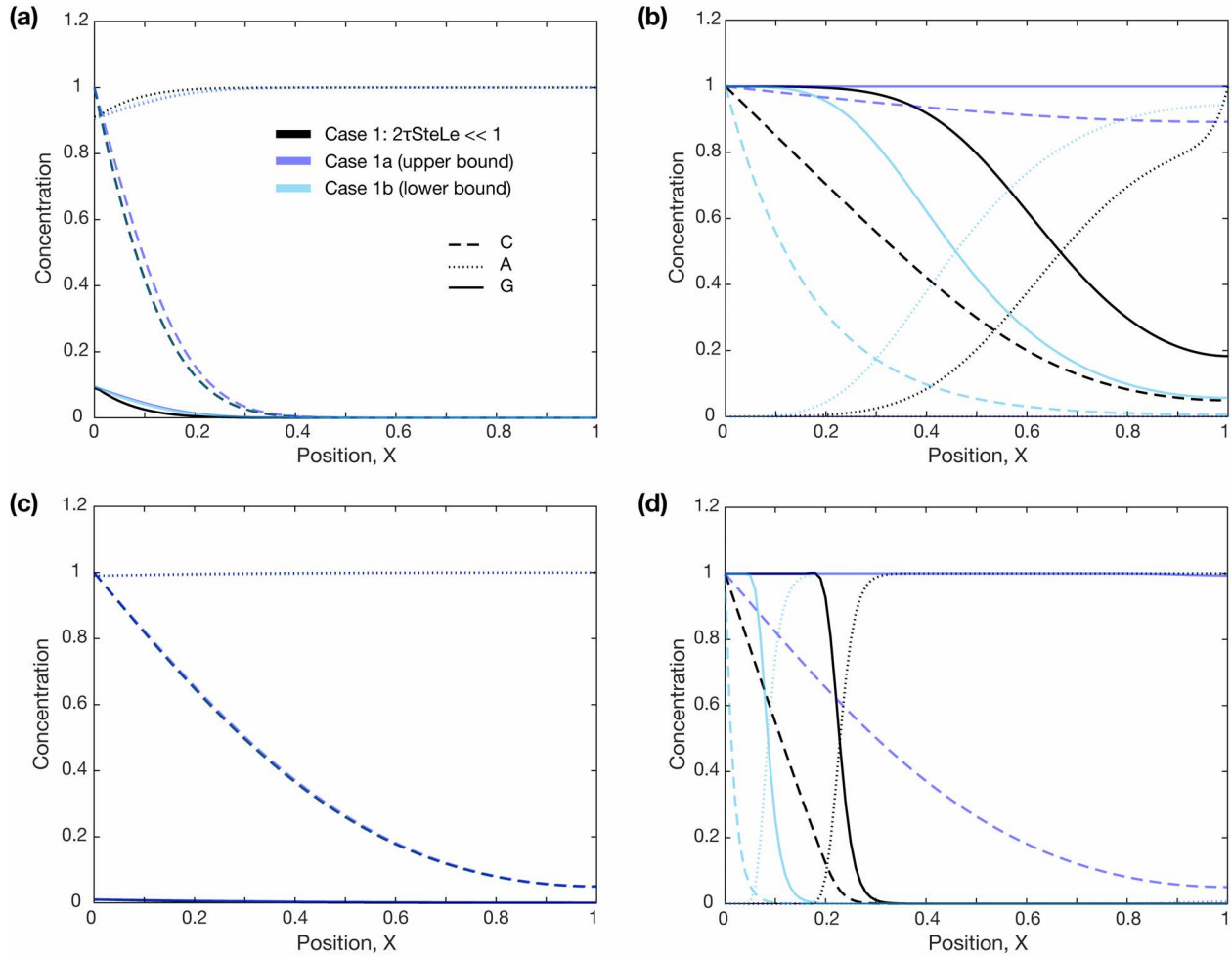


Figure 3.5: Comparison of the solution of Case 1 - melting proceeding much faster than the diffusion of the salt to its approximate upper and lower bound solutions for (a) $\tau = 0.01, K = 10$ (b) $\tau = 1, K = 10$ (c) $K = 0.1, \tau = 0.1$ (d) $K = 1000, \tau = 0$.

For Case 2 – where the rate of melting is comparable to the rate to the diffusion of the salt, we evaluated the dependence of this solution on K values (Figure 3.6). This case looks at the regime in which the diffusion kinetics are on the same order as the melting, so the diffusion is equally quasi-steady, and there is no dependence on τ . For this case the temporal change in the solution is captured by the variations in K . As this is also a special case of the full solution presented in Figure 3.3a, the result of varying K is similar. Figure 3.6 shows that as K increases, salt concentration decreases, alginate concentration decreases, and gel concentration increases. As time, $s(t)$, and K increase, there is an increase in gel concentrations as there is more time for the reactions to take place. Because, by definition, the salt concentration has to be above zero for $X < 1$ (see lower bound Case 2b), the reaction is never diffusion limited. Also, since Case 2 is a subset of the general solution for conditions in which $2\tau LeSte \sim 1$ the curves are similar in shape to the curves in Figure 3.3a for $2\tau LeSte = 0.995$. The gel concentration is close to 1 except immediately adjacent to the melting interface, the alginate concentration is essentially zero except near the melting interface, and the salt concentration profile is linear.

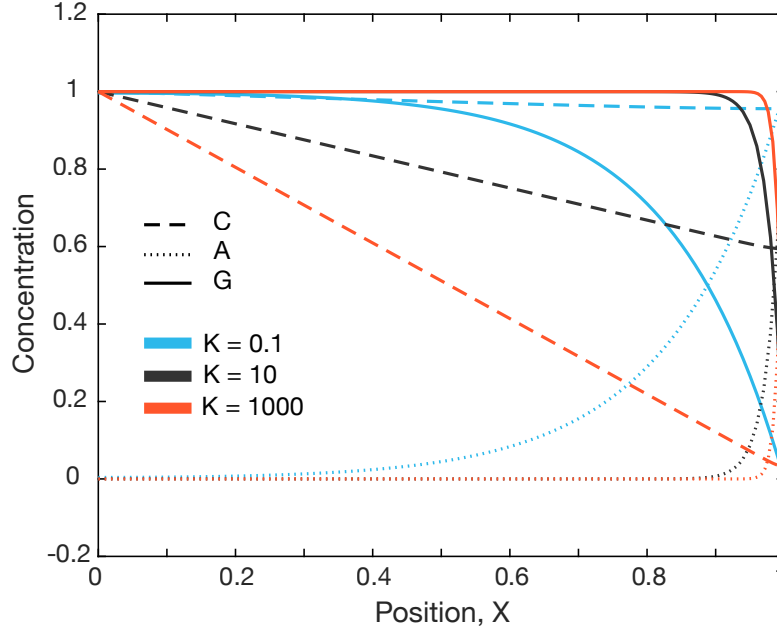


Figure 3.6: Variation of the concentration of the three species with dimensionless variable K , for the regime where rate of melting equals the rate of diffusion of the salt (Case 2)

We also compared the actual Case 2 result (using Eqs. (3.48)-(3.49)) with the approximate upper bound solution (Case 2a) and lower bound solution (Case 2b). Figure 3.7 shows the real concentrations and the bounding concentrations for the small K and large K limits. Figure 3.7 shows poor convergence for salt concentration as neither Case 2a or 2b appear to be close to the real salt concentration whether K be small (Figure 3.7a) or large (Figure 3.7b), although the gel concentrations converge for small K .

This result suggests a weak dependence of the gel concentration on the salt concentration when K is small. Therefore, for small K , the gel concentration could be reasonably approximated using

$$G(K) = 1 - \frac{\cosh\left(\sqrt{\frac{KC_o}{D}} X\right)}{\cosh\left(\sqrt{\frac{KC_o}{D}}\right)} \quad (3.56)$$

obtained by substituting the upper bound for C (Eq. (3.51)) into Eq. (3.55).

On the other hand, for large K , the gel concentration could be reasonably approximated as

$$G(K) = 1 \quad (3.57)$$

Eqs. (3.56) and (3.57) are closed-form approximations for the solution of cross-linking of an alginate slab in which the rate of melting matches the rate of diffusion. At the start of melting (small time) the concentration profile of the gel can be determined using Eq. (3.56) and at later times (after significant melting) by Eq. (3.57). The condition analyzed in Case 2 presents the ideal scenario for the cross-linking of a frozen alginate slab, because it represents a case in which the

entire melted domain is completely cross-linked as it melts and thereby provides the structure with mechanical integrity.

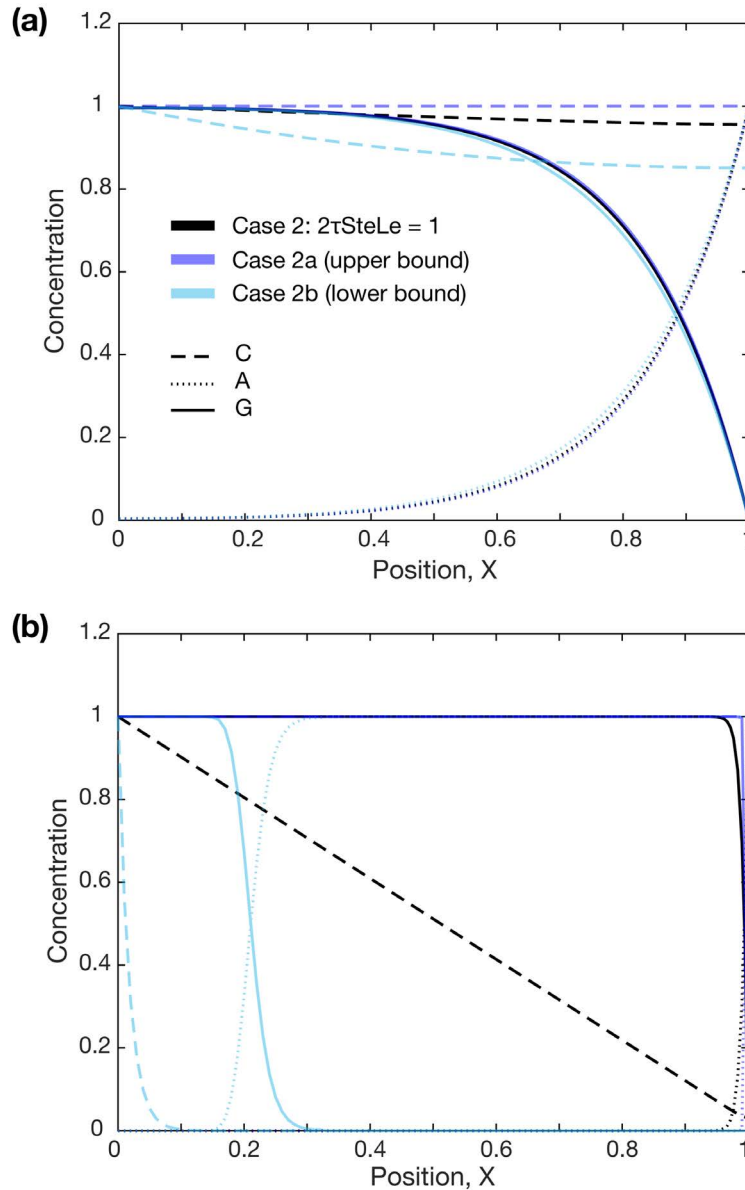


Figure 3.7: Comparison of the solution of Case 2 - rate of melting equals the rate of diffusion of the salt to its approximate upper and lower bound solutions for **(a)** $K = 0.1$ **(b)** $K = 1000$

The analysis above shows that to achieve an optimal melting and cross-linking protocol the temperature on the outer surface should continuously vary in time and with the position of the change of phase interface, such that at all times the Stefan (Ste) number dependence on the Lewis (Le) number and a typical dimensionless time τ , satisfies the condition $Ste \geq 1/2\tau Le$ and at all times $Ste < 1$.

3.4. Conclusion

In summary, we presented a full solution for the 1-D melting-diffusion-reaction problem describing the cross-linking of a slab of alginate with a calcium salt. Applying certain simplifying assumptions, we have been able to derive useful closed-form solutions for special cases and evaluate when they are applicable. From the solutions we found that for optimal cross-linking during melting of frozen alginate the surrounding temperature driving melting, T_0 , should be controlled and varied in time so that $Ste \geq 1/2\tau Le$ and $Ste < 1$. Note that the Lewis number, Le , is a material parameter and so relatively constant in the melted region and the time constant, τ , is an equivalent independent time variable. Under this condition, we present approximate expressions for determining the gel concentration profile throughout the melting. This condition and these expressions can be used to optimally crosslink frozen alginate scaffolds without sacrificing structural integrity. This could improve the applicability of 3D cryoprinting as now the alginate-based scaffolds fabricated at subfreezing temperatures may be thawed and crosslinked under controlled conditions without losing shape fidelity and geometric structure of the printed object. Furthermore, this analysis can be utilized to vary the mechanical properties of the printed scaffold structure; by controlling the melting, the extent of cross-linking can be regulated.

Chapter 4

4. Microstructure and mechanical properties of cryoprinted constructs

4.1. Introduction

3D bioprinting at subfreezing temperature is a new approach which improves mechanical properties of soft hydrogel bio-inks during printing without compromising printability of the bio-ink. And freezing modulated cross-linking is a technique for maintaining appropriate mechanical strength after the fabricated frozen scaffold is thawed. By controlling the extent of cross-linking using controlled melting, the resulting mechanical properties of the cryoprinted constructs can be regulated. Another convenient consequence of the preceding methods that enable scaffold fabrication at subfreezing temperatures is the potential to control microstructure using ice formation in a process similar to ice templating, which has been used in tissue engineering with cast alginate and freeze drying [117,118]. Since microstructure can influence the mechanical properties of hydrogels such as alginate, the ability to manipulate microstructure could be important for controlling the mechanical properties of cryoprinted hydrogel scaffolds. One way to manipulate this microstructure is by controlling the formation of ice. Freezing rate and temperature have been used to control the ice crystal formation during freezing, and consequently the pore architecture of alginate hydrogels [117,118]. Due to the tight crystallographic structure of ice, dendrites of controlled dimensions can be directed throughout a frozen structure. In order to understand this ice formation during cryoprinting, we used a simplified fundamental study to investigate the effect of several freezing parameters on the resulting microstructure of alginate bio-inks in a 1-D system that lends itself to simpler characterization – directional solidification.

Directional solidification is a technique used to achieve controlled cooling of various substances. It typically involves moving a substance from a high temperature region to a low temperature region across a fixed temperature gradient. The system is designed such that the temperature distribution in the treated material is one dimensional in the direction of the temperature gradient. This results in a material with a uniform temperature history throughout its cross section. Directional solidification was first introduced by Bridgman [119], and later modified by Stockbarger [120] for the controlled growth of single crystal semiconductors. The Bridgman-Stockbarger, [119,120], solidification process is a one-dimensional (1D) solidification process in which the material to be treated is transported vertically along a temperature gradient between a temperature above and a temperature below the materials phase transformation temperature. A variant of the technique called the “horizontal directional solidification method” was developed in the early 1960s by K Bagdasarov (indirect information from reference [121]). Horizontal directional solidification methods use a flat-bottomed crucible with short sidewalls rather than the enclosed ampoule and vertical configuration, characteristic of the Bridgman-Stockbarger method. Horizontal directional solidification was applied in the early 1980s for the study of the process of freezing in biological materials by Rubinsky [122,123]. Since then, directional solidification of biological materials has been used in: fundamental research on freezing of biological

materials[124–127]; cryopreservation of biological materials [128–130]; and for tissue engineering [30,131–133]. In all these applications it is important to control the cooling rates during freezing. Since the survival of living biological matter after freezing is strongly dependent on the cooling rates during freezing [87,88]. Directional solidification is frequently used because it is thought to provide better control and uniformity over the temperature distribution during freezing of large samples. In tissue engineering, directional solidification of aqueous biomaterials, such as agar or alginate, is used to generate ice crystals in predetermined directions and with specified dimensions. Upon thawing or freeze drying the space occupied by the ice crystals provide venues for cell growth and diffusion of nutrients in tissue engineering. The temperature distribution during freezing and the attendant cooling rates during freezing affect both the direction of the ice crystals and their dimensions during directional solidification.

We built a horizontal directional solidification system, similar to the one used by Rubinsky [122,123], to study the formation of ice crystals in alginate bio-inks under varying conditions. Prior to the study, we performed a numerical analysis to verify the temperature distribution during directional solidification of an aqueous solution. In analyzing this 1-D simplified model for 3D cryoprinting, we realized that previous experimental studies on directional solidification of aqueous solutions relied on limited heat transfer analysis to characterize temperature distribution and phase change in the solidifying biological matter. The studies in the literature assume an infinitesimally thin layer of freezing solution at the same temperature as the moving substrate, which is only valid for a limited set of conditions and not necessarily applicable in all directional solidification studies. In reality the layer is not infinitesimally thin.

So, in this chapter, we perform a mathematical analysis to examine the effect of the thickness of the freezing material on the cooling rates during directional solidification. This analysis will show that the temperature distribution during directional solidification of aqueous materials is one dimensional only for very thin biological samples and becomes two dimensional (2-D) with an increase in the thickness of the sample and other design parameters. The freezing rates obtained by considering this thickness in a 2-D model may differ from those obtained from a 1-D model ignoring thickness, by several factors. The work discussed here also appears in the published work, [77]. With these findings we design and build an appropriate directional solidification device to study 3D cryoprinting of biological matter. Since the effect of freezing rate on ice crystal size and porosity has previously been established [117,118], the experimental studies focus on the effect of temperature gradient on the direction and control of ice dendrites and a less studied phenomenon – how the ice-controlled microstructure is influenced by cross-linking in a hydrogel? Additionally, using this directional device we evaluate the advantage of freezing modulated cross-linking by exploring the effect of the alginate freezing and cross-linking sequence on the micro structure of frozen sodium alginate under controlled freezing conditions. The study clarifies the appropriate window for cross-linking when also freezing in order to get a particular microstructure. This microstructure information is especially applicable for the design of 3D cryoprinting and freezing modulated cross-linking processes, and the manufacture of single layer tissues using directional freeze-casting.

4.2. Analysis of directional solidification of aqueous solutions

4.2.1. Mathematical model of directional device

Simplified model:

Figure 4.1 shows a schematic of a typical directional solidification process of an aqueous specimen on a directional device [122,123]. Briefly, as shown in Figure 4.1, the directional device consists of two constant temperature surfaces, one maintained at a high temperature, T_h , and the other at a low temperature, T_c , with T_h being higher than the materials phase change temperature, T_{ph} , and T_c less than the materials phase change temperature. The constant temperature surfaces are placed a fixed distance apart, l , from each other and a thin rigid conductive material (substrate) is placed on top of the surfaces, in good thermal contact, connecting both constant temperature surfaces.

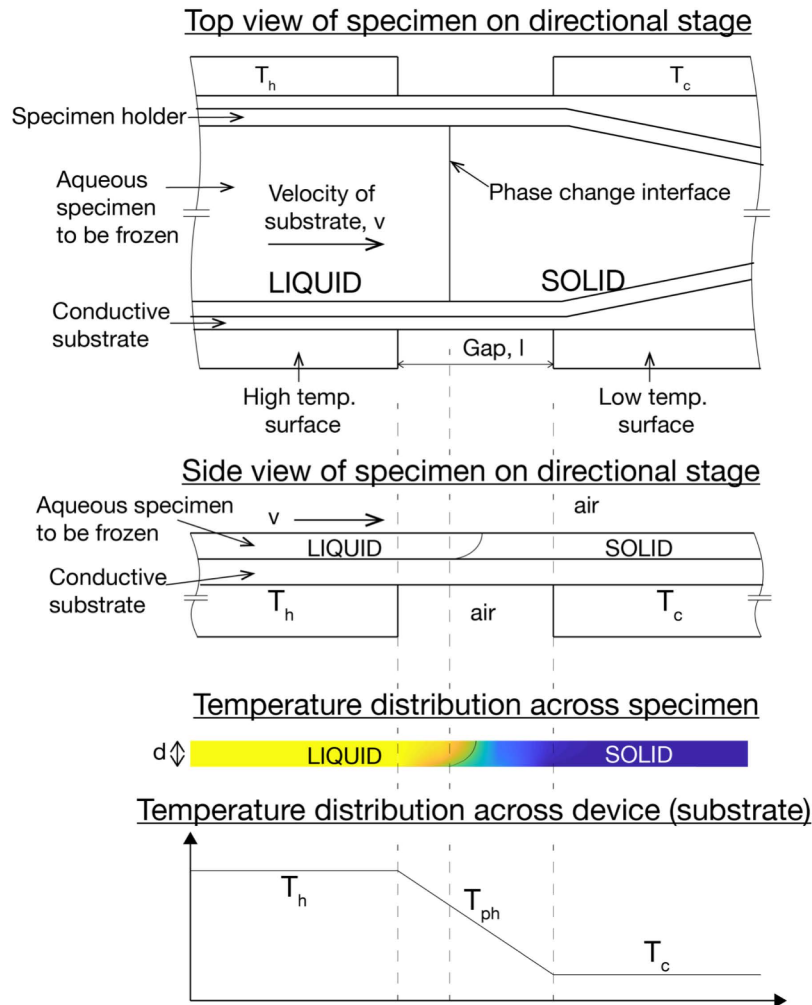


Figure 4.1: Schematic of the directional solidification process. The liquid specimen is placed on top of a conductive substrate restricted from free flowing by the specimen holder (mold). The conductive substrate and specimen are then placed on the constant temperature surfaces, with the substrate spanning between the high temperature surface and the low temperature surface. The specimen starts initially on the high temperature surface and is frozen as the conductive substrate on which the specimen is carried is moved at a velocity, v , from the high temperature surface to the low temperature surface. The specimen holder is interchangeable and serves to define the thickness of the specimen, d . Air is contained between the gap and above the substrate and assumed to be effectively insulating.

This conductive substrate conducts heat from the high temperature surface to the low temperature surface through a fixed temperature gradient determined by the constant temperature surfaces and the gap between the constant temperatures. Assuming that the gap is occupied by air and that it acts as an insulating layer between the constant temperature modules, the temperature gradient on the conductive substrate across the gap is given by Eqn. (4.1):

$$\frac{\partial T}{\partial x} = \frac{T_h - T_c}{l} \quad (4.1)$$

The consequent temperature distribution in the substrate is shown in Figure 4.1. In typical directional solidification processes a thin layer of the aqueous material of interest (specimen) is placed on the substrate. To begin freezing this specimen, the conductive substrate spanning the gap and connecting the two constant temperature surfaces, is moved across from the high temperature surface towards the low temperature surface, with a constant velocity, v . During this movement, heat is conducted through the thin layer of the aqueous specimen through the substrate to the constant temperature surfaces as it is moved across with velocity, v . Assuming that the layer of aqueous specimen is infinitesimally thin relative to the thickness of the substrate, the specimen takes the temperature of the substrate. This is the basic model currently used in directional solidification of biological materials. When the temperature distribution in the substrate and the aqueous specimen are fully developed, i.e. at quasi steady state (temperature is only a function of space), the effective freezing rate through the specimen is given by Eqn. (4.2).

$$\frac{dT}{dt} = \frac{\partial T}{\partial x} \frac{dx}{dt} = v \frac{\partial T}{\partial x} = \frac{T_h - T_c}{l} v \quad (4.2)$$

By fixing the temperature gradient and the velocity, an unlimited amount of material can be directionally frozen at a constant freezing rate. This is the practical value of the directional solidification.

Obviously, a linear temperature distribution in the substrate, as that shown in Figure 4.1, depends on several parameters such as, the substrate material, the velocity of translation, and the gap between the constant temperature surfaces. So, the condition of a linear temperature distribution in the substrate as it moves, is only valid provided certain conditions outlined in [122,123], are satisfied. Those conditions are listed below

$$[5] \dots \dots \dots \frac{d_{SS} k_{SS} (T_h - T_c)}{d \rho L v l} \gg 1 \quad (4.3)$$

$$[1.5 \times 10^{-1}] \dots \dots \dots \frac{v l}{\alpha_{SS}} \ll 1 \quad (4.4)$$

$$[6.9 \times 10^2] \dots \dots \dots \left| \frac{k_{SS} d_{SS} (T_h - T_c)}{2 h l^2 (T_\infty - T_c)} \right| \gg 1 \quad (4.5)$$

where, k_{SS} is the thermal conductivity of the substrate, d_{SS} is the thickness of the substrate, α_{SS} is the thermal diffusivity of the substrate, d is the thickness of aqueous specimen, ρ is the density of the aqueous specimen, L is the latent heat of fusion of the aqueous specimen, h is the coefficient

of convection to the surrounding, and T_{∞} is the temperature of the surrounding. The values in the brackets of Eqns. (4.3 – 4.5) were calculated for the example case in the results section.

The first condition (Eqn. 4.3) compares the heat transfer by conduction through the substrate to the latent heat required for freezing of the specimen at the same rate as the substrate velocity. This condition is required for a fixed interface location at steady state. The second (Eqn. 4.4) compares the heat transfer by conduction through the substrate to the heat transfer as a result of advection of the specimen due to the moving substrate. The last (Eqn. 4.5) compares the heat transfer by conduction through the substrate to the heat transfer to the environment.

Representative model:

The analysis in the ideal (simplified) model assumes that the substrate is moving with a low velocity which has no effect on the substrate temperature and that the aqueous sample is thin therefore its temperature distribution is the same as that of the substrate [122,123]. Here, we will examine the temperature distribution during directional solidification when these assumptions are void. First, we will examine the temperature distribution in a real specimen. While, it would be possible to develop a complete model of every component in the design, we are particularly interested in the temperature distribution in the solidifying aqueous specimen and adding complexity will distract. Therefore, we will focus on the specimen and the substrate within and around the gap where temperature gradients are present and phase change occurs.

Suppose the aqueous specimen to be frozen is infinitesimally thin, the cooling rate would be uniform throughout the thickness. As this is not the case in an aqueous layer of real dimensions, we sought to determine the uniformity of freezing rate through a specimen of finite thickness, d . Uniformity in freezing rate is of importance since the principal reason for the directional solidification device is to freeze aqueous specimens at constant cooling rates. Uniformity of freezing rates directly manifest in the profile of the freezing interface relative to the isotherms, since the interface location is fixed in time. A vertical interface and vertical isotherms would indicate same freezing rate through the thickness of the sample (the condition at zero velocity and low Bi number). Therefore, a model to determine the location and shape of the phase change interface and temperature distribution for an aqueous specimen undergoing freezing on a directional solidification apparatus was developed. The location and shape of the interface was calculated in order to obtain the temperature distribution and concurrently the temperature gradient following the interface.

For this analysis, a stationary frame of reference (control volume) was selected as shown in Figure 4.2. It encompasses the area of interest in the directional solidification system where there are temperature gradients and where phase change takes place in the specimen. This control volume consists of a portion of the specimen and substrate on the high temperature surface, the entire gap between the constant temperature surfaces, and a portion of the specimen and substrate on the low temperature surface. At steady state, conditions within this control volume are invariant in time, and the aqueous specimen and conductive substrate move in and out of the control volume. Therefore, the following governing equations for the temperatures in the substrate and in the liquid and solid phases of the solidifying specimen were used. There is conduction heat transfer in both the x and the y -directions, as well as advection heat transfer as a result of the movement of material in and out of the stationary control volume.

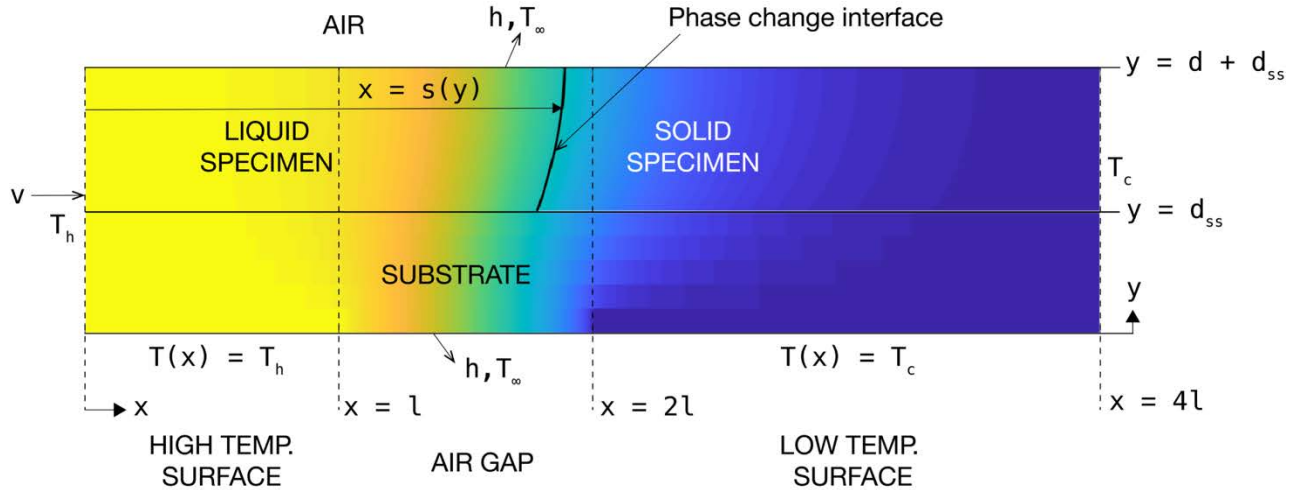


Figure 4.2: The stationary reference frame for the mathematical model comprising a portion of the specimen and substrate over the high temperature surface, the entire gap, l , and a portion of the specimen and substrate over the low temperature surface. It shows the temperature distribution in the solid and liquid regions of the specimen as well as the temperature distribution in the conductive substrate. The specimen on the substrate moves into the frame in liquid form with a velocity, v at $x = 0$. The phase change interface located at $x = s(y)$ is a function of y and separates the liquid region of the specimen from the solid region. The liquid region spans from $0 > x > s(y)$ and the solid region spans from $s(y) > x > 4l$. There is no phase change in the solid substrate. The extent of the control volume ($x = 4l$) is far from the gap so that the assumption that the temperature at that boundary is the low temperature is valid. The boundary conditions at $y = 0$ are T_h over the high temperature surface ($0 < x < l$), convection to air over the gap ($l < x < 2l$), and T_c over the low temperature surface ($2l < x < 4l$). The boundary condition at the top boundary is convection to room temperature air, with a convection coefficient h .

Therefore, the governing equation for the temperature in the substrate is

$$\frac{\partial^2 T_{SS}}{\partial x^2} + \frac{\partial^2 T_{SS}}{\partial y^2} = \frac{v}{\alpha_{SS}} \frac{\partial T_{SS}}{\partial x} \quad (4.6)$$

Where, v is the velocity of the moving specimen and substrate and $T_{SS}(x, y)$ is the temperature distribution in the substrate. Similarly, the governing equation for the liquid portion of the specimen is

$$\frac{\partial^2 T_L}{\partial x^2} + \frac{\partial^2 T_L}{\partial y^2} = \frac{v}{\alpha_L} \frac{\partial T_L}{\partial x} \quad (4.7)$$

where, α_L is the thermal diffusivity of the liquid specimen and $T_L(x, y)$ is the temperature distribution in the liquid region of the specimen. The governing equation for the solid portion of the specimen is

$$\frac{\partial^2 T_S}{\partial x^2} + \frac{\partial^2 T_S}{\partial y^2} = \frac{v}{\alpha_S} \frac{\partial T_S}{\partial x} \quad (4.8)$$

where, α_S is the thermal diffusivity of the solid and $T_S(x, y)$ is the temperature distribution in the solid region.

The boundary conditions for the system were as follows. At the initial point of entry ($x = 0$), both specimen and substrate are assumed to be far from the gap therefore not affected by the temperature gradient and hence at the temperature of the high temperature surface, T_h (Eqn. (4.9)).

$$T_{SS}(0, y) = T_L(0, y) = T_h \quad (4.9)$$

Similarly, the specimen and substrate are assumed to be far enough from the gap at the exit of the control volume ($x = 4l$) such that they are at the temperature of the low temperature surface, T_c (Eqn. (4.10)).

$$T_{SS}(4l, y) = T_S(4l, y) = T_c \quad (4.10)$$

The bottom boundary of the substrate ($y = 0$) is, at T_h when it is in contact with the high temperature surface ($x < l$), at T_c when it is contact with the low temperature surface ($x > 2l$), and exposed to air at room temperature, T_∞ , within the gap ($l < x < 2l$) (Eqn. (4.11)). This assumes perfect contact between the substrate and the constant temperature surfaces and that air acts as an insulating layer with convection coefficient, $h = 0$.

$$\begin{cases} T_{SS}(x, 0) = T_h, & x < l \\ k_L \frac{\partial T_{SS}}{\partial y} \Big|_{y=0} = h(T_\infty - T_{SS}(x, 0)), & l < x < 2l \\ T_{SS}(x, 0) = T_c, & x > l \end{cases} \quad (4.11)$$

Lastly, we assume convection from the exposed top surface of the specimen ($y = d + d_{SS}$) to the surrounding air at temperature, T_∞ , with convection coefficient, h (Eqn. (4.12)).

$$\begin{cases} k_L \frac{\partial T_L}{\partial y} \Big|_{y=d+d_{SS}} = h(T_L(x, d + d_{SS}) - T_\infty), & x < s(d + d_{SS}) \\ k_S \frac{\partial T_S}{\partial y} \Big|_{y=d+d_{SS}} = h(T_S(x, d + d_{SS}) - T_\infty), & x > s(d + d_{SS}) \end{cases} \quad (4.12)$$

where s , is the location of the phase change interface.

A continuity of temperatures is required at the transition from the substrate to the specimen ($y = d_{SS}$), with the assumption that the specimen is in perfect contact with the substrate.

$$T_{SS}(x, d_{SS}) = \begin{cases} T_L(x, d_{SS}), & x < s(d_{SS}) \\ T_S(x, d_{SS}), & x > s(d_{SS}) \end{cases} \quad (4.13)$$

Although the mathematical formulation so far is trivial, the noteworthy aspect of this problem resides in the conditions at the change of phase interface. While the location of the change of phase interface is unknown, it must still satisfy continuity in temperature and continuity in heat flux in a frame of reference stationary in space through which the solidifying fluid flows. Thermodynamics

dictates that at the change of phase interface, $x = s(y)$, the temperature has to be the phase transition temperature, creating a coupling condition (Eqn. 4.14) that ties the temperature in the liquid regime to the temperature in the solid regime

$$T_L(s(y), y) = T_S(s(y), y) = T_{ph}, \quad d_{SS} < y < d_{SS} + d \quad (4.14)$$

In addition to this condition, the interfacial energy balance at the freezing interface has to be satisfied.

$$\begin{aligned} -k_S \frac{\partial T_S(s(x, y))}{\partial x} - k_L \frac{\partial T_L(s(x, y))}{\partial y} + k_L \frac{\partial T_L(s(x, y))}{\partial x} - k_S \frac{\partial T_S(s(x, y))}{\partial y} \\ = v(\rho_L L + (\rho_L c_{p,L} - \rho_S c_{p,S}) T_{ph}) \end{aligned} \quad (4.15)$$

The equations and conditions outlined above make this an ill-posed problem where the solutions for the temperature distribution in the liquid and solid are dependent on each other and on the location of the interface, which is unknown. The change of phase interface although unknown still has to satisfy two equations (Eqns. (4.14) and (4.15)).

In order to solve this problem a numerical finite difference scheme was developed as outlined in appendix 8.3. Using the finite difference formulation, the solution for the interface was obtained using the iterative algorithm outlined in Figure 4.3 and described below.

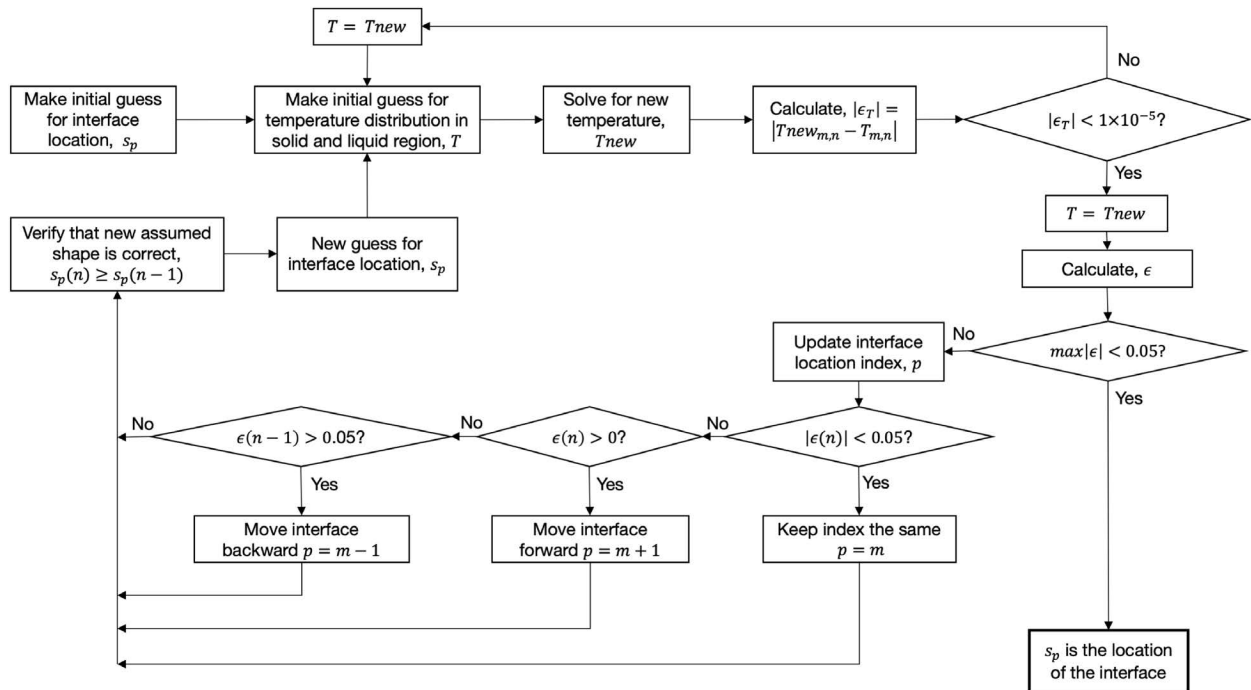


Figure 4.3: Numerical iteration algorithm for determining the interface location and temperature distribution for a given set of device and freezing layer parameters

First, an initial guess for the interface position is assumed, $s_p(n)$. Where $p = m$, the assumed x index where the interface is located. Using this interface position, an initial guess for

the temperature is generated in both the liquid and solid regions assuming a linear temperature gradient in x . Then, a new temperature distribution is calculated in the liquid and solid regions as well as in the substrate. The calculations proceed using a simple Gauss-Seidel iteration scheme where temperatures for the current iteration are calculated using a combination of temperatures from the current iteration for previous nodes and temperatures from the previous iteration for nodes ahead of the current node. A check is performed at each node to establish whether the node is in the substrate, the liquid specimen, the solid specimen, or at the phase change interface, in order to select what properties would be used to calculate the temperature. For a certain value of n in the region of the specimen, if the m value of the node is less than interface index value p ($x_m(n) < s_p(n)$), then it is assumed to be liquid and the liquid properties are used to solve the temperature distribution. Whereas, if the m value of the node is greater than interface index value p ($x_m(n) > s_p(n)$), then it is assumed to be solid and the solid properties are used. Otherwise, the interface is at the node ($x_m(n) = s_p(n)$) and the temperature is the phase change temperature.

New temperature distributions are calculated iteratively until the following error criteria for temperature is met.

$$1 \times 10^{-5}K > |\epsilon_T| = |T_{m,n}^i - T_{m,n}^{i-1}| \quad (4.16)$$

Once the temperature distribution is determined, the error in the interfacial energy balance $|\epsilon|$ is calculated for all values of n using Eqns. (A7.3.8 or A7.3.9) depending on whether the node is internal or external, respectively. This loops repeatedly until the interface error criteria is met.

$$\max|\epsilon| < 0.05 \quad (4.17)$$

If the criterion is not met, a new interface location is determined by updating the interface index p , as described in Figure 4.3 and the iteration loop is repeated. The correct interface solution is obtained once the error criteria is met.

The eventual solution for temperature and interface location is then used to calculate the cooling rate during freezing, using Eqn. (4.18) below

$$F(y) = \frac{\partial T_S(s(x, y))}{\partial t} = \frac{\partial T_S(s(x, y))}{\partial x} \frac{dx}{dt} + \frac{\partial T_S(s(x, y))}{\partial y} \frac{dy}{dt} = v \frac{\partial T_S(s(x, y))}{\partial x} \quad (4.18)$$

which assumes that the interface location is fixed in time and the specimen velocity is solely in the x -direction. Therefore, the freezing rate is only dependent on the velocity and temperature gradient in the x -direction.

4.2.2. Results and validation of device design

Input parameters for mathematical model:

To focus ideas, we studied a few configurations of interest. Since most aqueous biological specimens and biomaterials for 3D printing are composed mostly of water, the physical and thermophysical properties for pure water were used for all calculations (Table 4.1). Additionally,

our experimental device uses a stainless-steel slide as the conductive substrate, so for calculations involving the substrate parameters, the properties for stainless steel from Table 4.2 were used.

Table 4.1: Physical and thermophysical properties of water

$\rho_L, \frac{kg}{m^3}$	$k_L, \frac{W}{m^{\circ}C}$	$c_{p,L}, \frac{kJ}{kg^{\circ}C}$	$\alpha_L, \frac{m^2}{s}$	$\rho_S, \frac{kg}{m^3}$	$k_S, \frac{W}{m^{\circ}C}$	$c_{p,S}, \frac{kJ}{kg^{\circ}C}$	$\alpha_S, \frac{m^2}{s}$	$L, \frac{kJ}{kg}$	$T_{ph}, ^{\circ}C$
1000	0.64	4.19	1.52e-7	919	2.34	1.94	1.31e-6	333e-6	0

Table 4.2: Properties of the stainless-steel substrate

$\rho_{SS}, \frac{kg}{m^3}$	$k_{SS}, \frac{W}{m^{\circ}C}$	$c_{SS}, \frac{kJ}{kg^{\circ}C}$	$\alpha_{SS}, \frac{m^2}{s}$	d_{SS}, mm
7700	15	0.5	3.89e-6	1.25

The temperatures of the high temperature ($T_h = 40^{\circ}C$) and low temperature ($T_c = -40^{\circ}C$) surfaces were also fixed for the calculations unless otherwise stated. All other parameters (l, v, d) for the specimen and the device were varied for the results discussed. For simplicity, an adiabatic condition ($h = 0 W/m^2K$) was assumed for the top boundary of the specimen and the bottom boundary of the substrate within the gap (shown in the results to be a reasonable assumption).

Results from mathematical model:

First, we sought to understand how the actual calculated freezing rate (cooling rate immediately after the phase change interface) in the specimen compared with the expected freezing rate based on the temperature gradient in the substrate. For this, the temperature distribution over a region of interest spanning the gap (See Figure 4.2) was calculated for the liquid and solid regions of a layer of aqueous specimen and the substrate on which it was transported. The gap between the constant temperature surfaces was fixed at $l = 4mm$, for an effective gradient of $20^{\circ}C/mm$. The interface location, temperature distribution, and freezing rates were then calculated for varying velocities.

Figure 4.4a shows the resulting location of the freezing interface from the initial point of freezing ($s(y) - s(d_{SS})$) for different substrate velocities. The shape of the interface is parabolic, with the location of the freezing interface increasing with thickness through the sample. The slope increases rapidly closer to the bottom of the sample and slows near the top of the sample as shown in Figure 4.4a. The overall difference in freezing interface location from the initial point of freezing on the substrate also increases as the velocity increases.

Figure 4.4b shows a plot of the ratio of the actual cooling rate at the interface as a function of y , $F(y)$, to the expected cooling rate based on a linear gradient in the substrate, $(T_c - T_h)v/l$, for a range of velocities. There is an initial increase in freezing rate from that at the point in contact with the substrate as y increases, after which the cooling rate remains approximately constant at a cooling rate higher than the cooling rate corresponding to the gradient on the substrate. As seen from Figure 4.4b, the mean normalized cooling rate increases from about 0.9 to about 1.7 as the velocity increases from 0.1mm/s to 0.3mm/s. So, the actual cooling rate goes from being about 10% below the expected cooling rate to about 70% more than the expected cooling rate just by increasing the velocity three-fold. This acute effect of velocity on cooling rate is mainly due to shift in location of the freezing interface. The farther away the interface is from the location of the phase change temperature on the substrate, the higher the temperature gradients become.

This is better illustrated in Figure 4.4c which compares the temperature at the top of the specimen, $T(y = d + d_{SS})$, to the temperature of at the bottom of the specimen in contact with the substrate, $T(y = d_{SS})$, for a specimen moving through the gap at different velocities. It shows that, as the velocity is increased, the temperature profile at the top of the specimen deviates further from the temperature profile at the bottom of the specimen. For example, at a velocity of 0.1mm/s there is about a 6°C difference between the top and bottom temperatures in the specimen when the bottom temperature is at the melting point, whereas that difference grows to about 12°C at a velocity of 0.15mm/s and about 16°C at a velocity of 0.2mm/s. There is also an increasingly pronounced change in slope at the transition from the liquid portion to the solid portion as the velocity increases. In the liquid portion, the temperature gradient at the top is lower than the temperature gradient at the bottom, but once the specimen solidifies, there is a sharp transition to a higher temperature gradient at the top than at the bottom. This transition in slopes is more prominent as the velocity increases indicating larger deviations in the freezing rate from the ideal case. Therefore, as seen from Figure 4.4b, at lower velocities, the normalized mean freezing rate is closer to 1.

A direct consequence of the lower slopes in the liquid region in Figure 4.4c is the shift in the location of the freezing point. This overall shift in position of the phase change interface from the initial point of solidification at the substrate,

$$s_{shift} = s(d + d_{SS}) - s(d_{SS}) \quad (4.19)$$

dictates the deviation from the ideal freezing rate. If s_{shift} is small then the temperature gradient would be closer to the ideal 1D case. Therefore, the following criteria was developed to evaluate how close the model is to the ideal case. As s_{shift}/d gets smaller the mean normalized freezing rate, $F_{mean}l/(T_c - T_h)v$, approaches 1.

So, in order to better understand the freezing conditions, an equation to predict s_{shift} was developed as follows. First, a plot of this interface shift versus the substrate velocity was generated (Figure 4.4d). From Figure 4.4d, there is a linear relationship between velocity and the interface shift, if all other parameters remain constant. This is further supported by the proportional scaling of interface location with velocity, seen in Fig. 4.4a. Similarly, to probe the dependence of s_{shift} on specimen thickness, interface locations were calculated for different values of d , ranging from 0.5mm to 2mm using the mathematical model, while keeping the other parameters constant ($v = 0.2mm/s$ and $l = 4mm$). Figure 4.4e shows the results. It indicates that s_{shift} increases as specimen thickness increases. Lastly, s_{shift} was evaluated for a range of temperature gradients (Figure 4.4f). Temperature gradient was varied by changing the gap, l , while leaving the high and low temperatures the same. A range of temperature gradients from $10 \frac{^{\circ}C}{mm}$ to $25 \frac{^{\circ}C}{mm}$ were evaluated while keeping all other parameters constant ($v = 0.2mm/s$ and $d = 1.5mm$). Figure 4.4f shows that the interface shift is independent of the temperature gradient i.e. as the temperature gradient increases, s_{shift} remains unchanged. The actual location of the freezing interface changes but the shape of the interface does not.

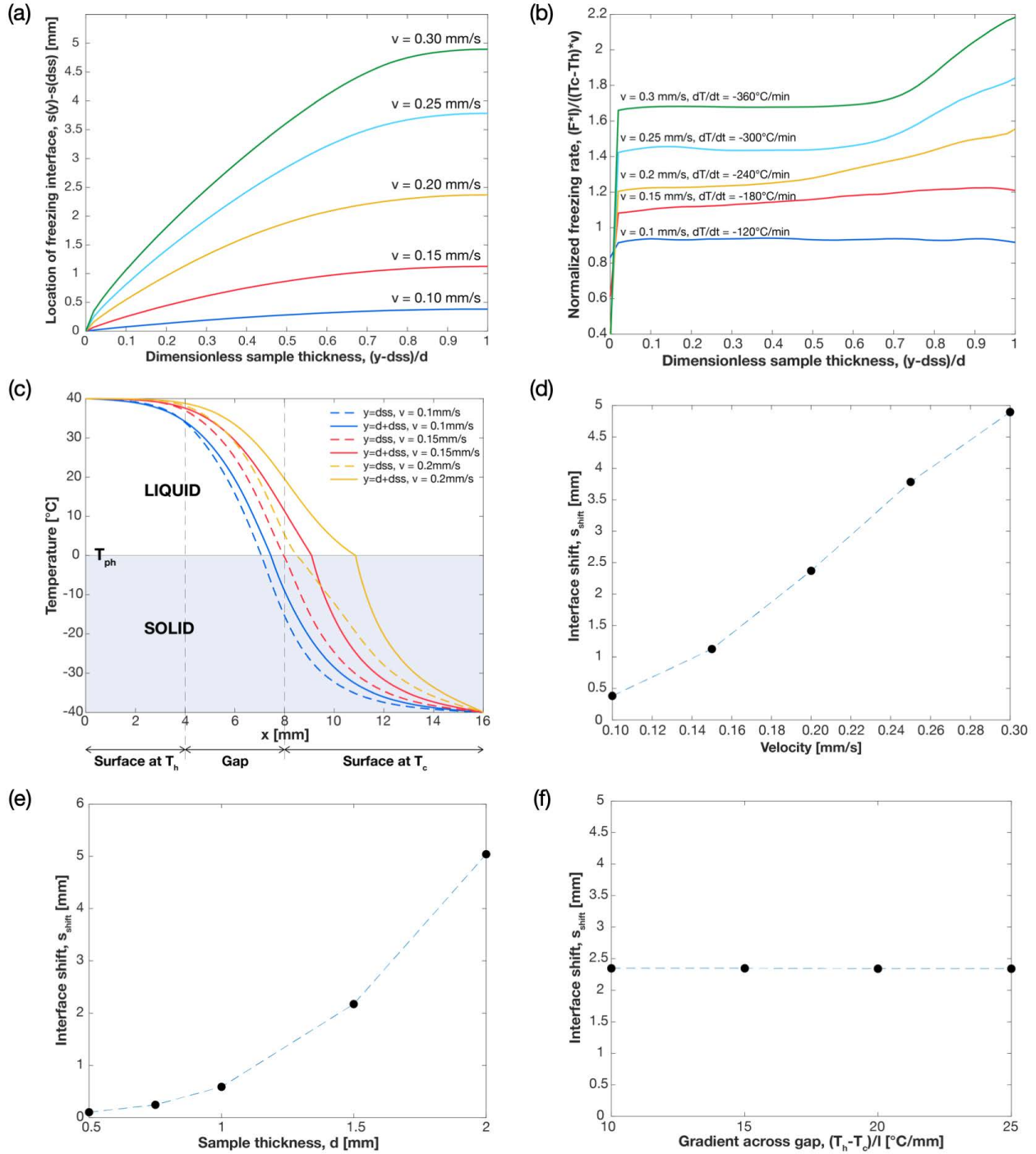


Figure 4.4: (a) Interface shape through the thickness of the specimen for different values of velocity. (b) Normalized freezing rate, $F(y)l/((T_c - T_h)v)$, through the thickness of the specimen for different values of velocity. (c) Temperature at the bottom ($y = d_{SS}$) and top of the specimen ($y = d + d_{SS}$) as it moves across the gap (d) Interface shift over entire specimen thickness, s_{shift} , as a function of velocity (e) Interface shift over entire specimen thickness, s_{shift} , as a function of specimen thickness (f) Interface shift over entire specimen thickness, s_{shift} , as a function of temperature gradient across gap

Based on the results in Figs. 4.4d-f and scaling analysis, an empirical relation for the interface shift was assumed as shown below.

$$s_{shift} = \Phi \frac{vd^2}{\alpha_L} \quad (4.20)$$

Where Φ is a constant. According to Eqn. (4.18), higher cooling rates can be achieved in two ways; either by increasing velocity or increasing temperature gradient. However, from Eqn. (4.20), the former increases s_{shift} while the latter has no effect on it. Therefore, if higher cooling rates are desired, in order to approach the ideal cooling rate (i.e. minimize s_{shift}), it is preferable to decrease gap size or increase the temperature difference, rather than increase the velocity. This is because, for a given temperature gradient, the effect of advection is higher at greater velocities so there is a bigger shift in the interface location and therefore more variance in the cooling rate at the interface.

Similarly, to better understand how the mean cooling rate depends on the device and specimen parameters, the normalized freezing rate, $F_{mean}l/(T_c - T_h)v$, was plotted as a function of three different parameters: velocity, thickness, and gradient (see Figure 4.5). The results from these plots show that the mean normalized freezing rate increases with increasing velocity, decreases with increasing gradient, and decreases with specimen thickness. As a result, an empirical equation for normalized mean freezing rate was developed based on the model results to predict the mean freezing rate simply based on the device and specimen parameters. The resulting Eqn. (4.21) was obtained by fitting the results of the model to the requisite parameters

$$\frac{F_{mean}l}{(T_c - T_h)v} = 0.47 \left(1 + \frac{v(l - 0.75d)}{2\alpha_L} \right) \quad (4.21)$$

This equation is only approximate and most useful for understanding trends. If exact cooling rates are needed, the full model should be used.

Figure 4.5 shows a comparison of the normalized mean freezing rate obtained from the model with the normalized mean freezing rate predicted using Eqn. (4.21). It shows that the equation adequately predicts the cooling conditions expected as a function of various parameters. From the equation and the figure, it is clear that the normalized mean cooling rate increases with velocity and gap length and decreases with sample thickness.

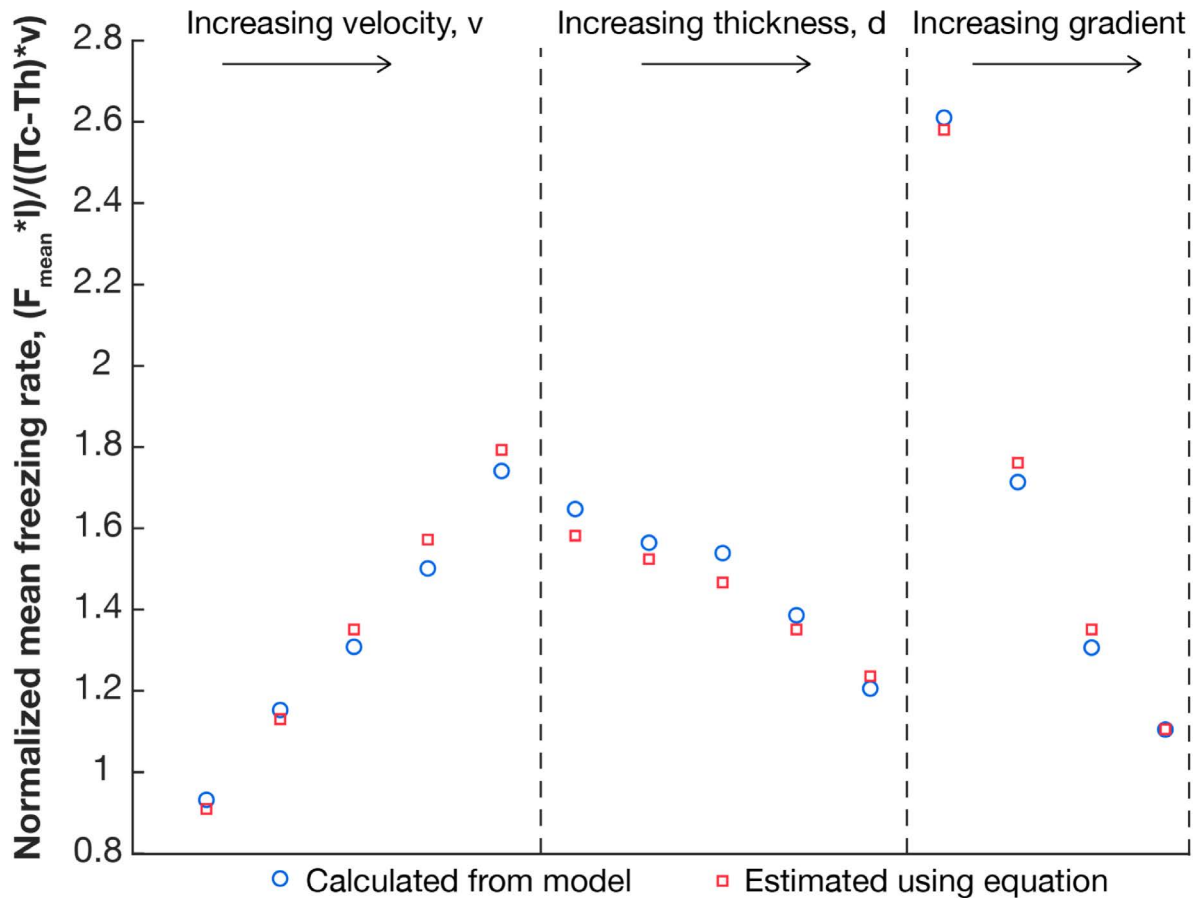


Figure 4.5: Comparison of the normalized mean freezing rate, $F_{mean}l/(T_c - T_h)v$ obtained from the model with that obtained from using the approximate empirical equation (Eqn. (4.21)) for different variations in the freezing device and specimen parameters. This figure shows that there is an agreement between the model and the empirical equation (Eqn. (4.21)). Note: the horizontal axis values for velocity correspond to the same axis values in Figure 4.4 (d)-(f) respectively.

In summary, results from the mathematical model were used to develop correlations between freezing rate and the design parameters during the directional solidification of a thick aqueous biological specimen. The model demonstrates the conditions under which the solidification of a thick aqueous layer on a directional device conforms to either the 2D formulation or the 1D idealized representation. The equations developed indicate a preference for the selection of certain design parameters when devising an experiment to freeze a sample on a horizontal directional device. This improved understanding is useful for the design of representative studies involving cooling of biological materials under controlled conditions. One of those such applications, is in the 3D cryoprinting. Since cell survival and hydrogel porosity after freezing is highly dependent on cooling rate during the freezing process, controlling the thermal history during 3D cryoprinting is of importance in tissue engineering. Directional solidification provides a simplified platform to easily simulate and characterize the freezing occurring during the cryoprinting process. However, for the directional solidification simulations to be most beneficial, they have to be representative. Therefore, the development of a representative mathematical model for directional solidification should further enable accurate design of studies that facilitate the development of cryoprinting protocols.

Experimental Validation:

The results from this mathematical model were validated using experiments. The parameters for the experiments were as follows: high temperature, $T_h = 40^\circ\text{C}$, low temperature, $T_c = -40^\circ\text{C}$, gap distance, $l = 4\text{ mm}$, velocity, $v = 0.2\text{ mm/s}$, and specimen thickness, $d = 1.5\text{ mm}$ for an effective cooling rate of about $240^\circ\text{C}/\text{min}$. The sample was a 4% sodium alginate solution (Sigma Aldrich, St. Louis, MO). T-type Thermocouples were inserted at different depths in the sample (one at the bottom and one at the top as shown in Figures 4.6a-b) to measure the thermal history as the sample was frozen. The directional device used is described later in this chapter.

Figure 4.6c shows the temperature reading from a thermocouple placed at the top of the sample and a thermocouple placed at the bottom of the sample. It indicates that there is indeed a lag in temperature between the bottom and the top of the sample as the model predicts. When the bottom temperature gets to 0°C the temperature at the top is still at approximately 10°C . This is similar to the lag seen in Figure 4.4c. Additionally, the gradient immediately after the freezing point ($\sim 0^\circ\text{C}$) is steeper at the top of the sample than at the bottom of the sample similar to the temperature profiles in Figure 4.4c. These results are presented for comparison as the actual values do not match the simulated results for pure water presented in Figure 4.4c.

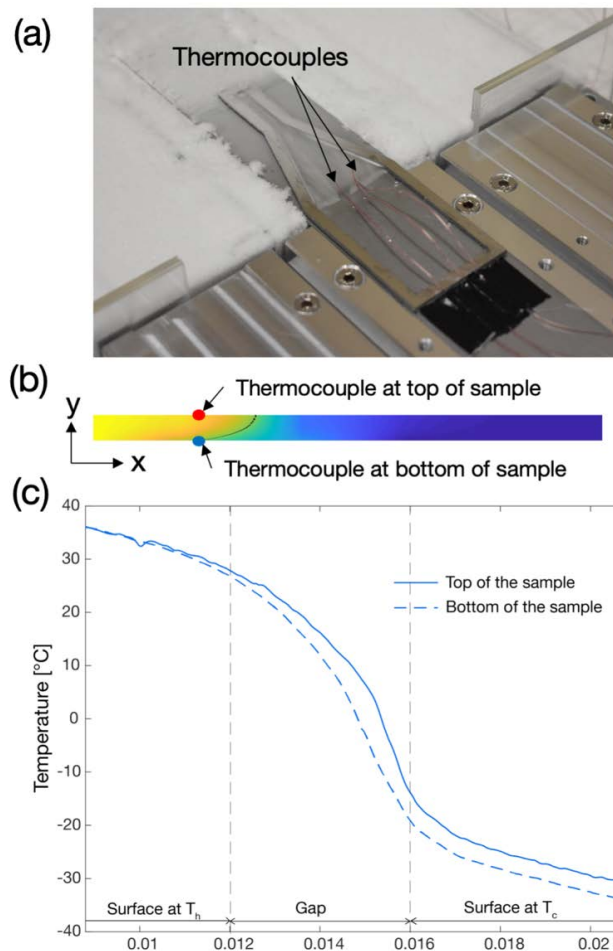


Figure 4.6: (a) Experimental setup showing the directional solidification of 4% alginate solution in a 1.5mm thick specimen holder. (b) Location of the thermocouples to record temperature history during freezing. The two

thermocouples were placed at the same x – location within the sample and different y – locations. One was placed at the bottom to measure the temperature closer to the substrate while the other was placed at the top surface of the specimen to measure the temperature within the specimen farthest away from the substrate (c) Measured temperature profiles at the top and bottom of the specimen frozen on a horizontal directional device across a fixed temperature gradient.

The differences in results can be attributed to the difference in thermal properties between water and the 4% alginate used in the experiment. Additionally, there is a steeper decent in temperature while the specimen is still approaching the gap from the high temperature surface compared to the model results. This is because the model assumes perfect contact between the substrate and the high temperature surface, whereas in reality there is a contact resistance between them in the experimental apparatus. Although this gradient affects the initial cooling rates of the samples, as seen from Figure 4.6c, the expected temperature gradient is achieved closer to the freezing point. The same steeper gradient in temperature after the gap could also be due to thermal contact resistance between the substrate and the constant temperature surface. Other possible sources of discrepancy between the model and the experimental results are, conduction through the thermocouple which may cool the surrounding liquid around the thermocouples and the effect of air on the thermocouple placed on the top of the sample. Despite these errors in the experimental setup, there is a clear difference in profiles at the top and the bottom of the samples and the temperature difference is similar to that predicted by the model in Figure 4.4c.

Since the results from the mathematical model can be realized in an experimental setup, the model could be used to design an appropriate study, using a directional solidification device, that accurately simulates the freezing of an aqueous biological material like alginate during 3D cryoprinting.

4.3. Design of directional solidification device

Based on the analysis above, we designed and built a directional solidification device for the study of freezing of aqueous bio-inks such as alginate. This device was loosely based on previously designed 1-D directional solidification devices built for controlled freezing of biomaterials [134]. The device was used in the past to mimic the freezing process in single slices of large biological organs [135], and for use in manufacturing of single layer tissues with controlled porosity, through freezing and freeze drying [132]

Figure 4.7 is a schematic of the actual directional device built and utilized. This device consists of two Microcool CP3001 cold plates (Wieland Microcool, Decatur, AL). These cold plates are hollow to allow fluid circulation between finned microchannels for rapid heat exchange at their surfaces. Mounted to each cold plate are three 120mm x 60mm customized aluminum plates, with grooves to keep the stainless-steel slide moving in a linear path. Translating along these grooves is a stainless-steel plate on which the liquid sample is placed, contained edgewise with a walled perimeter. Stainless steel was selected for its relatively high thermal conductivity and magnetic properties. A strong, permanent magnet is positioned under each of the temperature-regulated modules to attract the steel to the module and reduce thermal contact resistance. The walled perimeter is shaped to control the origin and direction of ice nucleation. Between the cold plates and the aluminum plates are Omega KHA-106 thin film polyimide heaters (Omega Engineering, Norwalk, CT), working in conjunction with Omega Platinum Series CN32PT-220 temperature controllers (Omega Engineering, Norwalk, CT) and Omega Type J thermocouples

(Omega Engineering, Norwalk, CT) to regulate surface temperatures. The thermocouples are placed on the leading edge of the aluminum blocks as shown in the Figure 4.7 to ensure controlled cooling within the gap. Methanol at dry ice temperature ($\sim -78^{\circ}\text{C}$) was circulated through the low temperature cold plate using a submersible pump. The cold side controller regulates the methanol pump and thin film heater based on input from the thermocouple to keep it at the cold temperature while the hot side controller regulates only a thin film heater. This system provides temperature regulation within $\pm 0.3^{\circ}\text{C}$ of the setpoint.

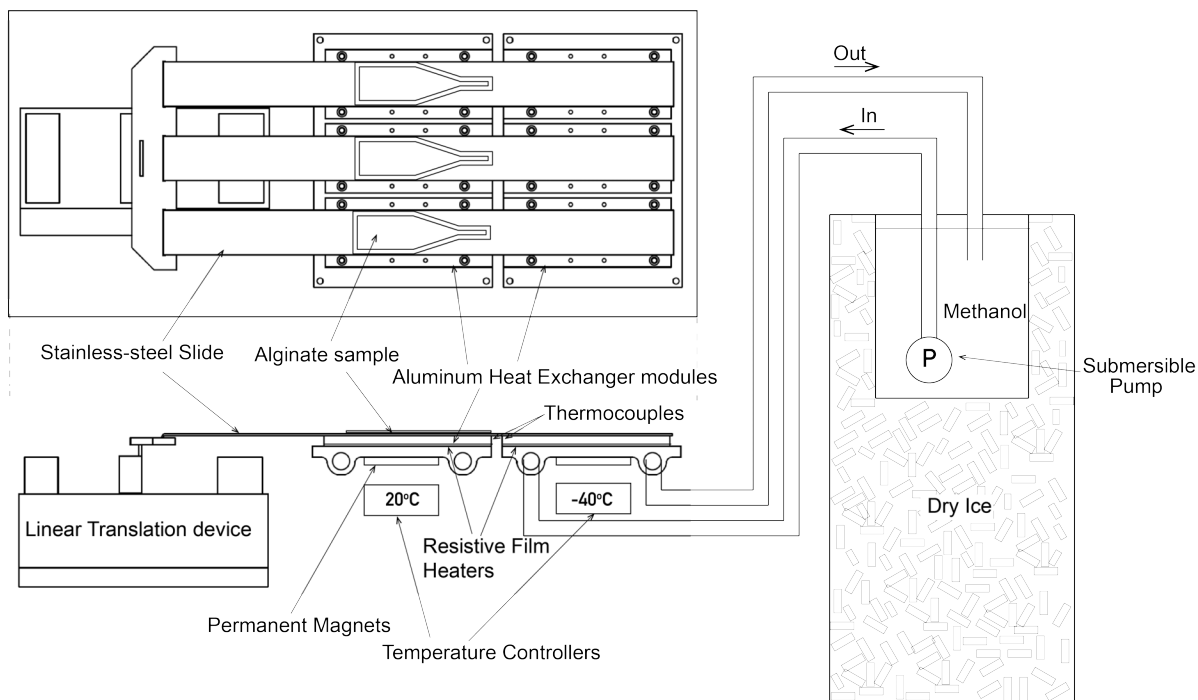


Figure 4.7: Detailed diagram of the directional device designed

4.4. Experimental studies of ice formation and microstructure using directional solidification

We devised several experimental studies employing this directional solidification device for controlled freezing of biomaterials. These studies are relevant to the manufacturing of single layer tissues through alginate casting and freeze drying [132] and similarly, to the simulation of freezing of large biological organs [135], and as an analog for the study 3D cryoprinting using aqueous hydrogels. In a series of studies, ice morphology, hydrogel microstructure, mechanical properties, and cross-linking are observed and analyzed for directional freezing of alginate to simulate 3D cryoprinting with alginate bio-inks.

4.4.1. Effect of cross-linking on ice morphology

Before evaluating the effect of cross-linking on microstructure, we investigated differences in ice morphology in crosslinked and non-crosslinked alginate, since ice crystals can dictate microstructure in frozen hydrogels [136]. In this study, samples of alginate that were part

crosslinked and part non-crosslinked were frozen under continuous monitoring and the ice crystal morphology in crosslinked alginate was compared to the ice crystal morphology in non-crosslinked alginate frozen under identical conditions.

Materials and Methods:

Materials: 2% sodium alginate was prepared by adding the appropriate amount of sodium alginate powder (molecular weight: 222g/mol) (Spectrum Chemical Mfg. Corp. Gardena, CA) to deionized (DI) water. The solution was then mixed on a magnetic stir plate until homogenous and then allowed to settle in the refrigerator (set to 4°C) for at least 24 hours before use. For cross-linking, a 2% w/v solution of calcium chloride (CaCl₂) was made by adding 4g of CaCl₂ dihydrate powder (Fisher Scientific, Fairlawn, NJ) to 200ml of water and the resulting CaCl₂ solution contained in an atomizer spray bottle.

Procedure: First, the alginate solution is poured into a 0.75mm sample holder until full, for a sample thickness of 0.75mm. To make part of the sample crosslinked, a portion (approximately the first half of the length) of the solution cast in the sample holder was covered with a microscope slide and the uncovered length of the sample was sprayed with the 2% CaCl₂ solution to initiate cross-linking. The resulting sample was half crosslinked and half non-crosslinked. The sample was then frozen directionally on the directional device, beginning with the non-crosslinked portion, until the entire sample was frozen. In these experiments, the high temperature surface of the directional device was set to 40°C and the low temperature surface to -40°C. A 4mm gap in between them was maintained using 4 microscope slides, each 1mm thick placed in between the plates as shown in Figure 4.8, for a resulting temperature gradient of 20°C/mm. A cooling rate of 120°C/min was achieved by moving the sample at a velocity of 6mm/min using a modified syringe pump (Harvard Apparatus, Holliston, MA) to translate the stainless-steel slide. The morphological appearance of the ice crystals was monitored with the microscope and recorded.

Microscopy: The ice crystal morphology at the freezing interface was captured using an Olympus SZ61 light microscope at 8x magnification (Olympus Corporation, Tokyo, Japan) placed above the directional device, focused on the gap between the high and low temperature modules, as shown in Figure 4.8. Freezing of each sample was recorded using an Olympus C-7070 digital camera (Olympus Corporation, Tokyo, Japan) as the sample traversed the temperature gradient across the gap.

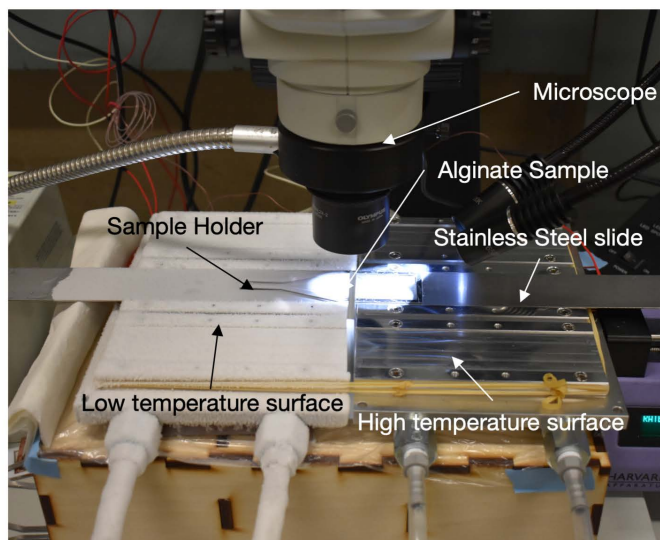


Figure 4.8: Picture of the experimental setup for monitoring the directional solidification on an aqueous solution

Results:

The video stills in Figure 4.9 illustrate the difference in the ice crystal morphology in the non-crosslinked region compared to the crosslinked region during freezing. In the non-crosslinked alginate, the ice crystals are dendritic and align parallel to the direction of the temperature gradient (Figure 4.9a). As the freezing interface proceeds closer to the cross-linked region, ice dendrites retain their directional alignment but some random nucleation of ice crystals can be observed at the interface (Figure 4.9b). As soon as the freezing interface reaches the crosslinked region of the alginate sample, ice crystals cease forming dendrites and instead nucleate, forming varying sizes of ice crystal pockets within the hydrogel structure (Figure 4.9c). In the fully crosslinked region shown in Figure 4.9c the directional organization of ice dendrites is completely lost and there is evidence of supercooling at the freezing interface and random nucleation of ice in the different pockets of supercooled water entrapped by the crosslinked alginate. These ice pockets form as the water sequestered within the crosslinked alginate matrix nucleates and that ice nucleate grows until all the water in each pocket is completely frozen. Because the water molecules are not free flowing like in the alginate solution, each ice nucleus cannot grow continuously to form dendrites.

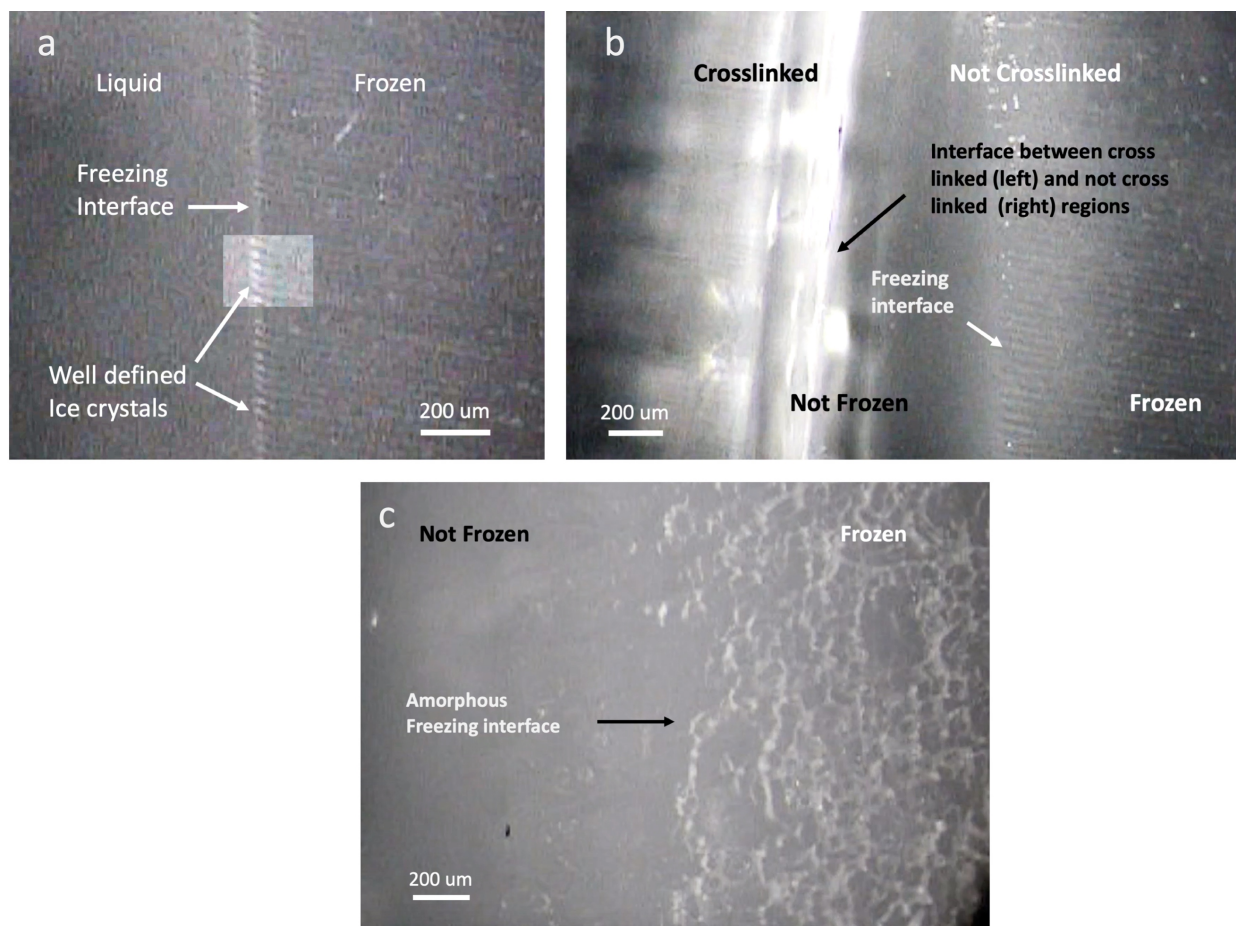


Figure 4.9: Images obtained from the video of the directional freezing process of an alginate sample that is part crosslinked and part non-crosslinked (a) The ice dendrites forming within the non-crosslinked portion of the alginate sample as its frozen on the directional stage (b) Ice crystal dendrites as the freezing interface approaches the interface between the crosslinked and the non-crosslinked region. (c) Random ice nucleation in the crosslinked portion leads to the amorphous ice crystal structure as ice pockets form in the crosslinked region of the alginate. The ice is opaque.

4.4.2. *Effect of cross-linking application sequence on resulting alginate microstructure*

The previous study showed the differences in ice morphology during freezing of crosslinked and non-crosslinked alginate. Using this knowledge of the ice structure we proceed to develop alginate samples with different microstructures. This study focuses on the microstructure of crosslinked alginate samples that have been processed by freezing. It provides a better understanding of the microstructure expected after 3D cryoprinting and freezing modulated cross-linking. Here, we compare the microstructure of alginate solutions that are frozen before cross-linking with those frozen after cross-linking.

Materials and Methods:

Sample preparation: Sodium alginate mixtures of several compositions (1% w/v, 2% w/v, 3%w/v and 4% w/v) were prepared by adding the appropriate amount of sodium alginate powder

(molecular weight: 222g/mol) to deionized (DI) water as previously described. 2% w/v solution of calcium chloride (CaCl_2) was also used for the cross-linking.

Procedure: Two different sets of samples were prepared for several compositions (1% w/v, 2% w/v, 3%w/v and 4% w/v) of alginate; crosslinked samples made by spraying 2% CaCl_2 on the alginate solution casted in a 1.5mm sample holder prior to freezing and non-crosslinked samples of alginate solution also contained in a 1.5mm sample holder. A fixed cooling rate of $120^\circ\text{C}/\text{min}$ achieved on the directional device using a high temperature surface set to 20°C , a low temperature surface to -40°C , and a gap of 6mm, and a sample velocity of 12mm/min was used for these experiments. Each composition of sodium alginate was frozen using the directional device in two groups. First, the alginate sample was crosslinked before freezing by spraying 2% CaCl_2 solution on the 1.5mm thick sample resting on the stainless-steel slide on the high temperature module. The sample remained there for 10 minutes after spraying with CaCl_2 to allow sufficient time for cross-linking to take place. After 10 minutes, the sample is moved across the gap at a constant velocity (constant freezing rate) until the entire sample is across on the low temperature module of the directional stage and frozen. The sample is left stationary for another 10 minutes after which it is translated in reverse manner thawing it at the same rate as the freezing. Once the entire sample is melted and on the high temperature surface, the sample is removed and stored for microscopy or mechanical testing. Likewise, for the second batch of experiments where the cross-linking was done after freezing, a new sample is filled into the sample holder. Without cross-linking, the sample is moved across the gap at a constant velocity of 12 mm/min to the low temperature surface. Once there, the sample is sprayed with 2% w/v CaCl_2 solution and remains on the low temperature surface for an additional 10 minutes similar to the first batch. Then the sample is thawed in reverse at the same rate. Diffusion rate of CaCl_2 into alginate is slower at lower temperatures so the bulk of the cross-linking process takes place during the thawing process. After the entire sample reaches the high temperature module, the sample is removed and stored for microscopy or mechanical testing.

Microscopy: Optical micrographs were obtained for the samples prepared above. First the samples are transferred from the sample holder onto a microscope slide and stored in the refrigerator until ready to image. The samples were then imaged on an Olympus IX71 inverted light microscope (Olympus Corporation, Tokyo, Japan) equipped with an Olympus DP71 digital microscope camera at 10x and 20x magnifications.

Results:

Figure 4.10 shows light microscopy images of samples frozen before cross-linking and those frozen after cross-linking. There is a clear difference in the resulting microstructure in the different samples for the same composition. Those crosslinked before freezing (Figures 4.10a-b) have a microstructure typical to regular crosslinked hydrogels that have not been frozen. The liquid water pockets are trapped within polymer chain links. However, the samples crosslinked after freezing (Figure 4.10c-d) have distinct directionality corresponding to the ice dendrites present through the sample (see Figure 4.9a) while it was being crosslinked. The ice crystal dendrites formed in alignment with the direction of the temperature gradient and after cross-linking and melting of the ice, leave behind the unique directional microchannels in the crosslinked hydrogel. These microchannels created by the dendrites are present continuously throughout the thickness of the sample and, in each layer, run essentially parallel to each other. The microchannels are

formed as a result of the tight crystallographic structure of ice which rejects the alginate chains during freezing and forces them into the boundaries between the ice dendrites. During cross-linking, those alginate chains get arrested in place between the ice dendrites, leaving open channels where the ice previously resided upon thawing.

These differences in microstructure for cross-linking before freezing versus after freezing may be attributed to the binding of the free water by polymer chains when crosslinked thereby limiting the ability of the water molecules to attach to the ice crystals to form dendritic structure. The ice crystals forming need to circumnavigate crosslinked alginate polymer chains, leading to the random organization in the densely crosslinked structure.

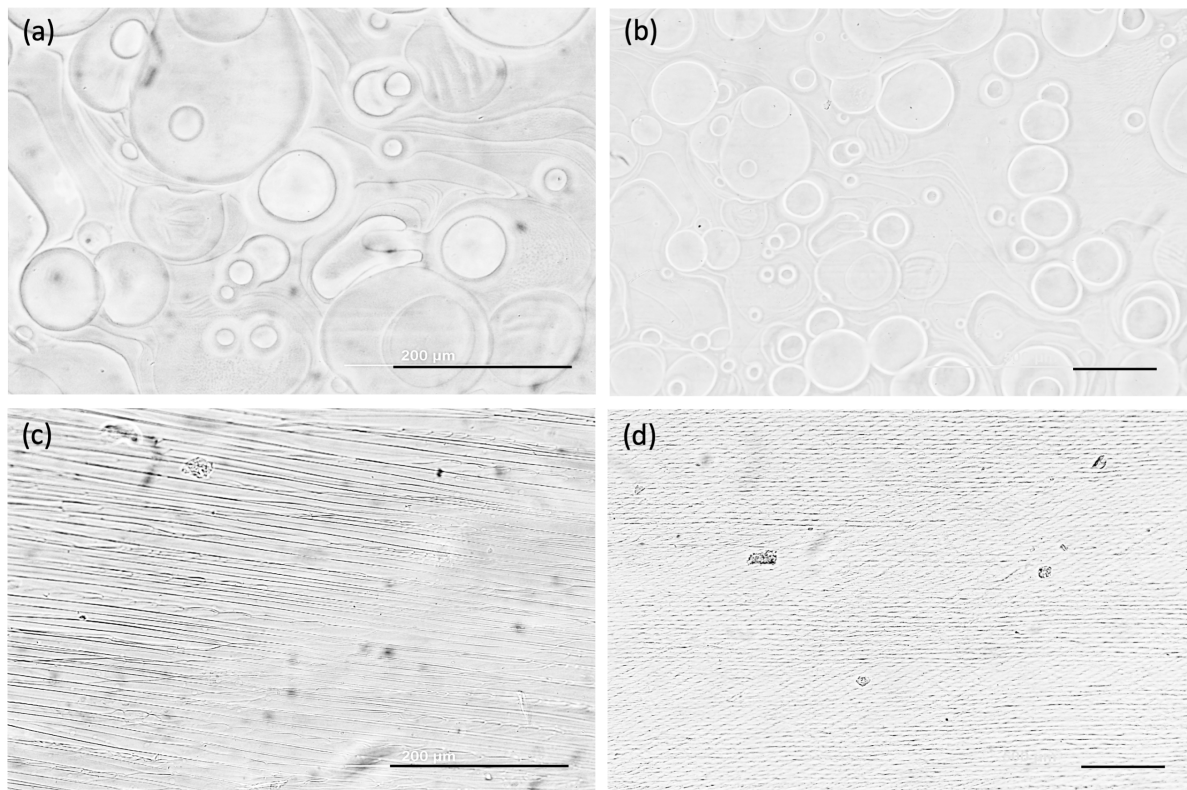


Figure 4.10: Micrographs showing the difference in microstructure for directionally frozen structures crosslinked before freezing (a&b) from those crosslinked after directional freezing (c&d) at 100x (a&c) and 200x (b&d) magnifications. (200um scale bars)

4.4.3. *Effect of cross-linking density on alginate microstructure*

Having found an effect of cross-linking before freezing on the ability to form directional microstructure in alginate hydrogels, we performed an additional study to evaluate the influence of cross-linking density. The purpose of this study was to answer the question: what is the threshold for cross-linking density before directional microstructure as a result of ice dendrite formation is impeded in alginate?

Materials and Methods:

Sample preparation: 2.4% w/v sodium alginate solution was first prepared. Then, multiple aqueous calcium carbonate (CaCO_3) (Acros Organics, New Jersey) and D-(+)-Gluconic acid δ -lactone (GDL) (Sigma-Aldrich Co, St. Louis, MO) solutions were mixed individually. Calcium carbonate was used - as opposed to CaCl_2 - for its low cross-linking rate due to high pH in the absence of GDL, permitting greater homogeneity in the crosslinked mixture. GDL was used to buffer the alkalinity of calcium carbonate, allowing quick cross-linking after calcium ion incorporation. The alkalinity of the CaCO_3 solution prevents the dissolution of the CaCO_3 and limits the Ca^{2+} ions available for cross-linking. The concentrations of the CaCO_3 solutions were determined under the assumption that one Ca^{2+} ion would bind two sodium alginate carboxyl groups. This saturated molar ratio was designated as 1x cross-linking, for notation. Three CaCO_3 solutions were prepared such that when mixed with a specific volume of alginate would dilute it to 2% w/v. Furthermore, their calcium ion molarities would crosslink the alginate to 0.125x, 0.0625x, and 0.03125x (where x signifies the multiplier for the saturated molar ratio designated 1x). These values were chosen to maintain fluidity during processing as well as structure after freeze drying, while providing substantial cross-linking differences for comparison. Mixing CaCO_3 with alginate involved constant resuspension, gradual micro pipetting and stirring for 20 minutes. After forming three aqueous sodium alginate and CaCO_3 suspensions, aqueous GDL was incorporated. GDL was added in equal volume to CaCO_3 , providing a 2:1 GDL to CaCO_3 molar ratio to each suspension [71]. Mixing GDL involved gradual micro-pipetting and stirring for 20 minutes to prevent clusters. Once thoroughly stirred, each solution was stored in a 4°C refrigerator for at least 24 hours.

Experimental procedure: Each solution was deposited into a 5mm thick sample holder resting on the stainless-steel substrate. This larger sample thickness allows easier removal of the sample after freezing and better structural integrity after freeze drying. A cooling rate of 60°C/min was achieved in the directional device by setting the high temperature surface to 40°C, the low temperature surface to -40°C, maintaining a 4mm gap between the two surfaces, and moving the samples 3mm/min. Each sample was frozen across the directional device as previously described. Once frozen, each sample was removed from the mold and freeze dried for 24 hours using a Martin Christ Alpha 1-2 1d freeze dryer (Martin Christ, Germany). This process was repeated twice for each of the three cross-linking densities, resulting in six samples.

Electron Microscopy: Micrographs were obtained of each cross-linking density using a Hitachi TM-1000 scanning electron microscope (SEM) at 15kV. Images of cross sections perpendicular to the direction of ice growth (transverse), cross sections parallel to the direction of ice growth (lateral), and top surfaces were obtained at various magnifications.

Results:

The effect of the cross-linking to various densities before freezing was investigated with electron microscopy. The results depict a progression from an aligned structure to a more random structure as the cross-linking density is increased (Figure 4.11). At a 0.03125x cross-linking density the pores appear aligned and directed parallel to the direction of the temperature gradient (Figure 4.11a,d and g). This is similar in structure to the samples crosslinked after freezing (Figure 4.10c-d), suggesting a lightly crosslinked structure has enough free water molecules for the continuous attachment to ice dendrites. Similarly, at a 0.0625x cross-linking density there is still alignment in the lateral and top cross sections (Figure 4.11e and h), although there is greater non-

uniformity in the pore sizes in the transverse section (Figure 4.11b). At a cross-linking density of 0.125x, there is a clear loss of directional alignment similar to samples crosslinked before freezing (Figures 4.9c and 4.10a-b). There is no significant difference in the microstructure in the transverse (Figure 4.11c) and lateral (Figure 4.11f) cross sections of the sample with the highest cross-linking density suggesting a lack of pore alignment, unlike in lower cross-linking density samples. At the higher cross-linking density, the directional dendritic ice crystals cannot develop as in the lower cross-linking densities.

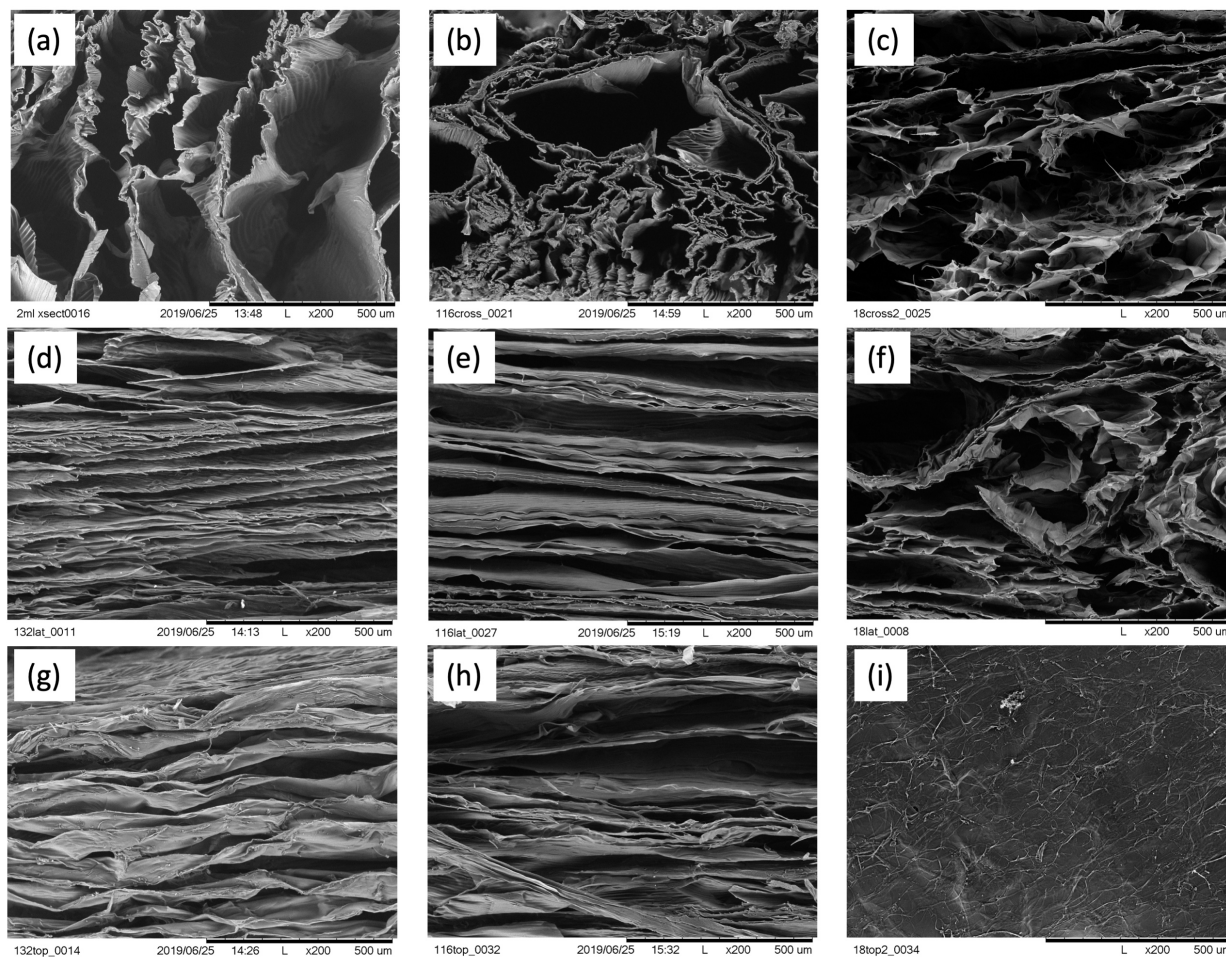


Figure 4.11: Micrographs showing the difference in microstructure as a function of cross-linking (a) Transverse cross section of 0.03125x crosslinked alginate (b) Transverse cross section of 0.0625x crosslinked alginate (c) Transverse cross section of 0.125x crosslinked alginate (d) Lateral cross section of 0.03125x crosslinked alginate (e) Lateral cross section of 0.0625x crosslinked alginate (f) Lateral cross section of 0.125x crosslinked alginate (g) Top section of 0.03125x crosslinked alginate (h) Top cross section of 0.0625x crosslinked alginate (i) Top cross section of 0.125x crosslinked alginate (500um scale bars)

Effect of directional microstructure on mechanical properties of alginate

Lastly, we evaluated the effect of directional microstructure on the mechanical properties of the resulting alginate hydrogel made using directional solidification. Researchers have previously shown that hydrogels with anisotropic microstructures made using directional freezing exhibit anisotropic mechanical properties, with higher strengths and moduli in the alignment direction

[137,138]. So, the aligned anisotropic microstructure shown in 4.4.2 and 4.4.3 suggests similar anisotropy in the mechanical properties of the alginate gel. Tensile tests were conducted to evaluate the mechanical properties of different compositions of alginate, comparing those crosslinked before freezing (which have isotropic microstructure) to those crosslinked after freezing (which have aligned anisotropic microstructure).

Materials and Methods:

Sample preparation and experimental procedure for this study is identical to that used for the microstructure study in section 4.4.2

Mechanical Tensile Tests: Tensile tests were done on the alginate samples prepared in the study described in 4.4.2. Once the samples are removed from the sample holder and transferred to the microscope slide they are covered with a filter paper soaked in PBS, wrapped in parafilm and stored in the refrigerator at 4°C until ready for testing. The tests were performed within 48 hours of the samples being made. The PBS solution was used to maintain hydration in the different samples. From each directional frozen sample, up to four mechanical testing strips about 40mm long by 10mm samples were obtained. Three strips were cut with 40mm lengthwise dimension along the grains of the ice crystal growth and one strip across the ice crystal growth dimension. Clamps to hold the alginate strips were made using waterproof sand paper. Each clamp was a strip of sand paper about 45mm by 90mm in size. The clamps were folded in half to 45mm by 45mm and approximately 10mm on one end of the strip was glued in between using non-expanding gorilla glue. The same was repeated for the other end such that there was about 15-20mm in between the glued ends forming the effective length of the test strip. Each test strip is then loaded onto a Shimadzu Universal Tensile test machine (Shimadzu Corp, Tokyo, Japan) with a 100N load cell. All tests were done at a fixed strain rate of 50mm/min.

Statistical methods: All data is presented as the mean \pm standard deviation. Mechanical test data is presented for 3-6 repeats. Single factor t-tests were performed on the mechanical testing results to determine statistical significance.

Results:

Figure 4.12a compares the elastic moduli of the samples crosslinked before freezing with those crosslinked after freezing for various compositions. The mean elastic moduli of the samples crosslinked before freezing were 15.3kPa, 17.9kPa, and 24.1kPa for 2%, 3% and 4% w/v alginate solutions respectively. The respective means of the samples crosslinked after freezing were 31.1kPa, 31.6kPa, and 57.7kPa. Although, the mean elastic modulus increases going from the non-aligned microstructure in the samples crosslinked before freezing to the aligned microstructure in the samples crosslinked after freezing, statistical analysis showed no significant difference in the means. Figure 4.12b compares the failure stresses of the samples crosslinked before freezing with those crosslinked after freezing at different compositions of alginate. The mean stresses at failure of the samples crosslinked before freezing were 4.7kPa, 5.0kPa, and 9.2kPa for 2%, 3% and 4% alginate solutions respectively. The mean stresses at failure of the samples crosslinked after freezing were 13.2kPa, 11.3kPa, 18.1kPa respectively. There is also no significant difference in the mean failure stresses between those crosslinked before freezing and those crosslinked after freezing.

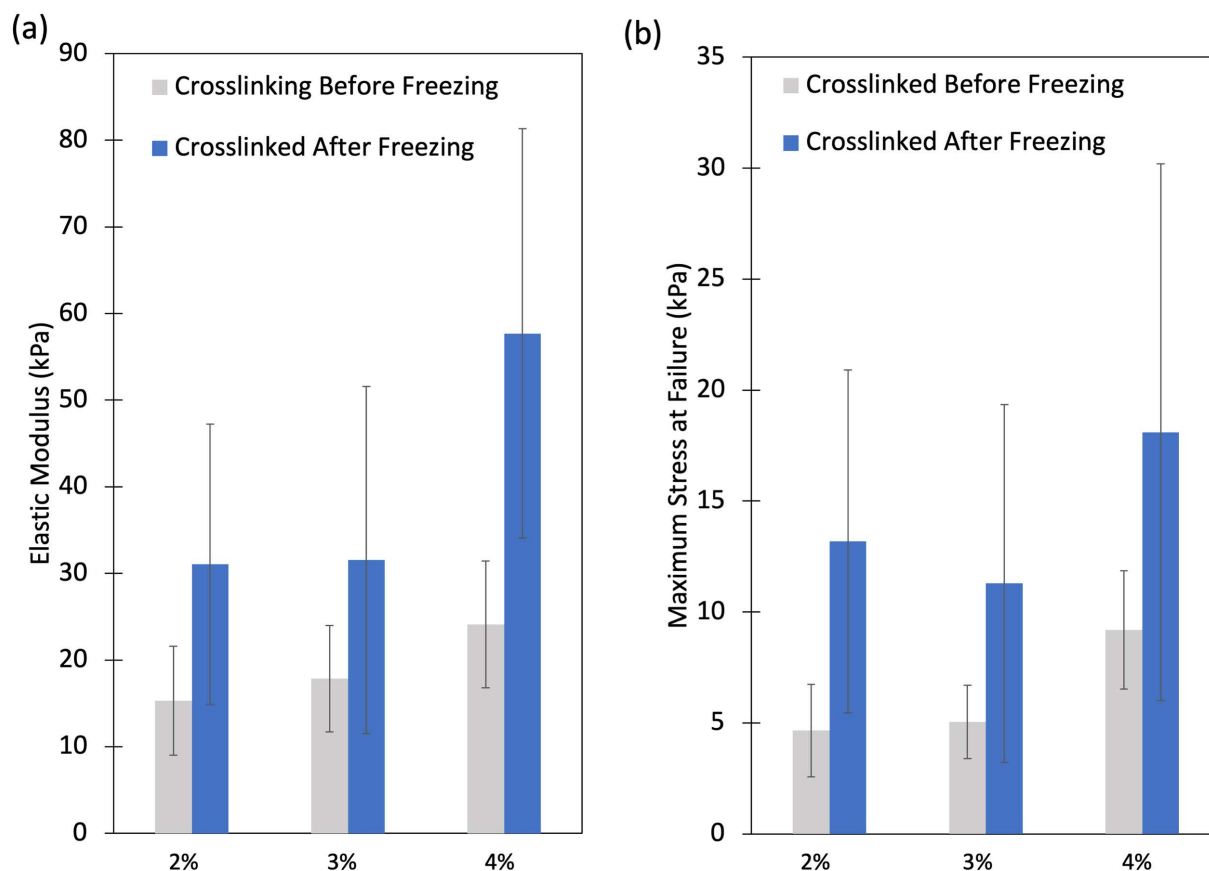


Figure 4.12: (a) Comparison of elastic moduli for different compositions of alginate frozen directionally and crosslinked either before or after freezing. (b) Comparison of failure stress for different compositions of alginate frozen directionally and crosslinked either before or after freezing. Data were analyzed using t tests ($p < 0.05$)

Absence of statistical significance in these results may be attributed to the large error bars for the mean elastic moduli and failure stresses. This large variance could be due to the high strain rate used for the tensile tests and the use of PBS which contains phosphates that could react with the Ca^{2+} to weaken the gel bonds [139]. As such there is reason to perform more rigorous mechanical testing studies with slower strain rates and a different samples storage process to verify if the absence of significance in the statistical analysis is a real finding or an experimental artifact.

4.5. Discussion and conclusion

During 3D cryoprinting of an aqueous hydrogel bio-ink like alginate, the water crystallizes forming ice which increases the mechanical rigidity of the aqueous hydrogels during printing. The formation of these ice crystals, however, can alter the microstructure of the resulting hydrogel construct after freezing modulated cross-linking, which in turn may lead to unpredictable mechanical properties. So, to investigate the effect of this ice formation on microstructure and mechanical properties, we utilized directional solidification to simulate the freezing of aqueous biomaterial solutions at controlled cooling rates. The directional solidification setup simplifies the freezing to 1-D for fundamental study of the ice formation.

Before building the directional solidification device we revisited this 1-D freezing assumption and developed mathematical relations to correct for 2-D deviations resulting from increased sample thickness. The results of this analysis show that, unlike a 1-D model, location of the freezing interface could vary through the thickness of a sample during a directional solidification process. The shift in location of the interface from the location of the phase change temperature on the substrate has a direct effect on the cooling rate through the sample at the phase change interface. This interface shift is a function of velocity, temperature gradient, sample thickness, and its thermophysical properties. It can be calculated and used to evaluate deviation from one dimensionality. The cooling rate at the change of phase interface in the bulk freezing region is different from that on the solidification substrate, however it is uniform and well defined. Therefore, when analyzing the process of freezing during directional solidification it is important to realize this departure from one dimensionality and to correlate the process parameters to the actual thermal conditions in the bulk solidifying region. It should be emphasized that many experimental studies on directional solidification of aqueous solutions and biological matter may require readjustment of analysis, in view of these findings.

Following this, we built a directional device and used it to perform several studies comparing the effect of cross-linking before freezing (typical of 3D bioprinting processes) with the effect of cross-linking after freezing. Cross-linking after freezing applies to the process of fabricating scaffolds at subfreezing temperature using 3D cryoprinting and cross-linking those frozen scaffolds during thawing with freezing modulated cross-linking.

The first study looking at ice morphology showed a difference in the ice crystal formation in crosslinked alginate versus in non-crosslinked alginate. The dendritic formation of ice crystals in the non-crosslinked alginate was in stark contrast to the random nucleating ice crystals sequestered in random pockets formed by crosslinked polymer chains. The alignment of the ice dendrites with the temperature gradient provides a means to control the ice crystal structure and consequently the microstructure of the non-crosslinked alginate solution. This represents an advantage of the coupled process of 3D cryoprinting and freezing modulated cross-linking.

This observation was further exploited in the second study where we observed the microstructure of the alginate after freezing and thawing for alginate gels constructed by cross-linking before freezing and those constructed by cross-linking after freezing. As expected, the directional alignment of the microstructure was evident in the gel constructed by cross-linking after freezing since this allows for the ice dendrite formation. Ice dendrites are able to impose lasting microchannels in the microstructure of the resulting gel. Microchannels that could be of interest to tissue engineering, as currently two challenges to generation of large tissue and organs are vascularization and maturation [26,140,141]. The ability to generate microchannels in particular directions and of particular sizes (by simply controlling cooling rate, temperature gradient, and initial direction of ice nucleate during 3D cryoprinting) could be useful for nutrient and waste transfer, and improved oxygen transport to cells in large tissue constructs, buying time for angiogenesis. Control over the size of these microchannels and the direction of porosity could also be used to modulate cell invasion and cell motility which could be important for the maturation of artificial tissue constructs into living tissue.

The third study extends the work on microstructure by looking at the sensitivity of microstructure to cross-linking density. The results showed that even with some cross-linking it is possible to control the microstructure using ice formation and obtain the preferred aligned microstructure with long microchannels. This could be advantageous in 3D cryoprinting processes

where partial cross-linking before printing might be needed to augment the fluid properties of the bio-ink during extrusion.

The final study focuses on the relationship between the mechanical properties of the alginate structure and the microstructure. Although, the results presented were inconclusive, there is evidence of some anisotropy in mechanical properties in the samples with anisotropic microstructure. This is in line with previous work from others showing increases in mechanical properties of directionally frozen anisotropic hydrogels compared to their isotropic counterparts [137,138]. A benefit of this increased mechanical strength and anisotropy is the ability to control the mechanical properties by just controlling temperature gradients during 3D cryoprinting. With directional stiffnesses of the hydrogel constructs, cells behaviors mediated by matrix stiffness like differentiation, growth, and migration could be controlled [142,143]. This level of control is more than that which can be achieved by simply varying composition. Since the results of this study were unconvincing, further work still needs to be done to evaluate this mechanical property dependence to ensure the large variance in elastic modulus is not as a result of the strain rate used, water content, or the sample preparation conditions. It should be emphasized, that we did not examine the entire range of cooling rates of interest in freezing of biological materials (spanning 0.1 °C/min to 1000 °C/min) or the entire range of materials compositions for tissue engineering.

In conclusion, the results presented here illustrate the usefulness of directional solidification as a tool to study 3D cryoprinting and to control microstructure.

Chapter 5

5. Parallel multilayer cryolithography for mass manufacturing

5.1. Introduction

In the previous chapters we established the benefits of 3D bioprinting at subfreezing temperatures and demonstrated the feasibility of several techniques that facilitate the creation of soft hydrogel scaffolds from start to finish. One of those methods is 3D cryoprinting which suffers from similar limitations associated with a primarily prototype-focused manufacturing method like 3D printing. One of the limitations which has hampered the use of 3D bioprinting for tissue engineering is print duration. Although 3D printing has gained a lot of popularity as a rapid prototyping method, it is still a lengthy process. It is sufficient for small volume manufacturing but loses efficiency and cost advantages as the manufacturing scale gets larger. This is because the printing process is typically linear. It involves the use of a printer head capable of moving horizontally in the x - y plane and a printing platform which moves in the vertical, z plane. These movements are computer controlled in conventional 3D printing allowing for precise and repeatable formation of complex shapes. A 3D object is made of an assembly of single volume elements (voxels), in which one element is added to the other in one device, until the entire object is produced. The placement of these voxels is sequential, one placed after the previous in the x - y plane until a layer is completed before another layer can be deposited. The serial nature of this process does not lend itself to scale up for mass manufacture in an economically feasible manner [78]. Instead most successful high volume manufacturing technologies benefit from parallelization when moving from producing one part to much higher quantities [79]. 3D printing has therefore been mostly confined to use in rapid prototyping and small batch processes. In these contexts, 3D printing is considered rapid when compared to other manufacturing techniques that require significant upfront time and/or monetary investment like injection molding etc. However, when it comes to bioprinting, these manufacturing and time limitations can become prohibitive. Printing of large organs on a realistic scale can take several hours. This can lead to microbial contamination of the biological material during printing and in processes involving cells, causing cell death as a result of ischemia and lack of nutrition.

To solve this issue, we developed a parallel manufacturing process, employing both multilayer lithography (MLL) and cryoprinting called parallel multilayer cryolithography. This technique incorporates parallelization of 3D printing with the concept of controlled temperature freezing during 3D printing for tissue engineering (introduced in chapter 2 as cryoprinting) aimed at overcoming the issues with 3D printing of soft biological materials [1,144]. Although cryoprinting improves elements of 3D bioprinting, it is still a linear process and as such not easily scalable for mass manufacturing. Multilayer cryolithography (MLCL) enables parallelization of 3D printing, resulting in higher efficiency for manufacturing. It allows for the simultaneous printing of the layers that make up the object and quick assembly of these printed layers to form the object. The concept of manufacturing single layers and binding them together is not new, and

is the basis for the process known in additive manufacturing as “laminated object manufacturing” (LOM)[145]. However, there is a major difference between objects produced by conventional lamination and those of relevance to the tissue engineering. Unlike LOM, the materials being used for tissue engineering are highly viscous liquids or gels with low moduli, which in thin layers, cannot withstand the forces of gravity or the loads that would be typical with LOM. This is the major differentiator of this method. Biological matter consists mostly of liquids which cannot be manipulated in thin layers the same way paper, plastics, ceramics, and metals are in LOM. So, a technology to facilitate the transport of a 2-D layer made of aqueous solutions and/or organic matter lacking mechanical rigidity from the site where the 2-D structure is manufactured to the site where the 3D object is assembled, under the force of gravity, had to be developed. By incorporating this with freezing, the 2-D layers can be assembled into a 3D object.

Here, we will discuss the principles behind 3D parallel multilayer cryolithography and its advantages, and using an example device we will demonstrate the use of this technology for the manufacture of a hydrogel scaffold for tissue engineering. While the technology is relevant to applications involving tissue engineering with cells, the fabrication process demonstrated here uses acellular biomaterial solutions. The material used in this example, sodium alginate, is one of the most commonly used materials in tissue engineering [146–148]. The components of the device used are described and the resulting printed products are analyzed. The work described here was also published as [80].

5.2. Principles of parallel additive manufacturing

Parallel additive manufacturing by MLCL can be broken into four main aspects: a) generating multiple 2-D layers in parallel, b) moving 2-D layers to the 3D assembly site, c) assembling the 2-D layers into a 3D object, and d) preserving the 3D object. Figure 5.1 outlines the step by step process involved in making a biological object using parallel additive manufacturing with MLCL. First, there is a need to generate 2-D layers in a fast, repeatable manner. This can be achieved by depositing a layer of biomaterial onto a hydrophilic lithography plate using a 2-D printer. A major advantage of this technique is that the printing of different layers can be done simultaneously with attention to individual layer details on several 2-D printers in parallel rather than serially, as is done in regular fused deposition 3D printing. In regular 3D printing, the object to be printed is computationally sliced into several layers of fixed thicknesses and each layer is printed with single voxels deposited in 2-D and fused onto the previous layer in a sequential manner until the 3D object is formed. With parallel MLCL the printing of those individual layers is parallelized and fusing the layers together is done using freezing in a subsequent step at a different station to save time.

The next step involves the transfer of the printed 2D layers to the staging platform where they are picked up and moved to the assembly site. In order for the layers to be picked up they have to be inverted and moved to the staging platform. This could be achieved using a servomotor attached to the print platform, which rotates the hydrophilic lithographic plate to the staging platform as shown in steps 2 and 3 of Figure 5.1. This step is challenging for aqueous biological matter, but by using a hydrophilic lithographic plate and because the layers are only a few hundred microns thick, surface adhesion forces and surface tension ensures the layer remains attached to the surface during the rotation and inversion. The print platform is attached to the hydrophilic lithography plate by an electromagnet (or alternatively by vacuum suction) which is activated during the rotation. Once the lithography plate has been rotated to and placed inverted on the

staging platform, the electromagnet is deactivated and the platform rotates back to its original position where a new lithography plate can be placed and another layer printed. This step takes advantage of the hydrophilicity of biological materials and materials typically used for bioprinting like hydrogels which contain mostly water.

After a lithography plate with the attached 2D layers has been inverted, it is picked up by a robot arm so that the printed layer is upside down as shown in Figure 5.1 (steps 3, 4 and 5). Several approaches were explored to enable this transport under the force of gravity. A simple technique of utilizing a hydrophilic material, such as a plasma cleaned glass microscope slide, for the lithography plate surface was selected for the example in this paper. The hydrophilic bonds between the lithography plate surface (plasma cleaned glass microscope slide) and the hydrogel deposited on that surface, are sufficiently strong to allow the deposited 2-D biomaterial layer on the lithography plate to be held in any direction in the gravitational field, provided that the thickness of the biomaterial layer is such that the surface adhesion force on the contact area is greater than its weight.

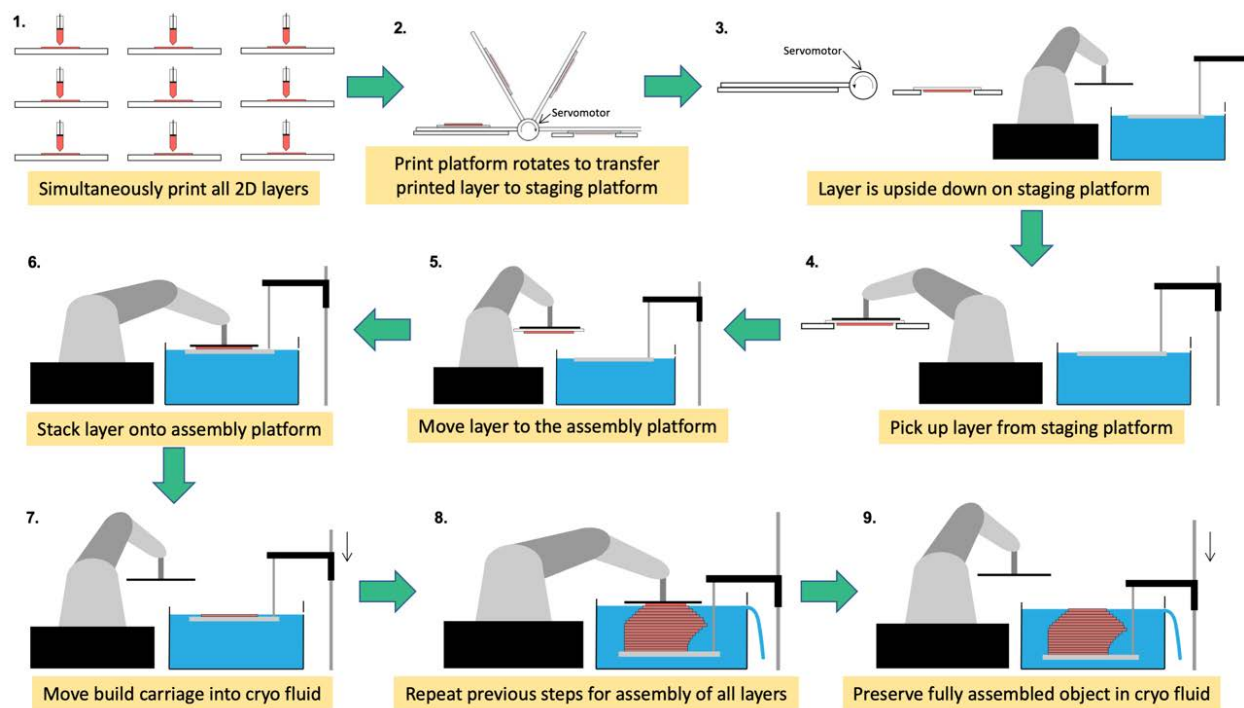


Figure 5.1: Process outline of the steps involved for the assembly of a biological product using parallel multilayer cryolithography. First, the 2D layers are printed simultaneously. Next, the printed layers are flipped over and transferred to a staging platform to be picked up by a robot and transferred to the assembly platform. The layer is stacked on the assembly platform or on a previously assembled layer. Then, the layer is subsequently immersed into the cryogenic fluid to be preserved. The same steps are then repeated for the next layer until the full object is assembled and frozen in the cryogenic fluid.

Next, the robot moves the inverted layer of biomaterial to the assembly platform where it is either placed directly on the assembly surface (if it is the first layer as in Figure 5.1 step 6) or deposited onto the previously deposited layers (Figure 5.1 step 8). While the robot holds the lithography plate in place, the 2-D layer of biomaterial adheres to the surface or previous layer by freezing. To ensure attachment of the first layer to the assembly platform, the surface of the

assembly platform should be made out of an equal or more hydrophilic surface than the lithography plate. The hydrophilic attraction combined with the freezing forces would guarantee that the attachment forces between the layer and the assembly surface is more than the force holding the layer to the lithography plate. Also, for subsequent layers, the attachment forces between the new layer and the previous are designed to be stronger than the hydrophilic bonds to the lithography plate, allowing the lithography plate to be removed, leaving the 2-D biomaterial layer on the assembly surface. The length of time for which the biomaterial layer needs to be in contact with the assembly platform or previous layer for freezing to occur, has to be determined to ensure that the layer detaches completely from the lithography plate. If the assembly contact time is too long, the layer also freezes to the lithographic plate making detachment challenging. Conversely, if the assembly contact time is too short, the layer will not adequately bind to the surface resulting in partial or no attachment to the assembly platform or previous layer. The optimal time, t , could be estimated using the following equation, where l is the thickness of the layer, α_s is the thermal diffusivity of the solid phase, and λ is a constant that may be determined experimentally or estimated from Neumann's solution [99].

$$t = \frac{l^2}{4\lambda^2\alpha_s} \quad (5.1)$$

Lastly, after the lithography plate is lifted from the assembly platform leaving behind the 2-D biomaterial layer, the freezing process can be controlled in two ways. One of these freezing methods is more relevant to large tissues. For large structures, the build platform is lowered into a cryogenic fluid bath to ensure solidification and preservation of the printed layer as shown in Figure 5.1 steps 7 and 9. The use of a cryogenic fluid allows for better control over the temperature in each layer and the freezing rate. By maintaining the cooling fluid at a constant temperature and keeping the fluid level a fixed distance away from the active assembly (deposition) plane, the cooling rate in each deposited layer can be controlled throughout the entire layer. The second method of freezing is useful for printing of smaller volumes of tissue. For smaller structures, keeping the temperature of the assembly surface at a controlled subfreezing temperature is sufficient for solidification and preservation. The steps for this method are illustrated in Figure 5.2. Both methods can be used for controlled freezing and as mentioned above, the first is required for large volumes and freezing with high cooling rates while the second is sufficient for freezing of smaller volumes and or where lower cooling rates are adequate. In MLCL, the freezing of each layer can be controlled using the methods developed for controlled freezing of individual voxel elements during 3D cryoprinting previously discussed [1,76].

The steps in Figure 5.2 are repeated for all the printed 2-D layers until the entire object is assembled. Although freezing is used in the assembly step to fuse the layers together, because this method needs to be applicable for the manufacture of biological constructs that will be used at physiological temperature (37°C) which is above the freezing temperature of the printing bio-ink, additional steps have to be implemented to maintain integrity after thawing. If the object is simply held together by freezing it would disintegrate when the temperature is raised. So, the biological material has to be crosslinked. This can be done using the previously described freezing modulated cross-linking. Other methods for cross-linking such as thermal cross-linking or UV cross-linking could also similarly be implemented during the assembly depending on the material used.

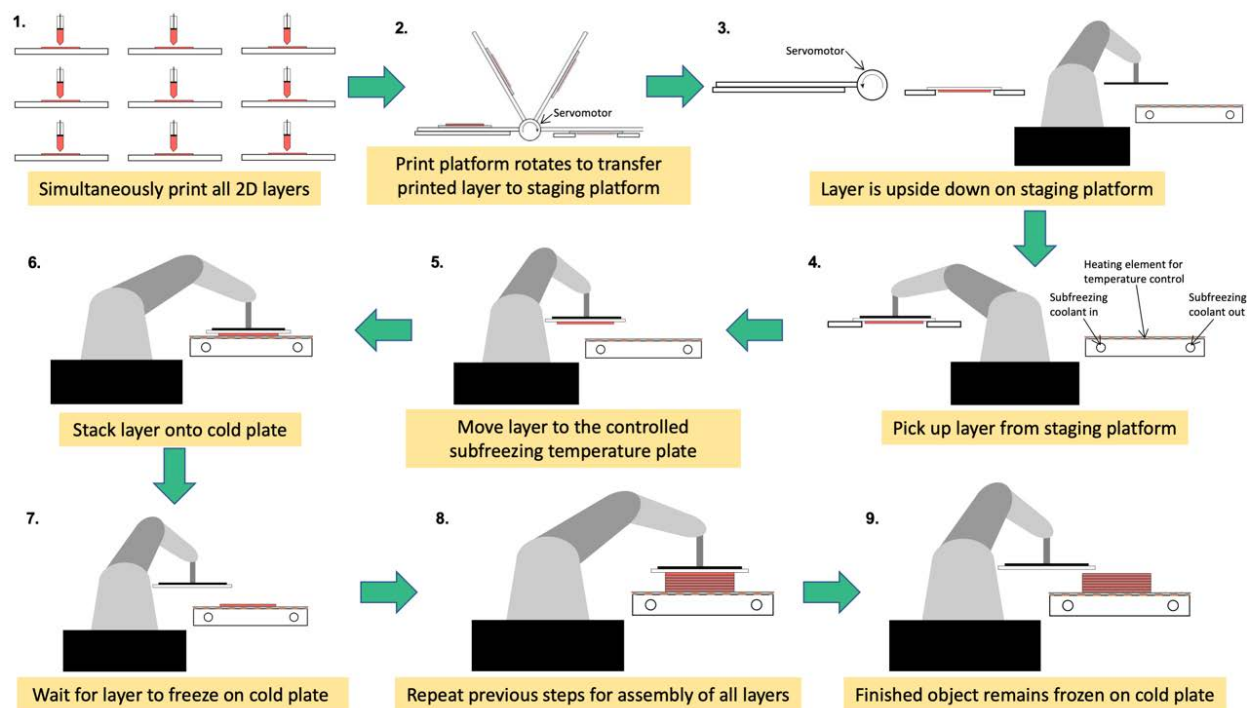


Figure 5.2: Modified outline of the MLCL process using a controlled temperature surface. First, the 2D layers are printed simultaneously. Next, the printed layers are flipped over and transferred to a staging platform where it is picked up by a robot and transferred to the assembly platform. The layer is stacked on a cold assembly surface or on a previously assembled layer. The layer freezes after deposition and another layer can be assembled. These steps are repeated until the entire object has been made.

5.3. Device description and implementation

5.3.1. Parallel MLCL device

To illustrate this process, a proof of concept device was developed. The device consists of a 2-D bioprinter to print individual 2-D layers onto a rigid hydrophilic substrate, a robotic arm to transfer the printed layer to the assembly surface, a motorized build platform to control the height of the assembly surface, and a cryogenic bath for the freezing of the printed layers.

For the 2-D bioprinter, a 3D printer (Flashforge USA, Los Angeles, CA) was modified as shown in Figure 5.3. The printer board was changed to a DuetWifi (Duet3D by Think3dPrint3d and Esher3d) for easier control of print settings and the extruder was redesigned to allow for printing of highly viscous biomaterials (Figure 5.3b). The printer extruder was changed to allow for the printing of liquids and gels from a syringe. In the new extruder the motor was mounted above the syringe and aligned with the syringe plunger in order to apply maximal axial force on the plunger with minimal moment as shown in Figure 5.3b. The motor was also placed on the moving carriage with its back face in direct contact with the syringe plunger so that its weight facilitates the pushing of the syringe. This design results in the lead screw extending upwards out of the extruder with the motor being driven in reverse to extrude from the syringe and forward driven to retract. The print platform was also reconfigured for easy interchange of 3" x 2" glass microscope slides which were used as the hydrophilic lithography plates (Figure 5.3c). The robotic

arm was a DOBOT Magician (Shenzhen Yuejiang Technology Co. Ltd, Shenzhen, PRC) equipped with a vacuum pump activated suction cup to pick up and release the lithography plates. A robot was used to ensure consistency in the placement of layers. The assembly surface was a glass slide placed on a liquid cooled aluminum cooling block with a resistive heating element and thermocouple in between connected to a temperature controller to regulate the temperature of the surface (Figure 5.2 panel 4).

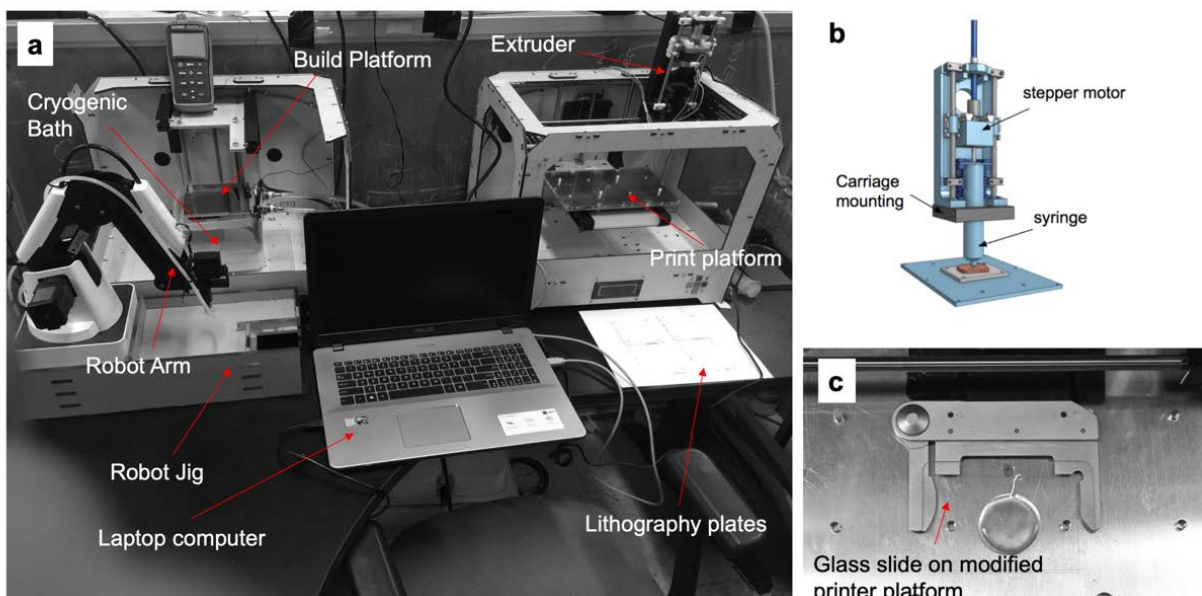


Figure 5.3: Device for the implementation of parallel additive manufacturing. **(a)** overall setup for experiment showing the 2-D printer for layer printing, robot arm for movement of layers, build platform, and cryogenic bath **(b)** CAD model of redesigned extrusion mechanism for the extrusion of high viscosity biomaterials **(c)** modified printing platform showing interchangeable lithography plate

5.3.2. Implementation

Overall setup:

The experiment setup consists of the modified 3D printer described above to print the 2-D layers, a DOBOT robotic arm on a jig, a liquid cooled cooling block with temperature control, and a computer to control the 2-D printer, the DOBOT, and the temperature of the cooling block, as shown in Figure 5.3. Freezing during assembly was accomplished using the second method (Figure 5.2) which uses a controlled temperature assembly platform rather than a cryogenic liquid bath. The assembly platform was an ATS CP-1002 Aluminum cold plate with 99% Isopropyl alcohol (Florida Laboratories) circulating cooling fluid at -55°C , cooled by a PolyScience Low temperature cooler Model IP-60 (PolyScience, Niles, IL). An Omega Platinum series CN32PT-220 temperature controller (Omega Engineering, Norwalk, CT) was used to regulate the temperature of the cold plate. Temperature of the assembly surface was measured using an Omega self-adhesive thermocouple type J (Omega Engineering, Norwalk, CT) placed between the glass slide and the cold plate and regulated by a 4" x 4" Omega Kapton Polyimide insulated flexible heater KHA-404 (Omega Engineering, Norwalk, CT) also placed between the slide and the top of the cold plate. The glass slide assembly surface was maintained at a set temperature of $-20^{\circ}\text{C} \pm 0.5^{\circ}\text{C}$.

Materials:

Alginate is a polysaccharide derived from seaweed. It is able to form a gel in the presence of certain divalent cations, such as calcium. As mentioned earlier, sodium alginate is one of the most commonly used materials in tissue engineering [132,146,147,149,150]. It is used with freezing and freeze drying for producing scaffolds [151]. Encapsulation of cells with sodium alginate also has a protective effect on frozen cells, e.g. hepatocytes [152]. Here, 4% w/v Sodium Alginate hydrogel was prepared by mixing the appropriate mass of sodium alginate (Molecular Weight: 222 g/mol) (Spectrum Chemical Mfg. Corp., Gardena, CA) in the appropriate volume of distilled water (Fisher Science Education, Nazareth, PA). The mixture is stirred on a magnetic stir plate until homogenous. A drop of blue food coloring (Safeway, Berkeley, CA) was added to a 40mL volume of the 4% sodium alginate mixture and stirred until the color was uniform. The printed sodium alginate hydrogels were crosslinked after printing by immersing in a 1% w/v CaCl_2 solution prepared by mixing the appropriate mass of CaCl_2 dihydrate (Fisher Scientific, Fair Lawn, NJ) in distilled water.

Experimental Procedure:

First, the shape to be printed is designed in a 3D CAD software (Onshape, Cambridge, MA) and then exported as a STL file to be sliced into elements in a 3D print slicing application, Ultimaker Cura (Ultimaker B.V., The Netherlands) which converts 3D models into instructions and x, y, z movements interpretable by the printer, known as G-code. The slicing software typically divides the model into multiple voxels and layers to be printed. Instead of slicing the overall model, each layer was modeled separately and sliced such that each layer could be printed independently. Mirror images of the layers to be printed should be used since the layers get inverted before stacking. For the experiments performed, the model was a 30mm diameter cylinder 5mm in height. A layer height of 500 μm was selected, so although the printer only moves in 2-D the actual print is about 500 μm thick. With these specifications, the software divides the model into ten layers. Since the splitting of the layers had to be done manually, a cylinder 30mm in diameter and 500 μm height was modeled and sliced instead, to be printed ten times. For the experiments, each layer was produced separately, independent of the assembly process. Since each layer of a cylinder was symmetric and identical there was no need for mirroring or designing different individual layers. But note that mirroring and unique layer design would be needed to generate complex geometry.

After the G-code has been generated for each layer, the alginate hydrogel bio-ink is drawn into the 5ml syringe equipped with a 1mm nozzle and the syringe is placed in the extruder. Then a layer of hydrogel is printed onto the lithography plate as shown in Figure 5.4a-b. The bulk of time saved in the parallel additive method is in printing of the 2-D layers as needed for the assembly process. The 2-D printing was done on a plasma cleaned glass microscope slide serving as the hydrophilic lithography plate. After each layer is printed the lithography plate with the printed layer is removed and placed in a staging area and another blank lithography plate is put in its place for a new layer to be printed onto it. The above step is repeated until 10 individual layers had been printed (Figure 5.4c shows four of them). It is important to note that, although in this experiment the layers are printed sequentially on one printer, in practice the printing of the individual layers is split between several printers to generate the layers simultaneously. As indicated earlier, the 2-D layers were printed independent of the 3D assembly in such a way as to provide the robot arm with a 2-D lithography plate at an optimal time.

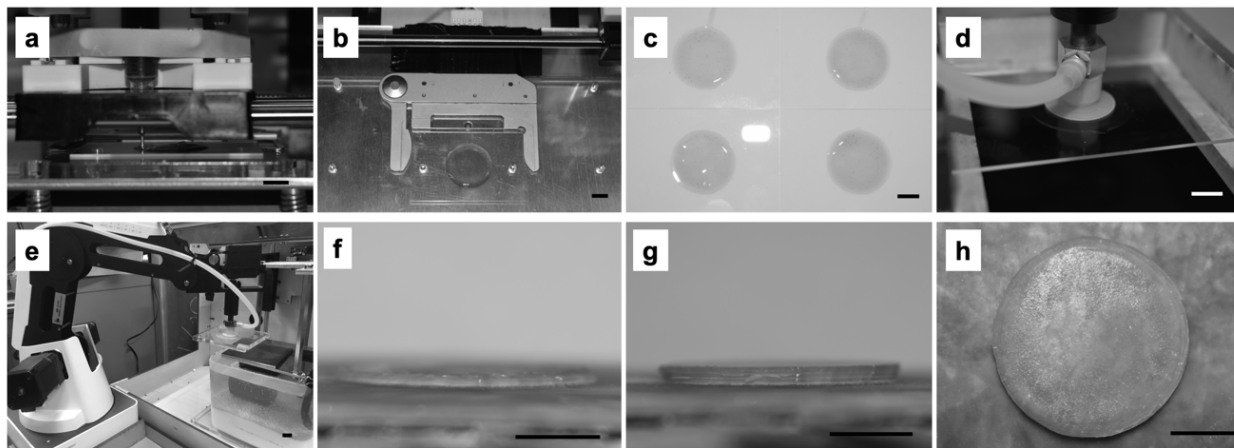


Figure 5.4: Step by step illustration of the parallel multilayer cryolithography process (a) printing of single layer (b) a single printed 2-D layer (c) several printed layers of the cylinder ready for assembly (d) single layer on robot platform about to be picked up for assembly (e) movement and assembly of layer on assembly platform by robot (f) first layer on assembly platform (g) after assembly of four layers on assembly platform (h) finished assembly of cylinder (1cm scale bar unless otherwise stated)

Next, the first plate is transferred onto the robot arm jig with the printed layer upside down (Figure 5.4d), ready for stacking. The plate was moved manually in this case, but in practice, would be moved automatically as described in Figures 5.1-5.2. The plate with the layer is then moved by the robot from the jig to the cooled assembly surface at a subfreezing temperature of $-20^{\circ}\text{C} \pm 0.5^{\circ}\text{C}$ (Figure 5.4e). The robot dwells there for about 2 seconds to allow the layer to freeze to the plate. Next, the robot lifts the lithography plate from the build platform leaving behind the layer which adheres to the build platform (Figure 5.4f). The plate is then moved back to the robot platform. The lithography plate on the jig is replaced, just in time, with the second plate with a 2-D layer of hydrogel upside down. There is a wait time of about 2 seconds before the robot begins moving again to ensure full freezing of the first layer to the assembly plate. For the proof of concept, both the wait times and dwell times were chosen based on trial and error, to obtain the optimal attachment, rather than by temperature, thermal conductivity, and layer thickness-based calculations.

This plate with the second layer is then moved by the robot from the jig to the build platform which automatically moves down the thickness of one layer ($500\mu\text{m}$) such that the new layer is directly on top of the previous. The robot jig repeatedly moves between the same two locations; the pickup point where it picks up and drops off the lithography plate, and the build point which does not change with layers. The height difference from layer to layer is offset by the lowering of the build platform. The robot, holding the second lithography plate, dwells on the first layer to allow the second layer to freeze to the first layer. Then the lithography plate is returned back to the robot jig by the robot arm leaving behind the second layer which is now attached to the first by freezing. At this point, the stacked layers are being held together by the freezing. Bonding by freezing is not new and has been described by many others, e.g. [32–34,75,153–155]. The novelty of this method is that instead of binding element by element, as in the previous methods, binding is layer by layer.

The above two steps are then repeated for all the other layers until the tenth (final) layer. Figures 5.4g-h show the side and top views, respectively, of the assembly after the deposition of the fourth layer. The wait time between layers and the dwell times for attachment differs from

layer to layer during the assembly process. These wait times and dwell times depend on the thermal conductivity of the material being used, the thickness of the layers, the temperature of the build surface, and the layer being printed. The parameters for optimal binding between layers were determined by several trials. In a case where the layers would be cooled using immersion in a cooling fluid rather than from the build surface, as described in [1], the wait times and dwell times would be more uniform as they would not depend on the layer being printed. In this example, the print surface was kept at a constant sub-freezing temperature, without immersion in the cooling fluid, as described in [32], because of the relative ease to use of the Tan et al method.

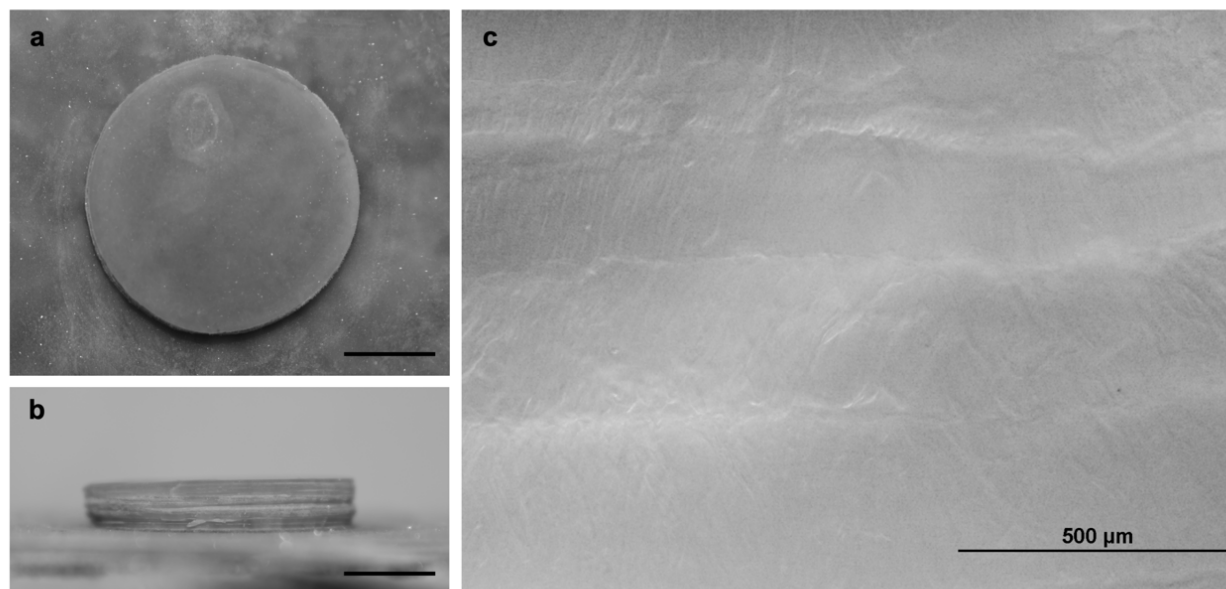


Figure 5.5: Example of a finished cylinder and its cross section showing continuity. **(a)** top view of fully assembled cylinder **(b)** side view of fully assembled cylinder consisting of 10 layers **(c)** cross section of cylinder showing continuity between the layers (1cm scale bar unless otherwise stated)

At the end, a total of ten assembled layers are stacked together and held together by freezing. Figures 5.5a and b show the completed print of a cylinder comprising 10 layers, each about 500 μ m thick. The finished frozen assembly was sprayed with 1% w/v CaCl₂ using an atomizer spray to initiate cross-linking. The whole assembly was then subsequently submerged in a 1% w/v CaCl₂ solution at 1°C and stored in a refrigerator at about 1°C. The crosslinked assembly was removed from the CaCl₂ solution after 24 hours and stored in the refrigerator until analysis of the cross-section.

To illustrate the myriad of complex shapes that could be done using this process, additional tests were similarly done for a hollow cylinder that could serve as a blood vessel and a rectangular macro porous grid scaffold. Figure 5.6a shows a single 2-D layer of the ring after printing. The layer is about 500 μ m and was assembled into the structure seen in Figures 5.6b-c. Figure 5.6d-e show single 2D layers of a grid structure printed out of sodium alginate before assembly.

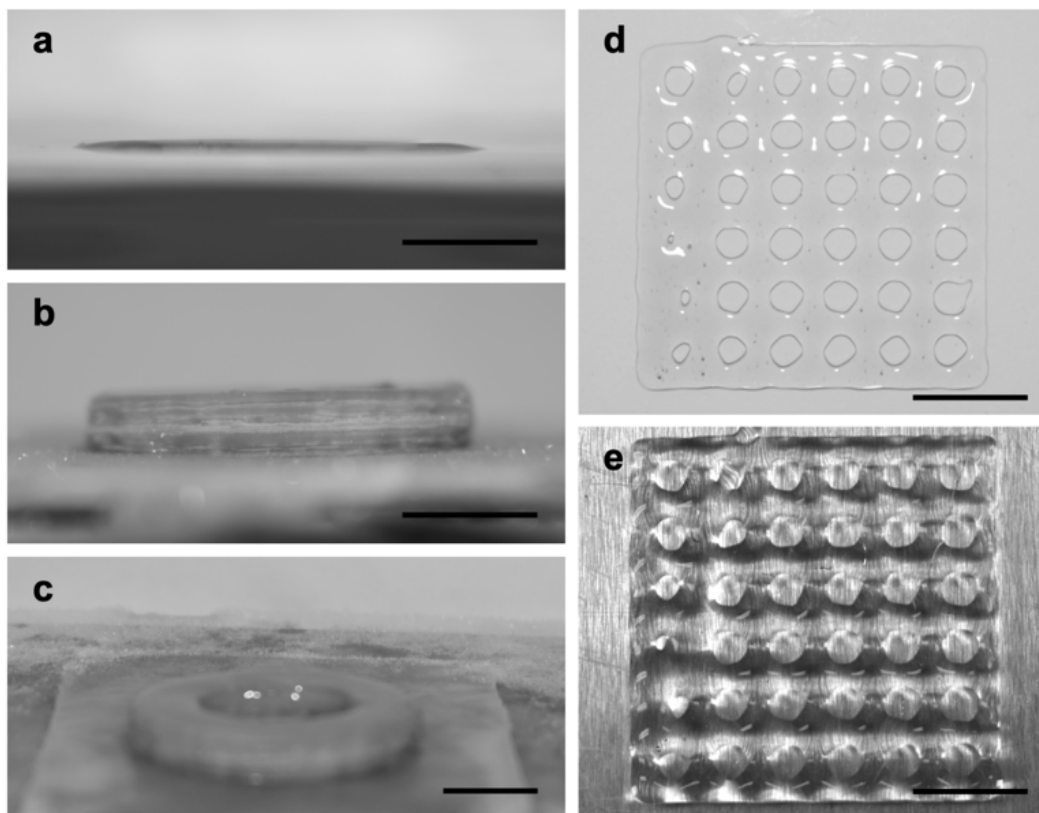


Figure 5.6: An example of more complex ring and grid structures showing the thin layers and the assembly process **(a)** single layer of the ring structure, about 500 μ m thick **(b)** side view of fully assembled ring structure after the 10th layer **(c)** full assembly of ring structure that could represent a blood vessel (30mm OD and 20mm ID) **(d)(e)** single layer of grid structure (1cm scale bar unless otherwise stated)

5.4. Discussion and conclusion

A proof of concept device capable of printing cohesive 3D hydrogel structures faster than conventional 3D printing and with potentially better control over microstructure was developed and implemented. The device was used to showcase the advantages of the MLCL technology which could allow for easy adaptability of bioprinting methods for mass manufacturing of tissue engineered products and scaffolds. With the device we demonstrated some MLCL advantages like the creation of complex geometries. Because the technique involves the creation of separate independent layers, there was some concern about the combination of those layers to form a contiguous structure. As such, we explored layer continuity and illustrate that continuity and interlayer bonding is achievable using MLCL. Figure 5.5c showed cohesion between layers in the cross section through an assembled cylinder. After the assembly had been crosslinked as described above, a thin axial section about 1mm thick was sliced from the cylinder and viewed under a microscope (Olympus IX7 inverted microscope). This microscope image is shown in Figure 5.5c. Qualitatively, the images show minimal difference between the cross-linking within a layer and the cross-linking between the layers. This ability to create a continuous structure from several individual layers makes this technique more favorable than regular 3D printing since similar cohesion is achieved in the printed sample but in less time [144]. Although at the microscale there

may be a difference between the intralayer bonding and the interlayer bonding in the alginate cylinder, MLCL does not inhibit the continuity of the printed sample at the macroscale.

In summary, MLCL provides a way to make biological matter in less time than in regular 3D bioprinting process, while incorporating preservation. Integrated with 3D cryoprinting and freezing modulated cross-linking MLCL could be advantageous for making large tissue structures rapidly. The proof of concept demonstrated here does not fully capture the possibilities of MLCL so future avenues for this work could be focused on optimization and characterization to maximize the advantages of the process.

Chapter 6

6. Conclusion

3D printed tissue geometries typically fabricated using 3D bioprinting have so far been difficult to realize at scales required for human organs, especially for soft tissue organs like the hearts and lungs. The reasons limiting this translation include; limitations to vascularization, which lead to premature death of cells within the construct; inadequate material properties, which affects the size and resolution of scaffolds; lengthy print times, which can lead to dehydration and tissue necrosis; and limited scalability for mass manufacturing. To address these limitations, we developed a new 3D bioprinting technique called 3D cryoprinting which employs phase change at subfreezing temperatures to provide structural stability in soft tissue scaffolds with inadequate mechanical properties and provide preservation for cell-laden tissue constructs. In this work, we explored 3D cryoprinting in detail with the goal of advancing this novel method of bioprinting so that it may be used for development of large soft tissue scaffolds and eventually whole organ systems. In doing so, we developed methods to control and optimize the cryoprinting process and preserve the geometry and mechanical structure of fabricated tissue constructs. We also studied the underlying effects of cryoprinting on mechanical properties and microstructure, and we devised a new method of translation to mass manufacturing. It is my opinion that techniques and models developed here could one day lead to the successful creation of these anatomically accurate geometric scaffolds for soft tissue and organs, and in addition to advances in vascularization and preservation, bring us closer to realizing the goal of developing artificial organs to augment the supply of organs for transplants.

6.1. Major findings

In a bid to resolve some of the emergent questions with 3D cryoprinting we developed various solutions and gained further understanding about 3D bioprinting at subfreezing temperature which we summarize below.

In chapter 2, we sought to resolve the issues of solidification in large objects and cell viability during printing. We explored the hypothesis that freezing during printing can be controlled and controlling freezing benefits the formation of soft 3D scaffolds and improves cell viability. In support of testing this hypothesis, we developed an advanced thermal phase change model for an extrusion-based printing process and used this model to design experiments and develop better techniques for the freezing of biological material being printed, as outlined in chapter 2. We use the model to understand how several printing parameters directly affect thermal history, solidification, and freezing rates. We also demonstrated some other benefits of the model, like its potential to be used for the optimization of cell survival during 3D printing and potential for use in an inverse manner to achieve predesignated outcomes. In designing experiments for verification of the model, we utilized new techniques for non-contact measurement of surface thermal history during cryoprinting. These real-time passive measurement techniques can be used

in conjunction with the inverse thermal phase change models to achieve localized control during 3D cryoprinting and other additive manufacturing process.

A product of the novel 3D cryoprinting approach is the resulting frozen scaffold structures, which then need to be matured in bioreactors at above freezing temperatures. This need for structural integrity at physiological temperatures (37°C) spawned a new thawing procedure for frozen hydrogel structures called freezing modulated cross-linking. Chapter 3 is therefore a natural continuation of the cryoprinting work from which the frozen scaffolds are developed. Here freezing modulated cross-linking is first described. As the name indicates, the technique combines chemical cross-linking with thermally controlled melting to produce optimum mechanical results by modulating cross-linking kinetics. Although loosely derived from previous work in the food industry and pharmaceutical industry, understanding of this relatively complex process for organ scale systems entailed the development of intricate forward and inverse models for the melting-diffusion-reaction and multispecies transport. With the aid of the mathematical model, we found the parameters required for optimal structural stability of thawed soft hydrogel constructs made using alginate. These findings could prove useful in the design of protocols for the thawing of the frozen 3D cryoprinted scaffolds made at subfreezing temperature for the purpose of organ and tissue development.

At this point, based on the experimental observations, we additionally posited that the combination of freezing with cross-linking could yield distinct and varying microstructures. This hypothesis was investigated in chapter 4 with the development of a directional solidification system to controllably freeze biological materials. Several sequences of cross-linking and freezing were studied to determine the most appropriate window for cross-linking during the freezing and thawing process of a scaffold generated at subfreezing temperatures. The findings in chapter 4 justified the need for doing cross-linking during thawing; a characteristic of the coupled 3D cryoprinting and freezing modulated cross-linking process. The results showed a significant benefit to controlling microstructure when the cross-linking is done after freezing, as well as possible benefits to mechanical properties and diffusive transport properties. This potential for control could be integrated nicely with the previous model developed for freezing based 3D cryoprinting in chapter 2. The resulting microstructure from the printing and thawing sequence developed prior are beneficial to even general tissue engineering applications. The development of this study using the directional device also led to a generalized analysis of horizontal directional devices used for aqueous biological matter, and significant findings about the accuracy and representativeness of previous 1-D directional device models.

Lastly, in chapter 5, an application-oriented technique was developed with the intent of translating the principles learned while developing 3D cryoprinting, to mass manufacturing. As previously stated, prolonged 3D printing times have a negative impact on the ability to construct large tissue using 3D bioprinting and as a result essentially hamper the ability to develop full scale human organs. Therefore, in order to improve speed and efficiency we developed a new technique which relies on the parallelization of the 3D printing process and is made possible with the use of thermally induced freezing. Other practical concerns addressed during the development of 3D cryolithography and the working principle were outlined in chapter 5. This new method called parallel multilayer cryolithography, shown in the proof of concept to result in continuous structures hardly distinguishable from regular 3D printing processes, has the potential to revolutionize the additive manufacturing industry beyond just 3D bioprinting.

In summary this work showed that 3D cryoprinting in conjunction with freezing modulated cross-linking provide a promising alternative way to make soft tissue scaffolds that bring us closer

to solving the organ supply crisis. And when needing to scale to mass manufacturing, parallel cryolithography could also be applied. Although we initially set out to tackle issues related to developing geometry of tissue scaffolds, some of the other findings in this work incorporate solutions to vascularization and cryopreservation, two important aspects of tissue engineering needed to develop fully functional organs for transplant.

6.2. Future perspective

This work also gave rise to several developments which could potentially be applied to the following future areas of research:

First, is for the optimization of additive manufacturing processes. Currently, most additive manufacturing protocols are developed ad-hoc and by trial and error with minimal regard for how the process parameters influence the properties of the resulting object as long as the print is successful. This is sufficient for rapid prototyping purposes and for making non-engineered components. However, to increase the adoption of additive manufacturing for development of specialized components reliably and with predictable properties it is important to better understand the effect of process parameters. As a result, several researchers are now working on digital analogues and mathematical models to predict several properties in 3D printed parts. So far, a lot of those efforts have been focused on the laser sintering and laser melting field, with little work done in other 3D printing modalities. In the near term we would continue the development of the 3D printing thermal models and further develop 3D inverse models for generalized additive manufacturing processes. Inverse models based on the thermal phase change models developed from this work are agnostic to the material being used for printing as long as there is a temperature change during the printing process, which makes them applicable to a wide range of additive manufacturing processes. By developing an inverse model for extrusion based additive manufacturing and other AM processes, we could control the thermal history of additively manufactured parts and in turn influence microstructure, stress and several other thermally modulated parameters. With further developments of this model, other constitutive relations can be integrated to expand to other applications. One immediate application could be controlling the properties of metal objects fabricated using a newly emerging approach like metal fused filament fabrication [156].

Secondly, in continuation of this work, fully bioactive scaffolds can be constructed and matured to realize bioprinting of full-scale organs. In this dissertation, we demonstrate the feasibility of 3D cryoprinting using proof of concept devices and models of biological matter, but stop short of illustrating these processes in a fully functioning biological scaffold. Future work could focus on performing cell survival studies and developing inverse models to design a protocol for optimizing survivability of cells in bioactive scaffolds fabricated by bioprinting at subfreezing temperatures. Successful demonstration of improved cell survival would propel this approach to the forefront of tissue engineering considerations and could lead to the development of fully functioning tissue engineered organs.

Lastly, the control of healthy or cancerous cells using thermal methods could be beneficial for cancer therapy as well as other cellular therapies. The findings from this work suggest a potential controllability of cell mechano-transduction using freezing induced regulation or simply thermally controlled mediation – control of freezing and temperature gradients can be used to influence mechano-transduction. It is well established that mechanical properties of the ECM such as porosity, strength, and modulus, modulate the behavior of cells. By harnessing the thermal

dependence of those material properties, one can modify ECM properties of native tissue or artificial engineered tissue and selectively influence cell motility, differentiation, and survival. If successful, this could provide new therapies for eradicating of cancer cells or other cell-based therapies.

6.3. Closing statement

In closing, we set out to investigate a new approach to 3D bioprinting, 3D cryoprinting, that had not been previously examined. With the prospect that this approach could bridge the gaps in 3D bioprinting technology and rejuvenate the field of tissue engineering by introducing new ideas for overcoming some of the persistent 3D bioprinting limitations. Over the course of this work we advanced this technique and showed promising results that illustrate the benefits of 3D cryoprinting to the field of bioprinting and tissue engineering. This rapidly evolving field has seen immense developments in techniques and materials over the past 20 years and it is my hope 3D cryoprinting plays a crucial role in the continuous advancements in this field. Further developments and testing by researchers in the thermal science field and the manufacturing field could one day see this exciting method used to fabricate full scale human organs for transplant patients.

7. Bibliography

- [1] Adamkiewicz, M., and Rubinsky, B., 2015, “Cryogenic 3D Printing for Tissue Engineering,” *Cryobiology*, **71**(3), pp. 518–521.
- [2] 2020, “Organ Procurement and Transplantation Network,” Definitions.
- [3] Giwa, S., Lewis, J. K., Alvarez, L., Langer, R., Roth, A. E., Church, G. M., Markmann, J. F., Sachs, D. H., Chandraker, A., Wertheim, J. A., Rothblatt, M., Boyden, E. S., Eidbo, E., Lee, W. P. A., Pomahac, B., Brandacher, G., Weinstock, D. M., Elliott, G., Nelson, D., Acker, J. P., Uygun, K., Schmalz, B., Weegman, B. P., Tocchio, A., Fahy, G. M., Storey, K. B., Rubinsky, B., Bischof, J., Elliott, J. A. W., Woodruff, T. K., Morris, G. J., Demirci, U., Brockbank, K. G. M., Woods, E. J., Ben, R. N., Baust, J. G., Gao, D., Fuller, B., Rabin, Y., Kravitz, D. C., Taylor, M. J., and Toner, M., 2017, “The Promise of Organ and Tissue Preservation to Transform Medicine,” *Nat. Biotechnol.*, **35**(6), pp. 530–542.
- [4] Nerem, R. M., and Sambanis, A., 1995, “Tissue Engineering: From Biology to Biological Substitutes,” *Tissue Eng.*, **1**(1), pp. 3–13.
- [5] Khademhosseini, A., and Langer, R., 2016, “A Decade of Progress in Tissue Engineering,” *Nat. Protoc.*, **11**(10), pp. 1775–1781.
- [6] Langer, R., and Vacanti, J., 2016, “Advances in Tissue Engineering,” *Journal of Pediatric Surgery*, pp. 8–12.
- [7] Khademhosseini, A., Vacanti, J. P., and Langer, R., 2009, “Progress in Tissue,” *Sci. Am.*, **300**(5), pp. 64–71.
- [8] Langer, R., and Vacanti, J. P., 1993, “Tissue Engineering,” *Science (80-.)*, **260**(5110), pp. 920–926.
- [9] Caplin, J. D., Granados, N. G., James, M. R., Montazami, R., and Hashemi, N., 2015, “Microfluidic Organ-on-a-Chip Technology for Advancement of Drug Development and Toxicology,” *Adv. Healthc. Mater.*, **4**(10), pp. 1426–1450.
- [10] Ma, X., Liu, J., Zhu, W., Tang, M., Lawrence, N., Yu, C., Gou, M., and Chen, S., 2018, “3D Bioprinting of Functional Tissue Models for Personalized Drug Screening and in Vitro Disease Modeling,” *Adv. Drug Deliv. Rev.*, **132**, pp. 235–251.
- [11] Busbee, T. A., Lewis, J. A., Kolesky, D. B., Truby, R. L., Gladman, A. S., and Homan, K. A., 2014, “3D Bioprinting of Vascularized, Heterogeneous Cell-Laden Tissue Constructs,” *Adv. Mater.*, **26**(19), pp. 3124–3130.
- [12] Heinrich, M. A., Bansal, R., Lammers, T., Zhang, Y. S., Michel Schiffelers, R., and Prakash, J., 2019, “3D-Bioprinted Mini-Brain: A Glioblastoma Model to Study Cellular Interactions and Therapeutics,” *Adv. Mater.*, **31**(14).
- [13] Noor, N., Shapira, A., Edri, R., Gal, I., Wertheim, L., and Dvir, T., 2019, “3D Printing of Personalized Thick and Perfusable Cardiac Patches and Hearts,” *Adv. Sci.*
- [14] Wang, Z., Lee, S. J., Cheng, H. J., Yoo, J. J., and Atala, A., 2018, “3D Bioprinted Functional and Contractile Cardiac Tissue Constructs,” *Acta Biomater.*, **70**, pp. 48–56.
- [15] Ozbolat, I. T., and Yu, Y., 2013, “Bioprinting toward Organ Fabrication: Challenges and Future Trends,” *IEEE Trans. Biomed. Eng.*, **60**(3), pp. 691–699.
- [16] Murphy, S. V., and Atala, A., 2014, “3D Bioprinting of Tissues and Organs,” *Nat. Biotechnol.*, **32**(8), pp. 773–785.
- [17] Francoise, M., Karoly, J., Chirag, K., Benjamin, S., Scott, D., Bradley, H., Stephen, C., and Forgacs, G., 2012, “Toward Engineering Functional Organ Modules by Additive Manufacturing,” *Biofabrication*, **4**, p. 022001.

- [18] Hospodiuk, M., Dey, M., Sosnoski, D., and Ozbolat, I. T., 2017, “The Bioink: A Comprehensive Review on Bioprintable Materials,” *Biotechnol. Adv.*, **35**(2), pp. 217–239.
- [19] Vijayavenkataraman, S., Yan, W. C., Lu, W. F., Wang, C. H., and Fuh, J. Y. H., 2018, “3D Bioprinting of Tissues and Organs for Regenerative Medicine,” *Adv. Drug Deliv. Rev.*, **132**, pp. 296–332.
- [20] Skardal, A., and Atala, A., 2015, “Biomaterials for Integration with 3-D Bioprinting,” *Ann. Biomed. Eng.*, **43**(3), pp. 730–746.
- [21] Noh, S., Myung, N., Park, M., Kim, S., Zhang, S.-U., and Kang, H.-W., 2017, “3D Bioprinting for Tissue Engineering,” *Clinical Regenerative Medicine in Urology*, pp. 105–123.
- [22] Lee, S. J., Kengla, C., Yoo, J. J., Atala, A., Ko, I. K., and Kang, H.-W., 2016, “A 3D Bioprinting System to Produce Human-Scale Tissue Constructs with Structural Integrity,” *Nat. Biotechnol.*, **34**(3), pp. 312–319.
- [23] Bishop, E. S., Mostafa, S., Pakvasa, M., Luu, H. H., Lee, M. J., Wolf, J. M., Ameer, G. A., He, T. C., and Reid, R. R., 2017, “3-D Bioprinting Technologies in Tissue Engineering and Regenerative Medicine: Current and Future Trends,” *Genes Dis.*, **4**(4), pp. 185–195.
- [24] Grigoryan, B., Paulsen, S. J., Corbett, D. C., Sazer, D. W., Fortin, C. L., Zaita, A. J., Greenfield, P. T., Calafat, N. J., Gounley, J. P., Ta, A. H., Johansson, F., Randles, A., Rosenkrantz, J. E., Louis-Rosenberg, J. D., Galie, P. A., Stevens, K. R., and Miller, J. S., 2019, “Multivascular Networks and Functional Intravascular Topologies within Biocompatible Hydrogels,” *Science*, **364**(6439), pp. 458–464.
- [25] Jiang, T., Munguia-Lopez, J. G., Flores-Torres, S., Kort-Mascort, J., and Kinsella, J. M., 2019, “Extrusion Bioprinting of Soft Materials: An Emerging Technique for Biological Model Fabrication,” *Appl. Phys. Rev.*, **6**(1).
- [26] Aljohani, W., Ullah, M. W., Zhang, X., and Yang, G., 2018, “Bioprinting and Its Applications in Tissue Engineering and Regenerative Medicine,” *Int. J. Biol. Macromol.*, **107**(PartA), pp. 261–275.
- [27] Mandrycky, C., Wang, Z., Kim, K., and Kim, D. H., 2016, “3D Bioprinting for Engineering Complex Tissues,” *Biotechnol. Adv.*, **34**(4), pp. 422–434.
- [28] An, J., Teoh, J. E. M., Suntornond, R., and Chua, C. K., 2015, “Design and 3D Printing of Scaffolds and Tissues,” *Engineering*, **1**(2), pp. 261–268.
- [29] Do, A. V., Khorsand, B., Geary, S. M., and Salem, A. K., 2015, “3D Printing of Scaffolds for Tissue Regeneration Applications,” *Adv. Healthc. Mater.*, **4**(12), pp. 1742–1762.
- [30] Hollister, S. J., 2005, “Porous Scaffold Design for Tissue Engineering,” *Nat. Mater.*, **4**(7), pp. 518–524.
- [31] Kang, H. W., Kengla, C., Lee, S. J., Yoo, J. J., and Atala, A., 2014, “3-D Organ Printing Technologies for Tissue Engineering Applications,” *Rapid Prototyping of Biomaterials: Principles and Applications*, pp. 236–253.
- [32] Tan, Z., Parisi, C., Di Silvio, L., Dini, D., and Forte, A. E., 2017, “Cryogenic 3D Printing of Super Soft Hydrogels,” *Sci. Rep.*, **7**(1).
- [33] Pham, C. B., Leong, K. F., Lim, T. C., and Chian, K. S., 2008, “Rapid Freeze Prototyping Technique in Bio-Plotters for Tissue Scaffold Fabrication,” *Rapid Prototyp. J.*, **14**(4), pp. 246–253.
- [34] Kim, G., Ahn, S., Yoon, H., Kim, Y., and Chun, W., 2009, “A Cryogenic Direct-Plotting System for Fabrication of 3D Collagen Scaffolds for Tissue Engineering,” *J. Mater. Chem.*, **19**(46), pp. 8817–8823.

- [35] Wang, C., Zhao, Q., and Wang, M., 2017, "Cryogenic 3D Printing for Producing Hierarchical Porous and RhBMP-2-Loaded Ca-P/PLLA Nanocomposite Scaffolds for Bone Tissue Engineering," *Biofabrication*, **9**(2), p. 025031.
- [36] Cohen, D. L., Malone, E., Lipson, H., and Bonassar, L. J., 2006, "Direct Freeform Fabrication of Seeded Hydrogels in Arbitrary Geometries," *Tissue Eng.*, **12**(5), pp. 1325–1335.
- [37] Lee, V. K., and Dai, G., 2017, "Printing of Three-Dimensional Tissue Analogs for Regenerative Medicine," *Ann. Biomed. Eng.*, **45**(1), pp. 115–131.
- [38] Gudapati, H., Dey, M., and Ozbolat, I., 2016, "A Comprehensive Review on Droplet-Based Bioprinting: Past, Present and Future," *Biomaterials*.
- [39] Phillippi, J. A., Miller, E., Weiss, L., Huard, J., Waggoner, A., and Campbell, P., 2008, "Microenvironments Engineered by Inkjet Bioprinting Spatially Direct Adult Stem Cells Toward Muscle- and Bone-Like Subpopulations," *Stem Cells*.
- [40] Xu, T., Zhao, W., Zhu, J. M., Albanna, M. Z., Yoo, J. J., and Atala, A., 2013, "Complex Heterogeneous Tissue Constructs Containing Multiple Cell Types Prepared by Inkjet Printing Technology," *Biomaterials*.
- [41] Binder, K. W., Allen, A. J., Yoo, J. J., and Atala, A., 2011, "Drop-on-Demand Inkjet Bioprinting: A Primer," *Gene Ther. Regul.*
- [42] Moroni, L., Boland, T., Burdick, J. A., De Maria, C., Derby, B., Forgacs, G., Groll, J., Li, Q., Malda, J., Mironov, V. A., Mota, C., Nakamura, M., Shu, W., Takeuchi, S., Woodfield, T. B. F., Xu, T., Yoo, J. J., and Vozzi, G., 2018, "Biofabrication: A Guide to Technology and Terminology," *Trends Biotechnol.*, **36**(4), pp. 384–402.
- [43] Gao, G., Schilling, A. F., Hubbell, K., Yonezawa, T., Truong, D., Hong, Y., Dai, G., and Cui, X., 2015, "Improved Properties of Bone and Cartilage Tissue from 3D Inkjet-Bioprinted Human Mesenchymal Stem Cells by Simultaneous Deposition and Photocrosslinking in PEG-GelMA," *Biotechnol. Lett.*
- [44] Compaan, A. M., Christensen, K., and Huang, Y., 2017, "Inkjet Bioprinting of 3D Silk Fibroin Cellular Constructs Using Sacrificial Alginate," *ACS Biomater. Sci. Eng.*
- [45] Taboas, J. M., Maddox, R. D., Krebsbach, P. H., and Hollister, S. J., 2003, "Indirect Solid Free Form Fabrication of Local and Global Porous, Biomimetic and Composite 3D Polymer-Ceramic Scaffolds," *Biomaterials*, **24**(1), pp. 181–194.
- [46] Temple, J. P., Hutton, D. L., Hung, B. P., Huri, P. Y., Cook, C. A., Kondragunta, R., Jia, X., and Grayson, W. L., 2014, "Engineering Anatomically Shaped Vascularized Bone Grafts with HASCs and 3D-Printed PCL Scaffolds," *J. Biomed. Mater. Res. - Part A*, **102**(12), pp. 4317–4325.
- [47] Ozbolat, I. T., and Hospodiuk, M., 2016, "Current Advances and Future Perspectives in Extrusion-Based Bioprinting," *Biomaterials*.
- [48] Wu, Z., Su, X., Xu, Y., Kong, B., Sun, W., and Mi, S., 2016, "Bioprinting Three-Dimensional Cell-Laden Tissue Constructs with Controllable Degradation," *Sci. Rep.*, **6**.
- [49] Yu, Y., and Ozbolat, I. T., 2014, "Tissue Strands as 'Bioink' for Scale-up Organ Printing," *2014 36th Annual International Conference of the IEEE Engineering in Medicine and Biology Society, EMBC 2014*.
- [50] Kesti, M., Eberhardt, C., Pagliccia, G., Kenkel, D., Grande, D., Boss, A., and Zenobi-Wong, M., 2015, "Bioprinting Complex Cartilaginous Structures with Clinically Compliant Biomaterials," *Adv. Funct. Mater.*, **25**(48), pp. 7406–7417.
- [51] Billiet, T., Gevaert, E., De Schryver, T., Cornelissen, M., and Dubruel, P., 2014, "The 3D

- Printing of Gelatin Methacrylamide Cell-Laden Tissue-Engineered Constructs with High Cell Viability,” *Biomaterials*.
- [52] Suntornnond, R., An, J., and Chua, C. K., 2017, “Bioprinting of Thermoresponsive Hydrogels for Next Generation Tissue Engineering: A Review,” *Macromol. Mater. Eng.*, **302**(1).
- [53] Kang, H. W., Lee, S. J., Ko, I. K., Kengla, C., Yoo, J. J., and Atala, A., 2016, “A 3D Bioprinting System to Produce Human-Scale Tissue Constructs with Structural Integrity,” *Nat. Biotechnol.*, **34**(3), pp. 312–319.
- [54] Daly, A. C., Cunniffe, G. M., Sathy, B. N., Jeon, O., Alsberg, E., and Kelly, D. J., 2016, “3D Bioprinting of Developmentally Inspired Templates for Whole Bone Organ Engineering,” *Adv. Healthc. Mater.*, **5**(18), pp. 2353–2362.
- [55] Pati, F., Jang, J., Ha, D. H., Won Kim, S., Rhie, J. W., Shim, J. H., Kim, D. H., and Cho, D. W., 2014, “Printing Three-Dimensional Tissue Analogues with Decellularized Extracellular Matrix Bioink,” *Nat. Commun.*, **5**.
- [56] Hinton, T. J., Jallerat, Q., Palchesko, R. N., Park, J. H., Grodzicki, M. S., Shue, H.-J., Ramadan, M. H., Hudson, A. R., and Feinberg, A. W., 2015, “Three-Dimensional Printing of Complex Biological Structures by Freeform Reversible Embedding of Suspended Hydrogels,” *Sci. Adv.*, **1**(9), p. e1500758.
- [57] Hinton, T. J., Hudson, A., Pusch, K., Lee, A., and Feinberg, A. W., 2016, “3D Printing PDMS Elastomer in a Hydrophilic Support Bath via Freeform Reversible Embedding,” *ACS Biomater. Sci. Eng.*, **2**(10), pp. 1781–1786.
- [58] Lee, A., Hudson, A. R., Shiwardski, D. J., Tashman, J. W., Hinton, T. J., Yerneni, S., Bliley, J. M., Campbell, P. G., and Feinberg, A. W., 2019, “3D Bioprinting of Collagen to Rebuild Components of the Human Heart,” *Science* (80-).
- [59] Jeon, O., Lee, Y. B., Hinton, T. J., Feinberg, A. W., and Alsberg, E., 2019, “Cryopreserved Cell-Laden Alginate Microgel Bioink for 3D Bioprinting of Living Tissues,” *Mater. Today Chem.*
- [60] Guillemot, F., Souquet, A., Catros, S., Guillotin, B., Lopez, J., Faucon, M., Pippenger, B., Bareille, R., Rémy, M., Bellance, S., Chabassier, P., Fricain, J. C., and Amédée, J., 2010, “High-Throughput Laser Printing of Cells and Biomaterials for Tissue Engineering,” *Acta Biomaterialia*.
- [61] Guillotin, B., Souquet, A., Catros, S., Duocastella, M., Pippenger, B., Bellance, S., Bareille, R., Rémy, M., Bordenave, L., Amédée, J., and Guillemot, F., 2010, “Laser Assisted Bioprinting of Engineered Tissue with High Cell Density and Microscale Organization,” *Biomaterials*.
- [62] Michael, S., Sorg, H., Peck, C. T., Koch, L., Deiwick, A., Chichkov, B., Vogt, P. M., and Reimers, K., 2013, “Tissue Engineered Skin Substitutes Created by Laser-Assisted Bioprinting Form Skin-Like Structures in the Dorsal Skin Fold Chamber in Mice,” *PLoS One*.
- [63] Derakhshanfar, S., Mbeleck, R., Xu, K., Zhang, X., Zhong, W., and Xing, M., 2018, “3D Bioprinting for Biomedical Devices and Tissue Engineering: A Review of Recent Trends and Advances,” *Bioact. Mater.*, **3**(2), pp. 144–156.
- [64] Hockaday, L. A., Kang, K. H., Colangelo, N. W., Cheung, P. Y. C., Duan, B., Malone, E., Wu, J., Girardi, L. N., Bonassar, L. J., Lipson, H., Chu, C. C., and Butcher, J. T., 2012, “Rapid 3D Printing of Anatomically Accurate and Mechanically Heterogeneous Aortic Valve Hydrogel Scaffolds,” *Biofabrication*, **4**(3).

- [65] Wang, Z., Abdulla, R., Parker, B., Samanipour, R., Ghosh, S., and Kim, K., 2015, “A Simple and High-Resolution Stereolithography-Based 3D Bioprinting System Using Visible Light Crosslinkable Bioinks,” *Biofabrication*, **7**(4).
- [66] Kelly, B. E., Bhattacharya, I., Heidari, H., Shusteff, M., Spadaccini, C. M., and Taylor, H. K., 2019, “Volumetric Additive Manufacturing via Tomographic Reconstruction,” *Science* (80-).
- [67] Nishiyama, Y., Nakamura, M., Henmi, C., Yamaguchi, K., Mochizuki, S., Nakagawa, H., and Takiura, K., 2009, “Development of a Three-Dimensional Bioprinter: Construction of Cell Supporting Structures Using Hydrogel and State-Of-The-Art Inkjet Technology,” *J. Biomech. Eng.*, **131**(3), p. 035001.
- [68] Barnes, J. M., Przybyla, L., and Weaver, V. M., 2017, “Tissue Mechanics Regulate Brain Development, Homeostasis and Disease,” *J. Cell Sci.*
- [69] Tabriz, A. G., Hermida, M. A., Leslie, N. R., and Shu, W., 2015, “Three-Dimensional Bioprinting of Complex Cell Laden Alginate Hydrogel Structures,” *Biofabrication*, **7**(4).
- [70] Growney Kalaf, E. A., Flores, R., Bledsoe, J. G., and Sell, S. A., 2016, “Characterization of Slow-Gelling Alginate Hydrogels for Intervertebral Disc Tissue-Engineering Applications,” *Mater. Sci. Eng. C*, **63**, pp. 198–210.
- [71] Kuo, C. K., and Ma, P. X., 2001, “Ionically Crosslinked Alginate Hydrogels as Scaffolds for Tissue Engineering: Part 1. Structure, Gelation Rate and Mechanical Properties,” *Biomaterials*, **22**(6), pp. 511–521.
- [72] Choi, D. J., Park, S. J., Gu, B. K., Kim, Y. J., Chung, S., and Kim, C. H., 2018, “Effect of the Pore Size in a 3D Bioprinted Gelatin Scaffold on Fibroblast Proliferation,” *J. Ind. Eng. Chem.*, **67**, pp. 388–395.
- [73] Ehrlich, L. E., Fahy, G. M., Wowk, B. G., Malen, J. A., and Rabin, Y., 2017, “Thermal Analyses of a Human Kidney and a Rabbit Kidney During Cryopreservation by Vitrification,” *J. Biomech. Eng.*, **140**(1), p. 011005.
- [74] Fahy, G. M., Wowk, B., Wu, J., Phan, J., Rasch, C., Chang, A., and Zendejas, E., 2004, “Cryopreservation of Organs by Vitrification: Perspectives and Recent Advances,” *Cryobiology*, pp. 157–178.
- [75] Liao, C.-Y., Wu, W.-J., Hsieh, C.-T., Tseng, C.-S., Dai, N.-T., and Hsu, S., 2016, “Design and Development of a Novel Frozen-Form Additive Manufacturing System for Tissue Engineering Applications,” *3D Print. Addit. Manuf.*, **3**(4), pp. 216–225.
- [76] Ukpai, G., and Rubinsky, B., 2020, “A Three-Dimensional Model for Analysis and Control of Phase Change Phenomena during 3D Printing of Biological Tissue,” *Bioprinting*, **18**.
- [77] Ukpai, G., and Rubinsky, B., 2020, “A Mathematical Analysis of Directional Solidification of Aqueous Solutions,” *J. Heat Transfer*.
- [78] Holweg, M., 2015, “The Limits of 3d Printing,” *Harv. Bus. Rev.*, p. 5.
- [79] G. Putnika, A. Slugab, H. ElMaraghyc, R. Tetid, Y. Korene, T. Toliolf, B. H., 2013, “Scalability in Manufacturing Systems Design and Operation: State-of-the-Art and Future Developments Roadmap,” *CIRP Ann. - Manuf. Technol.*, **62**(2), pp. 751–774.
- [80] Ukpai, G., Sahyoun, J., Stuart, R., Wang, S., Xiao, Z., and Rubinsky, B., 2019, “A Parallel Multiple Layer Cryolithography Device for the Manufacture of Biological Material for Tissue Engineering,” *J. Med. Devices, Trans. ASME*, **13**(3).
- [81] Naghieh, S., Karamooz-Ravari, M. R., Sarker, M. D., Karki, E., and Chen, X., 2018, “Influence of Crosslinking on the Mechanical Behavior of 3D Printed Alginate Scaffolds:

- Experimental and Numerical Approaches,” *J. Mech. Behav. Biomed. Mater.*, **80**, pp. 111–118.
- [82] Lee, J. M., and Yeong, W. Y., 2016, “Design and Printing Strategies in 3D Bioprinting of Cell-Hydrogels: A Review,” *Adv. Healthc. Mater.*, **5**(22), pp. 2856–2865.
- [83] Liao, C.-Y., Wu, W.-J., Hsieh, C.-T., Tseng, C.-S., Dai, N.-T., and Hsu, S., 2016, “Design and Development of a Novel Frozen-Form Additive Manufacturing System for Tissue Engineering Applications,” *3D Print. Addit. Manuf.*, **3**(4), pp. 216–225.
- [84] Kim, G., Ahn, S., Yoon, H., Kim, Y., and Chun, W., 2009, “A Cryogenic Direct-Plotting System for Fabrication of 3D Collagen Scaffolds for Tissue Engineering,” *J. Mater. Chem.*, **19**(46), pp. 8817–8823.
- [85] Akiyama, Y., Shinose, M., Watanabe, H., Yamada, S., and Kanda, Y., 2019, “Cryoprotectant-Free Cryopreservation of Mammalian Cells by Superflash Freezing,” *Proc. Natl. Acad. Sci.*, **116**(16), pp. 7738–7743.
- [86] Mazur, P., 1996, “Chapter 10 Principles of Medical Cryobiology: The Freezing of Living Cells, Tissues, and Organs,” *Princ. Med. Biol.*
- [87] Mazur, P., 1984, “Freezing of Living Cells: Mechanisms and Implications,” *Am. J. Physiol.*, **247**(3 Pt 1), pp. C125–C142.
- [88] Mazur, P., 1970, “Cryobiology: The Freezing of Biological Systems,” *Science (80-)*, **168**(3934), pp. 939–949.
- [89] Hubel, A., and Skubitz, A. P. N., 2017, “Principles of Cryopreservation,” *Biobanking of Human Biospecimens: Principles and Practice*, pp. 1–21.
- [90] Jiang, Z., Zhao, G., Hossain, S. M. C., and Gao, D., 2017, “Coupled Experimental-Modeling Analyses of Heat Transfer in Ex-Vivo VS55-Perfused Porcine Hepatic Tissue Being Plunged in Liquid Nitrogen for Vitreous Cryopreservation,” *Int. J. Heat Mass Transf.*, **106**, pp. 970–979.
- [91] Bellehumeur, C., Li, L., Sun, Q., and Gu, P., 2004, “Modeling of Bond Formation between Polymer Filaments in the Fused Deposition Modeling Process,” *J. Manuf. Process.*, **6**(2), pp. 170–178.
- [92] Zhang, Y., and Chou, K., 2008, “A Parametric Study of Part Distortions in Fused Deposition Modelling Using Three-Dimensional Finite Element Analysis,” *Proc. Inst. Mech. Eng. Part B J. Eng. Manuf.*, **222**(8), pp. 959–967.
- [93] Zhang, Y., and Chou, Y., 2006, “Three-Dimensional Finite Element Analysis Simulations of the Fused Deposition Modelling Process,” *Proc. Inst. Mech. Eng. Part B J. Eng. Manuf.*, **220**(10), pp. 1663–1671.
- [94] Nickel, A. H., Barnett, D. M., and Prinz, F. B., 2001, “Thermal Stresses and Deposition Patterns in Layered Manufacturing,” *Mater. Sci. Eng. A*, **317**(1–2), pp. 59–64.
- [95] Loh, L. E., Chua, C. K., Yeong, W. Y., Song, J., Mapar, M., Sing, S. L., Liu, Z. H., and Zhang, D. Q., 2015, “Numerical Investigation and an Effective Modelling on the Selective Laser Melting (SLM) Process with Aluminium Alloy 6061,” *Int. J. Heat Mass Transf.*, **80**, pp. 288–300.
- [96] Li, Y., Zhou, K., Tan, P., Tor, S. B., Chua, C. K., and Leong, K. F., 2018, “Modeling Temperature and Residual Stress Fields in Selective Laser Melting,” *Int. J. Mech. Sci.*, **136**, pp. 24–35.
- [97] Huang, Y., Yang, L. J., Du, X. Z., and Yang, Y. P., 2016, “Finite Element Analysis of Thermal Behavior of Metal Powder during Selective Laser Melting,” *Int. J. Therm. Sci.*, **104**, pp. 146–157.

- [98] Neiva, E., Badia, S., Martín, A. F., and Chiumenti, M., 2019, “A Scalable Parallel Finite Element Framework for Growing Geometries. Application to Metal Additive Manufacturing,” *Int. J. Numer. Methods Eng.*
- [99] Hahn, D. W., and Özişik, M. N., 2012, “Phase-Change Problems,” *Heat Conduction*, pp. 452–495.
- [100] Idelsohn, S. R., Storti, M. A., and Crivelli, L. A., 1994, “Numerical Methods in Phase-Change Problems,” *Arch. Comput. Methods Eng.*, **1**(1), pp. 49–74.
- [101] Fukusako, S., 1990, “Thermophysical Properties of Ice, Snow, and Sea Ice,” *Int. J. Thermophys.*, **11**(2), pp. 353–372.
- [102] Zhang, C., Zhou, Y., Zhang, L., Wu, L., Chen, Y., Xie, D., and Chen, W., 2018, “Hydrogel Cryopreservation System: An Effective Method for Cell Storage,” *Int. J. Mol. Sci.*
- [103] Yang, J., Gao, L., Liu, M., Sui, X., Zhu, Y., Wen, C., and Zhang, L., 2019, “Advanced Biotechnology for Cell Cryopreservation,” *Trans. Tianjin Univ.*
- [104] Leibo, S. P., and Mazur, P., 1971, “The Role of Cooling Rates in Low-Temperature Preservation,” *Cryobiology*.
- [105] Serra, M., Correia, C., Malpique, R., Brito, C., Jensen, J., Bjorquist, P., Carrondo, M. J. T., and Alves, P. M., 2011, “Microencapsulation Technology: A Powerful Tool for Integrating Expansion and Cryopreservation of Human Embryonic Stem Cells,” *PLoS One*, **6**(8).
- [106] Zorlutuna, P., Vrana, N. E., and Khademhosseini, A., 2013, “The Expanding World of Tissue Engineering: The Building Blocks and New Applications of Tissue Engineered Constructs,” *IEEE Rev. Biomed. Eng.*, **6**, pp. 47–62.
- [107] Maitra, J., and Shukla, V. K., 2014, “Cross-Linking in Hydrogels - A Review,” *Am. J. Polym. Sci.*, **4**(2), pp. 25–31.
- [108] Freeman, F. E., and Kelly, D. J., 2017, “Tuning Alginate Bioink Stiffness and Composition for Controlled Growth Factor Delivery and to Spatially Direct MSC Fate within Bioprinted Tissues,” *Sci. Rep.*, **7**(1).
- [109] Gurikov, P., and Smirnova, I., 2018, “Non-Conventional Methods for Gelation of Alginate,” *Gels*, **4**(1), p. 14.
- [110] Lee, P., and Rogers, M. A., 2012, “Effect of Calcium Source and Exposure-Time on Basic Caviar Spherification Using Sodium Alginate,” *Int. J. Gastron. Food Sci.*, **1**(2), pp. 96–100.
- [111] Fu, H., Liu, Y., Adrià, F., Shao, X., Cai, W., and Chipot, C., 2014, “From Material Science to Avant-Garde Cuisine. the Art of Shaping Liquids into Spheres,” *J. Phys. Chem. B*, **118**(40), pp. 11747–11756.
- [112] Shan, L., Gao, Y., Zhang, Y., Yu, W., Yang, Y., Shen, S., Zhang, S., Zhu, L., Xu, L., Tian, B., and Yun, J., 2016, “Fabrication and Use of Alginate-Based Cryogel Delivery Beads Loaded with Urea and Phosphates as Potential Carriers for Bioremediation,” *Ind. Eng. Chem. Res.*, **55**(28), pp. 7655–7660.
- [113] de Farias, Y. B., and Zapata Noreña, C. P., 2019, “Reverse Encapsulation Using Double Controlled Gelification for the Production of Spheres with Liquid Light Soy Sauce-Core,” *Int. J. Gastron. Food Sci.*, **16**.
- [114] Ho, M. H., Kuo, P. Y., Hsieh, H. J., Hsien, T. Y., Hou, L. T., Lai, J. Y., and Wang, D. M., 2004, “Preparation of Porous Scaffolds by Using Freeze-Extraction and Freeze-Gelation Methods,” *Biomaterials*, **25**(1), pp. 129–138.

- [115] Mikkelsen, A., and Elgsaeter, A., 1995, "Density Distribution of Calcium-induced Alginate Gels. A Numerical Study," *Biopolymers*, **36**(1), pp. 17–41.
- [116] Williams, H., McPhail, M., Mondal, S., and Münch, A., 2018, "Modeling Gel Fiber Formation in an Emerging Coaxial Flow from a Nozzle," *J. Fluids Eng. Trans. ASME*, **141**(1).
- [117] Yuan, N. Y., Lin, Y. A., Ho, M. H., Wang, D. M., Lai, J. Y., and Hsieh, H. J., 2009, "Effects of the Cooling Mode on the Structure and Strength of Porous Scaffolds Made of Chitosan, Alginate, and Carboxymethyl Cellulose by the Freeze-Gelation Method," *Carbohydr. Polym.*, **78**(2), pp. 349–356.
- [118] Zmora, S., Glicklis, R., and Cohen, S., 2002, "Tailoring the Pore Architecture in 3-D Alginate Scaffolds by Controlling the Freezing Regime during Fabrication," *Biomaterials*, **23**(20), pp. 4087–4094.
- [119] Bridgman, P. W., 1925, "Certain Physical Properties of Single Crystals of Tungsten, Antimony, Bismuth, Tellurium, Cadmium, Zinc, and Tin," *Proc. Am. Acad. Arts Sci.*, **60**(6), pp. 305–383.
- [120] Stockbarger, D. C., 1936, "The Production of Large Single Crystals of Lithium Fluoride," *Rev. Sci. Instrum.*, **7**(3), pp. 133–136.
- [121] Arzakantsyan, M., Ananyan, N., Gevorgyan, V., and Chanteloup, J.-C., 2012, "Growth of Large 90 Mm Diameter Yb:YAG Single Crystals with Bagdasarov Method," *Opt. Mater. Express*, **2**(9), p. 1219.
- [122] Rubinsky, B., and Ikeda, M., 1985, "A Cryomicroscope Using Directional Solidification for the Controlled Freezing of Biological Material," *Cryobiology*, **22**(1), pp. 55–68.
- [123] Rubinsky, B., 1985, "Directional Solidification for the Controlled Freezing of Biomaterials. US Patent 4,531,373."
- [124] Rubinsky, B., Lee, C., and Chaw, M., 1993, "Experimental Observations and Theoretical Studies on Solidification Processes in Saline Solutions," *Exp. Therm. Fluid Sci.*, **6**(2), pp. 157–167.
- [125] Hubel, A., Darr, T. B., Chang, A., and Dantzig, J., 2007, "Cell Partitioning during the Directional Solidification of Trehalose Solutions," *Cryobiology*, **55**(3), pp. 182–188.
- [126] Chang, A., Dantzig, J. A., Darr, B. T., and Hubel, A., 2007, "Modeling the Interaction of Biological Cells with a Solidifying Interface," *J. Comput. Phys.*, **226**(2), pp. 1808–1829.
- [127] Zinchenko, Y., Laureano, E., and Coger, R. N., 2005, "Use of Directional Solidification to Quantify the Thermophysical Properties of DMSO-Based Cryoprotectant Solutions," *Cell Preserv. Technol.*, **2**(4), pp. 276–289.
- [128] Arav, A., and Saragusty, J., 2014, "Directional Freezing of Spermatozoa and Embryos," *Reprod. Fertil. Dev.*, **26**(1), pp. 83–90.
- [129] Arav, A., Gavish, Z., Elami, A., Natan, Y., Revel, A., Silber, S., Gosden, R. G., and Patrizio, P., 2010, "Ovarian Function 6 Years after Cryopreservation and Transplantation of Whole Sheep Ovaries," *Reprod. Biomed. Online*, **20**(1), pp. 48–52.
- [130] Gao, D., Watson, P. F., He, L., Yu, J., and Critser, J., 2003, "Development of a Directional Solidification Device for Cell Cryopreservation," *Cell Preserv. Technol.*, **1**(4), pp. 231–238.
- [131] Francis, N. L., Hunger, P. M., Donius, A. E., Riblett, B. W., Zavaliangos, A., Wegst, U. G. K., and Wheatley, M. A., 2013, "An Ice-Templated, Linearly Aligned Chitosan-Alginate Scaffold for Neural Tissue Engineering," *J. Biomed. Mater. Res. - Part A*, **101**(12), pp. 3493–3503.

- [132] Preciado, J. A., Skandakumaran, P., Cohen, S., and Rubinsky, B., 2003, "Utilization of Directional Freezing for the Construction of Tissue Engineering Scaffolds," *Heat Transfer, Volume 4*, pp. 3–6.
- [133] Riblett, B. W., Donius, A. E., Wegst, U. G. K., Clyne, A. M., Meghri, N. W., and Martin, E. J., 2010, "Directionally Solidified Biopolymer Scaffolds: Mechanical Properties and Endothelial Cell Responses," *Jom*, **62**(7), pp. 71–75.
- [134] Rubinsky, B., and Ikeda, M., 1985, "A Cryomicroscope Using Directional Solidification for the Controlled Freezing of Biological Matter.," *Cryobiology*, **22**(1), pp. 55–68.
- [135] Rubinsky, B., and Pegg, D. E., 1988, "A Mathematical Model for the Freezing Process in Biological Tissue," *Proc. R. Soc. B Biol. Sci.*, **234**(1276), pp. 343–358.
- [136] O'Brien, F. J., Harley, B. A., Yannas, I. V., and Gibson, L., 2004, "Influence of Freezing Rate on Pore Structure in Freeze-Dried Collagen-GAG Scaffolds," *Biomaterials*, **25**(6), pp. 1077–1086.
- [137] Chen, M., Zhu, J., Qi, G., He, C., and Wang, H., 2012, "Anisotropic Hydrogels Fabricated with Directional Freezing and Radiation-Induced Polymerization and Crosslinking Method," *Mater. Lett.*, **89**, pp. 104–107.
- [138] Zhu, J., Wang, J., Liu, Q., Liu, Y., Wang, L., He, C., and Wang, H., 2013, "Anisotropic Tough Poly(2-Hydroxyethyl Methacrylate) Hydrogels Fabricated by Directional Freezing Redox Polymerization," *J. Mater. Chem. B*, **1**(7), pp. 978–986.
- [139] Østberg, T., Lund, E. M., and Graffner, C., 1994, "Calcium Alginate Matrices for Oral Multiple Unit Administration: IV. Release Characteristics in Different Media," *Int. J. Pharm.*, **112**(3), pp. 241–248.
- [140] Bishop, E. S., Mostafa, S., Pakvasa, M., Luu, H. H., Lee, M. J., Wolf, J. M., Ameer, G. A., He, T. C., and Reid, R. R., 2017, "3-D Bioprinting Technologies in Tissue Engineering and Regenerative Medicine: Current and Future Trends," *Genes Dis.*
- [141] Cornelissen, D.-J., Faulkner-Jones, A., and Shu, W., 2017, "Current Developments in 3D Bioprinting for Tissue Engineering," *Curr. Opin. Biomed. Eng.*, **2**, pp. 76–82.
- [142] Saez, A., Ghibaud, M., Buguin, A., Silberzan, P., and Ladoux, B., 2007, "Rigidity-Driven Growth and Migration of Epithelial Cells on Microstructured Anisotropic Substrates," *Proc. Natl. Acad. Sci.*
- [143] Hadjipanayi, E., Mudera, V., and Brown, R. A., 2009, "Guiding Cell Migration in 3D: A Collagen Matrix with Graded Directional Stiffness," *Cell Motil. Cytoskeleton*, **66**(3), pp. 121–128.
- [144] Zawada, B., Ukpai, G., Powell-Palm, M. J., and Rubinsky, B., 2018, "Multi-Layer Cryolithography for Additive Manufacturing," *Prog. Addit. Manuf.*, **3**(4), pp. 245–255.
- [145] Feygin, M., 1989, "Laminated Object Manufacturing," *Ind. Laser Rev.*, **3.10**(D), pp. 1–2.
- [146] Lee, K. Y., and Mooney, D. J., 2012, "Alginate: Properties and Biomedical Applications," *Prog. Polym. Sci.*, **37**(1), pp. 106–126.
- [147] Andersen, T., Strand, B. L., Formo, K., Alsberg, E., and Christensen, B. E., 2011, "Alginates as Biomaterials in Tissue Engineering," *Carbohydr. Chem.*, **37**, pp. 227–258.
- [148] Augst D, A., Kong Joon, H., and Mooney J, D., 2006, "Alginate Hydrogels as Biomaterials," *Macromol. Biosci.*, **6**, pp. 623–633.
- [149] Peng, Z. F., Shi, S. L., Jin, H. X., Yao, G. D., Wang, E. Y., Yang, H. Y., Song, W. Y., and Sun, Y. P., 2015, "Impact of Oxygen Concentrations on Fertilization, Cleavage, Implantation, and Pregnancy Rates of in Vitro Generated Human Embryos," *Int. J. Clin. Exp. Med.*, **8**(4), pp. 6179–6185.

- [150] Avti, P. K., Patel, S. C., Uppal, P., O'Malley, G., Garlow, J., and Sitharaman, B., 2012, "Nanobiomaterials for Tissue Engineering," *Tissue Engineering: Principles and Practices*, pp. 11-1-11-24.
- [151] Shapiro, L., and Cohen, S., 1997, "Novel Alginate Sponges for Cell Culture and Transplantation," *Biomaterials*, **18**(8), pp. 583-590.
- [152] Mahler, S., Desille, M., Frémond, B., Chesné, C., Guillouzo, A., Campion, J. P., and Clément, B., 2003, "Hypothermic Storage and Cryopreservation of Hepatocytes: The Protective Effect of Alginate Gel against Cell Damages," *Cell Transplant.*, **12**(6), pp. 579-592.
- [153] Xiong, Z; Yan, YN; Wang, SG ; Zhang, RJ; Zhang, C., 2002, "Fabrication of Porous Scaffolds for Bone Tissue Engineering via Low-Temperature Deposition," *Scr. Mater.*, **46**(11), pp. 771-776.
- [154] Liu, L., Xiong, Z., Yan, Y., Zhang, R., Wang, X., and Jin, L., 2009, "Multinozzle Low-Temperature Deposition System for Construction of Gradient Tissue Engineering Scaffolds," *J. Biomed. Mater. Res. - Part B Appl. Biomater.*, **88**(1), pp. 254-263.
- [155] Yen, H. J., Hsu, S. H., Tseng, C. S., Huang, J. P., and Tsai, C. L., 2009, "Fabrication of Precision Scaffolds Using Liquid-Frozen Deposition Manufacturing for Cartilage Tissue Engineering," *Tissue Eng Part A*, **15**(5), pp. 965-975.
- [156] Gibson, M. A., Mykulowycz, N. M., Shim, J., Fontana, R., Schmitt, P., Roberts, A., Ketkaew, J., Shao, L., Chen, W., Bordeenithikasem, P., Myerberg, J. S., Fulop, R., Verminski, M. D., Sachs, E. M., Chiang, Y. M., Schuh, C. A., John Hart, A., and Schroers, J., 2018, "3D Printing Metals like Thermoplastics: Fused Filament Fabrication of Metallic Glasses," *Mater. Today*.

8. Appendix

8.1. Code for Extrusion 3D printing thermal phase change model

Model for Phase change in a 3D extruded shape

```
% Model for phase change in a 3D shape made of cuboids
function [... Outputs
    xMast,...   Array of node x coordinates
    yMast,...   Array of node y coordinates
    zMast,...   Array of node z coordinates
    cTMast,...  Array of Temperature distribution
    cfMast,...  Array of Phase fraction distribution
    ccMast,...  Array of Cooling rate distribution
    plotProbe, ... Results at the probe locations
    indexRecord... Stores number of nodes in simulation
] = volelmt_phchnng_3D_modplot...
(... Inputs
    T,...       Temperature distribution (°C)
    f,...       Phase fraction distribution
    BC,...      Boundary conditions
    p,...       Initial number of x divisions
    q,...       Initial number of y divisions
    r,...       Initial number of z divisions
    totaltimesteps,... Total number of time steps
    Tsurf,...   Temperature of the printing surface
    dt,...      Time step for thermal phase change model
    dtprint... Time step for extrusion printing model
)

% Material Properties

    % Ice/Water(Solid) properties at -20degC
ps = 919.4;           % Density (kg/m^3)
ks = 2.2;            % Thermal conductivity (W/mK)
cs = 1943;          % Specific Heat Capacity (J/kgK)
    % Water (Liquid)
pl = 1000;          % Density (kg/m^3)
kl = 0.55575;      % Thermal conductivity (W/mK)
cl = 4186;          % Specific Heat Capacity (J/kgK)
    % Phase change quantities
Tm = 0;            % Phase change temperature (°C)
L = 333.6e3;       % Latent heat of fusion (J/kg)

%% Initialization of parameters
d = 1e-3;          % length of added cubic volume
dx = d/p;          % size of x mesh
dy = d/q;          % size of y mesh
dz = d/r;          % size of z mesh
globalorigin = [0 0 0]; % Global origin
punit = p;
qunit = q;
runit = r;
```

```

plotProbe = zeros(totaltimesteps,10);
direction = zeros(3500,1);
origin = zeros(3500,3);
layer = 1;

psub = p;
qsub = q;
rsub = r;
ri = r;

% closed square shape
direction(1:50) = ones(50,1);
direction(51:100)= 3*ones(50,1);
direction(101:150)= 2*ones(50,1);
direction(151:195)= 4*ones(45,1);
direction(196)= 5;
direction(197:246) = ones(50,1);
direction(247:296)= 3*ones(50,1);
direction(297:346)= 2*ones(50,1);
direction(347:391)= 4*ones(45,1);
direction(392)= 5;
direction(393:442) = ones(50,1);
direction(443:492)= 3*ones(50,1);
direction(493:542)= 2*ones(50,1);
direction(543:587)= 4*ones(45,1);
direction(588)= 5;
direction(589:638) = ones(50,1);
direction(639:688)= 3*ones(50,1);
direction(689:738)= 2*ones(50,1);
direction(739:783)= 4*ones(45,1);
direction(784)= 5;
direction(785:834) = ones(50,1);
direction(835:884)= 3*ones(50,1);
direction(885:934)= 2*ones(50,1);
direction(935:979)= 4*ones(45,1);
direction(980)= 5;
direction(981:1030) = ones(50,1);
direction(1031:1080)= 3*ones(50,1);
direction(1081:1130)= 2*ones(50,1);
direction(1131:1175)= 4*ones(45,1);
direction(1176)= 5;
direction(1177:1226) = ones(50,1);
direction(1227:1276)= 3*ones(50,1);
direction(1277:1326)= 2*ones(50,1);
direction(1327:1371)= 4*ones(45,1);
direction(1372)= 5;
direction(1373:1422) = ones(50,1);
direction(1423:1472)= 3*ones(50,1);
direction(1473:1522)= 2*ones(50,1);
direction(1523:1567)= 4*ones(45,1);
direction(1568)= 5;
direction(1569:1618) = ones(50,1);
direction(1619:1668)= 3*ones(50,1);
direction(1669:1718)= 2*ones(50,1);
direction(1719:1763)= 4*ones(45,1);
direction(1764)= 5;
direction(1765:1814) = ones(50,1);
direction(1815:1864)= 3*ones(50,1);

```

```

direction(1865:1914)= 2*ones(50,1);
direction(1915:1959)= 4*ones(45,1);
direction(1960)= 5;
direction(1961:2010) = ones(50,1);
direction(2011:2060)= 3*ones(50,1);
direction(2061:2110)= 2*ones(50,1);
direction(2111:2155)= 4*ones(45,1);
direction(2156)= 5;
direction(2157:2206) = ones(50,1);
direction(2207:2256)= 3*ones(50,1);
direction(2257:2306)= 2*ones(50,1);
direction(2307:2351)= 4*ones(45,1);
direction(2352)= 5;
direction(2353:2402) = ones(50,1);
direction(2403:2452)= 3*ones(50,1);
direction(2453:2502)= 2*ones(50,1);
direction(2503:2547)= 4*ones(45,1);

for step = 1:length(direction)

    if direction(step) == 0
    elseif direction(step) == 1
        psub = psub + 1;
        origin(step,1) = psub;
        origin(step,2) = qsub-qunit;
        origin(step,3) = rsub-runit;
    elseif direction(step) == 2
        psub = psub - 1;
        origin(step,1) = psub-punit;
        origin(step,2) = qsub-qunit;
        origin(step,3) = rsub-runit;
    elseif direction(step) == 3
        qsub = qsub + 1;
        origin(step,1) = psub-punit;
        origin(step,2) = qsub;
        origin(step,3) = rsub-runit;
    elseif direction(step) == 4
        qsub = qsub - 1;
        origin(step,1) = psub-punit;
        origin(step,2) = qsub-qunit;
        origin(step,3) = rsub-runit;
    elseif direction(step) == 5
        origin(step,1) = psub-punit;
        origin(step,2) = qsub-2*qunit-1;
        origin(step,3) = r*layer+1;
        layer = layer+1;
        rsub = r*layer+1;
        qsub = qsub-1-qunit;
    else
        error('direction of build invalid. Enter number between 0 and 5
inclusive')
    end
end

% Check that time step meets stability criterion;
dtlimit = (dx^2*ps*cs/ks);
if dt > dtlimit/5
    error('Time step too large for explicit method')

```

```

else
end

time = 0;
vprint = 20e-3; % Printing speed (m/s)

psub = p;
qsub = q;
% rsub = r;
layer = 1;
step = 0;

for timepoints = 1:totaltimesteps
    time = time + dt;

    if time >= (step+1)*dtprint
        step = step + 1;
        if direction(step) == 5
            layer = layer + 1;
        end
        if layer == 1
            runit = ri + 1;
        else
            runit = ri;
        end

        if direction(step) == 0
        elseif direction(step) == 1
            psub = psub + 1;
            if psub > p
                p = p + 1;
            end
            Tadd = NaN(qunit+1,runit);
            for j = 1:qunit+1
                for k = 1:runit
                    Tadd(j,k) = 20;
                end
                if layer == 1
                    Tadd(j,1) = Tsurf;
                end
            end
            fadd = ones(qunit+1,runit);
            for j = 1:qunit+1
                for k = 1:runit
                    if Tadd(j,k) < Tm
                        fadd(j,k) = 0;
                    elseif Tadd(j,k) > Tm
                        fadd(j,k) = 1;
                    else
                        fadd(j,k) = 0;
                    end
                end
            end
            for j = 1:qunit+1
                for k = 1:runit

```

```

Tadd(j,k);
fadd(j,k);
    T(origin(step,1)+1,origin(step,2)+j,origin(step,3)+k) =
    f(origin(step,1)+1,origin(step,2)+j,origin(step,3)+k) =
        end
    end
elseif direction(step) == 2
    psub = psub - 1;
    Tadd = NaN(qunit+1,runit);
    for j = 1:qunit+1
        for k = 1:runit
            Tadd(j,k) = 20;
        end
        if layer == 1
            Tadd(j,1) = Tsurf;
        end
    end
    fadd = ones(qunit+1,runit);
    for j = 1:qunit+1
        for k = 1:runit
            if Tadd(j,k) < Tm
                fadd(j,k) = 0;
            elseif Tadd(j,k) > Tm
                fadd(j,k) = 1;
            else
                fadd(j,k) = 0;
            end
        end
    end
    for j = 1:qunit+1
        for k = 1:runit
            Tadd(j,k);
            fadd(j,k);
            T(origin(step,1)+1,origin(step,2)+j,origin(step,3)+k) =
            f(origin(step,1)+1,origin(step,2)+j,origin(step,3)+k) =
                end
        end
    elseif direction(step) == 3
        qsub = qsub + 1;
        if qsub > q
            q = q + 1;
        end
        Tadd = NaN(punit+1,runit);
        for i = 1:punit+1
            for k = 1:runit
                Tadd(i,k) = 20;
            end
            if layer == 1
                Tadd(i,1) = Tsurf;
            end
        end
        fadd = ones(punit+1,runit+1);
        for i = 1:punit+1
            for k = 1:runit
                if Tadd(i,k) < Tm
                    fadd(i,k) = 0;
                elseif Tadd(i,k) > Tm
                    fadd(i,k) = 1;
                end
            end
        end
    end
end

```

```

        else
            fadd(i,k) = 0;
        end
    end
end
for i = 1:punit+1
    for k = 1:runit
        T(origin(step,1)+i,origin(step,2)+1,origin(step,3)+k) =
Tadd(i,k);
        f(origin(step,1)+i,origin(step,2)+1,origin(step,3)+k) =
fadd(i,k);
    end
end
elseif direction(step) == 4
    qsub = qsub - 1;
    Tadd = NaN(punit+1,runit);
    for i = 1:punit+1
        for k = 1:runit
            Tadd(i,k) = 20;
        end
        if layer == 1
            Tadd(i,1) = Tsurf;
        end
    end
    fadd = ones(punit+1,runit);
    for i = 1:punit+1
        for k = 1:runit
            if Tadd(i,k) < Tm
                fadd(i,k) = 0;
            elseif Tadd(i,k) > Tm
                fadd(i,k) = 1;
            else
                fadd(i,k) = 0;
            end
        end
    end
    for i = 1:punit+1
        for k = 1:runit
            T(origin(step,1)+i,origin(step,2)+1,origin(step,3)+k) =
Tadd(i,k);
            f(origin(step,1)+i,origin(step,2)+1,origin(step,3)+k) =
fadd(i,k);
        end
    end
elseif direction(step) == 5
    Tsub = NaN(punit+1,qunit+1,runit);
    for i = 1:punit+1
        for j = 1:qunit+1
            for k = 1:runit
                Tsub(i,j,k) = 20;
            end
        end
    end
    fsub = ones(punit+1,qunit+1,runit);
    for i = 1:punit+1
        for j = 1:qunit+1
            for k = 1:runit
                if Tsub(i,j,k) < Tm

```

```

        fsub(i,j,k) = 0;
    elseif Tsub(i,j,k) > Tm
        fsub(i,j,k) = 1;
    else
        fsub(i,j,k) = 0;
    end
end
end
end
for i = 1:punit+1
    for j = 1:qunit+1
        for k = 1:runit
            T(origin(step,1)+i,origin(step,2)+j,origin(step,3)+k)
= Tsub(i,j,k);
            f(origin(step,1)+i,origin(step,2)+j,origin(step,3)+k)
= fsub(i,j,k);
        end
    end
end
qsub = qsub-1-qunit;
rsub = ri*layer;
r = rsub;
else
    error('direction of build invalid. Enter number between 0 and 5
inclusive')
end
else
end
rlevel = r-ri+1; % indicates level of cooling fluid

[T,f,cdTdt] =
EnthalpySolv3DExpl(T,f,p,q,r,dx,dy,dz,dt,BC,ps,ks,cs,pl,kl,cl,Tm,L,rlevel);

% Store variables for plotting
idxc = 0;
for i = 1:p+1
    for j = 1:q+1
        for k = 1:r+1
            if isnan(T(i,j,k))
            else
                idxc = idxc + 1;
                Xi(idxc) = globalorigin(1)+dx*(i-1);
                Yi(idxc) = globalorigin(2)+dy*(j-1);
                Zi(idxc) = globalorigin(3)+dz*(k-1);
                CTi(idxc) = T(i,j,k);
                Cci(idxc) = cdTdt(i,j,k);
                if f(i,j,k) == 0
                    Cfi(idxc) = 0;
                else
                    Cfi(idxc) = 1;
                end
            end
        end
    end
end
end
xMast(timepoints,1:idxc) = single(Xi);
yMast(timepoints,1:idxc) = single(Yi);
zMast(timepoints,1:idxc) = single(Zi);

```

```

cTMast(timepoints,1:idxc) = single(CTi);
cfMast(timepoints,1:idxc) = single(Cfi);
ccMast(timepoints,1:idxc) = single(Cci);
indexRecord(timepoints) = idxc;
indexRecord = single(indexRecord);

clear Xi Yi Zi CTi Cfi Cci idxc

% Store probe values for plotting
ip = 5;
jp = 5;
kp = [5 9 13 17 21 25 29 33 37 41 45 49 53] ;
count = 0;
for probe = 1:13
    if p+1 >= ip && q+1 >= jp && r+1 >= kp(probe)
        Tp = T(ip,jp,kp(probe));
        fp = f(ip,jp,kp(probe));
        cdTdtp = cdTdt(ip,jp,kp(probe));
        count = count + 1;
        plotProbe(timepoints,count) = Tp;
        count = count + 1;
        plotProbe(timepoints,count) = fp;
        count = count + 1;
        plotProbe(timepoints,count) = cdTdtp;
    else
    end
end

end

```

Explicit formulation for the enthalpy algorithm

```

% This function calculates the temperature distribution in a 3D volume
undergoing phase change
% using the enthalpy method.
function [... Outputs
    T,...          Calculated temperature distribution (°C)
    f,...          Calculated phase fraction distribution
    cdTdt,...     Calculated cooling rate distribution (°C/dt)
    H...          Calculated enthalpy distribution (J/kg)
] = EnthalpySolv3DExpl...
(... Inputs to the function
T,...          Initial temperature distribution (°C)
f,...          Initial phase fraction distribution
p,...          number of x steps
q,...          number of y steps
r,...          number of z steps
dx,...         x step size (m)
dy,...         y step size (m)
dz,...         z step size (m)
dt,...         single time step to solve over (s)
BC,...         Boundary condition matrix containing the conditions for all 6
boundary conditions
ps,...         Density of solid (kg/m^3)
ks,...         Thermal conductivity of solid (W/mK)
cs,...         Specific heat capacity of solid (J/kgK)
pl,...         Density of liquid (kg/m^3)
kl,...         Thermal conductivity of liquid (W/mK)

```

```

    cl,...      Specific heat capacity of liquid (J/kgK)
    Tm,...      Phase change temperature (degC)
    L,...       Latent heat of fusion (J/kg)
    rlevel...   Liquid Level for the cryofluid (entered as an index)
)

p1 = p+1; q1 = q+1; r1 = r+1;
H = NaN(p1,q1,r1);
Told = T;

% Enthalpy Properties depending on condition
for i = 1:p1
    for j = 1:q1
        for k = 1:r1
            if isnan(T(i,j,k))
            else
                cp(i,j,k) = (1-f(i,j,k))*cs+f(i,j,k)*cl;
                H(i,j,k) = cp(i,j,k)*(T(i,j,k)-Tm)+f(i,j,k)*L;
                rho(i,j,k) = (1-f(i,j,k))*ps+f(i,j,k)*pl;
                kcond = ((1-f(i,j,k))*ks+f(i,j,k)*kl);
                Rx(i,j,k) = dx/(2*kcond);
                Ry(i,j,k) = dy/(2*kcond);
                Rz(i,j,k) = dz/(2*kcond);
            end
        end
    end
end

%% Solving function
BC1o = [BC(1,1) BC(1,2) BC(1,3)];
BC2o = [BC(2,1) BC(2,2) BC(2,3)];
BC3o = [BC(3,1) BC(3,2) BC(3,3)];
BC4o = [BC(4,1) BC(4,2) BC(4,3)];
BC5o = [BC(5,1) BC(5,2) BC(5,3)];
BC6o = [BC(6,1) BC(6,2) BC(6,3)];

Ho = H;

% Boundary Conditions
% Face nodes
% BC1 xmin
for i = 1
    for j = 2:q
        for k = 2:r
            if k > rlevel
                BC1 = BC6o;
                BC2 = BC6o;
                BC3 = BC6o;
                BC4 = BC6o;
                BC5 = BC5o;
                BC6 = BC6o;
            else
                BC1 = BC1o;
                BC2 = BC2o;
                BC3 = BC3o;
            end
        end
    end
end

```

```

BC4 = BC4o;
BC5 = BC5o;
BC6 = BC6o;
end

if isnan(T(i,j,k))
elseif BC1(1)==1 % Convection or insulated
    if isnan(T(i,j-1,k)) && isnan(T(i,j,k-1))
        if BC3(1) == 0 || BC5(1) == 0 % internal corner
        else
            tstar = dt/rho(i,j,k);
            Rconvx = BC1(2)/dx;
            Rconvy = BC3(2)/dy;
            Rconvz = BC5(2)/dz;
            Rplusx = 1/(dx*(Rx(i+1,j,k)+Rx(i,j,k)));
            Rplusy = 1/(dy*(Ry(i,j+1,k)+Ry(i,j,k)));
            Rplusz = 1/(dz*(Rz(i,j,k+1)+Rz(i,j,k)));
            Rtotal = Rconvx + Rconvy + Rconvz + Rplusx + Rplusy +
Rplusz;
            H(i,j,k) = (1-
(tstar/cp(i,j,k))*Rtotal)*Ho(i,j,k)+tstar*(...
                Rconvx*BC1(3)+Rplusx*(Ho(i+1,j,k)-
f(i+1,j,k)*L)/cp(i+1,j,k)+...
                Rconvy*BC3(3)+Rplusy*(Ho(i,j+1,k)-
f(i,j+1,k)*L)/cp(i,j+1,k)+...
                Rconvz*BC5(3)+Rplusz*(Ho(i,j,k+1)-
f(i,j,k+1)*L)/cp(i,j,k+1));
            end
        elseif isnan(T(i,j-1,k)) && isnan(T(i,j,k+1))
            if BC3(1) == 0 || BC6(1) == 0 % internal corner
            else
                tstar = dt/rho(i,j,k);
                Rconvx = BC1(2)/dx;
                Rconvy = BC3(2)/dy;
                Rconvz = BC6(2)/dz;
                Rplusx = 1/(dx*(Rx(i+1,j,k)+Rx(i,j,k)));
                Rplusy = 1/(dy*(Ry(i,j+1,k)+Ry(i,j,k)));
                Rminusz = 1/(dz*(Rz(i,j,k-1)+Rz(i,j,k)));
                Rtotal = Rconvx + Rconvy + Rminusz + Rplusx + Rplusy
+ Rconvz;
                H(i,j,k) = (1-
(tstar/cp(i,j,k))*Rtotal)*Ho(i,j,k)+tstar*(...
                    Rconvx*BC1(3)+Rplusx*(Ho(i+1,j,k)-
f(i+1,j,k)*L)/cp(i+1,j,k)+...
                    Rconvy*BC3(3)+Rplusy*(Ho(i,j+1,k)-
f(i,j+1,k)*L)/cp(i,j+1,k)+...
                    Rminusz*(Ho(i,j,k-1)-f(i,j,k-1)*L)/cp(i,j,k-
1)+Rconvz*BC6(3));
                end
            elseif isnan(T(i,j+1,k)) && isnan(T(i,j,k-1))
                if BC4(1) == 0 || BC5(1) == 0 % internal corner
                else
                    tstar = dt/rho(i,j,k);
                    Rconvx = BC1(2)/dx;
                    Rconvy = BC4(2)/dy;
                    Rconvz = BC5(2)/dz;
                    Rplusx = 1/(dx*(Rx(i+1,j,k)+Rx(i,j,k)));
                    Rminusy = 1/(dy*(Ry(i,j-1,k)+Ry(i,j,k)));

```

```

        Rplusz = 1/(dz*(Rz(i,j,k+1)+Rz(i,j,k)));
        Rtotal = Rconvx + Rminusy + Rconvz + Rplusx + Rconvy
+ Rplusz;
        H(i,j,k) = (1-
(tstar/cp(i,j,k))*Rtotal)*Ho(i,j,k)+tstar*(...
        Rconvx*BC1(3)+Rplusx*(Ho(i+1,j,k)-
f(i+1,j,k)*L)/cp(i+1,j,k)+...
        Rminusy*(Ho(i,j-1,k)-f(i,j-1,k)*L)/cp(i,j-
1,k)+Rconvy*BC4(3)+...
        Rconvz*BC5(3)+Rplusz*(Ho(i,j,k+1)-
f(i,j,k+1)*L)/cp(i,j,k+1));
        end
    elseif isnan(T(i,j+1,k)) && isnan(T(i,j,k+1))
        if BC4(1) == 0 || BC6(1) == 0 % internal corner
        else
            tstar = dt/rho(i,j,k);
            Rconvx = BC1(2)/dx;
            Rconvy = BC4(2)/dy;
            Rconvz = BC6(2)/dz;
            Rplusx = 1/(dx*(Rx(i+1,j,k)+Rx(i,j,k)));
            Rminusy = 1/(dy*(Ry(i,j-1,k)+Ry(i,j,k)));
            Rminusz = 1/(dz*(Rz(i,j,k-1)+Rz(i,j,k)));
            Rtotal = Rconvx + Rminusy + Rminusz + Rplusx + Rconvy
+ Rconvz;
            H(i,j,k) = (1-
(tstar/cp(i,j,k))*Rtotal)*Ho(i,j,k)+tstar*(...
            Rconvx*BC1(3)+Rplusx*(Ho(i+1,j,k)-
f(i+1,j,k)*L)/cp(i+1,j,k)+...
            Rminusy*(Ho(i,j-1,k)-f(i,j-1,k)*L)/cp(i,j-
1,k)+Rconvy*BC4(3)+...
            Rminusz*(Ho(i,j,k-1)-f(i,j,k-1)*L)/cp(i,j,k-
1)+Rconvz*BC6(3));
            end
        elseif isnan(T(i,j-1,k))
            if BC3(1) == 0 % internal edge
            else
                tstar = dt/rho(i,j,k);
                Rconvx = BC1(2)/dx;
                Rconvy = BC3(2)/dy;
                Rplusx = 1/(dx*(Rx(i+1,j,k)+Rx(i,j,k)));
                Rplusy = 1/(dy*(Ry(i,j+1,k)+Ry(i,j,k)));
                Rminusz = 1/(dz*(Rz(i,j,k-1)+Rz(i,j,k)));
                Rplusz = 1/(dz*(Rz(i,j,k+1)+Rz(i,j,k)));
                Rtotal = Rconvx + Rconvy + Rminusz + Rplusx + Rplusy
+ Rplusz;
                H(i,j,k) = (1-
(tstar/cp(i,j,k))*Rtotal)*Ho(i,j,k)+tstar*(...
                Rconvx*BC1(3)+Rplusx*(Ho(i+1,j,k)-
f(i+1,j,k)*L)/cp(i+1,j,k)+...
                Rconvy*BC3(3)+Rplusy*(Ho(i,j+1,k)-
f(i,j+1,k)*L)/cp(i,j+1,k)+...
                Rminusz*(Ho(i,j,k-1)-f(i,j,k-1)*L)/cp(i,j,k-
1)+Rplusz*(Ho(i,j,k+1)-f(i,j,k+1)*L)/cp(i,j,k+1));
                end
            elseif isnan(T(i,j+1,k))
                if BC4(1) == 0 % internal edge
                else
                    tstar = dt/rho(i,j,k);

```

```

Rconvx = BC1(2)/dx;
Rconvy = BC4(2)/dy;
Rplusx = 1/(dx*(Rx(i+1,j,k)+Rx(i,j,k)));
Rminusy = 1/(dy*(Ry(i,j-1,k)+Ry(i,j,k)));
Rminusz = 1/(dz*(Rz(i,j,k-1)+Rz(i,j,k)));
Rplusz = 1/(dz*(Rz(i,j,k+1)+Rz(i,j,k)));
Rtotal = Rconvx + Rminusy + Rminusz + Rplusx + Rconvy
+ Rplusz;
H(i,j,k) = (1-
(tstar/cp(i,j,k))*Rtotal)*Ho(i,j,k)+tstar*(...
Rconvx*BC1(3)+Rplusx*(Ho(i+1,j,k)-
f(i+1,j,k)*L)/cp(i+1,j,k)+...
Rminusy*(Ho(i,j-1,k)-f(i,j-1,k)*L)/cp(i,j-
1,k)+Rconvy*BC4(3)+...
Rminusz*(Ho(i,j,k-1)-f(i,j,k-1)*L)/cp(i,j,k-
1)+Rplusz*(Ho(i,j,k+1)-f(i,j,k+1)*L)/cp(i,j,k+1));
end
elseif isnan(T(i,j,k-1))
if BC5(1) == 0 % internal edge
else
tstar = dt/rho(i,j,k);
Rconvx = BC1(2)/dx;
Rconvz = BC5(2)/dz;
Rplusx = 1/(dx*(Rx(i+1,j,k)+Rx(i,j,k)));
Rminusy = 1/(dy*(Ry(i,j-1,k)+Ry(i,j,k)));
Rplusy = 1/(dy*(Ry(i,j+1,k)+Ry(i,j,k)));
Rplusz = 1/(dz*(Rz(i,j,k+1)+Rz(i,j,k)));
Rtotal = Rconvx + Rminusy + Rconvz + Rplusx + Rplusy
+ Rplusz;
H(i,j,k) = (1-
(tstar/cp(i,j,k))*Rtotal)*Ho(i,j,k)+tstar*(...
Rconvx*BC1(3)+Rplusx*(Ho(i+1,j,k)-
f(i+1,j,k)*L)/cp(i+1,j,k)+...
Rminusy*(Ho(i,j-1,k)-f(i,j-1,k)*L)/cp(i,j-
1,k)+Rplusy*(Ho(i,j+1,k)-f(i,j+1,k)*L)/cp(i,j+1,k)+...
Rconvz*BC5(3)+Rplusz*(Ho(i,j,k+1)-
f(i,j,k+1)*L)/cp(i,j,k+1));
end
elseif isnan(T(i,j,k+1))
if BC6(1) == 0 % internal edge
else
tstar = dt/rho(i,j,k);
Rconvx = BC1(2)/dx;
Rconvz = BC6(2)/dz;
Rplusx = 1/(dx*(Rx(i+1,j,k)+Rx(i,j,k)));
Rminusy = 1/(dy*(Ry(i,j-1,k)+Ry(i,j,k)));
Rplusy = 1/(dy*(Ry(i,j+1,k)+Ry(i,j,k)));
Rminusz = 1/(dz*(Rz(i,j,k-1)+Rz(i,j,k)));
Rtotal = Rconvx + Rminusy + Rminusz + Rplusx + Rplusy
+ Rconvz;
H(i,j,k) = (1-
(tstar/cp(i,j,k))*Rtotal)*Ho(i,j,k)+tstar*(...
Rconvx*BC1(3)+Rplusx*(Ho(i+1,j,k)-
f(i+1,j,k)*L)/cp(i+1,j,k)+...
Rminusy*(Ho(i,j-1,k)-f(i,j-1,k)*L)/cp(i,j-
1,k)+Rplusy*(Ho(i,j+1,k)-f(i,j+1,k)*L)/cp(i,j+1,k)+...
Rminusz*(Ho(i,j,k-1)-f(i,j,k-1)*L)/cp(i,j,k-
1)+Rconvz*BC6(3));

```

```

        end
    else
        tstar = dt/rho(i,j,k);
        Rconvx = BC1(2)/dx;
        Rplusx = 1/(dx*(Rx(i+1,j,k)+Rx(i,j,k)));
        Rminusy = 1/(dy*(Ry(i,j-1,k)+Ry(i,j,k)));
        Rplusy = 1/(dy*(Ry(i,j+1,k)+Ry(i,j,k)));
        Rminusz = 1/(dz*(Rz(i,j,k-1)+Rz(i,j,k)));
        Rplusz = 1/(dz*(Rz(i,j,k+1)+Rz(i,j,k)));
        Rtotal = Rconvx + Rminusy + Rminusz + Rplusx + Rplusy +
Rplusz;
        H(i,j,k) = (1-
(tstar/cp(i,j,k))*Rtotal)*Ho(i,j,k)+tstar*(...
        Rplusx*(Ho(i+1,j,k)-
f(i+1,j,k)*L)/cp(i+1,j,k)+Rconvx*BC1(3)+...
        Rminusy*(Ho(i,j-1,k)-f(i,j-1,k)*L)/cp(i,j-
1,k)+Rplusy*(Ho(i,j+1,k)-f(i,j+1,k)*L)/cp(i,j+1,k)+...
        Rminusz*(Ho(i,j,k-1)-f(i,j,k-1)*L)/cp(i,j,k-
1)+Rplusz*(Ho(i,j,k+1)-f(i,j,k+1)*L)/cp(i,j,k+1));
    end
    elseif BC1(1)==0
    else
        error('Invalid or no boundary condition entered for BC1')
    end
end
end
end
end
% BC2 xmax
for i = p1
    for j = 2:q
        for k = 2:r
            if k > rlevel
                BC1 = BC6o;
                BC2 = BC6o;
                BC3 = BC6o;
                BC4 = BC6o;
                BC5 = BC5o;
                BC6 = BC6o;
            else
                BC1 = BC1o;
                BC2 = BC2o;
                BC3 = BC3o;
                BC4 = BC4o;
                BC5 = BC5o;
                BC6 = BC6o;
            end
        end

        if isnan(T(i,j,k))
        elseif BC2(1)==1 % Convection or insulated
            if isnan(T(i,j-1,k)) && isnan(T(i,j,k-1))
                if BC3(1) == 0 || BC5(1) == 0 % internal corner
                else
                    tstar = dt/rho(i,j,k);
                    Rconvx = BC2(2)/dx;
                    Rconvy = BC3(2)/dy;
                    Rconvz = BC5(2)/dz;
                    Rminusx = 1/(dx*(Rx(i-1,j,k)+Rx(i,j,k)));
                    Rplusy = 1/(dy*(Ry(i,j+1,k)+Ry(i,j,k)));

```

```

Rplusz = 1/(dz*(Rz(i,j,k+1)+Rz(i,j,k)));
Rtotal = Rminusx + Rconvy + Rconvz + Rconvx + Rplusy
+ Rplusz;
H(i,j,k) = (1-
(tstar/cp(i,j,k))*Rtotal)*Ho(i,j,k)+tstar*(...
Rminusx*(Ho(i-1,j,k)-f(i-1,j,k)*L)/cp(i-
1,j,k)+Rconvx*BC2(3)+...
Rconvy*BC3(3)+Rplusy*(Ho(i,j+1,k)-
f(i,j+1,k)*L)/cp(i,j+1,k)+...
Rconvz*BC5(3)+Rplusz*(Hp(i,j,k+1)-
f(i,j,k+1)*L)/cp(i,j,k+1));
end
elseif isnan(T(i,j-1,k)) && isnan(T(i,j,k+1))
if BC3(1) == 0 || BC6(1) == 0 % internal corner
else
tstar = dt/rho(i,j,k);
Rconvx = BC2(2)/dx;
Rconvy = BC3(2)/dy;
Rconvz = BC6(2)/dz;
Rminusx = 1/(dx*(Rx(i-1,j,k)+Rx(i,j,k)));
Rplusy = 1/(dy*(Ry(i,j+1,k)+Ry(i,j,k)));
Rminusz = 1/(dz*(Rz(i,j,k-1)+Rz(i,j,k)));
Rtotal = Rminusx + Rconvy +Rminusz + Rconvx + Rplusy
+ Rconvz;
H(i,j,k) = (1-
(tstar/cp(i,j,k))*Rtotal)*Ho(i,j,k)+tstar*(...
Rminusx*(Ho(i-1,j,k)-f(i-1,j,k)*L)/cp(i-
1,j,k)+Rconvx*BC2(3)+...
Rconvy*BC3(3)+Rplusy*(Ho(i,j+1,k)-
f(i,j+1,k)*L)/cp(i,j+1,k)+...
Rminusz*(Ho(i,j,k-1)-f(i,j,k-1)*L)/cp(i,j,k-
1)+Rconvz*BC6(3));
end
elseif isnan(T(i,j+1,k)) && isnan(T(i,j,k-1))
if BC4(1) == 0 || BC5(1) == 0 % internal corner
else
tstar = dt/rho(i,j,k);
Rconvx = BC2(2)/dx;
Rconvy = BC4(2)/dy;
Rconvz = BC5(2)/dz;
Rminusx = 1/(dx*(Rx(i-1,j,k)+Rx(i,j,k)));
Rminusy = 1/(dy*(Ry(i,j-1,k)+Ry(i,j,k)));
Rplusz = 1/(dz*(Rz(i,j,k+1)+Rz(i,j,k)));
Rtotal = Rminusx + Rminusy + Rconvz + Rconvx + Rconvy
+ Rplusz;
H(i,j,k) = (1-
(tstar/cp(i,j,k))*Rtotal)*Ho(i,j,k)+tstar*(...
Rminusx*(Ho(i-1,j,k)-f(i-1,j,k)*L)/cp(i-
1,j,k)+Rconvx*BC2(3)+...
Rminusy*(Ho(i,j-1,k)-f(i,j-1,k)*L)/cp(i,j-
1,k)+Rconvy*BC4(3)+...
Rconvz*BC5(3)+Rplusz*(Ho(i,j,k+1)-
f(i,j,k+1)*L)/cp(i,j,k+1));
end
elseif isnan(T(i,j+1,k)) && isnan(T(i,j,k+1))
if BC4(1) == 0 || BC6(1) == 0 % internal corner
else
tstar = dt/rho(i,j,k);

```

```

Rconvx = BC2(2)/dx;
Rconvy = BC4(2)/dy;
Rconvz = BC6(2)/dz;
Rminusx = 1/(dx*(Rx(i-1,j,k)+Rx(i,j,k)));
Rminusy = 1/(dy*(Ry(i,j-1,k)+Ry(i,j,k)));
Rminusz = 1/(dz*(Rz(i,j,k-1)+Rz(i,j,k)));
Rtotal = Rminusx + Rminusy + Rminusz + Rconvx +
Rconvy + Rconvz;
H(i,j,k) = (1-
(tstar/cp(i,j,k))*Rtotal)*Ho(i,j,k)+tstar*(...
Rminusx*(Ho(i-1,j,k)-f(i-1,j,k)*L)/cp(i-
1,j,k)+Rconvx*BC2(3)+...
Rminusy*(Ho(i,j-1,k)-f(i,j-1,k)*L)/cp(i,j-
1,k)+Rconvy*BC4(3)+...
Rminusz*(Ho(i,j,k-1)-f(i,j,k-1)*L)/cp(i,j,k-
1)+Rconvz*BC6(2));
end
elseif isnan(T(i,j-1,k))
if BC3(1) == 0 % internal edge
else
tstar = dt/rho(i,j,k);
Rconvx = BC2(2)/dx;
Rconvy = BC3(2)/dy;
Rminusx = 1/(dx*(Rx(i-1,j,k)+Rx(i,j,k)));
Rplusy = 1/(dy*(Ry(i,j+1,k)+Ry(i,j,k)));
Rminusz = 1/(dz*(Rz(i,j,k-1)+Rz(i,j,k)));
Rplusz = 1/(dz*(Rz(i,j,k+1)+Rz(i,j,k)));
Rtotal = Rminusx + Rconvy + Rminusz + Rconvx + Rplusy
+ Rplusz;
H(i,j,k) = (1-
(tstar/cp(i,j,k))*Rtotal)*Ho(i,j,k)+tstar*(...
Rminusx*(Ho(i-1,j,k)-f(i-1,j,k)*L)/cp(i-
1,j,k)+Rconvx*BC2(3)+...
Rconvy*BC3(3)+Rplusy*(Ho(i,j+1,k)-
f(i,j+1,k)*L)/cp(i,j+1,k)+...
Rminusz*(Ho(i,j,k-1)-f(i,j,k-1)*L)/cp(i,j,k-
1)+Rplusz*(Ho(i,j,k+1)-f(i,j,k+1)*L)/cp(i,j,k+1));
end
elseif isnan(T(i,j+1,k))
if BC4(1) == 0 % internal edge
else
tstar = dt/rho(i,j,k);
Rconvx = BC2(2)/dx;
Rconvy = BC4(2)/dy;
Rminusx = 1/(dx*(Rx(i-1,j,k)+Rx(i,j,k)));
Rminusy = 1/(dy*(Ry(i,j-1,k)+Ry(i,j,k)));
Rminusz = 1/(dz*(Rz(i,j,k-1)+Rz(i,j,k)));
Rplusz = 1/(dz*(Rz(i,j,k+1)+Rz(i,j,k)));
Rtotal = Rminusx + Rminusy + Rminusz + Rconvx +
Rconvy + Rplusz;
H(i,j,k) = (1-
(tstar/cp(i,j,k))*Rtotal)*Ho(i,j,k)+tstar*(...
Rminusx*(Ho(i-1,j,k)-f(i-1,j,k)*L)/cp(i-
1,j,k)+Rconvx*BC2(3)+...
Rminusy*(Ho(i,j-1,k)-f(i,j-1,k)*L)/cp(i,j-
1,k)+Rconvy*BC4(3)+...
Rminusz*(Ho(i,j,k-1)-f(i,j,k-1)*L)/cp(i,j,k-
1)+Rplusz*(Ho(i,j,k+1)-f(i,j,k+1)*L)/cp(i,j,k+1));

```

```

end
elseif isnan(T(i,j,k-1))
if BC5(1) == 0 % internal edge
else
tstar = dt/rho(i,j,k);
Rconvx = BC2(2)/dx;
Rconvz = BC5(2)/dz;
Rminusx = 1/(dx*(Rx(i-1,j,k)+Rx(i,j,k)));
Rminusy = 1/(dy*(Ry(i,j-1,k)+Ry(i,j,k)));
Rplusy = 1/(dy*(Ry(i,j+1,k)+Ry(i,j,k)));
Rplusz = 1/(dz*(Rz(i,j,k+1)+Rz(i,j,k)));
Rtotal = Rminusx + Rminusy + Rconvz + Rconvx + Rplusy
+ Rplusz;
H(i,j,k) = (1-
(tstar/cp(i,j,k))*Rtotal)*Ho(i,j,k)+tstar*(...
Rminusx*(Ho(i-1,j,k)-f(i-1,j,k)*L)/cp(i-
1,j,k)+Rconvx*BC2(3)+...
Rminusy*(Ho(i,j-1,k)-f(i,j-1,k)*L)/cp(i,j-
1,k)+Rplusy*(Ho(i,j+1,k)-f(i,j+1,k)*L)/cp(i,j+1,k)+...
Rconvz*BC5(3)+Rplusz*(Ho(i,j,k+1)-
f(i,j,k+1)*L)/cp(i,j,k+1));
end
elseif isnan(T(i,j,k+1))
if BC6(1) == 0 % internal edge
else
tstar = dt/rho(i,j,k);
Rconvx = BC2(2)/dx;
Rconvz = BC6(2)/dz;
Rminusx = 1/(dx*(Rx(i-1,j,k)+Rx(i,j,k)));
Rminusy = 1/(dy*(Ry(i,j-1,k)+Ry(i,j,k)));
Rplusy = 1/(dy*(Ry(i,j+1,k)+Ry(i,j,k)));
Rminusz = 1/(dz*(Rz(i,j,k-1)+Rz(i,j,k)));
Rtotal = Rminusx + Rminusy + Rminusz + Rconvx +
Rplusy + Rconvz;
H(i,j,k) = (1-
(tstar/cp(i,j,k))*Rtotal)*Ho(i,j,k)+tstar*(...
Rminusx*(Ho(i-1,j,k)-f(i-1,j,k)*L)/cp(i-
1,j,k)+Rconvx*BC2(3)+...
Rminusy*(Ho(i,j-1,k)-f(i,j-1,k)*L)/cp(i,j-
1,k)+Rplusy*(Ho(i,j+1,k)-f(i,j+1,k)*L)/cp(i,j+1,k)+...
Rminusz*(Ho(i,j,k-1)-f(i,j,k-1)*L)/cp(i,j,k-
1)+Rconvz*BC6(3));
end
else
tstar = dt/rho(i,j,k);
Rconvx = BC2(2)/dx;
Rminusx = 1/(dx*(Rx(i-1,j,k)+Rx(i,j,k)));
Rminusy = 1/(dy*(Ry(i,j-1,k)+Ry(i,j,k)));
Rplusy = 1/(dy*(Ry(i,j+1,k)+Ry(i,j,k)));
Rminusz = 1/(dz*(Rz(i,j,k-1)+Rz(i,j,k)));
Rplusz = 1/(dz*(Rz(i,j,k+1)+Rz(i,j,k)));
Rtotal = Rminusx + Rminusy + Rminusz + Rconvx + Rplusy +
Rplusz;
H(i,j,k) = (1-
(tstar/cp(i,j,k))*Rtotal)*Ho(i,j,k)+tstar*(...
Rminusx*(Ho(i-1,j,k)-f(i-1,j,k)*L)/cp(i-
1,j,k)+Rconvx*BC2(3)+...

```

```

        Rminusy*(Ho(i,j-1,k)-f(i,j-1,k)*L)/cp(i,j-
1,k)+Rplusy*(Ho(i,j+1,k)-f(i,j+1,k)*L)/cp(i,j+1,k)+...
        Rminusz*(Ho(i,j,k-1)-f(i,j,k-1)*L)/cp(i,j,k-
1)+Rplusz*(Ho(i,j,k+1)-f(i,j,k+1)*L)/cp(i,j,k+1));
    end
    elseif BC2(1)==0
    else
        error('Invalid or no boundary condition entered for BC2')
    end
end
end
end
% BC3 ymin
for j = 1
    for i = 2:p
        for k = 2:r
            if k > rlevel
                BC1 = BC6o;
                BC2 = BC6o;
                BC3 = BC6o;
                BC4 = BC6o;
                BC5 = BC5o;
                BC6 = BC6o;
            else
                BC1 = BC1o;
                BC2 = BC2o;
                BC3 = BC3o;
                BC4 = BC4o;
                BC5 = BC5o;
                BC6 = BC6o;
            end

            if isnan(T(i,j,k))
            elseif BC3(1)==1 % Convection or insulated
                if isnan(T(i-1,j,k)) && isnan(T(i,j,k-1))
                    if BC1(1) == 0 || BC5(1) == 0 % internal corner
                        else
                            tstar = dt/rho(i,j,k);
                            Rconvx = BC1(2)/dx;
                            Rconvy = BC3(2)/dy;
                            Rconvz = BC5(2)/dz;
                            Rplusx = 1/(dx*(Rx(i+1,j,k)+Rx(i,j,k)));
                            Rplusy = 1/(dy*(Ry(i,j+1,k)+Ry(i,j,k)));
                            Rplusz = 1/(dz*(Rz(i,j,k+1)+Rz(i,j,k)));
                            Rtotal = Rconvx + Rconvy + Rconvz + Rplusx + Rplusy +
Rplusz;
                            H(i,j,k) = (1-
(tstar/cp(i,j,k))*Rtotal)*Ho(i,j,k)+tstar*(...
                                Rconvx*BC1(3)+Rplusx*(Ho(i+1,j,k)-
f(i+1,j,k)*L)/cp(i+1,j,k)+...
                                Rconvy*BC3(3)+Rplusy*(Ho(i,j+1,k)-
f(i,j+1,k)*L)/cp(i,j+1,k)+...
                                Rconvz*BC5(3)+Rplusz*(Ho(i,j,k+1)-
f(i,j,k+1)*L)/cp(i,j,k+1));
                            end
                        elseif isnan(T(i-1,j,k)) && isnan(T(i,j,k+1))
                            if BC1(1) == 0 || BC6(1) == 0 % internal corner
                                else

```

```

        tstar = dt/rho(i,j,k);
        Rconvx = BC1(2)/dx;
        Rconvy = BC3(2)/dy;
        Rconvz = BC6(2)/dz;
        Rplusx = 1/(dx*(Rx(i+1,j,k)+Rx(i,j,k)));
        Rplusy = 1/(dy*(Ry(i,j+1,k)+Ry(i,j,k)));
        Rminusz = 1/(dz*(Rz(i,j,k-1)+Rz(i,j,k)));
        Rtotal = Rconvx + Rconvy + Rminusz + Rplusx + Rplusy
+ Rconvz;
        H(i,j,k) = (1-
(tstar/cp(i,j,k))*Rtotal)*Ho(i,j,k)+tstar*(...
        Rconvx*BC1(3)+Rplusx*(Ho(i+1,j,k)-
f(i+1,j,k)*L)/cp(i+1,j,k)+...
        Rconvy*BC3(3)+Rplusy*(Ho(i,j+1,k)-
f(i,j+1,k)*L)/cp(i,j+1,k)+...
        Rminusz*(Ho(i,j,k-1)-f(i,j,k-1)*L)/cp(i,j,k-
1)+Rconvz*BC6(3));
    end
elseif isnan(T(i+1,j,k)) && isnan(T(i,j,k-1))
    if BC2(1) == 0 || BC5(1) == 0 % internal corner
    else
        tstar = dt/rho(i,j,k);
        Rconvx = BC2(2)/dx;
        Rconvy = BC3(2)/dy;
        Rconvz = BC5(2)/dz;
        Rminusx = 1/(dx*(Rx(i-1,j,k)+Rx(i,j,k)));
        Rplusy = 1/(dy*(Ry(i,j+1,k)+Ry(i,j,k)));
        Rplusz = 1/(dz*(Rz(i,j,k+1)+Rz(i,j,k)));
        Rtotal = Rminusx + Rconvy + Rconvz + Rconvx + Rplusy
+ Rplusz;
        H(i,j,k) = (1-
(tstar/cp(i,j,k))*Rtotal)*Ho(i,j,k)+tstar*(...
        Rminusx*(Ho(i-1,j,k)-f(i-1,j,k)*L)/cp(i-
1,j,k)+Rconvx*BC2(3)+...
        Rconvy*BC3(3)+Rplusy*(Ho(i,j+1,k)-
f(i,j+1,k)*L)/cp(i,j+1,k)+...
        Rconvz*BC5(3)+Rplusz*(Hp(i,j,k+1)-
f(i,j,k+1)*L)/cp(i,j,k+1));
    end
elseif isnan(T(i+1,j,k)) && isnan(T(i,j,k+1))
    if BC2(1) == 0 || BC6(1) == 0 % internal corner
    else
        tstar = dt/rho(i,j,k);
        Rconvx = BC2(2)/dx;
        Rconvy = BC3(2)/dy;
        Rconvz = BC6(2)/dz;
        Rminusx = 1/(dx*(Rx(i-1,j,k)+Rx(i,j,k)));
        Rplusy = 1/(dy*(Ry(i,j+1,k)+Ry(i,j,k)));
        Rminusz = 1/(dz*(Rz(i,j,k-1)+Rz(i,j,k)));
        Rtotal = Rminusx + Rconvy + Rminusz + Rconvx + Rplusy
+ Rconvz;
        H(i,j,k) = (1-
(tstar/cp(i,j,k))*Rtotal)*Ho(i,j,k)+tstar*(...
        Rminusx*(Ho(i-1,j,k)-f(i-1,j,k)*L)/cp(i-
1,j,k)+Rconvx*BC2(3)+...
        Rconvy*BC3(3)+Rplusy*(Ho(i,j+1,k)-
f(i,j+1,k)*L)/cp(i,j+1,k)+...

```

```

Rminusz*(Ho(i,j,k-1)-f(i,j,k-1)*L)/cp(i,j,k-
1)+Rconvz*BC6(3));
end
elseif isnan(T(i-1,j,k))
if BC1(1) == 0 % internal edge
else
tstar = dt/rho(i,j,k);
Rconvx = BC1(2)/dx;
Rconvy = BC3(2)/dy;
Rplusx = 1/(dx*(Rx(i+1,j,k)+Rx(i,j,k)));
Rplusy = 1/(dy*(Ry(i,j+1,k)+Ry(i,j,k)));
Rminusz = 1/(dz*(Rz(i,j,k-1)+Rz(i,j,k)));
Rplusz = 1/(dz*(Rz(i,j,k+1)+Rz(i,j,k)));
Rtotal = Rconvx + Rconvy + Rminusz + Rplusx + Rplusy
+ Rplusz;
H(i,j,k) = (1-
(tstar/cp(i,j,k))*Rtotal)*Ho(i,j,k)+tstar*(...
Rconvx*BC1(3)+Rplusx*(Ho(i+1,j,k)-
f(i+1,j,k)*L)/cp(i+1,j,k)+...
Rconvy*BC3(3)+Rplusy*(Ho(i,j+1,k)-
f(i,j+1,k)*L)/cp(i,j+1,k)+...
Rminusz*(Ho(i,j,k-1)-f(i,j,k-1)*L)/cp(i,j,k-
1)+Rplusz*(Ho(i,j,k+1)-f(i,j,k+1)*L)/cp(i,j,k+1));
end
elseif isnan(T(i+1,j,k))
if BC2(1) == 0 % internal edge
else
tstar = dt/rho(i,j,k);
Rconvx = BC2(2)/dx;
Rconvy = BC3(2)/dy;
Rminusx = 1/(dx*(Rx(i-1,j,k)+Rx(i,j,k)));
Rplusy = 1/(dy*(Ry(i,j+1,k)+Ry(i,j,k)));
Rminusz = 1/(dz*(Rz(i,j,k-1)+Rz(i,j,k)));
Rplusz = 1/(dz*(Rz(i,j,k+1)+Rz(i,j,k)));
Rtotal = Rminusx + Rconvy + Rminusz + Rconvx + Rplusy
+ Rplusz;
H(i,j,k) = (1-
(tstar/cp(i,j,k))*Rtotal)*Ho(i,j,k)+tstar*(...
Rminusx*(Ho(i-1,j,k)-f(i-1,j,k)*L)/cp(i-
1,j,k)+Rconvx*BC2(3)+...
Rconvy*BC3(3)+Rplusy*(Ho(i,j+1,k)-
f(i,j+1,k)*L)/cp(i,j+1,k)+...
Rminusz*(Ho(i,j,k-1)-f(i,j,k-1)*L)/cp(i,j,k-
1)+Rplusz*(Ho(i,j,k+1)-f(i,j,k+1)*L)/cp(i,j,k+1));
end
elseif isnan(T(i,j,k-1))
if BC5(1) == 0 % internal edge
else
tstar = dt/rho(i,j,k);
Rconvy = BC3(2)/dy;
Rconvz = BC5(2)/dz;
Rminusx = 1/(dx*(Rx(i-1,j,k)+Rx(i,j,k)));
Rplusx = 1/(dx*(Rx(i+1,j,k)+Rx(i,j,k)));
Rplusy = 1/(dy*(Ry(i,j+1,k)+Ry(i,j,k)));
Rplusz = 1/(dz*(Rz(i,j,k+1)+Rz(i,j,k)));
Rtotal = Rminusx + Rconvy + Rconvz + Rplusx + Rplusy
+ Rplusz;

```

```

        H(i,j,k) = (1-
(tstar/cp(i,j,k))*Rtotal)*Ho(i,j,k)+tstar*(...
        Rminusx*(Ho(i-1,j,k)-f(i-1,j,k)*L)/cp(i-
1,j,k)+Rplusx*(Ho(i+1,j,k)-f(i+1,j,k)*L)/cp(i+1,j,k)+...
        Rconvy*BC3(3)+Rplusy*(Ho(i,j+1,k)-
f(i,j+1,k)*L)/cp(i,j+1,k)+...
        Rconvz*BC5(3)+Rplusz*(Ho(i,j,k+1)-
f(i,j,k+1)*L)/cp(i,j,k+1));
    end
elseif isnan(T(i,j,k+1))
    if BC6(1) == 0 % internal edge
    else
        tstar = dt/rho(i,j,k);
        Rconvy = BC3(2)/dy;
        Rconvz = BC6(2)/dz;
        Rminusx = 1/(dx*(Rx(i-1,j,k)+Rx(i,j,k)));
        Rplusx = 1/(dx*(Rx(i+1,j,k)+Rx(i,j,k)));
        Rplusy = 1/(dy*(Ry(i,j+1,k)+Ry(i,j,k)));
        Rminusz = 1/(dz*(Rz(i,j,k-1)+Rz(i,j,k)));
        Rtotal = Rminusx + Rconvy + Rminusz + Rplusx + Rplusy
+ Rconvz;
        H(i,j,k) = (1-
(tstar/cp(i,j,k))*Rtotal)*Ho(i,j,k)+tstar*(...
        Rminusx*(Ho(i-1,j,k)-f(i-1,j,k)*L)/cp(i-
1,j,k)+Rplusx*(Ho(i+1,j,k)-f(i+1,j,k)*L)/cp(i+1,j,k)+...
        Rconvy*BC3(3)+Rplusy*(Ho(i,j+1,k)-
f(i,j+1,k)*L)/cp(i,j+1,k)+...
        Rminusz*(Ho(i,j,k-1)-f(i,j,k-1)*L)/cp(i,j,k-
1)+Rconvz*BC6(3));
    end
    else
        tstar = dt/rho(i,j,k);
        Rconvy = BC3(2)/dy;
        Rminusx = 1/(dx*(Rx(i-1,j,k)+Rx(i,j,k)));
        Rplusx = 1/(dx*(Rx(i+1,j,k)+Rx(i,j,k)));
        Rplusy = 1/(dy*(Ry(i,j+1,k)+Ry(i,j,k)));
        Rminusz = 1/(dz*(Rz(i,j,k-1)+Rz(i,j,k)));
        Rplusz = 1/(dz*(Rz(i,j,k+1)+Rz(i,j,k)));
        Rtotal = Rminusx + Rconvy + Rminusz + Rplusx + Rplusy +
Rplusz;
        H(i,j,k) = (1-
(tstar/cp(i,j,k))*Rtotal)*Ho(i,j,k)+tstar*(...
        Rminusx*(Ho(i-1,j,k)-f(i-1,j,k)*L)/cp(i-
1,j,k)+Rplusx*(Ho(i+1,j,k)-f(i+1,j,k)*L)/cp(i+1,j,k)+...
        Rconvy*BC3(3)+Rplusy*(Ho(i,j+1,k)-
f(i,j+1,k)*L)/cp(i,j+1,k)+...
        Rminusz*(Ho(i,j,k-1)-f(i,j,k-1)*L)/cp(i,j,k-
1)+Rplusz*(Ho(i,j,k+1)-f(i,j,k+1)*L)/cp(i,j,k+1));
    end
    elseif BC3(1)==0
    else
        error('Invalid or no boundary condition entered for BC3')
    end
end
end
end
end
% BC4 ymax
for j = ql

```

```

for i = 2:p
    for k = 2:r
        if k > rlevel
            BC1 = BC6o;
            BC2 = BC6o;
            BC3 = BC6o;
            BC4 = BC6o;
            BC5 = BC5o;
            BC6 = BC6o;
        else
            BC1 = BC1o;
            BC2 = BC2o;
            BC3 = BC3o;
            BC4 = BC4o;
            BC5 = BC5o;
            BC6 = BC6o;
        end

        if isnan(T(i,j,k))
        elseif BC4(1)==1 % Convection or insulated
            if isnan(T(i-1,j,k)) && isnan(T(i,j,k-1))
                if BC1(1) == 0 || BC5(1) == 0 % internal corner
                    else
                        tstar = dt/rho(i,j,k);
                        Rconvx = BC1(2)/dx;
                        Rconvy = BC4(2)/dy;
                        Rconvz = BC5(2)/dz;
                        Rplusx = 1/(dx*(Rx(i+1,j,k)+Rx(i,j,k)));
                        Rminusy = 1/(dy*(Ry(i,j-1,k)+Ry(i,j,k)));
                        Rplusz = 1/(dz*(Rz(i,j,k+1)+Rz(i,j,k)));
                        Rtotal = Rconvx + Rminusy + Rconvz + Rplusx + Rconvy
+ Rplusz;
                        H(i,j,k) = (1-
(tstar/cp(i,j,k))*Rtotal)*Ho(i,j,k)+tstar*(...
                        Rconvx*BC1(3)+Rplusx*(Ho(i+1,j,k)-
f(i+1,j,k)*L)/cp(i+1,j,k)+...
                        Rminusy*(Ho(i,j-1,k)-f(i,j-1,k)*L)/cp(i,j-
1,k)+Rconvy*BC4(3)+...
                        Rconvz*BC5(3)+Rplusz*(Ho(i,j,k+1)-
f(i,j,k+1)*L)/cp(i,j,k+1));
                    end
                elseif isnan(T(i-1,j,k)) && isnan(T(i,j,k+1))
                    if BC1(1) == 0 || BC6(1) == 0 % internal corner
                        else
                            tstar = dt/rho(i,j,k);
                            Rconvx = BC1(2)/dx;
                            Rconvy = BC4(2)/dy;
                            Rconvz = BC6(2)/dz;
                            Rplusx = 1/(dx*(Rx(i+1,j,k)+Rx(i,j,k)));
                            Rminusy = 1/(dy*(Ry(i,j-1,k)+Ry(i,j,k)));
                            Rminusz = 1/(dz*(Rz(i,j,k-1)+Rz(i,j,k)));
                            Rtotal = Rconvx + Rminusy + Rminusz + Rplusx + Rconvy
+ Rconvz;
                            H(i,j,k) = (1-
(tstar/cp(i,j,k))*Rtotal)*Ho(i,j,k)+tstar*(...
                            Rconvx*BC1(3)+Rplusx*(Ho(i+1,j,k)-
f(i+1,j,k)*L)/cp(i+1,j,k)+...

```

```

1,k)+Rconvy*BC4(3)+...
1)+Rconvz*BC6(3));
end
elseif isnan(T(i+1,j,k)) && isnan(T(i,j,k-1))
if BC2(1) == 0 || BC5(1) == 0 % internal corner
else
tstar = dt/rho(i,j,k);
Rconvx = BC2(2)/dx;
Rconvy = BC4(2)/dy;
Rconvz = BC5(2)/dz;
Rminusx = 1/(dx*(Rx(i-1,j,k)+Rx(i,j,k)));
Rminusy = 1/(dy*(Ry(i,j-1,k)+Ry(i,j,k)));
Rplusz = 1/(dz*(Rz(i,j,k+1)+Rz(i,j,k)));
Rtotal = Rminusx + Rminusy + Rconvz + Rconvx + Rconvy
+ Rplusz;
H(i,j,k) = (1-
(tstar/cp(i,j,k))*Rtotal)*Ho(i,j,k)+tstar*(...
1,j,k)+Rconvx*BC2(3)+...
1,k)+Rconvy*BC4(3)+...
Rconvz*BC5(3)+Rplusz*(Ho(i,j,k+1)-
f(i,j,k+1)*L)/cp(i,j,k+1));
end
elseif isnan(T(i+1,j,k)) && isnan(T(i,j,k+1))
if BC2(1) == 0 || BC6(1) == 0 % internal corner
else
tstar = dt/rho(i,j,k);
Rconvx = BC2(2)/dx;
Rconvy = BC4(2)/dy;
Rconvz = BC6(2)/dz;
Rminusx = 1/(dx*(Rx(i-1,j,k)+Rx(i,j,k)));
Rminusy = 1/(dy*(Ry(i,j-1,k)+Ry(i,j,k)));
Rminusz = 1/(dz*(Rz(i,j,k-1)+Rz(i,j,k)));
Rtotal = Rminusx + Rminusy + Rminusz + Rconvx +
Rconvy + Rconvz;
H(i,j,k) = (1-
(tstar/cp(i,j,k))*Rtotal)*Ho(i,j,k)+tstar*(...
1,j,k)+Rconvx*BC2(3)+...
1,k)+Rconvy*BC4(3)+...
Rminusz*(Ho(i,j,k-1)-f(i,j,k-1)*L)/cp(i,j,k-
1)+Rconvz*BC6(2));
end
elseif isnan(T(i-1,j,k))
if BC1(1) == 0 % internal edge
else
tstar = dt/rho(i,j,k);
Rconvx = BC1(2)/dx;
Rconvy = BC4(2)/dy;
Rplusx = 1/(dx*(Rx(i+1,j,k)+Rx(i,j,k)));
Rminusy = 1/(dy*(Ry(i,j-1,k)+Ry(i,j,k)));
Rminusz = 1/(dz*(Rz(i,j,k-1)+Rz(i,j,k)));
Rplusz = 1/(dz*(Rz(i,j,k+1)+Rz(i,j,k)));

```

```

Rtotal = Rconvx + Rminusy + Rminusz + Rplusx + Rconvy
+ Rplusz;
    H(i,j,k) = (1-
(tstar/cp(i,j,k))*Rtotal)*Ho(i,j,k)+tstar*(...
    Rconvx*BC1(3)+Rplusx*(Ho(i+1,j,k)-
f(i+1,j,k)*L)/cp(i+1,j,k)+...
    Rminusy*(Ho(i,j-1,k)-f(i,j-1,k)*L)/cp(i,j-
1,k)+Rconvy*BC4(3)+...
    Rminusz*(Ho(i,j,k-1)-f(i,j,k-1)*L)/cp(i,j,k-
1)+Rplusz*(Ho(i,j,k+1)-f(i,j,k+1)*L)/cp(i,j,k+1));
    end
elseif isnan(T(i+1,j,k))
    if BC2(1) == 0 % internal edge
    else
        tstar = dt/rho(i,j,k);
        Rconvx = BC2(2)/dx;
        Rconvy = BC4(2)/dy;
        Rminusx = 1/(dx*(Rx(i-1,j,k)+Rx(i,j,k)));
        Rminusy = 1/(dy*(Ry(i,j-1,k)+Ry(i,j,k)));
        Rminusz = 1/(dz*(Rz(i,j,k-1)+Rz(i,j,k)));
        Rplusz = 1/(dz*(Rz(i,j,k+1)+Rz(i,j,k)));
        Rtotal = Rminusx + Rminusy + Rminusz + Rconvx +
Rconvy + Rplusz;
    H(i,j,k) = (1-
(tstar/cp(i,j,k))*Rtotal)*Ho(i,j,k)+tstar*(...
        Rminusx*(Ho(i-1,j,k)-f(i-1,j,k)*L)/cp(i-
1,j,k)+Rconvx*BC2(3)+...
        Rminusy*(Ho(i,j-1,k)-f(i,j-1,k)*L)/cp(i,j-
1,k)+Rconvy*BC4(3)+...
        Rminusz*(Ho(i,j,k-1)-f(i,j,k-1)*L)/cp(i,j,k-
1)+Rplusz*(Ho(i,j,k+1)-f(i,j,k+1)*L)/cp(i,j,k+1));
    end
elseif isnan(T(i,j,k-1))
    if BC5(1) == 0 % internal edge
    else
        tstar = dt/rho(i,j,k);
        Rconvy = BC4(2)/dy;
        Rconvz = BC5(2)/dz;
        Rminusx = 1/(dx*(Rx(i-1,j,k)+Rx(i,j,k)));
        Rplusx = 1/(dx*(Rx(i+1,j,k)+Rx(i,j,k)));
        Rminusy = 1/(dy*(Ry(i,j-1,k)+Ry(i,j,k)));
        Rplusz = 1/(dz*(Rz(i,j,k+1)+Rz(i,j,k)));
        Rtotal = Rminusx + Rminusy + Rconvz + Rplusx + Rconvy
+ Rplusz;
    H(i,j,k) = (1-
(tstar/cp(i,j,k))*Rtotal)*Ho(i,j,k)+tstar*(...
        Rminusx*(Ho(i-1,j,k)-f(i-1,j,k)*L)/cp(i-
1,j,k)+Rplusx*(Ho(i+1,j,k)-f(i+1,j,k)*L)/cp(i+1,j,k)+...
        Rminusy*(Ho(i,j-1,k)-f(i,j-1,k)*L)/cp(i,j-
1,k)+Rconvy*BC4(3)+...
        Rconvz*BC5(3)+Rplusz*(Ho(i,j,k+1)-
f(i,j,k+1)*L)/cp(i,j,k+1));
    end
elseif isnan(T(i,j,k+1))
    if BC6(1) == 0 % internal edge
    else
        tstar = dt/rho(i,j,k);
        Rconvy = BC4(2)/dy;

```

```

Rconvz = BC6(2)/dz;
Rminusx = 1/(dx*(Rx(i-1,j,k)+Rx(i,j,k)));
Rplusx = 1/(dx*(Rx(i+1,j,k)+Rx(i,j,k)));
Rminusy = 1/(dy*(Ry(i,j-1,k)+Ry(i,j,k)));
Rminusz = 1/(dz*(Rz(i,j,k-1)+Rz(i,j,k)));
Rtotal = Rminusx + Rminusy + Rminusz + Rplusx +
Rconvy + Rconvz;
H(i,j,k) = (1-
(tstar/cp(i,j,k))*Rtotal)*Ho(i,j,k)+tstar*(...
Rminusx*(Ho(i-1,j,k)-f(i-1,j,k)*L)/cp(i-
1,j,k)+Rplusx*(Ho(i+1,j,k)-f(i+1,j,k)*L)/cp(i+1,j,k)+...
Rminusy*(Ho(i,j-1,k)-f(i,j-1,k)*L)/cp(i,j-
1,k)+Rconvy*BC4(3)+...
Rminusz*(Ho(i,j,k-1)-f(i,j,k-1)*L)/cp(i,j,k-
1)+Rconvz*BC6(3));
end
else
tstar = dt/rho(i,j,k);
Rconvy = BC4(2)/dy;
Rminusx = 1/(dx*(Rx(i-1,j,k)+Rx(i,j,k)));
Rplusx = 1/(dx*(Rx(i+1,j,k)+Rx(i,j,k)));
Rminusy = 1/(dy*(Ry(i,j-1,k)+Ry(i,j,k)));
Rminusz = 1/(dz*(Rz(i,j,k-1)+Rz(i,j,k)));
Rplusz = 1/(dz*(Rz(i,j,k+1)+Rz(i,j,k)));
Rtotal = Rminusx + Rminusy + Rminusz + Rplusx + Rconvy +
Rplusz;
H(i,j,k) = (1-
(tstar/cp(i,j,k))*Rtotal)*Ho(i,j,k)+tstar*(...
Rminusx*(Ho(i-1,j,k)-f(i-1,j,k)*L)/cp(i-
1,j,k)+Rplusx*(Ho(i+1,j,k)-f(i+1,j,k)*L)/cp(i+1,j,k)+...
Rminusy*(Ho(i,j-1,k)-f(i,j-1,k)*L)/cp(i,j-
1,k)+Rconvy*BC4(3)+...
Rminusz*(Ho(i,j,k-1)-f(i,j,k-1)*L)/cp(i,j,k-
1)+Rplusz*(Ho(i,j,k+1)-f(i,j,k+1)*L)/cp(i,j,k+1));
end
elseif BC4(1)==0
else
error('Invalid or no boundary condition entered for BC4')
end
end
end
end
% BC5 zmin
for k = 1
for j = 2:q
for i = 2:p
if isnan(T(i,j,k))
elseif BC5(1)==1 % Convection or insulated
if isnan(T(i-1,j,k)) && isnan(T(i,j-1,k))
if BC1(1) == 0 || BC3(1) == 0 % internal corner
else
tstar = dt/rho(i,j,k);
Rconvx = BC1(2)/dx;
Rconvy = BC3(2)/dy;
Rconvz = BC5(2)/dz;
Rplusx = 1/(dx*(Rx(i+1,j,k)+Rx(i,j,k)));
Rplusy = 1/(dy*(Ry(i,j+1,k)+Ry(i,j,k)));
Rplusz = 1/(dz*(Rz(i,j,k+1)+Rz(i,j,k)));

```

```

Rtotal = Rconvx + Rconvy + Rconvz + Rplusx + Rplusy +
Rplusz;
    H(i,j,k) = (1-
(tstar/cp(i,j,k))*Rtotal)*Ho(i,j,k)+tstar*(...
    Rconvx*BC1(3)+Rplusx*(Ho(i+1,j,k)-
f(i+1,j,k)*L)/cp(i+1,j,k)+...
    Rconvy*BC3(3)+Rplusy*(Ho(i,j+1,k)-
f(i,j+1,k)*L)/cp(i,j+1,k)+...
    Rconvz*BC5(3)+Rplusz*(Ho(i,j,k+1)-
f(i,j,k+1)*L)/cp(i,j,k+1));
    end
elseif isnan(T(i-1,j,k)) && isnan(T(i,j+1,k))
    if BC1(1) == 0 || BC4(1) == 0 % internal corner
    else
        tstar = dt/rho(i,j,k);
        Rconvx = BC1(2)/dx;
        Rconvy = BC4(2)/dy;
        Rconvz = BC5(2)/dz;
        Rplusx = 1/(dx*(Rx(i+1,j,k)+Rx(i,j,k)));
        Rminusy = 1/(dy*(Ry(i,j-1,k)+Ry(i,j,k)));
        Rplusz = 1/(dz*(Rz(i,j,k+1)+Rz(i,j,k)));
        Rtotal = Rconvx + Rminusy + Rconvz + Rplusx + Rconvy
+ Rplusz;
        H(i,j,k) = (1-
(tstar/cp(i,j,k))*Rtotal)*Ho(i,j,k)+tstar*(...
        Rconvx*BC1(3)+Rplusx*(Ho(i+1,j,k)-
f(i+1,j,k)*L)/cp(i+1,j,k)+...
        Rminusy*(Ho(i,j-1,k)-f(i,j-1,k)*L)/cp(i,j-
1,k)+Rconvy*BC4(3)+...
        Rconvz*BC5(3)+Rplusz*(Ho(i,j,k+1)-
f(i,j,k+1)*L)/cp(i,j,k+1));
        end
elseif isnan(T(i+1,j,k)) && isnan(T(i,j-1,k))
    if BC2(1) == 0 || BC3(1) == 0 % internal corner
    else
        tstar = dt/rho(i,j,k);
        Rconvx = BC2(2)/dx;
        Rconvy = BC3(2)/dy;
        Rconvz = BC5(2)/dz;
        Rminusx = 1/(dx*(Rx(i-1,j,k)+Rx(i,j,k)));
        Rplusy = 1/(dy*(Ry(i,j+1,k)+Ry(i,j,k)));
        Rplusz = 1/(dz*(Rz(i,j,k+1)+Rz(i,j,k)));
        Rtotal = Rminusx + Rconvy + Rconvz + Rconvx + Rplusy
+ Rplusz;
        H(i,j,k) = (1-
(tstar/cp(i,j,k))*Rtotal)*Ho(i,j,k)+tstar*(...
        Rminusx*(Ho(i-1,j,k)-f(i-1,j,k)*L)/cp(i-
1,j,k)+Rconvx*BC2(3)+...
        Rconvy*BC3(3)+Rplusy*(Ho(i,j+1,k)-
f(i,j+1,k)*L)/cp(i,j+1,k)+...
        Rconvz*BC5(3)+Rplusz*(Hp(i,j,k+1)-
f(i,j,k+1)*L)/cp(i,j,k+1));
        end
elseif isnan(T(i+1,j,k)) && isnan(T(i,j+1,k))
    if BC2(1) == 0 || BC4(1) == 0 % internal corner
    else
        tstar = dt/rho(i,j,k);
        Rconvx = BC2(2)/dx;

```

```

Rconvy = BC4(2)/dy;
Rconvz = BC5(2)/dz;
Rminusx = 1/(dx*(Rx(i-1,j,k)+Rx(i,j,k)));
Rminusy = 1/(dy*(Ry(i,j-1,k)+Ry(i,j,k)));
Rplusz = 1/(dz*(Rz(i,j,k+1)+Rz(i,j,k)));
Rtotal = Rminusx + Rminusy + Rconvz + Rconvx + Rconvy
+ Rplusz;
H(i,j,k) = (1-
(tstar/cp(i,j,k))*Rtotal)*Ho(i,j,k)+tstar*(...
Rminusx*(Ho(i-1,j,k)-f(i-1,j,k)*L)/cp(i-
1,j,k)+Rconvx*BC2(3)+...
Rminusy*(Ho(i,j-1,k)-f(i,j-1,k)*L)/cp(i,j-
1,k)+Rconvy*BC4(3)+...
Rconvz*BC5(3)+Rplusz*(Ho(i,j,k+1)-
f(i,j,k+1)*L)/cp(i,j,k+1));
end
elseif isnan(T(i-1,j,k))
if BC1(1) == 0 % internal edge
else
tstar = dt/rho(i,j,k);
Rconvx = BC1(2)/dx;
Rconvz = BC5(2)/dz;
Rplusx = 1/(dx*(Rx(i+1,j,k)+Rx(i,j,k)));
Rminusy = 1/(dy*(Ry(i,j-1,k)+Ry(i,j,k)));
Rplusy = 1/(dy*(Ry(i,j+1,k)+Ry(i,j,k)));
Rplusz = 1/(dz*(Rz(i,j,k+1)+Rz(i,j,k)));
Rtotal = Rconvx + Rminusy + Rconvz + Rplusx + Rplusy
+ Rplusz;
H(i,j,k) = (1-
(tstar/cp(i,j,k))*Rtotal)*Ho(i,j,k)+tstar*(...
Rconvx*BC1(3)+Rplusx*(Ho(i+1,j,k)-
f(i+1,j,k)*L)/cp(i+1,j,k)+...
Rminusy*(Ho(i,j-1,k)-f(i,j-1,k)*L)/cp(i,j-
1,k)+Rplusy*(Ho(i,j+1,k)-f(i,j+1,k)*L)/cp(i,j+1,k)+...
Rconvz*BC5(3)+Rplusz*(Ho(i,j,k+1)-
f(i,j,k+1)*L)/cp(i,j,k+1));
end
elseif isnan(T(i+1,j,k))
if BC2(1) == 0 % internal edge
else
tstar = dt/rho(i,j,k);
Rconvx = BC2(2)/dx;
Rconvz = BC5(2)/dz;
Rminusx = 1/(dx*(Rx(i-1,j,k)+Rx(i,j,k)));
Rminusy = 1/(dy*(Ry(i,j-1,k)+Ry(i,j,k)));
Rplusy = 1/(dy*(Ry(i,j+1,k)+Ry(i,j,k)));
Rplusz = 1/(dz*(Rz(i,j,k+1)+Rz(i,j,k)));
Rtotal = Rminusx + Rminusy + Rconvz + Rconvx + Rplusy
+ Rplusz;
H(i,j,k) = (1-
(tstar/cp(i,j,k))*Rtotal)*Ho(i,j,k)+tstar*(...
Rminusx*(Ho(i-1,j,k)-f(i-1,j,k)*L)/cp(i-
1,j,k)+Rconvx*BC2(3)+...
Rminusy*(Ho(i,j-1,k)-f(i,j-1,k)*L)/cp(i,j-
1,k)+Rplusy*(Ho(i,j+1,k)-f(i,j+1,k)*L)/cp(i,j+1,k)+...
Rconvz*BC5(3)+Rplusz*(Ho(i,j,k+1)-
f(i,j,k+1)*L)/cp(i,j,k+1));
end

```

```

elseif isnan(T(i,j-1,k))
    if BC3(1) == 0 % internal edge
    else
        tstar = dt/rho(i,j,k);
        Rconvy = BC3(2)/dy;
        Rconvz = BC5(2)/dz;
        Rminusx = 1/(dx*(Rx(i-1,j,k)+Rx(i,j,k)));
        Rplusx = 1/(dx*(Rx(i+1,j,k)+Rx(i,j,k)));
        Rplusy = 1/(dy*(Ry(i,j+1,k)+Ry(i,j,k)));
        Rplusz = 1/(dz*(Rz(i,j,k+1)+Rz(i,j,k)));
        Rtotal = Rminusx + Rconvy + Rconvz + Rplusx + Rplusy
+ Rplusz;
        H(i,j,k) = (1-
(tstar/cp(i,j,k))*Rtotal)*Ho(i,j,k)+tstar*(...
            Rminusx*(Ho(i-1,j,k)-f(i-1,j,k)*L)/cp(i-
1,j,k)+Rplusx*(Ho(i+1,j,k)-f(i+1,j,k)*L)/cp(i+1,j,k)+...
            Rconvy*BC3(3)+Rplusy*(Ho(i,j+1,k)-
f(i,j+1,k)*L)/cp(i,j+1,k)+...
            Rconvz*BC5(3)+Rplusz*(Ho(i,j,k+1)-
f(i,j,k+1)*L)/cp(i,j,k+1));
        end
    elseif isnan(T(i,j+1,k))
    if BC4(1) == 0 % internal edge
    else
        tstar = dt/rho(i,j,k);
        Rconvy = BC4(2)/dy;
        Rconvz = BC5(2)/dz;
        Rminusx = 1/(dx*(Rx(i-1,j,k)+Rx(i,j,k)));
        Rplusx = 1/(dx*(Rx(i+1,j,k)+Rx(i,j,k)));
        Rminusy = 1/(dy*(Ry(i,j-1,k)+Ry(i,j,k)));
        Rplusz = 1/(dz*(Rz(i,j,k+1)+Rz(i,j,k)));
        Rtotal = Rminusx + Rminusy + Rconvz + Rplusx + Rconvy
+ Rplusz;
        H(i,j,k) = (1-
(tstar/cp(i,j,k))*Rtotal)*Ho(i,j,k)+tstar*(...
            Rminusx*(Ho(i-1,j,k)-f(i-1,j,k)*L)/cp(i-
1,j,k)+Rplusx*(Ho(i+1,j,k)-f(i+1,j,k)*L)/cp(i+1,j,k)+...
            Rminusy*(Ho(i,j-1,k)-f(i,j-1,k)*L)/cp(i,j-
1,k)+Rconvy*BC4(3)+...
            Rconvz*BC5(3)+Rplusz*(Ho(i,j,k+1)-
f(i,j,k+1)*L)/cp(i,j,k+1));
        end
    else
        tstar = dt/rho(i,j,k);
        Rconvz = BC5(2)/dz;
        Rminusx = 1/(dx*(Rx(i-1,j,k)+Rx(i,j,k)));
        Rplusx = 1/(dx*(Rx(i+1,j,k)+Rx(i,j,k)));
        Rminusy = 1/(dy*(Ry(i,j-1,k)+Ry(i,j,k)));
        Rplusy = 1/(dy*(Ry(i,j+1,k)+Ry(i,j,k)));
        Rplusz = 1/(dz*(Rz(i,j,k+1)+Rz(i,j,k)));
        Rtotal = Rminusx + Rminusy + Rconvz + Rplusx + Rplusy +
Rplusz;
        H(i,j,k) = (1-
(tstar/cp(i,j,k))*Rtotal)*Ho(i,j,k)+tstar*(...
            Rminusx*(Ho(i-1,j,k)-f(i-1,j,k)*L)/cp(i-
1,j,k)+Rplusx*(Ho(i+1,j,k)-f(i+1,j,k)*L)/cp(i+1,j,k)+...
            Rminusy*(Ho(i,j-1,k)-f(i,j-1,k)*L)/cp(i,j-
1,k)+Rplusy*(Ho(i,j+1,k)-f(i,j+1,k)*L)/cp(i,j+1,k)+...

```



```

Rconvy = BC4(2)/dy;
Rconvz = BC6(2)/dz;
Rplusx = 1/(dx*(Rx(i+1,j,k)+Rx(i,j,k)));
Rminusy = 1/(dy*(Ry(i,j-1,k)+Ry(i,j,k)));
Rminusz = 1/(dz*(Rz(i,j,k-1)+Rz(i,j,k)));
Rtotal = Rconvx + Rminusy + Rminusz + Rplusx + Rconvy
+ Rconvz;
H(i,j,k) = (1-
(tstar/cp(i,j,k))*Rtotal)*Ho(i,j,k)+tstar*(...
Rconvx*BC1(3)+Rplusx*(Ho(i+1,j,k)-
f(i+1,j,k)*L)/cp(i+1,j,k)+...
Rminusy*(Ho(i,j-1,k)-f(i,j-1,k)*L)/cp(i,j-
1,k)+Rconvy*BC4(3)+...
Rminusz*(Ho(i,j,k-1)-f(i,j,k-1)*L)/cp(i,j,k-
1)+Rconvz*BC6(3));
end
elseif isnan(T(i+1,j,k)) && isnan(T(i,j-1,k))
if BC2(1) == 0 || BC3(1) == 0 % internal corner
else
tstar = dt/rho(i,j,k);
Rconvx = BC2(2)/dx;
Rconvy = BC3(2)/dy;
Rconvz = BC6(2)/dz;
Rminusx = 1/(dx*(Rx(i-1,j,k)+Rx(i,j,k)));
Rplusy = 1/(dy*(Ry(i,j+1,k)+Ry(i,j,k)));
Rminusz = 1/(dz*(Rz(i,j,k-1)+Rz(i,j,k)));
Rtotal = Rminusx + Rconvy + Rminusz + Rconvx + Rplusy
+ Rconvz;
H(i,j,k) = (1-
(tstar/cp(i,j,k))*Rtotal)*Ho(i,j,k)+tstar*(...
Rminusx*(Ho(i-1,j,k)-f(i-1,j,k)*L)/cp(i-
1,j,k)+Rconvx*BC2(3)+...
Rconvy*BC3(3)+Rplusy*(Ho(i,j+1,k)-
f(i,j+1,k)*L)/cp(i,j+1,k)+...
Rminusz*(Ho(i,j,k-1)-f(i,j,k-1)*L)/cp(i,j,k-
1)+Rconvz*BC6(3));
end
elseif isnan(T(i+1,j,k)) && isnan(T(i,j+1,k))
if BC2(1) == 0 || BC4(1) == 0 % internal corner
else
tstar = dt/rho(i,j,k);
Rconvx = BC2(2)/dx;
Rconvy = BC4(2)/dy;
Rconvz = BC6(2)/dz;
Rminusx = 1/(dx*(Rx(i-1,j,k)+Rx(i,j,k)));
Rminusy = 1/(dy*(Ry(i,j-1,k)+Ry(i,j,k)));
Rminusz = 1/(dz*(Rz(i,j,k-1)+Rz(i,j,k)));
Rtotal = Rminusx + Rminusy + Rminusz + Rconvx +
Rconvy + Rconvz;
H(i,j,k) = (1-
(tstar/cp(i,j,k))*Rtotal)*Ho(i,j,k)+tstar*(...
Rminusx*(Ho(i-1,j,k)-f(i-1,j,k)*L)/cp(i-
1,j,k)+Rconvx*BC2(3)+...
Rminusy*(Ho(i,j-1,k)-f(i,j-1,k)*L)/cp(i,j-
1,k)+Rconvy*BC4(3)+...
Rminusz*(Ho(i,j,k-1)-f(i,j,k-1)*L)/cp(i,j,k-
1)+Rconvz*BC6(2));
end

```

```

elseif isnan(T(i-1,j,k))
    if BC1(1) == 0 % internal edge
    else
        tstar = dt/rho(i,j,k);
        Rconvx = BC1(2)/dx;
        Rconvz = BC6(2)/dz;
        Rplusx = 1/(dx*(Rx(i+1,j,k)+Rx(i,j,k)));
        Rminusy = 1/(dy*(Ry(i,j-1,k)+Ry(i,j,k)));
        Rplusy = 1/(dy*(Ry(i,j+1,k)+Ry(i,j,k)));
        Rminusz = 1/(dz*(Rz(i,j,k-1)+Rz(i,j,k)));
        Rtotal = Rconvx + Rminusy + Rminusz + Rplusx + Rplusy
+ Rconvz;
        H(i,j,k) = (1-
(tstar/cp(i,j,k))*Rtotal)*Ho(i,j,k)+tstar*(...
        Rconvx*BC1(3)+Rplusx*(Ho(i+1,j,k)-
f(i+1,j,k)*L)/cp(i+1,j,k)+...
        Rminusy*(Ho(i,j-1,k)-f(i,j-1,k)*L)/cp(i,j-
1,k)+Rplusy*(Ho(i,j+1,k)-f(i,j+1,k)*L)/cp(i,j+1,k)+...
        Rminusz*(Ho(i,j,k-1)-f(i,j,k-1)*L)/cp(i,j,k-
1)+Rconvz*BC6(3));
    end
elseif isnan(T(i+1,j,k))
    if BC2(1) == 0 % internal edge
    else
        tstar = dt/rho(i,j,k);
        Rconvx = BC2(2)/dx;
        Rconvz = BC6(2)/dz;
        Rminusx = 1/(dx*(Rx(i-1,j,k)+Rx(i,j,k)));
        Rminusy = 1/(dy*(Ry(i,j-1,k)+Ry(i,j,k)));
        Rplusy = 1/(dy*(Ry(i,j+1,k)+Ry(i,j,k)));
        Rminusz = 1/(dz*(Rz(i,j,k-1)+Rz(i,j,k)));
        Rtotal = Rminusx + Rminusy + Rminusz + Rconvx +
Rplusy + Rconvz;
        H(i,j,k) = (1-
(tstar/cp(i,j,k))*Rtotal)*Ho(i,j,k)+tstar*(...
        Rminusx*(Ho(i-1,j,k)-f(i-1,j,k)*L)/cp(i-
1,j,k)+Rconvx*BC2(3)+...
        Rminusy*(Ho(i,j-1,k)-f(i,j-1,k)*L)/cp(i,j-
1,k)+Rplusy*(Ho(i,j+1,k)-f(i,j+1,k)*L)/cp(i,j+1,k)+...
        Rminusz*(Ho(i,j,k-1)-f(i,j,k-1)*L)/cp(i,j,k-
1)+Rconvz*BC6(3));
    end
elseif isnan(T(i,j-1,k))
    if BC3(1) == 0 % internal edge
    else
        tstar = dt/rho(i,j,k);
        Rconvy = BC3(2)/dy;
        Rconvz = BC6(2)/dz;
        Rminusx = 1/(dx*(Rx(i-1,j,k)+Rx(i,j,k)));
        Rplusx = 1/(dx*(Rx(i+1,j,k)+Rx(i,j,k)));
        Rplusy = 1/(dy*(Ry(i,j+1,k)+Ry(i,j,k)));
        Rminusz = 1/(dz*(Rz(i,j,k-1)+Rz(i,j,k)));
        Rtotal = Rminusx + Rconvy + Rminusz + Rplusx + Rplusy
+ Rconvz;
        H(i,j,k) = (1-
(tstar/cp(i,j,k))*Rtotal)*Ho(i,j,k)+tstar*(...
        Rminusx*(Ho(i-1,j,k)-f(i-1,j,k)*L)/cp(i-
1,j,k)+Rplusx*(Ho(i+1,j,k)-f(i+1,j,k)*L)/cp(i+1,j,k)+...

```

```

                                Rconvy*BC3(3)+Rplusy*(Ho(i,j+1,k)-
f(i,j+1,k)*L)/cp(i,j+1,k)+...
                                Rminusz*(Ho(i,j,k-1)-f(i,j,k-1)*L)/cp(i,j,k-
1)+Rconvz*BC6(3));
                                end
                                elseif isnan(T(i,j+1,k))
                                if BC4(1) == 0 % internal edge
                                else
                                        tstar = dt/rho(i,j,k);
                                        Rconvy = BC4(2)/dy;
                                        Rconvz = BC6(2)/dz;
                                        Rminusx = 1/(dx*(Rx(i-1,j,k)+Rx(i,j,k)));
                                        Rplusx = 1/(dx*(Rx(i+1,j,k)+Rx(i,j,k)));
                                        Rminusy = 1/(dy*(Ry(i,j-1,k)+Ry(i,j,k)));
                                        Rminusz = 1/(dz*(Rz(i,j,k-1)+Rz(i,j,k)));
                                        Rtotal = Rminusx + Rminusy + Rminusz + Rplusx +
Rconvy + Rconvz;
                                        H(i,j,k) = (1-
(tstar/cp(i,j,k))*Rtotal)*Ho(i,j,k)+tstar*(...
                                        Rminusx*(Ho(i-1,j,k)-f(i-1,j,k)*L)/cp(i-
1,j,k)+Rplusx*(Ho(i+1,j,k)-f(i+1,j,k)*L)/cp(i+1,j,k)+...
                                        Rminusy*(Ho(i,j-1,k)-f(i,j-1,k)*L)/cp(i,j-
1,k)+Rconvy*BC4(3)+...
                                        Rminusz*(Ho(i,j,k-1)-f(i,j,k-1)*L)/cp(i,j,k-
1)+Rconvz*BC6(3));
                                        end
                                else
                                        tstar = dt/rho(i,j,k);
                                        Rconvz = BC6(2)/dz;
                                        Rminusx = 1/(dx*(Rx(i-1,j,k)+Rx(i,j,k)));
                                        Rplusx = 1/(dx*(Rx(i+1,j,k)+Rx(i,j,k)));
                                        Rminusy = 1/(dy*(Ry(i,j-1,k)+Ry(i,j,k)));
                                        Rplusy = 1/(dy*(Ry(i,j+1,k)+Ry(i,j,k)));
                                        Rminusz = 1/(dz*(Rz(i,j,k-1)+Rz(i,j,k)));
                                        Rtotal = Rminusx + Rminusy + Rminusz + Rplusx + Rplusy +
Rconvz;
                                        H(i,j,k) = (1-
(tstar/cp(i,j,k))*Rtotal)*Ho(i,j,k)+tstar*(...
                                        Rminusx*(Ho(i-1,j,k)-f(i-1,j,k)*L)/cp(i-
1,j,k)+Rplusx*(Ho(i+1,j,k)-f(i+1,j,k)*L)/cp(i+1,j,k)+...
                                        Rminusy*(Ho(i,j-1,k)-f(i,j-1,k)*L)/cp(i,j-
1,k)+Rplusy*(Ho(i,j+1,k)-f(i,j+1,k)*L)/cp(i,j+1,k)+...
                                        Rminusz*(Ho(i,j,k-1)-f(i,j,k-1)*L)/cp(i,j,k-
1)+Rconvz*BC6(3));
                                        end
                                elseif BC6(1)==0
                                else
                                        error('Invalid or no boundary condition entered for BC6')
                                end
                                end
                                end
                                end

% Edge Nodes
for i = 1
    for j = 1
        for k = 2:r % Edge 1
            if k > rlevel

```

```

BC1 = BC6o;
BC2 = BC6o;
BC3 = BC6o;
BC4 = BC6o;
BC5 = BC5o;
BC6 = BC6o;
else
BC1 = BC1o;
BC2 = BC2o;
BC3 = BC3o;
BC4 = BC4o;
BC5 = BC5o;
BC6 = BC6o;
end

if isnan(T(i,j,k))
elseif BC1(1) == 0 || BC3(1) == 0
else
if isnan(T(i,j,k-1))
if BC5(1) == 0 % internal corner
else
tstar = dt/rho(i,j,k);
Rconvx = BC1(2)/dx;
Rconvy = BC3(2)/dy;
Rconvz = BC5(2)/dz;
Rplusx = 1/(dx*(Rx(i+1,j,k)+Rx(i,j,k)));
Rplusy = 1/(dy*(Ry(i,j+1,k)+Ry(i,j,k)));
Rplusz = 1/(dz*(Rz(i,j,k+1)+Rz(i,j,k)));
Rtotal = Rconvx + Rconvy + Rconvz + Rplusx + Rplusy +
Rplusz;
H(i,j,k) = (1-
(tstar/cp(i,j,k))*Rtotal)*Ho(i,j,k)+tstar*(...
Rconvx*BC1(3)+Rplusx*(Ho(i+1,j,k)-
f(i+1,j,k)*L)/cp(i+1,j,k)+...
Rconvy*BC3(3)+Rplusy*(Ho(i,j+1,k)-
f(i,j+1,k)*L)/cp(i,j+1,k)+...
Rconvz*BC5(3)+Rplusz*(Ho(i,j,k+1)-
f(i,j,k+1)*L)/cp(i,j,k+1));
end
elseif isnan(T(i,j,k+1))
if BC6(1) == 0 % internal corner
else
tstar = dt/rho(i,j,k);
Rconvx = BC1(2)/dx;
Rconvy = BC3(2)/dy;
Rconvz = BC6(2)/dz;
Rplusx = 1/(dx*(Rx(i+1,j,k)+Rx(i,j,k)));
Rplusy = 1/(dy*(Ry(i,j+1,k)+Ry(i,j,k)));
Rminusz = 1/(dz*(Rz(i,j,k-1)+Rz(i,j,k)));
Rtotal = Rconvx + Rconvy + Rminusz + Rplusx + Rplusy
+ Rconvz;
H(i,j,k) = (1-
(tstar/cp(i,j,k))*Rtotal)*Ho(i,j,k)+tstar*(...
Rconvx*BC1(3)+Rplusx*(Ho(i+1,j,k)-
f(i+1,j,k)*L)/cp(i+1,j,k)+...
Rconvy*BC3(3)+Rplusy*(Ho(i,j+1,k)-
f(i,j+1,k)*L)/cp(i,j+1,k)+...

```

```

Rminusz*(Ho(i,j,k-1)-f(i,j,k-1)*L)/cp(i,j,k-
1)+Rconvz*BC6(3));
    end
    else
        tstar = dt/rho(i,j,k);
        Rconvx = BC1(2)/dx;
        Rconvy = BC3(2)/dy;
        Rplusx = 1/(dx*(Rx(i+1,j,k)+Rx(i,j,k)));
        Rplusy = 1/(dy*(Ry(i,j+1,k)+Ry(i,j,k)));
        Rminusz = 1/(dz*(Rz(i,j,k-1)+Rz(i,j,k)));
        Rplusz = 1/(dz*(Rz(i,j,k+1)+Rz(i,j,k)));
        Rtotal = Rconvx + Rconvy + Rminusz + Rplusx + Rplusy +
Rplusz;
        H(i,j,k) = (1-
(tstar/cp(i,j,k))*Rtotal)*Ho(i,j,k)+tstar*(...
        Rconvx*BC1(3)+Rplusx*(Ho(i+1,j,k)-
f(i+1,j,k)*L)/cp(i+1,j,k)+...
        Rconvy*BC3(3)+Rplusy*(Ho(i,j+1,k)-
f(i,j+1,k)*L)/cp(i,j+1,k)+...
        Rminusz*(Ho(i,j,k-1)-f(i,j,k-1)*L)/cp(i,j,k-
1)+Rplusz*(Ho(i,j,k+1)-f(i,j,k+1)*L)/cp(i,j,k+1));
    end
end
end
end
for j = q1
    for k = 2:r % Edge 2
        if k > rlevel
            BC1 = BC6o;
            BC2 = BC6o;
            BC3 = BC6o;
            BC4 = BC6o;
            BC5 = BC5o;
            BC6 = BC6o;
        else
            BC1 = BC1o;
            BC2 = BC2o;
            BC3 = BC3o;
            BC4 = BC4o;
            BC5 = BC5o;
            BC6 = BC6o;
        end

        if isnan(T(i,j,k))
        elseif BC1(1) == 0 || BC4(1) == 0
        else
            if isnan(T(i,j,k-1))
                if BC5(1) == 0 % internal corner
                    else
                        tstar = dt/rho(i,j,k);
                        Rconvx = BC1(2)/dx;
                        Rconvy = BC4(2)/dy;
                        Rconvz = BC5(2)/dz;
                        Rplusx = 1/(dx*(Rx(i+1,j,k)+Rx(i,j,k)));
                        Rminusy = 1/(dy*(Ry(i,j-1,k)+Ry(i,j,k)));
                        Rplusz = 1/(dz*(Rz(i,j,k+1)+Rz(i,j,k)));
                        Rtotal = Rconvx + Rminusy + Rconvz + Rplusx + Rconvy
+ Rplusz;

```

```

        H(i,j,k) = (1-
(tstar/cp(i,j,k))*Rtotal)*Ho(i,j,k)+tstar*(...
        Rconvx*BC1(3)+Rplusx*(Ho(i+1,j,k)-
f(i+1,j,k)*L)/cp(i+1,j,k)+...
        Rminusy*(Ho(i,j-1,k)-f(i,j-1,k)*L)/cp(i,j-
1,k)+Rconvy*BC4(3)+...
        Rconvz*BC5(3)+Rplusz*(Ho(i,j,k+1)-
f(i,j,k+1)*L)/cp(i,j,k+1));
        end
elseif isnan(T(i,j,k+1))
    if BC6(1) == 0 % internal corner
    else
        tstar = dt/rho(i,j,k);
        Rconvx = BC1(2)/dx;
        Rconvy = BC4(2)/dy;
        Rconvz = BC6(2)/dz;
        Rplusx = 1/(dx*(Rx(i+1,j,k)+Rx(i,j,k)));
        Rminusy = 1/(dy*(Ry(i,j-1,k)+Ry(i,j,k)));
        Rminusz = 1/(dz*(Rz(i,j,k-1)+Rz(i,j,k)));
        Rtotal = Rconvx + Rminusy + Rminusz + Rplusx + Rconvy
+ Rconvz;
        H(i,j,k) = (1-
(tstar/cp(i,j,k))*Rtotal)*Ho(i,j,k)+tstar*(...
        Rconvx*BC1(3)+Rplusx*(Ho(i+1,j,k)-
f(i+1,j,k)*L)/cp(i+1,j,k)+...
        Rminusy*(Ho(i,j-1,k)-f(i,j-1,k)*L)/cp(i,j-
1,k)+Rconvy*BC4(3)+...
        Rminusz*(Ho(i,j,k-1)-f(i,j,k-1)*L)/cp(i,j,k-
1)+Rconvz*BC6(3));
        end
    else
        tstar = dt/rho(i,j,k);
        Rconvx = BC1(2)/dx;
        Rconvy = BC4(2)/dy;
        Rplusx = 1/(dx*(Rx(i+1,j,k)+Rx(i,j,k)));
        Rminusy = 1/(dy*(Ry(i,j-1,k)+Ry(i,j,k)));
        Rminusz = 1/(dz*(Rz(i,j,k-1)+Rz(i,j,k)));
        Rplusz = 1/(dz*(Rz(i,j,k+1)+Rz(i,j,k)));
        Rtotal = Rconvx + Rminusy + Rminusz + Rplusx + Rconvy +
Rplusz;
        H(i,j,k) = (1-
(tstar/cp(i,j,k))*Rtotal)*Ho(i,j,k)+tstar*(...
        Rconvx*BC1(3)+Rplusx*(Ho(i+1,j,k)-
f(i+1,j,k)*L)/cp(i+1,j,k)+...
        Rminusy*(Ho(i,j-1,k)-f(i,j-1,k)*L)/cp(i,j-
1,k)+Rconvy*BC4(3)+...
        Rminusz*(Ho(i,j,k-1)-f(i,j,k-1)*L)/cp(i,j,k-
1)+Rplusz*(Ho(i,j,k+1)-f(i,j,k+1)*L)/cp(i,j,k+1));
        end
    end
end
end
for k = 1
    for j = 2:q % Edge 3
        if isnan(T(i,j,k))
        elseif BC1(1) == 0 || BC5(1) == 0
        else
            if isnan(T(i,j-1,k))

```

```

if BC3(1) == 0 % internal corner
else
    tstar = dt/rho(i,j,k);
    Rconvx = BC1(2)/dx;
    Rconvy = BC3(2)/dy;
    Rconvz = BC5(2)/dz;
    Rplusx = 1/(dx*(Rx(i+1,j,k)+Rx(i,j,k)));
    Rplusy = 1/(dy*(Ry(i,j+1,k)+Ry(i,j,k)));
    Rplusz = 1/(dz*(Rz(i,j,k+1)+Rz(i,j,k)));
    Rtotal = Rconvx + Rconvy + Rconvz + Rplusx + Rplusy +
Rplusz;
    H(i,j,k) = (1-
(tstar/cp(i,j,k))*Rtotal)*Ho(i,j,k)+tstar*(...
    Rconvx*BC1(3)+Rplusx*(Ho(i+1,j,k)-
f(i+1,j,k)*L)/cp(i+1,j,k)+...
    Rconvy*BC3(3)+Rplusy*(Ho(i,j+1,k)-
f(i,j+1,k)*L)/cp(i,j+1,k)+...
    Rconvz*BC5(3)+Rplusz*(Ho(i,j,k+1)-
f(i,j,k+1)*L)/cp(i,j,k+1));
    end
elseif isnan(T(i,j+1,k))
if BC4(1) == 0 % internal corner
else
    tstar = dt/rho(i,j,k);
    Rconvx = BC1(2)/dx;
    Rconvy = BC4(2)/dy;
    Rconvz = BC5(2)/dz;
    Rplusx = 1/(dx*(Rx(i+1,j,k)+Rx(i,j,k)));
    Rminusy = 1/(dy*(Ry(i,j-1,k)+Ry(i,j,k)));
    Rplusz = 1/(dz*(Rz(i,j,k+1)+Rz(i,j,k)));
    Rtotal = Rconvx + Rminusy + Rconvz + Rplusx + Rconvy
+ Rplusz;
    H(i,j,k) = (1-
(tstar/cp(i,j,k))*Rtotal)*Ho(i,j,k)+tstar*(...
    Rconvx*BC1(3)+Rplusx*(Ho(i+1,j,k)-
f(i+1,j,k)*L)/cp(i+1,j,k)+...
    Rminusy*(Ho(i,j-1,k)-f(i,j-1,k)*L)/cp(i,j-
1,k)+Rconvy*BC4(3)+...
    Rconvz*BC5(3)+Rplusz*(Ho(i,j,k+1)-
f(i,j,k+1)*L)/cp(i,j,k+1));
    end
else
    tstar = dt/rho(i,j,k);
    Rconvx = BC1(2)/dx;
    Rconvz = BC5(2)/dz;
    Rplusx = 1/(dx*(Rx(i+1,j,k)+Rx(i,j,k)));
    Rminusy = 1/(dy*(Ry(i,j-1,k)+Ry(i,j,k)));
    Rplusy = 1/(dy*(Ry(i,j+1,k)+Ry(i,j,k)));
    Rplusz = 1/(dz*(Rz(i,j,k+1)+Rz(i,j,k)));
    Rtotal = Rconvx + Rminusy + Rconvz + Rplusx + Rplusy +
Rplusz;
    H(i,j,k) = (1-
(tstar/cp(i,j,k))*Rtotal)*Ho(i,j,k)+tstar*(...
    Rconvx*BC1(3)+Rplusx*(Ho(i+1,j,k)-
f(i+1,j,k)*L)/cp(i+1,j,k)+...
    Rminusy*(Ho(i,j-1,k)-f(i,j-1,k)*L)/cp(i,j-
1,k)+Rplusy*(Ho(i,j+1,k)-f(i,j+1,k)*L)/cp(i,j+1,k)+...

```



```

Rtotal = Rconvx + Rminusy + Rminusz + Rplusx + Rconvy
+ Rconvz;
    H(i,j,k) = (1-
(tstar/cp(i,j,k))*Rtotal)*Ho(i,j,k)+tstar*(...
    Rconvx*BC1(3)+Rplusx*(Ho(i+1,j,k)-
f(i+1,j,k)*L)/cp(i+1,j,k)+...
    Rminusy*(Ho(i,j-1,k)-f(i,j-1,k)*L)/cp(i,j-
1,k)+Rconvy*BC4(3)+...
    Rminusz*(Ho(i,j,k-1)-f(i,j,k-1)*L)/cp(i,j,k-
1)+Rconvz*BC6(3));
    end
else
    tstar = dt/rho(i,j,k);
    Rconvx = BC1(2)/dx;
    Rconvz = BC6(2)/dz;
    Rplusx = 1/(dx*(Rx(i+1,j,k)+Rx(i,j,k)));
    Rminusy = 1/(dy*(Ry(i,j-1,k)+Ry(i,j,k)));
    Rplusy = 1/(dy*(Ry(i,j+1,k)+Ry(i,j,k)));
    Rminusz = 1/(dz*(Rz(i,j,k-1)+Rz(i,j,k)));
    Rtotal = Rconvx + Rminusy + Rminusz + Rplusx + Rplusy +
Rconvz;
    H(i,j,k) = (1-
(tstar/cp(i,j,k))*Rtotal)*Ho(i,j,k)+tstar*(...
    Rconvx*BC1(3)+Rplusx*(Ho(i+1,j,k)-
f(i+1,j,k)*L)/cp(i+1,j,k)+...
    Rminusy*(Ho(i,j-1,k)-f(i,j-1,k)*L)/cp(i,j-
1,k)+Rplusy*(Ho(i,j+1,k)-f(i,j+1,k)*L)/cp(i,j+1,k)+...
    Rminusz*(Ho(i,j,k-1)-f(i,j,k-1)*L)/cp(i,j,k-
1)+Rconvz*BC6(3));
    end
end
end
end
for i = p1
    for j = 1
        for k = 2:r % Edge 5
            if k > rlevel
                BC1 = BC6o;
                BC2 = BC6o;
                BC3 = BC6o;
                BC4 = BC6o;
                BC5 = BC5o;
                BC6 = BC6o;
            else
                BC1 = BC1o;
                BC2 = BC2o;
                BC3 = BC3o;
                BC4 = BC4o;
                BC5 = BC5o;
                BC6 = BC6o;
            end

            if isnan(T(i,j,k))
            elseif BC2(1) == 0 || BC3(1) == 0
            else
                if isnan(T(i,j,k-1))
                    if BC5(1) == 0 % internal corner

```

```

else
    tstar = dt/rho(i,j,k);
    Rconvx = BC2(2)/dx;
    Rconvy = BC3(2)/dy;
    Rconvz = BC5(2)/dz;
    Rminusx = 1/(dx*(Rx(i-1,j,k)+Rx(i,j,k)));
    Rplusy = 1/(dy*(Ry(i,j+1,k)+Ry(i,j,k)));
    Rplusz = 1/(dz*(Rz(i,j,k+1)+Rz(i,j,k)));
    Rtotal = Rminusx + Rconvy + Rconvz + Rconvx + Rplusy
+ Rplusz;
    H(i,j,k) = (1-
(tstar/cp(i,j,k))*Rtotal)*Ho(i,j,k)+tstar*(...
    Rminusx*(Ho(i-1,j,k)-f(i-1,j,k)*L)/cp(i-
1,j,k)+Rconvx*BC2(3)+...
    Rconvy*BC3(3)+Rplusy*(Ho(i,j+1,k)-
f(i,j+1,k)*L)/cp(i,j+1,k)+...
    Rconvz*BC5(3)+Rplusz*(Hp(i,j,k+1)-
f(i,j,k+1)*L)/cp(i,j,k+1));
end
elseif isnan(T(i,j,k+1))
    if BC6(1) == 0 % internal corner
    else
        tstar = dt/rho(i,j,k);
        Rconvx = BC2(2)/dx;
        Rconvy = BC3(2)/dy;
        Rconvz = BC6(2)/dz;
        Rminusx = 1/(dx*(Rx(i-1,j,k)+Rx(i,j,k)));
        Rplusy = 1/(dy*(Ry(i,j+1,k)+Ry(i,j,k)));
        Rminusz = 1/(dz*(Rz(i,j,k-1)+Rz(i,j,k)));
        Rtotal = Rminusx + Rconvy + Rminusz + Rconvx + Rplusy
+ Rconvz;
        H(i,j,k) = (1-
(tstar/cp(i,j,k))*Rtotal)*Ho(i,j,k)+tstar*(...
        Rminusx*(Ho(i-1,j,k)-f(i-1,j,k)*L)/cp(i-
1,j,k)+Rconvx*BC2(3)+...
        Rconvy*BC3(3)+Rplusy*(Ho(i,j+1,k)-
f(i,j+1,k)*L)/cp(i,j+1,k)+...
        Rminusz*(Ho(i,j,k-1)-f(i,j,k-1)*L)/cp(i,j,k-
1)+Rconvz*BC6(3));
    end
    else
        tstar = dt/rho(i,j,k);
        Rconvx = BC2(2)/dx;
        Rconvy = BC3(2)/dy;
        Rminusx = 1/(dx*(Rx(i-1,j,k)+Rx(i,j,k)));
        Rplusy = 1/(dy*(Ry(i,j+1,k)+Ry(i,j,k)));
        Rminusz = 1/(dz*(Rz(i,j,k-1)+Rz(i,j,k)));
        Rplusz = 1/(dz*(Rz(i,j,k+1)+Rz(i,j,k)));
        Rtotal = Rminusx + Rconvy + Rminusz + Rconvx + Rplusy +
Rplusz;
        H(i,j,k) = (1-
(tstar/cp(i,j,k))*Rtotal)*Ho(i,j,k)+tstar*(...
        Rminusx*(Ho(i-1,j,k)-f(i-1,j,k)*L)/cp(i-
1,j,k)+Rconvx*BC2(3)+...
        Rconvy*BC3(3)+Rplusy*(Ho(i,j+1,k)-
f(i,j+1,k)*L)/cp(i,j+1,k)+...
        Rminusz*(Ho(i,j,k-1)-f(i,j,k-1)*L)/cp(i,j,k-
1)+Rplusz*(Ho(i,j,k+1)-f(i,j,k+1)*L)/cp(i,j,k+1));

```

```

end
end
end
for j = q1
for k = 2:r % Edge 6
if k > rlevel
BC1 = BC6o;
BC2 = BC6o;
BC3 = BC6o;
BC4 = BC6o;
BC5 = BC5o;
BC6 = BC6o;
else
BC1 = BC1o;
BC2 = BC2o;
BC3 = BC3o;
BC4 = BC4o;
BC5 = BC5o;
BC6 = BC6o;
end
if isnan(T(i,j,k))
elseif BC2(1) == 0 || BC4(1) == 0
else
if isnan(T(i,j,k-1))
if BC5(1) == 0 % internal corner
else
tstar = dt/rho(i,j,k);
Rconvx = BC2(2)/dx;
Rconvy = BC4(2)/dy;
Rconvz = BC5(2)/dz;
Rminusx = 1/(dx*(Rx(i-1,j,k)+Rx(i,j,k)));
Rminusy = 1/(dy*(Ry(i,j-1,k)+Ry(i,j,k)));
Rplusz = 1/(dz*(Rz(i,j,k+1)+Rz(i,j,k)));
Rtotal = Rminusx + Rminusy + Rconvz + Rconvx + Rconvy
+ Rplusz;
H(i,j,k) = (1-
(tstar/cp(i,j,k))*Rtotal)*Ho(i,j,k)+tstar*(...
Rminusx*(Ho(i-1,j,k)-f(i-1,j,k)*L)/cp(i-
1,j,k)+Rconvx*BC2(3)+...
Rminusy*(Ho(i,j-1,k)-f(i,j-1,k)*L)/cp(i,j-
1,k)+Rconvy*BC4(3)+...
Rconvz*BC5(3)+Rplusz*(Ho(i,j,k+1)-
f(i,j,k+1)*L)/cp(i,j,k+1));
end
elseif isnan(T(i,j,k+1))
if BC6(1) == 0 % internal corner
else
tstar = dt/rho(i,j,k);
Rconvx = BC2(2)/dx;
Rconvy = BC4(2)/dy;
Rconvz = BC6(2)/dz;
Rminusx = 1/(dx*(Rx(i-1,j,k)+Rx(i,j,k)));
Rminusy = 1/(dy*(Ry(i,j-1,k)+Ry(i,j,k)));
Rminusz = 1/(dz*(Rz(i,j,k-1)+Rz(i,j,k)));
Rtotal = Rminusx + Rminusy + Rminusz + Rconvx +
Rconvy + Rconvz;

```

```

                H(i,j,k) = (1-
(tstar/cp(i,j,k))*Rtotal)*Ho(i,j,k)+tstar*(...
                Rminusx*(Ho(i-1,j,k)-f(i-1,j,k)*L)/cp(i-
1,j,k)+Rconvx*BC2(3)+...
                Rminusy*(Ho(i,j-1,k)-f(i,j-1,k)*L)/cp(i,j-
1,k)+Rconvy*BC4(3)+...
                Rminusz*(Ho(i,j,k-1)-f(i,j,k-1)*L)/cp(i,j,k-
1)+Rconvz*BC6(2));
            end
        else
            tstar = dt/rho(i,j,k);
            Rconvx = BC2(2)/dx;
            Rconvy = BC4(2)/dy;
            Rminusx = 1/(dx*(Rx(i-1,j,k)+Rx(i,j,k)));
            Rminusy = 1/(dy*(Ry(i,j-1,k)+Ry(i,j,k)));
            Rminusz = 1/(dz*(Rz(i,j,k-1)+Rz(i,j,k)));
            Rplusz = 1/(dz*(Rz(i,j,k+1)+Rz(i,j,k)));
            Rtotal = Rminusx + Rminusy + Rminusz + Rconvx + Rconvy +
Rplusz;
                H(i,j,k) = (1-
(tstar/cp(i,j,k))*Rtotal)*Ho(i,j,k)+tstar*(...
                Rminusx*(Ho(i-1,j,k)-f(i-1,j,k)*L)/cp(i-
1,j,k)+Rconvx*BC2(3)+...
                Rminusy*(Ho(i,j-1,k)-f(i,j-1,k)*L)/cp(i,j-
1,k)+Rconvy*BC4(3)+...
                Rminusz*(Ho(i,j,k-1)-f(i,j,k-1)*L)/cp(i,j,k-
1)+Rplusz*(Ho(i,j,k+1)-f(i,j,k+1)*L)/cp(i,j,k+1));
            end
        end
    end
end
for k = 1
    for j = 2:q % Edge 7
        if isnan(T(i,j,k))
            elseif BC2(1) == 0 || BC5(1) == 0
            else
                if isnan(T(i,j-1,k))
                    if BC3(1) == 0 % internal corner
                    else
                        tstar = dt/rho(i,j,k);
                        Rconvx = BC2(2)/dx;
                        Rconvy = BC3(2)/dy;
                        Rconvz = BC5(2)/dz;
                        Rminusx = 1/(dx*(Rx(i-1,j,k)+Rx(i,j,k)));
                        Rplusy = 1/(dy*(Ry(i,j+1,k)+Ry(i,j,k)));
                        Rplusz = 1/(dz*(Rz(i,j,k+1)+Rz(i,j,k)));
                        Rtotal = Rminusx + Rconvy + Rconvz + Rconvx + Rplusy
+ Rplusz;
                            H(i,j,k) = (1-
(tstar/cp(i,j,k))*Rtotal)*Ho(i,j,k)+tstar*(...
                            Rminusx*(Ho(i-1,j,k)-f(i-1,j,k)*L)/cp(i-
1,j,k)+Rconvx*BC2(3)+...
                            Rconvy*BC3(3)+Rplusy*(Ho(i,j+1,k)-
f(i,j+1,k)*L)/cp(i,j+1,k)+...
                            Rconvz*BC5(3)+Rplusz*(Hp(i,j,k+1)-
f(i,j,k+1)*L)/cp(i,j,k+1));
                        end
                    elseif isnan(T(i,j+1,k))

```

```

        if BC4(1) == 0 % internal corner
        else
            tstar = dt/rho(i,j,k);
            Rconvx = BC2(2)/dx;
            Rconvy = BC4(2)/dy;
            Rconvz = BC5(2)/dz;
            Rminusx = 1/(dx*(Rx(i-1,j,k)+Rx(i,j,k)));
            Rminusy = 1/(dy*(Ry(i,j-1,k)+Ry(i,j,k)));
            Rplusz = 1/(dz*(Rz(i,j,k+1)+Rz(i,j,k)));
            Rtotal = Rminusx + Rminusy + Rconvz + Rconvx + Rconvy
+ Rplusz;
            H(i,j,k) = (1-
(tstar/cp(i,j,k))*Rtotal)*Ho(i,j,k)+tstar*(...
            Rminusx*(Ho(i-1,j,k)-f(i-1,j,k)*L)/cp(i-
1,j,k)+Rconvx*BC2(3)+...
            Rminusy*(Ho(i,j-1,k)-f(i,j-1,k)*L)/cp(i,j-
1,k)+Rconvy*BC4(3)+...
            Rconvz*BC5(3)+Rplusz*(Ho(i,j,k+1)-
f(i,j,k+1)*L)/cp(i,j,k+1));
        end
    else
        tstar = dt/rho(i,j,k);
        Rconvx = BC2(2)/dx;
        Rconvz = BC5(2)/dz;
        Rminusx = 1/(dx*(Rx(i-1,j,k)+Rx(i,j,k)));
        Rminusy = 1/(dy*(Ry(i,j-1,k)+Ry(i,j,k)));
        Rplusy = 1/(dy*(Ry(i,j+1,k)+Ry(i,j,k)));
        Rplusz = 1/(dz*(Rz(i,j,k+1)+Rz(i,j,k)));
        Rtotal = Rminusx + Rminusy + Rconvz + Rconvx + Rplusy +
Rplusz;
        H(i,j,k) = (1-
(tstar/cp(i,j,k))*Rtotal)*Ho(i,j,k)+tstar*(...
            Rminusx*(Ho(i-1,j,k)-f(i-1,j,k)*L)/cp(i-
1,j,k)+Rconvx*BC2(3)+...
            Rminusy*(Ho(i,j-1,k)-f(i,j-1,k)*L)/cp(i,j-
1,k)+Rplusy*(Ho(i,j+1,k)-f(i,j+1,k)*L)/cp(i,j+1,k)+...
            Rconvz*BC5(3)+Rplusz*(Ho(i,j,k+1)-
f(i,j,k+1)*L)/cp(i,j,k+1));
        end
    end
end
for k = r1
    if k > rlevel
        BC1 = BC6o;
        BC2 = BC6o;
        BC3 = BC6o;
        BC4 = BC6o;
        BC5 = BC5o;
        BC6 = BC6o;
    else
        BC1 = BC1o;
        BC2 = BC2o;
        BC3 = BC3o;
        BC4 = BC4o;
        BC5 = BC5o;
        BC6 = BC6o;
    end
end

```

```

for j = 2:q % Edge 8
    if isnan(T(i,j,k))
    elseif BC2(1) == 0 || BC6(1) == 0
    else
        if isnan(T(i,j-1,k))
            if BC3(1) == 0 % internal corner
            else
                tstar = dt/rho(i,j,k);
                Rconvx = BC2(2)/dx;
                Rconvy = BC3(2)/dy;
                Rconvz = BC6(2)/dz;
                Rminusx = 1/(dx*(Rx(i-1,j,k)+Rx(i,j,k)));
                Rplusy = 1/(dy*(Ry(i,j+1,k)+Ry(i,j,k)));
                Rminusz = 1/(dz*(Rz(i,j,k-1)+Rz(i,j,k)));
                Rtotal = Rminusx + Rconvy + Rminusz + Rconvx + Rplusy
+ Rconvz;
                H(i,j,k) = (1-
(tstar/cp(i,j,k))*Rtotal)*Ho(i,j,k)+tstar*(...
                Rminusx*(Ho(i-1,j,k)-f(i-1,j,k)*L)/cp(i-
1,j,k)+Rconvx*BC2(3)+...
                Rconvy*BC3(3)+Rplusy*(Ho(i,j+1,k)-
f(i,j+1,k)*L)/cp(i,j+1,k)+...
                Rminusz*(Ho(i,j,k-1)-f(i,j,k-1)*L)/cp(i,j,k-
1)+Rconvz*BC6(3));
            end
        elseif isnan(T(i,j+1,k))
            if BC4(1) == 0 % internal corner
            else
                tstar = dt/rho(i,j,k);
                Rconvx = BC2(2)/dx;
                Rconvy = BC4(2)/dy;
                Rconvz = BC6(2)/dz;
                Rminusx = 1/(dx*(Rx(i-1,j,k)+Rx(i,j,k)));
                Rminusy = 1/(dy*(Ry(i,j-1,k)+Ry(i,j,k)));
                Rminusz = 1/(dz*(Rz(i,j,k-1)+Rz(i,j,k)));
                Rtotal = Rminusx + Rminusy + Rminusz + Rconvx +
Rconvy + Rconvz;
                H(i,j,k) = (1-
(tstar/cp(i,j,k))*Rtotal)*Ho(i,j,k)+tstar*(...
                Rminusx*(Ho(i-1,j,k)-f(i-1,j,k)*L)/cp(i-
1,j,k)+Rconvx*BC2(3)+...
                Rminusy*(Ho(i,j-1,k)-f(i,j-1,k)*L)/cp(i,j-
1,k)+Rconvy*BC4(3)+...
                Rminusz*(Ho(i,j,k-1)-f(i,j,k-1)*L)/cp(i,j,k-
1)+Rconvz*BC6(2));
            end
        else
            tstar = dt/rho(i,j,k);
            Rconvx = BC2(2)/dx;
            Rconvz = BC6(2)/dz;
            Rminusx = 1/(dx*(Rx(i-1,j,k)+Rx(i,j,k)));
            Rminusy = 1/(dy*(Ry(i,j-1,k)+Ry(i,j,k)));
            Rplusy = 1/(dy*(Ry(i,j+1,k)+Ry(i,j,k)));
            Rminusz = 1/(dz*(Rz(i,j,k-1)+Rz(i,j,k)));
            Rtotal = Rminusx + Rminusy + Rminusz + Rconvx + Rplusy +
Rconvz;

```

```

        H(i,j,k) = (1-
(tstar/cp(i,j,k))*Rtotal)*Ho(i,j,k)+tstar*(...
        Rminusx*(Ho(i-1,j,k)-f(i-1,j,k)*L)/cp(i-
1,j,k)+Rconvx*BC2(3)+...
        Rminusy*(Ho(i,j-1,k)-f(i,j-1,k)*L)/cp(i,j-
1,k)+Rplusy*(Ho(i,j+1,k)-f(i,j+1,k)*L)/cp(i,j+1,k)+...
        Rminusz*(Ho(i,j,k-1)-f(i,j,k-1)*L)/cp(i,j,k-
1)+Rconvz*BC6(3));
        end
    end
end
end
for j = 1
    for k = 1
        for i = 2:p % Edge 9
            if isnan(T(i,j,k))
            elseif BC3(1) == 0 || BC5(1) == 0
            else
                if isnan(T(i-1,j,k))
                    if BC1(1) == 0 % internal corner
                    else
                        tstar = dt/rho(i,j,k);
                        Rconvx = BC1(2)/dx;
                        Rconvy = BC3(2)/dy;
                        Rconvz = BC5(2)/dz;
                        Rplusx = 1/(dx*(Rx(i+1,j,k)+Rx(i,j,k)));
                        Rplusy = 1/(dy*(Ry(i,j+1,k)+Ry(i,j,k)));
                        Rplusz = 1/(dz*(Rz(i,j,k+1)+Rz(i,j,k)));
                        Rtotal = Rconvx + Rconvy + Rconvz + Rplusx + Rplusy +
Rplusz;
                        H(i,j,k) = (1-
(tstar/cp(i,j,k))*Rtotal)*Ho(i,j,k)+tstar*(...
                        Rconvx*BC1(3)+Rplusx*(Ho(i+1,j,k)-
f(i+1,j,k)*L)/cp(i+1,j,k)+...
                        Rconvy*BC3(3)+Rplusy*(Ho(i,j+1,k)-
f(i,j+1,k)*L)/cp(i,j+1,k)+...
                        Rconvz*BC5(3)+Rplusz*(Ho(i,j,k+1)-
f(i,j,k+1)*L)/cp(i,j,k+1));
                        end
                    elseif isnan(T(i+1,j,k))
                    if BC2(1) == 0 % internal corner
                    else
                        tstar = dt/rho(i,j,k);
                        Rconvx = BC2(2)/dx;
                        Rconvy = BC3(2)/dy;
                        Rconvz = BC5(2)/dz;
                        Rminusx = 1/(dx*(Rx(i-1,j,k)+Rx(i,j,k)));
                        Rplusy = 1/(dy*(Ry(i,j+1,k)+Ry(i,j,k)));
                        Rplusz = 1/(dz*(Rz(i,j,k+1)+Rz(i,j,k)));
                        Rtotal = Rminusx + Rconvy + Rconvz + Rconvx + Rplusy
+ Rplusz;
                        H(i,j,k) = (1-
(tstar/cp(i,j,k))*Rtotal)*Ho(i,j,k)+tstar*(...
                        Rminusx*(Ho(i-1,j,k)-f(i-1,j,k)*L)/cp(i-
1,j,k)+Rconvx*BC2(3)+...
                        Rconvy*BC3(3)+Rplusy*(Ho(i,j+1,k)-
f(i,j+1,k)*L)/cp(i,j+1,k)+...

```

```

                                Rconvz*BC5(3)+Rplusz*(Hp(i,j,k+1)-
f(i,j,k+1)*L)/cp(i,j,k+1));
                                end
                                else
                                tstar = dt/rho(i,j,k);
                                Rconvy = BC3(2)/dy;
                                Rconvz = BC5(2)/dz;
                                Rminusx = 1/(dx*(Rx(i-1,j,k)+Rx(i,j,k)));
                                Rplusx = 1/(dx*(Rx(i+1,j,k)+Rx(i,j,k)));
                                Rplusy = 1/(dy*(Ry(i,j+1,k)+Ry(i,j,k)));
                                Rplusz = 1/(dz*(Rz(i,j,k+1)+Rz(i,j,k)));
                                Rtotal = Rminusx + Rconvy + Rconvz + Rplusx + Rplusy +
Rplusz;
                                H(i,j,k) = (1-
(tstar/cp(i,j,k))*Rtotal)*Ho(i,j,k)+tstar*(...
                                Rminusx*(Ho(i-1,j,k)-f(i-1,j,k)*L)/cp(i-
1,j,k)+Rplusx*(Ho(i+1,j,k)-f(i+1,j,k)*L)/cp(i+1,j,k)+...
                                Rconvy*BC3(3)+Rplusy*(Ho(i,j+1,k)-
f(i,j+1,k)*L)/cp(i,j+1,k)+...
                                Rconvz*BC5(3)+Rplusz*(Ho(i,j,k+1)-
f(i,j,k+1)*L)/cp(i,j,k+1));
                                end
                                end
                                end
                                end
                                end
                                for k = r1
                                if k > rlevel
                                BC1 = BC6o;
                                BC2 = BC6o;
                                BC3 = BC6o;
                                BC4 = BC6o;
                                BC5 = BC5o;
                                BC6 = BC6o;
                                else
                                BC1 = BC1o;
                                BC2 = BC2o;
                                BC3 = BC3o;
                                BC4 = BC4o;
                                BC5 = BC5o;
                                BC6 = BC6o;
                                end
                                for i = 2:p % Edge 10
                                if isnan(T(i,j,k))
                                elseif BC3(1) == 0 || BC6(1) == 0
                                else
                                if isnan(T(i-1,j,k))
                                if BC1(1) == 0 % internal corner
                                else
                                tstar = dt/rho(i,j,k);
                                Rconvx = BC1(2)/dx;
                                Rconvy = BC3(2)/dy;
                                Rconvz = BC6(2)/dz;
                                Rplusx = 1/(dx*(Rx(i+1,j,k)+Rx(i,j,k)));
                                Rplusy = 1/(dy*(Ry(i,j+1,k)+Ry(i,j,k)));
                                Rminusz = 1/(dz*(Rz(i,j,k-1)+Rz(i,j,k)));
                                Rtotal = Rconvx + Rconvy + Rminusz + Rplusx + Rplusy
+ Rconvz;

```

```

                H(i,j,k) = (1-
(tstar/cp(i,j,k))*Rtotal)*Ho(i,j,k)+tstar*(...
                Rconvx*BC1(3)+Rplusx*(Ho(i+1,j,k)-
f(i+1,j,k)*L)/cp(i+1,j,k)+...
                Rconvy*BC3(3)+Rplusy*(Ho(i,j+1,k)-
f(i,j+1,k)*L)/cp(i,j+1,k)+...
                Rminusz*(Ho(i,j,k-1)-f(i,j,k-1)*L)/cp(i,j,k-
1)+Rconvz*BC6(3));
            end
        elseif isnan(T(i+1,j,k))
            if BC2(1) == 0 % internal corner
                else
                    tstar = dt/rho(i,j,k);
                    Rconvx = BC2(2)/dx;
                    Rconvy = BC3(2)/dy;
                    Rconvz = BC6(2)/dz;
                    Rminusx = 1/(dx*(Rx(i-1,j,k)+Rx(i,j,k)));
                    Rplusy = 1/(dy*(Ry(i,j+1,k)+Ry(i,j,k)));
                    Rminusz = 1/(dz*(Rz(i,j,k-1)+Rz(i,j,k)));
                    Rtotal = Rminusx + Rconvy + Rminusz + Rconvx + Rplusy
+ Rconvz;
                    H(i,j,k) = (1-
(tstar/cp(i,j,k))*Rtotal)*Ho(i,j,k)+tstar*(...
                    Rminusx*(Ho(i-1,j,k)-f(i-1,j,k)*L)/cp(i-
1,j,k)+Rconvx*BC2(3)+...
                    Rconvy*BC3(3)+Rplusy*(Ho(i,j+1,k)-
f(i,j+1,k)*L)/cp(i,j+1,k)+...
                    Rminusz*(Ho(i,j,k-1)-f(i,j,k-1)*L)/cp(i,j,k-
1)+Rconvz*BC6(3));
                end
            else
                tstar = dt/rho(i,j,k);
                Rconvy = BC3(2)/dy;
                Rconvz = BC6(2)/dz;
                Rminusx = 1/(dx*(Rx(i-1,j,k)+Rx(i,j,k)));
                Rplusx = 1/(dx*(Rx(i+1,j,k)+Rx(i,j,k)));
                Rplusy = 1/(dy*(Ry(i,j+1,k)+Ry(i,j,k)));
                Rminusz = 1/(dz*(Rz(i,j,k-1)+Rz(i,j,k)));
                Rtotal = Rminusx + Rconvy + Rminusz + Rplusx + Rplusy +
Rconvz;
                H(i,j,k) = (1-
(tstar/cp(i,j,k))*Rtotal)*Ho(i,j,k)+tstar*(...
                Rminusx*(Ho(i-1,j,k)-f(i-1,j,k)*L)/cp(i-
1,j,k)+Rplusx*(Ho(i+1,j,k)-f(i+1,j,k)*L)/cp(i+1,j,k)+...
                Rconvy*BC3(3)+Rplusy*(Ho(i,j+1,k)-
f(i,j+1,k)*L)/cp(i,j+1,k)+...
                Rminusz*(Ho(i,j,k-1)-f(i,j,k-1)*L)/cp(i,j,k-
1)+Rconvz*BC6(3));
            end
        end
    end
end
for j = q1
    for k = 1
        for i = 2:p % Edge 11
            if isnan(T(i,j,k))
                elseif BC4(1) == 0 || BC5(1) == 0

```

```

else
    if isnan(T(i-1,j,k))
        if BC1(1) == 0 % internal corner
            else
                tstar = dt/rho(i,j,k);
                Rconvx = BC1(2)/dx;
                Rconvy = BC4(2)/dy;
                Rconvz = BC5(2)/dz;
                Rplusx = 1/(dx*(Rx(i+1,j,k)+Rx(i,j,k)));
                Rminusy = 1/(dy*(Ry(i,j-1,k)+Ry(i,j,k)));
                Rplusz = 1/(dz*(Rz(i,j,k+1)+Rz(i,j,k)));
                Rtotal = Rconvx + Rminusy + Rconvz + Rplusx + Rconvy
+ Rplusz;
                H(i,j,k) = (1-
(tstar/cp(i,j,k))*Rtotal)*Ho(i,j,k)+tstar*(...
                Rconvx*BC1(3)+Rplusx*(Ho(i+1,j,k)-
f(i+1,j,k)*L)/cp(i+1,j,k)+...
                Rminusy*(Ho(i,j-1,k)-f(i,j-1,k)*L)/cp(i,j-
1,k)+Rconvy*BC4(3)+...
                Rconvz*BC5(3)+Rplusz*(Ho(i,j,k+1)-
f(i,j,k+1)*L)/cp(i,j,k+1));
            end
        elseif isnan(T(i+1,j,k))
            if BC2(1) == 0 % internal corner
                else
                    tstar = dt/rho(i,j,k);
                    Rconvx = BC2(2)/dx;
                    Rconvy = BC4(2)/dy;
                    Rconvz = BC5(2)/dz;
                    Rminusx = 1/(dx*(Rx(i-1,j,k)+Rx(i,j,k)));
                    Rminusy = 1/(dy*(Ry(i,j-1,k)+Ry(i,j,k)));
                    Rplusz = 1/(dz*(Rz(i,j,k+1)+Rz(i,j,k)));
                    Rtotal = Rminusx + Rminusy + Rconvz + Rconvx + Rconvy
+ Rplusz;
                    H(i,j,k) = (1-
(tstar/cp(i,j,k))*Rtotal)*Ho(i,j,k)+tstar*(...
                    Rminusx*(Ho(i-1,j,k)-f(i-1,j,k)*L)/cp(i-
1,j,k)+Rconvx*BC2(3)+...
                    Rminusy*(Ho(i,j-1,k)-f(i,j-1,k)*L)/cp(i,j-
1,k)+Rconvy*BC4(3)+...
                    Rconvz*BC5(3)+Rplusz*(Ho(i,j,k+1)-
f(i,j,k+1)*L)/cp(i,j,k+1));
                end
            else
                tstar = dt/rho(i,j,k);
                Rconvy = BC4(2)/dy;
                Rconvz = BC5(2)/dz;
                Rminusx = 1/(dx*(Rx(i-1,j,k)+Rx(i,j,k)));
                Rplusx = 1/(dx*(Rx(i+1,j,k)+Rx(i,j,k)));
                Rminusy = 1/(dy*(Ry(i,j-1,k)+Ry(i,j,k)));
                Rplusz = 1/(dz*(Rz(i,j,k+1)+Rz(i,j,k)));
                Rtotal = Rminusx + Rminusy + Rconvz + Rplusx + Rconvy +
Rplusz;
                H(i,j,k) = (1-
(tstar/cp(i,j,k))*Rtotal)*Ho(i,j,k)+tstar*(...
                Rminusx*(Ho(i-1,j,k)-f(i-1,j,k)*L)/cp(i-
1,j,k)+Rplusx*(Ho(i+1,j,k)-f(i+1,j,k)*L)/cp(i+1,j,k)+...

```

```

1,k)+Rconvy*BC4(3)+...
Rminusy*(Ho(i,j-1,k)-f(i,j-1,k)*L)/cp(i,j-
Rconvz*BC5(3)+Rplusz*(Ho(i,j,k+1)-
f(i,j,k+1)*L)/cp(i,j,k+1));
end
end
end
end
for k = r1
if k > rlevel
BC1 = BC6o;
BC2 = BC6o;
BC3 = BC6o;
BC4 = BC6o;
BC5 = BC5o;
BC6 = BC6o;
else
BC1 = BC1o;
BC2 = BC2o;
BC3 = BC3o;
BC4 = BC4o;
BC5 = BC5o;
BC6 = BC6o;
end

for i = 2:p % Edge 12
if isnan(T(i,j,k))
elseif BC4(1) == 0 || BC6(1) == 0
else
if isnan(T(i-1,j,k))
if BC1(1) == 0 % internal corner
else
tstar = dt/rho(i,j,k);
Rconvx = BC1(2)/dx;
Rconvy = BC4(2)/dy;
Rconvz = BC6(2)/dz;
Rplusx = 1/(dx*(Rx(i+1,j,k)+Rx(i,j,k)));
Rminusy = 1/(dy*(Ry(i,j-1,k)+Ry(i,j,k)));
Rminusz = 1/(dz*(Rz(i,j,k-1)+Rz(i,j,k)));
Rtotal = Rconvx + Rminusy + Rminusz + Rplusx + Rconvy
+ Rconvz;
H(i,j,k) = (1-
(tstar/cp(i,j,k))*Rtotal)*Ho(i,j,k)+tstar*(...
Rconvx*BC1(3)+Rplusx*(Ho(i+1,j,k)-
f(i+1,j,k)*L)/cp(i+1,j,k)+...
Rminusy*(Ho(i,j-1,k)-f(i,j-1,k)*L)/cp(i,j-
1,k)+Rconvy*BC4(3)+...
Rminusz*(Ho(i,j,k-1)-f(i,j,k-1)*L)/cp(i,j,k-
1)+Rconvz*BC6(3));
end
elseif isnan(T(i+1,j,k))
if BC2(1) == 0 % internal corner
else
tstar = dt/rho(i,j,k);
Rconvx = BC2(2)/dx;
Rconvy = BC4(2)/dy;
Rconvz = BC6(2)/dz;
Rminusx = 1/(dx*(Rx(i-1,j,k)+Rx(i,j,k)));

```

```

Rminusy = 1/(dy*(Ry(i,j-1,k)+Ry(i,j,k)));
Rminusz = 1/(dz*(Rz(i,j,k-1)+Rz(i,j,k)));
Rtotal = Rminusx + Rminusy + Rminusz + Rconvx +
Rconvy + Rconvz;
    H(i,j,k) = (1-
(tstar/cp(i,j,k))*Rtotal)*Ho(i,j,k)+tstar*(...
    Rminusx*(Ho(i-1,j,k)-f(i-1,j,k)*L)/cp(i-
1,j,k)+Rconvx*BC2(3)+...
    Rminusy*(Ho(i,j-1,k)-f(i,j-1,k)*L)/cp(i,j-
1,k)+Rconvy*BC4(3)+...
    Rminusz*(Ho(i,j,k-1)-f(i,j,k-1)*L)/cp(i,j,k-
1)+Rconvz*BC6(2));
    end
else
    tstar = dt/rho(i,j,k);
    Rconvy = BC4(2)/dy;
    Rconvz = BC6(2)/dz;
    Rminusx = 1/(dx*(Rx(i-1,j,k)+Rx(i,j,k)));
    Rplusx = 1/(dx*(Rx(i+1,j,k)+Rx(i,j,k)));
    Rminusy = 1/(dy*(Ry(i,j-1,k)+Ry(i,j,k)));
    Rminusz = 1/(dz*(Rz(i,j,k-1)+Rz(i,j,k)));
    Rtotal = Rminusx + Rminusy + Rminusz + Rplusx + Rconvy +
Rconvz;
    H(i,j,k) = (1-
(tstar/cp(i,j,k))*Rtotal)*Ho(i,j,k)+tstar*(...
    Rminusx*(Ho(i-1,j,k)-f(i-1,j,k)*L)/cp(i-
1,j,k)+Rplusx*(Ho(i+1,j,k)-f(i+1,j,k)*L)/cp(i+1,j,k)+...
    Rminusy*(Ho(i,j-1,k)-f(i,j-1,k)*L)/cp(i,j-
1,k)+Rconvy*BC4(3)+...
    Rminusz*(Ho(i,j,k-1)-f(i,j,k-1)*L)/cp(i,j,k-
1)+Rconvz*BC6(3));
    end
end
end
end

% Corner nodes
for i = 1
    for j = 1
        for k = 1 % Corner 1
            if isnan(T(i,j,k))
                elseif BC1(1) == 0 || BC3(1) == 0 || BC5(1) == 0
                    else
                        tstar = dt/rho(i,j,k);
                        Rconvx = BC1(2)/dx;
                        Rconvy = BC3(2)/dy;
                        Rconvz = BC5(2)/dz;
                        Rplusx = 1/(dx*(Rx(i+1,j,k)+Rx(i,j,k)));
                        Rplusy = 1/(dy*(Ry(i,j+1,k)+Ry(i,j,k)));
                        Rplusz = 1/(dz*(Rz(i,j,k+1)+Rz(i,j,k)));
                        Rtotal = Rconvx + Rconvy + Rconvz + Rplusx + Rplusy + Rplusz;
                        H(i,j,k) = (1-(tstar/cp(i,j,k))*Rtotal)*Ho(i,j,k)+tstar*(...
                            Rconvx*BC1(3)+Rplusx*(Ho(i+1,j,k)-
f(i+1,j,k)*L)/cp(i+1,j,k)+...
                            Rconvy*BC3(3)+Rplusy*(Ho(i,j+1,k)-
f(i,j+1,k)*L)/cp(i,j+1,k)+...

```

```

                                Rconvz*BC5(3)+Rplusz*(Ho(i,j,k+1)-
f(i,j,k+1)*L)/cp(i,j,k+1));
    end
end
for k = r1          % Corner 2
    if k > rlevel
        BC1 = BC6o;
        BC2 = BC6o;
        BC3 = BC6o;
        BC4 = BC6o;
        BC5 = BC5o;
        BC6 = BC6o;
    else
        BC1 = BC1o;
        BC2 = BC2o;
        BC3 = BC3o;
        BC4 = BC4o;
        BC5 = BC5o;
        BC6 = BC6o;
    end

    if isnan(T(i,j,k))
elseif BC1(1) == 0 || BC3(1) == 0 || BC6(1) == 0
else
        tstar = dt/rho(i,j,k);
        Rconvx = BC1(2)/dx;
        Rconvy = BC3(2)/dy;
        Rconvz = BC6(2)/dz;
        Rplusx = 1/(dx*(Rx(i+1,j,k)+Rx(i,j,k)));
        Rplusy = 1/(dy*(Ry(i,j+1,k)+Ry(i,j,k)));
        Rminusz = 1/(dz*(Rz(i,j,k-1)+Rz(i,j,k)));
        Rtotal = Rconvx + Rconvy + Rminusz + Rplusx + Rplusy +
Rconvz;
        H(i,j,k) = (1-(tstar/cp(i,j,k))*Rtotal)*Ho(i,j,k)+tstar*(...
        Rconvx*BC1(3)+Rplusx*(Ho(i+1,j,k)-
f(i+1,j,k)*L)/cp(i+1,j,k)+...
        Rconvy*BC3(3)+Rplusy*(Ho(i,j+1,k)-
f(i,j+1,k)*L)/cp(i,j+1,k)+...
        Rminusz*(Ho(i,j,k-1)-f(i,j,k-1)*L)/cp(i,j,k-
1)+Rconvz*BC6(3));
    end
end
end
for j = q1
    for k = 1          % Corner 3
        if isnan(T(i,j,k))
elseif BC1(1) == 0 || BC4(1) == 0 || BC5(1) == 0
else
            tstar = dt/rho(i,j,k);
            Rconvx = BC1(2)/dx;
            Rconvy = BC4(2)/dy;
            Rconvz = BC5(2)/dz;
            Rplusx = 1/(dx*(Rx(i+1,j,k)+Rx(i,j,k)));
            Rminusy = 1/(dy*(Ry(i,j-1,k)+Ry(i,j,k)));
            Rplusz = 1/(dz*(Rz(i,j,k+1)+Rz(i,j,k)));
            Rtotal = Rconvx + Rminusy + Rconvz + Rplusx + Rconvy +
Rplusz;
            H(i,j,k) = (1-(tstar/cp(i,j,k))*Rtotal)*Ho(i,j,k)+tstar*(...

```

```

                Rconvx*BC1(3)+Rplusx*(Ho(i+1,j,k)-
f(i+1,j,k)*L)/cp(i+1,j,k)+...
                Rminusy*(Ho(i,j-1,k)-f(i,j-1,k)*L)/cp(i,j-
1,k)+Rconvy*BC4(3)+...
                Rconvz*BC5(3)+Rplusz*(Ho(i,j,k+1)-
f(i,j,k+1)*L)/cp(i,j,k+1));
            end
        end
    for k = r1      % Corner 4
        if k > rlevel
            BC1 = BC6o;
            BC2 = BC6o;
            BC3 = BC6o;
            BC4 = BC6o;
            BC5 = BC5o;
            BC6 = BC6o;
        else
            BC1 = BC1o;
            BC2 = BC2o;
            BC3 = BC3o;
            BC4 = BC4o;
            BC5 = BC5o;
            BC6 = BC6o;
        end

        if isnan(T(i,j,k))
        elseif BC1(1) == 0 || BC4(1) == 0 || BC6(1) == 0
        else
            tstar = dt/rho(i,j,k);
            Rconvx = BC1(2)/dx;
            Rconvy = BC4(2)/dy;
            Rconvz = BC6(2)/dz;
            Rplusx = 1/(dx*(Rx(i+1,j,k)+Rx(i,j,k)));
            Rminusy = 1/(dy*(Ry(i,j-1,k)+Ry(i,j,k)));
            Rminusz = 1/(dz*(Rz(i,j,k-1)+Rz(i,j,k)));
            Rtotal = Rconvx + Rminusy + Rminusz + Rplusx + Rconvy +
Rconvz;
            H(i,j,k) = (1-(tstar/cp(i,j,k))*Rtotal)*Ho(i,j,k)+tstar*(...
                Rconvx*BC1(3)+Rplusx*(Ho(i+1,j,k)-
f(i+1,j,k)*L)/cp(i+1,j,k)+...
                Rminusy*(Ho(i,j-1,k)-f(i,j-1,k)*L)/cp(i,j-
1,k)+Rconvy*BC4(3)+...
                Rminusz*(Ho(i,j,k-1)-f(i,j,k-1)*L)/cp(i,j,k-
1)+Rconvz*BC6(3));
            end
        end
    end
end
for i = p1
    for j = 1
        for k = 1      % Corner 5
            if isnan(T(i,j,k))
            elseif BC2(1) == 0 || BC3(1) == 0 || BC5(1) == 0
            else
                tstar = dt/rho(i,j,k);
                Rconvx = BC2(2)/dx;
                Rconvy = BC3(2)/dy;
                Rconvz = BC5(2)/dz;

```

```

Rminusx = 1/(dx*(Rx(i-1,j,k)+Rx(i,j,k)));
Rplusy = 1/(dy*(Ry(i,j+1,k)+Ry(i,j,k)));
Rplusz = 1/(dz*(Rz(i,j,k+1)+Rz(i,j,k)));
Rtotal = Rminusx + Rconvy + Rconvz + Rconvx + Rplusy +
Rplusz;
    H(i,j,k) = (1-(tstar/cp(i,j,k))*Rtotal)*Ho(i,j,k)+tstar*(...
        Rminusx*(Ho(i-1,j,k)-f(i-1,j,k)*L)/cp(i-
1,j,k)+Rconvx*BC2(3)+...
        Rconvy*BC3(3)+Rplusy*(Ho(i,j+1,k)-
f(i,j+1,k)*L)/cp(i,j+1,k)+...
        Rconvz*BC5(3)+Rplusz*(Hp(i,j,k+1)-
f(i,j,k+1)*L)/cp(i,j,k+1));
    end
end
for k = r1      % Corner 6
    if k > rlevel
        BC1 = BC6o;
        BC2 = BC6o;
        BC3 = BC6o;
        BC4 = BC6o;
        BC5 = BC5o;
        BC6 = BC6o;
    else
        BC1 = BC1o;
        BC2 = BC2o;
        BC3 = BC3o;
        BC4 = BC4o;
        BC5 = BC5o;
        BC6 = BC6o;
    end

    if isnan(T(i,j,k))
    elseif BC2(1) == 0 || BC3(1) == 0 || BC6(1) == 0
    else
        tstar = dt/rho(i,j,k);
        Rconvx = BC2(2)/dx;
        Rconvy = BC3(2)/dy;
        Rconvz = BC6(2)/dz;
        Rminusx = 1/(dx*(Rx(i-1,j,k)+Rx(i,j,k)));
        Rplusy = 1/(dy*(Ry(i,j+1,k)+Ry(i,j,k)));
        Rminusz = 1/(dz*(Rz(i,j,k-1)+Rz(i,j,k)));
        Rtotal = Rminusx + Rconvy + Rminusz + Rconvx + Rplusy +
Rconvz;
        H(i,j,k) = (1-(tstar/cp(i,j,k))*Rtotal)*Ho(i,j,k)+tstar*(...
            Rminusx*(Ho(i-1,j,k)-f(i-1,j,k)*L)/cp(i-
1,j,k)+Rconvx*BC2(3)+...
            Rconvy*BC3(3)+Rplusy*(Ho(i,j+1,k)-
f(i,j+1,k)*L)/cp(i,j+1,k)+...
            Rminusz*(Ho(i,j,k-1)-f(i,j,k-1)*L)/cp(i,j,k-
1)+Rconvz*BC6(3));
        end
    end
end
for j = q1
    for k = 1      % Corner 7
        if isnan(T(i,j,k))
        elseif BC2(1) == 0 || BC4(1) == 0 || BC5(1) == 0
        else

```

```

        tstar = dt/rho(i,j,k);
        Rconvx = BC2(2)/dx;
        Rconvy = BC4(2)/dy;
        Rconvz = BC5(2)/dz;
        Rminusx = 1/(dx*(Rx(i-1,j,k)+Rx(i,j,k)));
        Rminusy = 1/(dy*(Ry(i,j-1,k)+Ry(i,j,k)));
        Rplusz = 1/(dz*(Rz(i,j,k+1)+Rz(i,j,k)));
        Rtotal = Rminusx + Rminusy + Rconvz + Rconvx + Rconvy +
Rplusz;
        H(i,j,k) = (1-(tstar/cp(i,j,k))*Rtotal)*Ho(i,j,k)+tstar*(...
            Rminusx*(Ho(i-1,j,k)-f(i-1,j,k)*L)/cp(i-
1,j,k)+Rconvx*BC2(3)+...
            Rminusy*(Ho(i,j-1,k)-f(i,j-1,k)*L)/cp(i,j-
1,k)+Rconvy*BC4(3)+...
            Rconvz*BC5(3)+Rplusz*(Ho(i,j,k+1)-
f(i,j,k+1)*L)/cp(i,j,k+1));
        end
    end
    for k = r1      % Corner 8
        if k > rlevel
            BC1 = BC6o;
            BC2 = BC6o;
            BC3 = BC6o;
            BC4 = BC6o;
            BC5 = BC5o;
            BC6 = BC6o;
        else
            BC1 = BC1o;
            BC2 = BC2o;
            BC3 = BC3o;
            BC4 = BC4o;
            BC5 = BC5o;
            BC6 = BC6o;
        end
    end

    if isnan(T(i,j,k))
    elseif BC2(1) == 0 || BC4(1) == 0 || BC6(1) == 0
    else
        tstar = dt/rho(i,j,k);
        Rconvx = BC2(2)/dx;
        Rconvy = BC4(2)/dy;
        Rconvz = BC6(2)/dz;
        Rminusx = 1/(dx*(Rx(i-1,j,k)+Rx(i,j,k)));
        Rminusy = 1/(dy*(Ry(i,j-1,k)+Ry(i,j,k)));
        Rminusz = 1/(dz*(Rz(i,j,k-1)+Rz(i,j,k)));
        Rtotal = Rminusx + Rminusy + Rminusz + Rconvx + Rconvy +
Rconvz;
        H(i,j,k) = (1-(tstar/cp(i,j,k))*Rtotal)*Ho(i,j,k)+tstar*(...
            Rminusx*(Ho(i-1,j,k)-f(i-1,j,k)*L)/cp(i-
1,j,k)+Rconvx*BC2(3)+...
            Rminusy*(Ho(i,j-1,k)-f(i,j-1,k)*L)/cp(i,j-
1,k)+Rconvy*BC4(3)+...
            Rminusz*(Ho(i,j,k-1)-f(i,j,k-1)*L)/cp(i,j,k-
1)+Rconvz*BC6(2));
        end
    end
end
end
end

```

```

% Internal nodes
for i = 2:p1-1
    for j = 2:q1-1
        for k = 2:r1-1
            if k > rlevel
                BC1 = BC6o;
                BC2 = BC6o;
                BC3 = BC6o;
                BC4 = BC6o;
                BC5 = BC5o;
                BC6 = BC6o;
            else
                BC1 = BC1o;
                BC2 = BC2o;
                BC3 = BC3o;
                BC4 = BC4o;
                BC5 = BC5o;
                BC6 = BC6o;
            end

            if isnan(T(i-1,j,k)) && isnan(T(i,j-1,k)) && isnan(T(i,j,k-1))
                if BC1(1) == 0 || BC3(1) == 0 || BC5(1) == 0 % Corner 1
                    else
                        tstar = dt/rho(i,j,k);
                        Rconvx = BC1(2)/dx;
                        Rconvy = BC3(2)/dy;
                        Rconvz = BC5(2)/dz;
                        Rplusx = 1/(dx*(Rx(i+1,j,k)+Rx(i,j,k)));
                        Rplusy = 1/(dy*(Ry(i,j+1,k)+Ry(i,j,k)));
                        Rplusz = 1/(dz*(Rz(i,j,k+1)+Rz(i,j,k)));
                        Rtotal = Rconvx + Rconvy + Rconvz + Rplusx + Rplusy +
Rplusz;
                        H(i,j,k) = (1-
(tstar/cp(i,j,k))*Rtotal)*Ho(i,j,k)+tstar*(...
                    Rconvx*BC1(3)+Rplusx*(Ho(i+1,j,k)-
f(i+1,j,k)*L)/cp(i+1,j,k)+...
                    Rconvy*BC3(3)+Rplusy*(Ho(i,j+1,k)-
f(i,j+1,k)*L)/cp(i,j+1,k)+...
                    Rconvz*BC5(3)+Rplusz*(Ho(i,j,k+1)-
f(i,j,k+1)*L)/cp(i,j,k+1));
                    end
                elseif isnan(T(i-1,j,k)) && isnan(T(i,j-1,k)) &&
isnan(T(i,j,k+1))
                    if BC1(1) == 0 || BC3(1) == 0 || BC6(1) == 0 % Corner 2
                        else
                            tstar = dt/rho(i,j,k);
                            Rconvx = BC1(2)/dx;
                            Rconvy = BC3(2)/dy;
                            Rconvz = BC6(2)/dz;
                            Rplusx = 1/(dx*(Rx(i+1,j,k)+Rx(i,j,k)));
                            Rplusy = 1/(dy*(Ry(i,j+1,k)+Ry(i,j,k)));
                            Rminusz = 1/(dz*(Rz(i,j,k-1)+Rz(i,j,k)));
                            Rtotal = Rconvx + Rconvy + Rminusz + Rplusx + Rplusy +
Rconvz;
                            H(i,j,k) = (1-
(tstar/cp(i,j,k))*Rtotal)*Ho(i,j,k)+tstar*(...

```

```

        Rconvx*BC1(3)+Rplusx*(Ho(i+1,j,k)-
f(i+1,j,k)*L)/cp(i+1,j,k)+...
        Rconvy*BC3(3)+Rplusy*(Ho(i,j+1,k)-
f(i,j+1,k)*L)/cp(i,j+1,k)+...
        Rminusz*(Ho(i,j,k-1)-f(i,j,k-1)*L)/cp(i,j,k-
1)+Rconvz*BC6(3));
    end
elseif isnan(T(i-1,j,k)) && isnan(T(i,j+1,k)) && isnan(T(i,j,k-
1))
    if BC1(1) == 0 || BC4(1) == 0 || BC5(1) == 0 % Corner 3
    else
        tstar = dt/rho(i,j,k);
        Rconvx = BC1(2)/dx;
        Rconvy = BC4(2)/dy;
        Rconvz = BC5(2)/dz;
        Rplusx = 1/(dx*(Rx(i+1,j,k)+Rx(i,j,k)));
        Rminusy = 1/(dy*(Ry(i,j-1,k)+Ry(i,j,k)));
        Rplusz = 1/(dz*(Rz(i,j,k+1)+Rz(i,j,k)));
        Rtotal = Rconvx + Rminusy + Rconvz + Rplusx + Rconvy +
Rplusz;
        H(i,j,k) = (1-
(tstar/cp(i,j,k))*Rtotal)*Ho(i,j,k)+tstar*(...
        Rconvx*BC1(3)+Rplusx*(Ho(i+1,j,k)-
f(i+1,j,k)*L)/cp(i+1,j,k)+...
        Rminusy*(Ho(i,j-1,k)-f(i,j-1,k)*L)/cp(i,j-
1,k)+Rconvy*BC4(3)+...
        Rconvz*BC5(3)+Rplusz*(Ho(i,j,k+1)-
f(i,j,k+1)*L)/cp(i,j,k+1));
    end
elseif isnan(T(i-1,j,k)) && isnan(T(i,j+1,k)) &&
isnan(T(i,j,k+1))
    if BC1(1) == 0 || BC4(1) == 0 || BC6(1) == 0 % Corner 4
    else
        tstar = dt/rho(i,j,k);
        Rconvx = BC1(2)/dx;
        Rconvy = BC4(2)/dy;
        Rconvz = BC6(2)/dz;
        Rplusx = 1/(dx*(Rx(i+1,j,k)+Rx(i,j,k)));
        Rminusy = 1/(dy*(Ry(i,j-1,k)+Ry(i,j,k)));
        Rminusz = 1/(dz*(Rz(i,j,k-1)+Rz(i,j,k)));
        Rtotal = Rconvx + Rminusy + Rminusz + Rplusx + Rconvy +
Rconvz;
        H(i,j,k) = (1-
(tstar/cp(i,j,k))*Rtotal)*Ho(i,j,k)+tstar*(...
        Rconvx*BC1(3)+Rplusx*(Ho(i+1,j,k)-
f(i+1,j,k)*L)/cp(i+1,j,k)+...
        Rminusy*(Ho(i,j-1,k)-f(i,j-1,k)*L)/cp(i,j-
1,k)+Rconvy*BC4(3)+...
        Rminusz*(Ho(i,j,k-1)-f(i,j,k-1)*L)/cp(i,j,k-
1)+Rconvz*BC6(3));
    end
elseif isnan(T(i+1,j,k)) && isnan(T(i,j-1,k)) && isnan(T(i,j,k-
1))
    if BC2(1) == 0 || BC3(1) == 0 || BC5(1) == 0 % Corner 5
    else
        tstar = dt/rho(i,j,k);
        Rconvx = BC2(2)/dx;
        Rconvy = BC3(2)/dy;

```

```

Rconvz = BC5(2)/dz;
Rminusx = 1/(dx*(Rx(i-1,j,k)+Rx(i,j,k)));
Rplusy = 1/(dy*(Ry(i,j+1,k)+Ry(i,j,k)));
Rplusz = 1/(dz*(Rz(i,j,k+1)+Rz(i,j,k)));
Rtotal = Rminusx + Rconvy + Rconvz + Rconvx + Rplusy +
Rplusz;
    H(i,j,k) = (1-
(tstar/cp(i,j,k))*Rtotal)*Ho(i,j,k)+tstar*(...
    Rminusx*(Ho(i-1,j,k)-f(i-1,j,k)*L)/cp(i-
1,j,k)+Rconvx*BC2(3)+...
    Rconvy*BC3(3)+Rplusy*(Ho(i,j+1,k)-
f(i,j+1,k)*L)/cp(i,j+1,k)+...
    Rconvz*BC5(3)+Rplusz*(Hp(i,j,k+1)-
f(i,j,k+1)*L)/cp(i,j,k+1));
    end
elseif isnan(T(i+1,j,k)) && isnan(T(i,j-1,k)) &&
isnan(T(i,j,k+1))
    if BC2(1) == 0 || BC3(1) == 0 || BC6(1) == 0 % Corner 6
    else
        tstar = dt/rho(i,j,k);
        Rconvx = BC2(2)/dx;
        Rconvy = BC3(2)/dy;
        Rconvz = BC6(2)/dz;
        Rminusx = 1/(dx*(Rx(i-1,j,k)+Rx(i,j,k)));
        Rplusy = 1/(dy*(Ry(i,j+1,k)+Ry(i,j,k)));
        Rminusz = 1/(dz*(Rz(i,j,k-1)+Rz(i,j,k)));
        Rtotal = Rminusx + Rconvy + Rminusz + Rconvx + Rplusy +
Rconvz;
        H(i,j,k) = (1-
(tstar/cp(i,j,k))*Rtotal)*Ho(i,j,k)+tstar*(...
            Rminusx*(Ho(i-1,j,k)-f(i-1,j,k)*L)/cp(i-
1,j,k)+Rconvx*BC2(3)+...
            Rconvy*BC3(3)+Rplusy*(Ho(i,j+1,k)-
f(i,j+1,k)*L)/cp(i,j+1,k)+...
            Rminusz*(Ho(i,j,k-1)-f(i,j,k-1)*L)/cp(i,j,k-
1)+Rconvz*BC6(3));
        end
elseif isnan(T(i+1,j,k)) && isnan(T(i,j+1,k)) && isnan(T(i,j,k-
1))
    if BC2(1) == 0 || BC4(1) == 0 || BC5(1) == 0 % Corner 7
    else
        tstar = dt/rho(i,j,k);
        Rconvx = BC2(2)/dx;
        Rconvy = BC4(2)/dy;
        Rconvz = BC5(2)/dz;
        Rminusx = 1/(dx*(Rx(i-1,j,k)+Rx(i,j,k)));
        Rminusy = 1/(dy*(Ry(i,j-1,k)+Ry(i,j,k)));
        Rplusz = 1/(dz*(Rz(i,j,k+1)+Rz(i,j,k)));
        Rtotal = Rminusx + Rminusy + Rconvz + Rconvx + Rconvy +
Rplusz;
        H(i,j,k) = (1-
(tstar/cp(i,j,k))*Rtotal)*Ho(i,j,k)+tstar*(...
            Rminusx*(Ho(i-1,j,k)-f(i-1,j,k)*L)/cp(i-
1,j,k)+Rconvx*BC2(3)+...
            Rminusy*(Ho(i,j-1,k)-f(i,j-1,k)*L)/cp(i,j-
1,k)+Rconvy*BC4(3)+...
            Rconvz*BC5(3)+Rplusz*(Ho(i,j,k+1)-
f(i,j,k+1)*L)/cp(i,j,k+1));

```

```

end
elseif isnan(T(i+1,j,k)) && isnan(T(i,j+1,k)) &&
isnan(T(i,j,k+1))
if BC2(1) == 0 || BC4(1) == 0 || BC6(1) == 0 % Corner 8
else
tstar = dt/rho(i,j,k);
Rconvx = BC2(2)/dx;
Rconvy = BC4(2)/dy;
Rconvz = BC6(2)/dz;
Rminusx = 1/(dx*(Rx(i-1,j,k)+Rx(i,j,k)));
Rminusy = 1/(dy*(Ry(i,j-1,k)+Ry(i,j,k)));
Rminusz = 1/(dz*(Rz(i,j,k-1)+Rz(i,j,k)));
Rtotal = Rminusx + Rminusy + Rminusz + Rconvx + Rconvy +
Rconvz;
H(i,j,k) = (1-
(tstar/cp(i,j,k))*Rtotal)*Ho(i,j,k)+tstar*(...
Rminusx*(Ho(i-1,j,k)-f(i-1,j,k)*L)/cp(i-
1,j,k)+Rconvx*BC2(3)+...
Rminusy*(Ho(i,j-1,k)-f(i,j-1,k)*L)/cp(i,j-
1,k)+Rconvy*BC4(3)+...
Rminusz*(Ho(i,j,k-1)-f(i,j,k-1)*L)/cp(i,j,k-
1)+Rconvz*BC6(2));
end
elseif isnan(T(i-1,j,k)) && isnan(T(i,j-1,k))
if BC1(1) == 0 || BC3(1) == 0 % Edge 1
else
tstar = dt/rho(i,j,k);
Rconvx = BC1(2)/dx;
Rconvy = BC3(2)/dy;
Rplusx = 1/(dx*(Rx(i+1,j,k)+Rx(i,j,k)));
Rplusy = 1/(dy*(Ry(i,j+1,k)+Ry(i,j,k)));
Rminusz = 1/(dz*(Rz(i,j,k-1)+Rz(i,j,k)));
Rplusz = 1/(dz*(Rz(i,j,k+1)+Rz(i,j,k)));
Rtotal = Rconvx + Rconvy + Rminusz + Rplusx + Rplusy +
Rplusz;
H(i,j,k) = (1-
(tstar/cp(i,j,k))*Rtotal)*Ho(i,j,k)+tstar*(...
Rconvx*BC1(3)+Rplusx*(Ho(i+1,j,k)-
f(i+1,j,k)*L)/cp(i+1,j,k)+...
Rconvy*BC3(3)+Rplusy*(Ho(i,j+1,k)-
f(i,j+1,k)*L)/cp(i,j+1,k)+...
Rminusz*(Ho(i,j,k-1)-f(i,j,k-1)*L)/cp(i,j,k-
1)+Rplusz*(Ho(i,j,k+1)-f(i,j,k+1)*L)/cp(i,j,k+1));
end
elseif isnan(T(i-1,j,k)) && isnan(T(i,j+1,k))
if BC1(1) == 0 || BC4(1) == 0 % Edge 2
else
tstar = dt/rho(i,j,k);
Rconvx = BC1(2)/dx;
Rconvy = BC4(2)/dy;
Rplusx = 1/(dx*(Rx(i+1,j,k)+Rx(i,j,k)));
Rminusy = 1/(dy*(Ry(i,j-1,k)+Ry(i,j,k)));
Rminusz = 1/(dz*(Rz(i,j,k-1)+Rz(i,j,k)));
Rplusz = 1/(dz*(Rz(i,j,k+1)+Rz(i,j,k)));
Rtotal = Rconvx + Rminusy + Rminusz + Rplusx + Rconvy +
Rplusz;
H(i,j,k) = (1-
(tstar/cp(i,j,k))*Rtotal)*Ho(i,j,k)+tstar*(...

```

```

        Rconvx*BC1(3)+Rplusx*(Ho(i+1,j,k)-
f(i+1,j,k)*L)/cp(i+1,j,k)+...
        Rminusy*(Ho(i,j-1,k)-f(i,j-1,k)*L)/cp(i,j-
1,k)+Rconvy*BC4(3)+...
        Rminusz*(Ho(i,j,k-1)-f(i,j,k-1)*L)/cp(i,j,k-
1)+Rplusz*(Ho(i,j,k+1)-f(i,j,k+1)*L)/cp(i,j,k+1));
    end
elseif isnan(T(i-1,j,k)) && isnan(T(i,j,k-1))
    if BC1(1) == 0 || BC5(1) == 0 % Edge 3
    else
        tstar = dt/rho(i,j,k);
        Rconvx = BC1(2)/dx;
        Rconvz = BC5(2)/dz;
        Rplusx = 1/(dx*(Rx(i+1,j,k)+Rx(i,j,k)));
        Rminusy = 1/(dy*(Ry(i,j-1,k)+Ry(i,j,k)));
        Rplusy = 1/(dy*(Ry(i,j+1,k)+Ry(i,j,k)));
        Rplusz = 1/(dz*(Rz(i,j,k+1)+Rz(i,j,k)));
        Rtotal = Rconvx + Rminusy + Rconvz + Rplusx + Rplusy +
Rplusz;
        H(i,j,k) = (1-
(tstar/cp(i,j,k))*Rtotal)*Ho(i,j,k)+tstar*(...
        Rconvx*BC1(3)+Rplusx*(Ho(i+1,j,k)-
f(i+1,j,k)*L)/cp(i+1,j,k)+...
        Rminusy*(Ho(i,j-1,k)-f(i,j-1,k)*L)/cp(i,j-
1,k)+Rplusy*(Ho(i,j+1,k)-f(i,j+1,k)*L)/cp(i,j+1,k)+...
        Rconvz*BC5(3)+Rplusz*(Ho(i,j,k+1)-
f(i,j,k+1)*L)/cp(i,j,k+1));
    end
elseif isnan(T(i-1,j,k)) && isnan(T(i,j,k+1))
    if BC1(1) == 0 || BC6(1) == 0 % Edge 4
    else
        tstar = dt/rho(i,j,k);
        Rconvx = BC1(2)/dx;
        Rconvz = BC6(2)/dz;
        Rplusx = 1/(dx*(Rx(i+1,j,k)+Rx(i,j,k)));
        Rminusy = 1/(dy*(Ry(i,j-1,k)+Ry(i,j,k)));
        Rplusy = 1/(dy*(Ry(i,j+1,k)+Ry(i,j,k)));
        Rminusz = 1/(dz*(Rz(i,j,k-1)+Rz(i,j,k)));
        Rtotal = Rconvx + Rminusy + Rminusz + Rplusx + Rplusy +
Rconvz;
        H(i,j,k) = (1-
(tstar/cp(i,j,k))*Rtotal)*Ho(i,j,k)+tstar*(...
        Rconvx*BC1(3)+Rplusx*(Ho(i+1,j,k)-
f(i+1,j,k)*L)/cp(i+1,j,k)+...
        Rminusy*(Ho(i,j-1,k)-f(i,j-1,k)*L)/cp(i,j-
1,k)+Rplusy*(Ho(i,j+1,k)-f(i,j+1,k)*L)/cp(i,j+1,k)+...
        Rminusz*(Ho(i,j,k-1)-f(i,j,k-1)*L)/cp(i,j,k-
1)+Rconvz*BC6(3));
    end
elseif isnan(T(i+1,j,k)) && isnan(T(i,j-1,k))
    if BC2(1) == 0 || BC3(1) == 0 % Edge 5
    else
        tstar = dt/rho(i,j,k);
        Rconvx = BC2(2)/dx;
        Rconvy = BC3(2)/dy;
        Rminusx = 1/(dx*(Rx(i-1,j,k)+Rx(i,j,k)));
        Rplusy = 1/(dy*(Ry(i,j+1,k)+Ry(i,j,k)));
        Rminusz = 1/(dz*(Rz(i,j,k-1)+Rz(i,j,k)));

```

```

Rplusz = 1/(dz*(Rz(i,j,k+1)+Rz(i,j,k)));
Rtotal = Rminusx + Rconvy + Rminusz + Rconvx + Rplusy +
Rplusz;
    H(i,j,k) = (1-
(tstar/cp(i,j,k))*Rtotal)*Ho(i,j,k)+tstar*(...
    Rminusx*(Ho(i-1,j,k)-f(i-1,j,k)*L)/cp(i-
1,j,k)+Rconvx*BC2(3)+...
    Rconvy*BC3(3)+Rplusy*(Ho(i,j+1,k)-
f(i,j+1,k)*L)/cp(i,j+1,k)+...
    Rminusz*(Ho(i,j,k-1)-f(i,j,k-1)*L)/cp(i,j,k-
1)+Rplusz*(Ho(i,j,k+1)-f(i,j,k+1)*L)/cp(i,j,k+1));
    end
elseif isnan(T(i+1,j,k)) && isnan(T(i,j+1,k))
    if BC2(1) == 0 || BC4(1) == 0 % Edge 6
    else
        tstar = dt/rho(i,j,k);
        Rconvx = BC2(2)/dx;
        Rconvy = BC4(2)/dy;
        Rminusx = 1/(dx*(Rx(i-1,j,k)+Rx(i,j,k)));
        Rminusy = 1/(dy*(Ry(i,j-1,k)+Ry(i,j,k)));
        Rminusz = 1/(dz*(Rz(i,j,k-1)+Rz(i,j,k)));
        Rplusz = 1/(dz*(Rz(i,j,k+1)+Rz(i,j,k)));
        Rtotal = Rminusx + Rminusy + Rminusz + Rconvx + Rconvy +
Rplusz;
        H(i,j,k) = (1-
(tstar/cp(i,j,k))*Rtotal)*Ho(i,j,k)+tstar*(...
            Rminusx*(Ho(i-1,j,k)-f(i-1,j,k)*L)/cp(i-
1,j,k)+Rconvx*BC2(3)+...
            Rminusy*(Ho(i,j-1,k)-f(i,j-1,k)*L)/cp(i,j-
1,k)+Rconvy*BC4(3)+...
            Rminusz*(Ho(i,j,k-1)-f(i,j,k-1)*L)/cp(i,j,k-
1)+Rplusz*(Ho(i,j,k+1)-f(i,j,k+1)*L)/cp(i,j,k+1));
        end
elseif isnan(T(i+1,j,k)) && isnan(T(i,j,k-1))
    if BC2(1) == 0 || BC5(1) == 0 % Edge 7
    else
        tstar = dt/rho(i,j,k);
        Rconvx = BC2(2)/dx;
        Rconvz = BC5(2)/dz;
        Rminusx = 1/(dx*(Rx(i-1,j,k)+Rx(i,j,k)));
        Rminusy = 1/(dy*(Ry(i,j-1,k)+Ry(i,j,k)));
        Rplusy = 1/(dy*(Ry(i,j+1,k)+Ry(i,j,k)));
        Rplusz = 1/(dz*(Rz(i,j,k+1)+Rz(i,j,k)));
        Rtotal = Rminusx + Rminusy + Rconvz + Rconvx + Rplusy +
Rplusz;
        H(i,j,k) = (1-
(tstar/cp(i,j,k))*Rtotal)*Ho(i,j,k)+tstar*(...
            Rminusx*(Ho(i-1,j,k)-f(i-1,j,k)*L)/cp(i-
1,j,k)+Rconvx*BC2(3)+...
            Rminusy*(Ho(i,j-1,k)-f(i,j-1,k)*L)/cp(i,j-
1,k)+Rplusy*(Ho(i,j+1,k)-f(i,j+1,k)*L)/cp(i,j+1,k)+...
            Rconvz*BC5(3)+Rplusz*(Ho(i,j,k+1)-
f(i,j,k+1)*L)/cp(i,j,k+1));
        end
elseif isnan(T(i+1,j,k)) && isnan(T(i,j,k+1))
    if BC2(1) == 0 || BC6(1) == 0 % Edge 8
    else
        tstar = dt/rho(i,j,k);

```

```

Rconvx = BC2(2)/dx;
Rconvz = BC6(2)/dz;
Rminusx = 1/(dx*(Rx(i-1,j,k)+Rx(i,j,k)));
Rminusy = 1/(dy*(Ry(i,j-1,k)+Ry(i,j,k)));
Rplusy = 1/(dy*(Ry(i,j+1,k)+Ry(i,j,k)));
Rminusz = 1/(dz*(Rz(i,j,k-1)+Rz(i,j,k)));
Rtotal = Rminusx + Rminusy + Rminusz + Rconvx + Rplusy +
Rconvz;
    H(i,j,k) = (1-
(tstar/cp(i,j,k))*Rtotal)*Ho(i,j,k)+tstar*(...
        Rminusx*(Ho(i-1,j,k)-f(i-1,j,k)*L)/cp(i-
1,j,k)+Rconvx*BC2(3)+...
        Rminusy*(Ho(i,j-1,k)-f(i,j-1,k)*L)/cp(i,j-
1,k)+Rplusy*(Ho(i,j+1,k)-f(i,j+1,k)*L)/cp(i,j+1,k)+...
        Rminusz*(Ho(i,j,k-1)-f(i,j,k-1)*L)/cp(i,j,k-
1)+Rconvz*BC6(3));
    end
elseif isnan(T(i,j-1,k)) && isnan(T(i,j,k-1))
    if BC3(1) == 0 || BC5(1) == 0 % Edge 9
    else
        tstar = dt/rho(i,j,k);
        Rconvy = BC3(2)/dy;
        Rconvz = BC5(2)/dz;
        Rminusx = 1/(dx*(Rx(i-1,j,k)+Rx(i,j,k)));
        Rplusx = 1/(dx*(Rx(i+1,j,k)+Rx(i,j,k)));
        Rplusy = 1/(dy*(Ry(i,j+1,k)+Ry(i,j,k)));
        Rplusz = 1/(dz*(Rz(i,j,k+1)+Rz(i,j,k)));
        Rtotal = Rminusx + Rconvy + Rconvz + Rplusx + Rplusy +
Rplusz;
        H(i,j,k) = (1-
(tstar/cp(i,j,k))*Rtotal)*Ho(i,j,k)+tstar*(...
            Rminusx*(Ho(i-1,j,k)-f(i-1,j,k)*L)/cp(i-
1,j,k)+Rplusx*(Ho(i+1,j,k)-f(i+1,j,k)*L)/cp(i+1,j,k)+...
            Rconvy*BC3(3)+Rplusy*(Ho(i,j+1,k)-
f(i,j+1,k)*L)/cp(i,j+1,k)+...
            Rconvz*BC5(3)+Rplusz*(Ho(i,j,k+1)-
f(i,j,k+1)*L)/cp(i,j,k+1));
        end
    elseif isnan(T(i,j-1,k)) && isnan(T(i,j,k+1))
        if BC3(1) == 0 || BC6(1) == 0 % Edge 10
        else
            tstar = dt/rho(i,j,k);
            Rconvy = BC3(2)/dy;
            Rconvz = BC6(2)/dz;
            Rminusx = 1/(dx*(Rx(i-1,j,k)+Rx(i,j,k)));
            Rplusx = 1/(dx*(Rx(i+1,j,k)+Rx(i,j,k)));
            Rplusy = 1/(dy*(Ry(i,j+1,k)+Ry(i,j,k)));
            Rminusz = 1/(dz*(Rz(i,j,k-1)+Rz(i,j,k)));
            Rtotal = Rminusx + Rconvy + Rminusz + Rplusx + Rplusy +
Rconvz;
            H(i,j,k) = (1-
(tstar/cp(i,j,k))*Rtotal)*Ho(i,j,k)+tstar*(...
                Rminusx*(Ho(i-1,j,k)-f(i-1,j,k)*L)/cp(i-
1,j,k)+Rplusx*(Ho(i+1,j,k)-f(i+1,j,k)*L)/cp(i+1,j,k)+...
                Rconvy*BC3(3)+Rplusy*(Ho(i,j+1,k)-
f(i,j+1,k)*L)/cp(i,j+1,k)+...
                Rminusz*(Ho(i,j,k-1)-f(i,j,k-1)*L)/cp(i,j,k-
1)+Rconvz*BC6(3));

```

```

end
elseif isnan(T(i,j+1,k)) && isnan(T(i,j,k-1))
    if BC4(1) == 0 || BC5(1) == 0 % Edge 11
    else
        tstar = dt/rho(i,j,k);
        Rconvy = BC4(2)/dy;
        Rconvz = BC5(2)/dz;
        Rminusx = 1/(dx*(Rx(i-1,j,k)+Rx(i,j,k)));
        Rplusx = 1/(dx*(Rx(i+1,j,k)+Rx(i,j,k)));
        Rminusy = 1/(dy*(Ry(i,j-1,k)+Ry(i,j,k)));
        Rplusz = 1/(dz*(Rz(i,j,k+1)+Rz(i,j,k)));
        Rtotal = Rminusx + Rminusy + Rconvz + Rplusx + Rconvy +
Rplusz;
        H(i,j,k) = (1-
(tstar/cp(i,j,k))*Rtotal)*Ho(i,j,k)+tstar*(...
        Rminusx*(Ho(i-1,j,k)-f(i-1,j,k)*L)/cp(i-
1,j,k)+Rplusx*(Ho(i+1,j,k)-f(i+1,j,k)*L)/cp(i+1,j,k)+...
        Rminusy*(Ho(i,j-1,k)-f(i,j-1,k)*L)/cp(i,j-
1,k)+Rconvy*BC4(3)+...
        Rconvz*BC5(3)+Rplusz*(Ho(i,j,k+1)-
f(i,j,k+1)*L)/cp(i,j,k+1));
    end
elseif isnan(T(i,j+1,k)) && isnan(T(i,j,k+1))
    if BC4(1) == 0 || BC6(1) == 0 % Edge 12
    else
        tstar = dt/rho(i,j,k);
        Rconvy = BC4(2)/dy;
        Rconvz = BC6(2)/dz;
        Rminusx = 1/(dx*(Rx(i-1,j,k)+Rx(i,j,k)));
        Rplusx = 1/(dx*(Rx(i+1,j,k)+Rx(i,j,k)));
        Rminusy = 1/(dy*(Ry(i,j-1,k)+Ry(i,j,k)));
        Rminusz = 1/(dz*(Rz(i,j,k-1)+Rz(i,j,k)));
        Rtotal = Rminusx + Rminusy + Rminusz + Rplusx + Rconvy +
Rconvz;
        H(i,j,k) = (1-
(tstar/cp(i,j,k))*Rtotal)*Ho(i,j,k)+tstar*(...
        Rminusx*(Ho(i-1,j,k)-f(i-1,j,k)*L)/cp(i-
1,j,k)+Rplusx*(Ho(i+1,j,k)-f(i+1,j,k)*L)/cp(i+1,j,k)+...
        Rminusy*(Ho(i,j-1,k)-f(i,j-1,k)*L)/cp(i,j-
1,k)+Rconvy*BC4(3)+...
        Rminusz*(Ho(i,j,k-1)-f(i,j,k-1)*L)/cp(i,j,k-
1)+Rconvz*BC6(3));
    end
elseif isnan(T(i-1,j,k))
    if BC1(1)==1
        tstar = dt/rho(i,j,k);
        Rconvx = BC1(2)/dx;
        Rplusx = 1/(dx*(Rx(i+1,j,k)+Rx(i,j,k)));
        Rminusy = 1/(dy*(Ry(i,j-1,k)+Ry(i,j,k)));
        Rplusy = 1/(dy*(Ry(i,j+1,k)+Ry(i,j,k)));
        Rminusz = 1/(dz*(Rz(i,j,k-1)+Rz(i,j,k)));
        Rplusz = 1/(dz*(Rz(i,j,k+1)+Rz(i,j,k)));
        Rtotal = Rconvx + Rminusy + Rminusz + Rplusx + Rplusy +
Rplusz;
        H(i,j,k) = (1-
(tstar/cp(i,j,k))*Rtotal)*Ho(i,j,k)+tstar*(...
        Rplusx*(Ho(i+1,j,k)-
f(i+1,j,k)*L)/cp(i+1,j,k)+Rconvx*BC1(3)+...

```

```

Rminusy*(Ho(i,j-1,k)-f(i,j-1,k)*L)/cp(i,j-
1,k)+Rplusy*(Ho(i,j+1,k)-f(i,j+1,k)*L)/cp(i,j+1,k)+...
Rminusz*(Ho(i,j,k-1)-f(i,j,k-1)*L)/cp(i,j,k-
1)+Rplusz*(Ho(i,j,k+1)-f(i,j,k+1)*L)/cp(i,j,k+1));
elseif BC1(1)==0
else
error('Invalid or no boundary condition entered for BC1')
end
elseif isnan(T(i+1,j,k))
if BC2(1)==1
tstar = dt/rho(i,j,k);
Rconvx = BC2(2)/dx;
Rminusx = 1/(dx*(Rx(i-1,j,k)+Rx(i,j,k)));
Rminusy = 1/(dy*(Ry(i,j-1,k)+Ry(i,j,k)));
Rplusy = 1/(dy*(Ry(i,j+1,k)+Ry(i,j,k)));
Rminusz = 1/(dz*(Rz(i,j,k-1)+Rz(i,j,k)));
Rplusz = 1/(dz*(Rz(i,j,k+1)+Rz(i,j,k)));
Rtotal = Rminusx + Rminusy + Rminusz + Rconvx + Rplusy +
Rplusz;
H(i,j,k) = (1-
(tstar/cp(i,j,k))*Rtotal)*Ho(i,j,k)+tstar*(...
Rminusx*(Ho(i-1,j,k)-f(i-1,j,k)*L)/cp(i-
1,j,k)+Rconvx*BC2(3)+...
Rminusy*(Ho(i,j-1,k)-f(i,j-1,k)*L)/cp(i,j-
1,k)+Rplusy*(Ho(i,j+1,k)-f(i,j+1,k)*L)/cp(i,j+1,k)+...
Rminusz*(Ho(i,j,k-1)-f(i,j,k-1)*L)/cp(i,j,k-
1)+Rplusz*(Ho(i,j,k+1)-f(i,j,k+1)*L)/cp(i,j,k+1));
elseif BC2(1)==0
else
error('Invalid or no boundary condition entered for BC2')
end
elseif isnan(T(i,j-1,k))
if BC3(1)==1
tstar = dt/rho(i,j,k);
Rconvy = BC3(2)/dy;
Rminusx = 1/(dx*(Rx(i-1,j,k)+Rx(i,j,k)));
Rplusx = 1/(dx*(Rx(i+1,j,k)+Rx(i,j,k)));
Rplusy = 1/(dy*(Ry(i,j+1,k)+Ry(i,j,k)));
Rminusz = 1/(dz*(Rz(i,j,k-1)+Rz(i,j,k)));
Rplusz = 1/(dz*(Rz(i,j,k+1)+Rz(i,j,k)));
Rtotal = Rminusx + Rconvy + Rminusz + Rplusx + Rplusy +
Rplusz;
H(i,j,k) = (1-
(tstar/cp(i,j,k))*Rtotal)*Ho(i,j,k)+tstar*(...
Rminusx*(Ho(i-1,j,k)-f(i-1,j,k)*L)/cp(i-
1,j,k)+Rplusx*(Ho(i+1,j,k)-f(i+1,j,k)*L)/cp(i+1,j,k)+...
Rconvy*BC3(3)+Rplusy*(Ho(i,j+1,k)-
f(i,j+1,k)*L)/cp(i,j+1,k)+...
Rminusz*(Ho(i,j,k-1)-f(i,j,k-1)*L)/cp(i,j,k-
1)+Rplusz*(Ho(i,j,k+1)-f(i,j,k+1)*L)/cp(i,j,k+1));
elseif BC3(1)==0
else
error('Invalid or no boundary condition entered for BC3')
end
elseif isnan(T(i,j+1,k))
if BC4(1)==1
tstar = dt/rho(i,j,k);
Rconvy = BC4(2)/dy;

```

```

Rminusx = 1/(dx*(Rx(i-1,j,k)+Rx(i,j,k)));
Rplusx = 1/(dx*(Rx(i+1,j,k)+Rx(i,j,k)));
Rminusy = 1/(dy*(Ry(i,j-1,k)+Ry(i,j,k)));
Rminusz = 1/(dz*(Rz(i,j,k-1)+Rz(i,j,k)));
Rplusz = 1/(dz*(Rz(i,j,k+1)+Rz(i,j,k)));
Rtotal = Rminusx + Rminusy + Rminusz + Rplusx + Rconvy +
Rplusz;
    H(i,j,k) = (1-
(tstar/cp(i,j,k))*Rtotal)*Ho(i,j,k)+tstar*(...
        Rminusx*(Ho(i-1,j,k)-f(i-1,j,k)*L)/cp(i-
1,j,k)+Rplusx*(Ho(i+1,j,k)-f(i+1,j,k)*L)/cp(i+1,j,k)+...
        Rminusy*(Ho(i,j-1,k)-f(i,j-1,k)*L)/cp(i,j-
1,k)+Rconvy*BC4(3)+...
        Rminusz*(Ho(i,j,k-1)-f(i,j,k-1)*L)/cp(i,j,k-
1)+Rplusz*(Ho(i,j,k+1)-f(i,j,k+1)*L)/cp(i,j,k+1));
    elseif BC4(1)==0
    else
        error('Invalid or no boundary condition entered for BC4')
    end
elseif isnan(T(i,j,k-1))
    if BC5(1)==1
        tstar = dt/rho(i,j,k);
        Rconvz = BC5(2)/dz;
        Rminusx = 1/(dx*(Rx(i-1,j,k)+Rx(i,j,k)));
        Rplusx = 1/(dx*(Rx(i+1,j,k)+Rx(i,j,k)));
        Rminusy = 1/(dy*(Ry(i,j-1,k)+Ry(i,j,k)));
        Rplusy = 1/(dy*(Ry(i,j+1,k)+Ry(i,j,k)));
        Rplusz = 1/(dz*(Rz(i,j,k+1)+Rz(i,j,k)));
        Rtotal = Rminusx + Rminusy + Rconvz + Rplusx + Rplusy +
Rplusz;
        H(i,j,k) = (1-
(tstar/cp(i,j,k))*Rtotal)*Ho(i,j,k)+tstar*(...
            Rminusx*(Ho(i-1,j,k)-f(i-1,j,k)*L)/cp(i-
1,j,k)+Rplusx*(Ho(i+1,j,k)-f(i+1,j,k)*L)/cp(i+1,j,k)+...
            Rminusy*(Ho(i,j-1,k)-f(i,j-1,k)*L)/cp(i,j-
1,k)+Rplusy*(Ho(i,j+1,k)-f(i,j+1,k)*L)/cp(i,j+1,k)+...
            Rconvz*BC5(3)+Rplusz*(Ho(i,j,k+1)-
f(i,j,k+1)*L)/cp(i,j,k+1));
        elseif BC5(1)==0
        else
            error('Invalid or no boundary condition entered for BC5')
        end
elseif isnan(T(i,j,k+1))
    if BC6(1)==1
        tstar = dt/rho(i,j,k);
        Rconvz = BC6(2)/dz;
        Rminusx = 1/(dx*(Rx(i-1,j,k)+Rx(i,j,k)));
        Rplusx = 1/(dx*(Rx(i+1,j,k)+Rx(i,j,k)));
        Rminusy = 1/(dy*(Ry(i,j-1,k)+Ry(i,j,k)));
        Rplusy = 1/(dy*(Ry(i,j+1,k)+Ry(i,j,k)));
        Rminusz = 1/(dz*(Rz(i,j,k-1)+Rz(i,j,k)));
        Rtotal = Rminusx + Rminusy + Rminusz + Rplusx + Rplusy +
Rconvz;
        H(i,j,k) = (1-
(tstar/cp(i,j,k))*Rtotal)*Ho(i,j,k)+tstar*(...
            Rminusx*(Ho(i-1,j,k)-f(i-1,j,k)*L)/cp(i-
1,j,k)+Rplusx*(Ho(i+1,j,k)-f(i+1,j,k)*L)/cp(i+1,j,k)+...

```

```

Rminusy*(Ho(i,j-1,k)-f(i,j-1,k)*L)/cp(i,j-
1,k)+Rplusy*(Ho(i,j+1,k)-f(i,j+1,k)*L)/cp(i,j+1,k)+...
Rminusz*(Ho(i,j,k-1)-f(i,j,k-1)*L)/cp(i,j,k-
1)+Rconvz*BC6(3));
elseif BC6(1)==0
else
error('Invalid or no boundary condition entered for BC6')
end
else
tstar = dt/rho(i,j,k);
Rminusx = 1/(dx*(Rx(i-1,j,k)+Rx(i,j,k)));
Rplusx = 1/(dx*(Rx(i+1,j,k)+Rx(i,j,k)));
Rminusy = 1/(dy*(Ry(i,j-1,k)+Ry(i,j,k)));
Rplusy = 1/(dy*(Ry(i,j+1,k)+Ry(i,j,k)));
Rminusz = 1/(dz*(Rz(i,j,k-1)+Rz(i,j,k)));
Rplusz = 1/(dz*(Rz(i,j,k+1)+Rz(i,j,k)));
Rtotal = Rminusx + Rminusy + Rminusz + Rplusx + Rplusy +
Rplusz;
H(i,j,k) = (1-(tstar/cp(i,j,k))*Rtotal)*Ho(i,j,k)+tstar*(...
Rminusx*(Ho(i-1,j,k)-f(i-1,j,k)*L)/cp(i-
1,j,k)+Rplusx*(Ho(i+1,j,k)-f(i+1,j,k)*L)/cp(i+1,j,k)+...
Rminusy*(Ho(i,j-1,k)-f(i,j-1,k)*L)/cp(i,j-
1,k)+Rplusy*(Ho(i,j+1,k)-f(i,j+1,k)*L)/cp(i,j+1,k)+...
Rminusz*(Ho(i,j,k-1)-f(i,j,k-1)*L)/cp(i,j,k-
1)+Rplusz*(Ho(i,j,k+1)-f(i,j,k+1)*L)/cp(i,j,k+1));
end
end
end

%%
% Calculate temperature from H
for i = 1:p1
for j = 1:q1
for k = 1:r1
if isnan(H(i,j,k))
else
if H(i,j,k) > c1*Tm + L
T(i,j,k) = (H(i,j,k)-L)/c1 + Tm;
elseif H(i,j,k) < cs*Tm
T(i,j,k) = H(i,j,k)/cs + Tm;
else
T(i,j,k) = Tm;
end
end
end
end
end

% Calculate phase fraction from T
for i = 1:p1
for j = 1:q1
for k = 1:r1
if isnan(T(i,j,k))
else
if T(i,j,k) < Tm
f(i,j,k) = 0;

```

```

                elseif T(i,j,k) > Tm
                    f(i,j,k) = 1;
                else
                    f(i,j,k) = H(i,j,k)/L;
                end
            end
        end
    end
end

% Calculate cooling rate
for i = 1:p1
    for j = 1:q1
        for k = 1:r1
            if isnan(T(i,j,k))
            else
                cdTdt(i,j,k) = (Told(i,j,k)-T(i,j,k))/dt;
            end
        end
    end
end
end

```

8.2. Algorithm for thermal image analysis for 3D cryoprinting experiments

```

clear
clc
timedif = 9.2; %Time span over which pictures were taken (minutes)
picnum = 5302:5509; %Range of picture numbers
dt = timedif/length(picnum);
time = 0:dt:dt*(length(picnum)-1);
points = [156 149; 157 149; 158 149];% points to record temperature

for piccount = 1:length(picnum)
    for point = 1:3
        RedIdx = [];
        GreenIdx = [];
        BlueIdx = [];

        filename = strcat('IR_',string(picnum(piccount)),'.jpg');
        I = imread(filename);
        pointXY = points(point,:);

        pointRed = I(pointXY(1),pointXY(2),1);
        pointGreen = I(pointXY(1),pointXY(2),2);
        pointBlue = I(pointXY(1),pointXY(2),3);

        p = 1;
        for i = 52:190
            vectorRed(p) = I(229,i,1);
            vectorGreen(p) = I(229,i,2);
            vectorBlue(p) = I(229,i,3);
            p = p + 1;
        end
    end
end

```

```

        something = sqrt((double(vectorRed) - double(pointRed)).^2 +
(double(vectorGreen) - double(pointGreen)).^2 + (double(vectorBlue) -
double(pointBlue)).^2);
        Idx = find(something == min(something));

        for j = 1:length(vectorRed)
            Temp(j) = -20 + 40*(j-1)/(length(vectorRed)-1);
        end

        meanTemp(point) = mean(Temp(Idx));
    end
    Temprange(piccount) = mean(meanTemp);
    error(piccount) = std(meanTemp);

end

%%
figure(2)
errorbar(time, Temprange, error, 'o')
xlabel('Time (mins)')
ylabel('Temperature (degC)')
title('Experimental measurement of temperature at a given point')
hold on

picnum = 5347;
filename = strcat('IR_', string(picnum), '.jpg');
Ipic = imread(filename);
figure(3)
image(Ipic)
set(gcf, 'position', [550, 50, 500, 500])
hold on
scatter(points(1,2), points(1,1), 5, [0 0 0])
scatter(points(2,2), points(2,1), 5, [0 0 0])
scatter(points(3,2), points(3,1), 5, [0 0 0])

%%
clear
load('PlotProbes_10_line.mat')
%%
for probe = 4:6
    startcount = 3*probe;
    config = 1;
    count = startcount;
    idx = find(plotProbe(:, count, config)~=0, 1, 'first');
    tvec = dt*idx:dt:dt*totaltimesteps;
    coolingrate = plotProbe(idx:totaltimesteps, count, config);
    count = count - 1;
    phasefrac = plotProbe(idx:totaltimesteps, count, config);
    count = count - 1;
    Temp = plotProbe(idx:totaltimesteps, count, config);

    linestyle = '-';
    color = [0 0.4470 0.7410];

    figure(2)

```

```

% Temperature Plot
plot(tvec/60,Temp,'LineWidth',1,'LineStyle',linestyle,'Marker','none')
xlabel('Time [mins]')
startidx = find(~isnan(plotProbe(:,count,config)),1,'first');
xlim([tvec(startidx)/60 max(tvec/60)])
ylim([-10 20])
ylabel('Temperature [degC]')
title('Comparison of Temperatures at a location in layer 2')
hold on
    
```

end

legend('AA','B1','B2','B3')

8.3. Finite difference scheme for directional solidification model

In order to solve the problem outlined in the representative model, a numerically finite difference formulation was developed as described below.

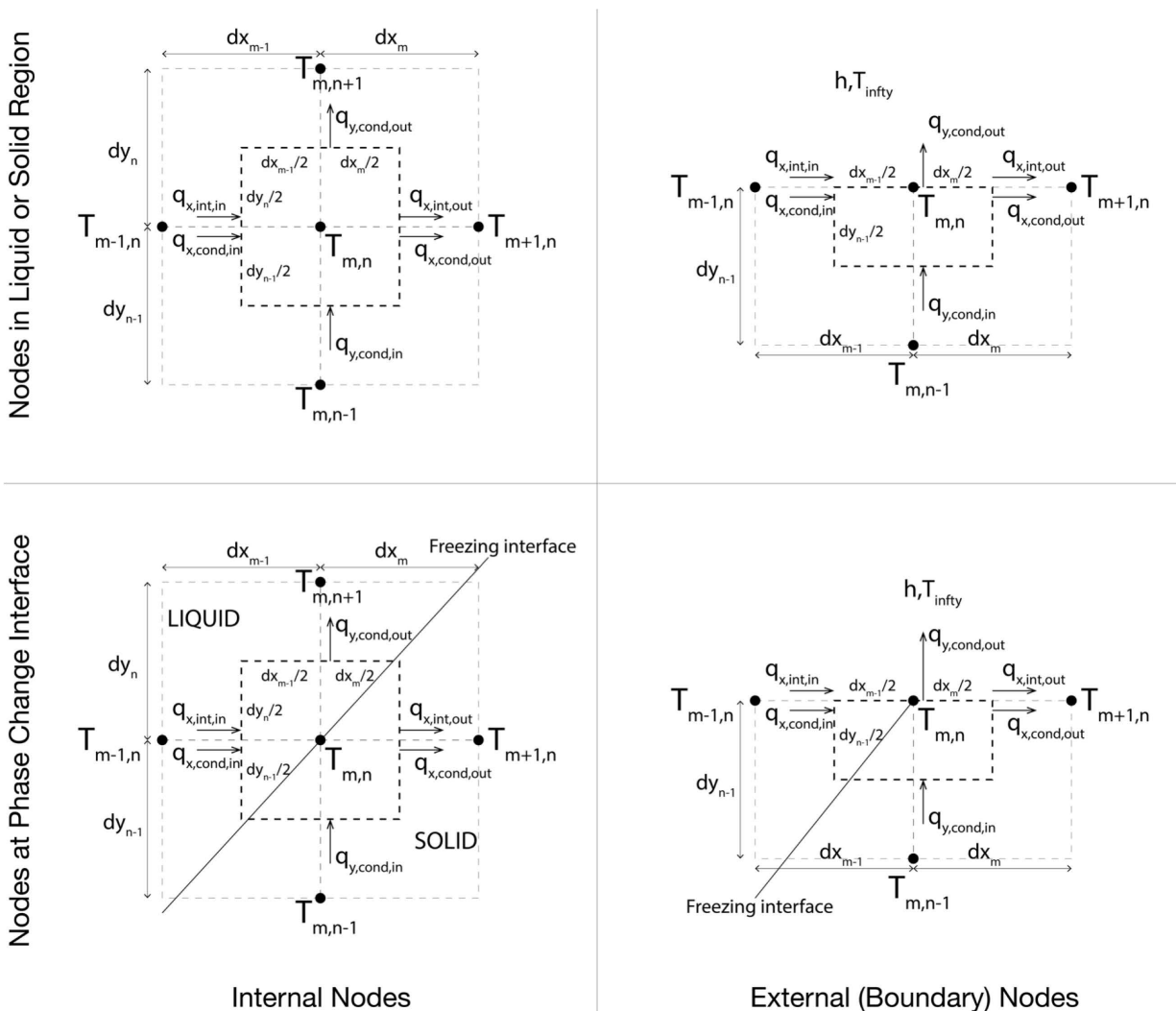


Figure A8.1: Finite difference formulation showing the different types of elements and nodes and various form of energy in and out of each element.

First, the control volume in Fig. 2 was divided into several rectangular finite difference elements with central nodes, (m, n) as shown in Fig. A1. Each element was assumed to have a uniform temperature corresponding to the temperature at the central node, $T_{m,n}$. By performing an energy balance on an element and solving for $T_{m,n}$ we get

$$T_{m,n}^i = \frac{(B_1 + C_1)T_{m-1,n}^i + B_2T_{m+1,n}^{i-1} + A_1T_{m,n-1}^i + A_2T_{m,n+1}^{i-1}}{C_1 + B_1 + B_2 + A_1 + A_2} \quad (A8.3.1)$$

$$A_1 = \frac{\alpha a}{dy_{n-1}}, \quad A_2 = \frac{\alpha a}{dy_n}, \quad B_1 = \frac{\alpha b}{dx_{m-1}}, \quad B_2 = \frac{\alpha b}{dx_m}, \quad C_1 = vb \quad (A8.3.2)$$

$$a = \frac{dx_m}{2} + \frac{dx_{m-1}}{2} \quad (A8.3.3)$$

$$b = \frac{dy_n}{2} + \frac{dy_{n-1}}{2} \quad (A8.3.4)$$

for an internal node in either the solid or liquid region. Where, i , designates the iteration number. Whereas, for an external node at the top boundary, the energy balance gives

$$T_{m,n}^i = \frac{(B_1 + C_1)T_{m-1,n}^i + B_2T_{m+1,n}^{i-1} + A_1T_{m,n-1}^i + D_1T_\infty}{C_1 + B_1 + B_2 + A_1 + D_1} \quad (A8.3.5)$$

$$D_1 = \frac{ha}{\rho c_p} \quad (A8.3.6)$$

$$b^* = \frac{dy_{n-1}}{2} \quad (A8.3.7)$$

Where b is replaced by b^* and all the other constants in Eqn. (A4.2) remain the same. For nodes at the phase change interface, the temperature is simply the phase change temperature

$$T_{m,n} = T_{ph} \quad (A8.3.8)$$

and the energy balance at the interface yields

$$vb(\rho_L c_{p,L}T_{m-1,n} - \rho_S c_{p,S}T_{m,n} + \rho_L L) + k_L \left(\frac{a}{dy_n}(T_{m,n+1} - T_{m,n}) - \frac{b}{dx_{m-1}}(T_{m,n} - T_{m-1,n}) \right) + k_S \left(\frac{b}{dx_m}(T_{m+1,n} - T_{m,n}) - \frac{a}{dy_{n-1}}(T_{m,n} - T_{m,n-1}) \right) = 0 = \epsilon \quad (A8.3.9)$$

for an internal node and

$$vb^*(\rho_L c_{p,L} T_{m-1,n} - \rho_S c_{p,S} T_{m,n} + \rho_L L) - k_L \left(\frac{b^*}{dx_{m-1}} (T_{m,n} - T_{m-1,n}) \right) - ha(T_{m,n} - T_\infty) + k_S \left(\frac{b^*}{dx_m} (T_{m+1,n} - T_{m,n}) - \frac{a}{dy_{n-1}} (T_{m,n} - T_{m,n-1}) \right) = 0 = \epsilon \quad (A8.3.10)$$

for an external (boundary) node.

8.4. Algorithm for directional solidification model

```

%%
clear
clc
close all
tic
%% Material properties
% Ice/Water(Solid) properties at -20degC
ps = 919.4; % Density (kg/m^3)
ks = 2.34; % Thermal conductivity (W/mK)
cs = 1943; % Specific Heat Capacity (J/kgK)
% Alginate (Approx. Water) (Liquid)
pl = 1000; % Density (kg/m^3)
kl = 0.6376; % Thermal conductivity (W/mK)
cl = 4186; % Specific Heat Capacity (J/kgK)
% Phase change quantities
Tm = 0; % Phase change temperature (K)
L = 333.6e3; % Latent heat of fusion (J/kg)
% Calculated quantities
as = ks/(ps*cs); % Solid thermal diffusivity (m^2/s)
al = kl/(pl*cl); % Liquid thermal diffusivity (m^2/s)

% Properties of Stainless-Steel slide
kss = 15; % Thermal Conductivity (W/mK)
pss = 7700; % Density (kg/m^3)
css = 500; % Specific Heat Capacity (J/kgK)
dss = 1.25e-3; % Slide Thickness (m)
ass = kss/(pss*css); % Solid thermal diffusivity (m^2/s)
Rcs = 0; % Contact resistance per unit area

% Physical conditions
TH = 40; % Hot side temperature (degC)
TC = -40; % Cold side temperature (degC)
Tinf = 20; % Room temperature for convection (degC)
g = 4e-3; % gap between plates (m)
v = 1e-4; % Velocity of sample (m/s)
d = 1.5e-3; % Thickness of layer (m)
h = 0; % Assumed convection coefficient (W/m^2K)

%% Initialization of parameters
grad = (TH-TC)/g; % gradient within the gap (degC/m)
n = 50; % number of y divisions
n2 = 10; % number of y stainless divisions

```

```

l = 2*g; % length of x to solve over to simulate
condition of x = inf
dy1 = d/n; % size of y mesh
dy2 = dss/n2; % size of y stainless mesh
m = 0; % Initializing dx step size
x(1) = 0; % Initializing x matrix
y(1) = 0; % Initializing y matrix

for i = 1:n2 % construction of y matrix for ss
    y(i+1) = y(i) + dy2;
    dy(i) = y(i+1)-y(i);
end

for i = n2+1:n+n2 % construction of y matrix for sample
    y(i+1) = y(i) + dy1;
    dy(i) = y(i+1)-y(i);
end

xm = (TH-Tm)/grad; % location of start of freezing

while 1 % dx mesh size before the freezing interface
    m = m + 1;
    dx(m) = dy1;
    x(m+1) = x(m)+dx(m);
    if x(m+1) > xm+0.75e-3
        m = m - 1;
        break
    end
end
while 1 % dx mesh size around the freezing interface
    m = m + 1;
    dx(m) = dy1/20;
    x(m+1) = x(m)+dx(m);
    if x(m+1) > xm+2e-3
        m = m - 1;
        break
    end
end
while 1 % dx mesh size after the freezing interface but within gap
    m = m + 1;
    dx(m) = dy1;
    x(m+1) = x(m)+dx(m);
    if x(m+1) > g
        break
    end
end
while 1 % dx mesh size after the gap interface
    m = m + 1;
    dx(m) = dy1;
    x(m+1) = x(m)+dx(m);
    if x(m+1) > l
        break
    end
end

mx = length(x); % number of x nodes
ny = length(y); % number of y nodes

```

```

T = TH*ones(mx,ny);           % Initialization of the temperature matrix
T(mx,:) = TC;                 % Boundary condition at x = infty

e = 1e-5;                      % Temperature error criteria for Gauss-Siedel
iteration scheme

sidx = xlsread('SSS_v1_d15_c2_ad.xlsx'); % load presaved s location
to start iteration
ds = round((sidx-sidx(1)));
% [val,idx] = min(abs(x-xm)); % location of freezing
interface on y=0
% sidx(1) = idx;
% sidx = sidx(1) + ds; % initial assumption of
interface location
% for i = 2:n+1
%     sidx(i) = sidx(i-1)+1;
% end

for i = 2:m % Temperature matrix based on
assumed interface location
    for j = 1:n2+1
        T(i,j) = TH + (TC-TH)*x(i)/g;
        if T(i,j) < TC
            T(i,j) = TC;
        end
    end
    for j = n2+2:ny
        inter = sidx(j-n2);
        if i < inter
            T(i,j) = TH + (Tm-TH)*(i-1)/(inter-1);
        elseif i > inter
            T(i,j) = TC + (Tm-TC)*(mx-i)/(mx-inter);
        else
            T(i,j) = Tm;
        end
    end
end

Tn = T;
sh = 0;

figure(5)
surface(x,y,T', 'EdgeColor', 'none')
colorbar
xlim([0 1])
ylim([0 dss+d])
set(gcf, 'position', [20,300,1200,300])

%% Solving for the temperature distribution

for t = 1:1000

```

```

if t > 1          % Start changing s guesses after the first loop
    ds = round((sidx-sidx(1)));
    [val,idx] = min(abs(T(:,n2+1)-Tm));
    sidx(1) = idx;
    sidx = sidx(1)+ds;
    for jp = 2:ny-n2
        if abs(er(jp)) < 5e-3
            sidx(jp) = sidx(jp);           % No change in interface
        position if error criteria is satisfied
        elseif er(jp) > 0
            sidx(jp) = sidx(jp) + 1;      % increase interface position
        index if error is positive
        else
            if er(jp) <= 5e-3
                sidx(jp) = sidx(jp);      % no change interface position
            index
            else
                sidx(jp) = sidx(jp) - 1;  % decrease interface position
            index
            end
        end
    end
    for jp = 2:ny-n2
        interface shape is correct
        if sidx(jp) < max(sidx(1:jp-1))
            sidx(jp) = max(sidx(1:jp-1));
        end
    end
end

while 1          % solving for temperature distribution
    Tdiff = 0;
    for i=2:m
        for j=1:n2+1
            if j == 1 % solution for y=0 boundary
                a = (dx(i-1)/2+dx(i)/2);
                b = dy(j)/2;
                A2 = ass*a/dy(j);
                B1 = ass*b/dx(i-1);
                B2 = ass*b/dx(i);
                C1 = v*b;
                if x(i) >= g
                    Tn(i,j) = TC;
                else
                    Tn(i,j) = ((B1+C1)*Tn(i-1,j)+B2*T(i+1,j)+A2*T(i,j+1))/(C1+B1+B2+A2);
                    if abs(Tn(i,j) - T(i,j)) > Tdiff
                        Tdiff = abs(Tn(i,j) - T(i,j));
                    end
                end
            end
            else
                a = (dx(i-1)/2+dx(i)/2);
                b = (dy(j-1)/2+dy(j)/2);
                A1 = ass*a/dy(j-1);
                A2 = ass*a/dy(j);
                B1 = ass*b/dx(i-1);
                B2 = ass*b/dx(i);
                C1 = v*b;
            end
        end
    end
end

```

```

        Tn(i,j) = ((B1+C1)*Tn(i-1,j)+B2*T(i+1,j)+A1*Tn(i,j-
1)+A2*T(i,j+1))/(C1+B1+B2+A1+A2);
        if abs(Tn(i,j) - T(i,j)) > Tdiff
            Tdiff = abs(Tn(i,j) - T(i,j));
        end
    end
end

for j=n2+2:ny
    inter = sidx(j-n2);
    if j == ny % solution for y=d boundary
        a = (dx(i-1)/2+dx(i)/2);
        b = dy(j-1)/2;
        if i < inter % node is liquid
            A1 = al*a/dy(j-1);
            B1 = al*b/dx(i-1);
            B2 = al*b/dx(i);
            C1 = v*b;
            D1 = h*a/(pl*c1);
        elseif i > inter % node is solid
            A1 = as*a/dy(j-1);
            B1 = as*b/dx(i-1);
            B2 = as*b/dx(i);
            C1 = v*b;
            D1 = h*a/(ps*cs);
        end
        if i == inter % node is at interface
            Tn(i,j) = Tm;
        else % node is either side of interface
            Tn(i,j) = ((B1+C1)*Tn(i-1,j)+B2*T(i+1,j)+A1*Tn(i,j-
1)+D1*Tinf)/(C1+B2+D1+B1+A1);
            if abs(Tn(i,j) - T(i,j)) > Tdiff
                Tdiff = abs(Tn(i,j) - T(i,j));
            end
        end
    else % solution for between y boundaries
        a = (dx(i-1)/2+dx(i)/2);
        b = (dy(j-1)/2+dy(j)/2);
        if i < inter % node is liquid
            A1 = al*a/dy(j-1);
            A2 = al*a/dy(j);
            B1 = al*b/dx(i-1);
            B2 = al*b/dx(i);
            C1 = v*b;
        elseif i > inter % node is solid
            A1 = as*a/dy(j-1);
            A2 = as*a/dy(j);
            B1 = as*b/dx(i-1);
            B2 = as*b/dx(i);
            C1 = v*b;
        end
        if i == inter % node is at interface
            Tn(i,j) = Tm;
        else % node is either side of interface
            Tn(i,j) = ((B1+C1)*Tn(i-1,j)+B2*T(i+1,j)+A1*Tn(i,j-
1)+A2*T(i,j+1))/(C1+B1+B2+A1+A2);
            if abs(Tn(i,j) - T(i,j)) > Tdiff
                Tdiff = abs(Tn(i,j) - T(i,j));
            end
        end
    end
end

```

```

end
end
end
end

T = Tn;
if Tdiff < e
    break
end
end

er(1) = 0;
for jp = 2:ny-n2          % Solving the energy equation at the interface
    i = sidx(jp);
    j = n2+jp;
    if j == ny           % error at inerface at y=d boundary
        a = (dx(i-1)/2+dx(i)/2);
        b = dy(j-1)/2;
        er(jp) = v*b*(pl*cl*T(i-1,j)-ps*cs*T(i,j)+pl*L)-kl*(b/dx(i-
1)*(T(i,j)-T(i-1,j)))...
            -h*a*(T(i,j)-Tinf)+ks*(b/dx(i)*(T(i+1,j)-T(i,j))-a/dy(j-
1)*(T(i,j)-T(i,j-1)));
    else                 % error at interface between y boundaries
        a = (dx(i-1)/2+dx(i)/2);
        b = (dy(j-1)/2+dy(j)/2);
        er(jp) = v*b*(pl*cl*T(i-1,j)-
ps*cs*T(i,j)+pl*L)+kl*(a/dy(j)*(T(i,j+1)-T(i,j))-b/dx(i-1)*(T(i,j)-T(i-
1,j)))...
            +ks*(b/dx(i)*(T(i+1,j)-T(i,j))-a/dy(j-1)*(T(i,j)-T(i,j-1)));
    end
end

max(abs(er))

if max(abs(er)) < 0.05
    break
end

end

%% Calculating the freezing rate
for j = n2+1:ny
    i = sidx(j-n2);
    dTdt(j-n2) = v*abs((Tn(i+1,j)-Tn(i,j))/dx(i));
end

for jp = 1:ny-n2      % interface location matrix
    s(jp) = x(sidx(jp));
    yp(jp) = y(jp+n2);
end

sshift = max(s) - s(1)

toc

```

```
%% Plotting the results

figure(1)
surface(x,y,T,'EdgeColor','none')
colorbar
hold on
plot(s,yp,'- k','LineWidth',1.5)
dmar = dss*ones(1,length(x));
plot(x,dmar,'- w','LineWidth',1.5)
xlim([0 1])
ylim([0 dss+d])
set(gcf,'position',[20,300,1200,300])

figure(2)
plot(yp,er)

figure(3)
plot(s,yp,'- k','LineWidth',1.5)
xlim([s(1) s(length(s))])
ylim([dss d+dss])

figure(4)
plot(yp,smooth(dTdt),'LineWidth',1.5)
xlim([dss d+dss])
xlabel('y')
ylabel('cooling rate (degC/s)')
```